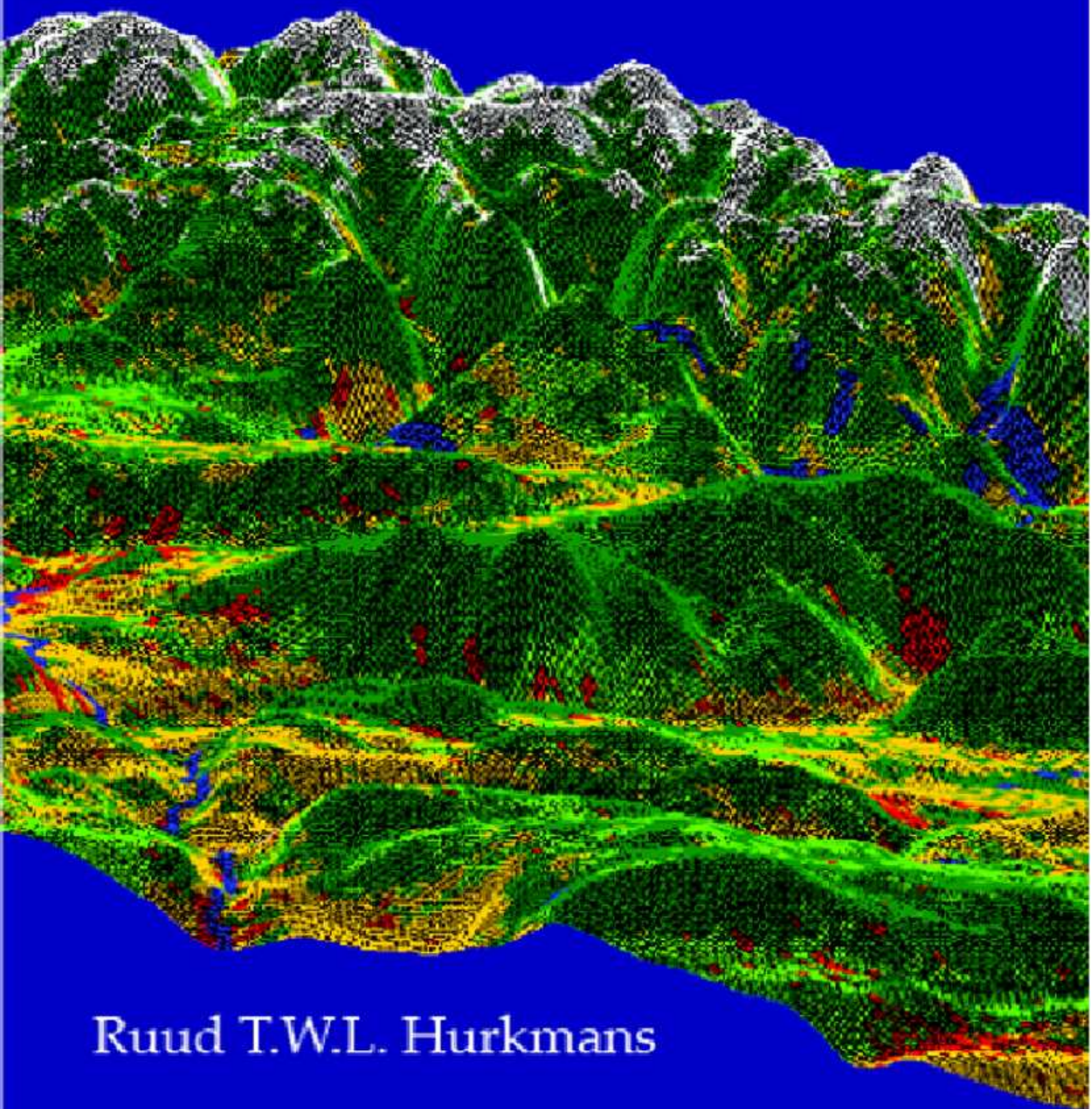


Effects of climate variability and land
use change on the water budget of
large river basins



Ruud T.W.L. Hurkmans

Effects of climate variability and land use change on the water budget of large river basins

Ruud T.W.L. Hurkmans

Promotoren:

Prof. dr. ir. P.A. Troch	Hoogleraar Hydrologie en Kwantitatief Waterbeheer, Wageningen Universiteit (1999–2005). Professor of Hydrology and Water Resources, Professor of Civil Engineering and Engineering Mechanics, University of Arizona, USA.
Prof. dr. ir. R. Uijlenhoet	Hoogleraar Hydrologie en Kwantitatief Waterbeheer, Wageningen Universiteit

Promotiecommissie:

Prof. dr. ir. M.F.P. Bierkens	Universiteit Utrecht
Prof. dr. B.J.J.M. van den Hurk	Universiteit Utrecht en KNMI, De Bilt
Dr. D. Jacob	Max Planck Institut für Meteorologie, Hamburg, Duitsland
Prof. dr. P. Kabat	Wageningen Universiteit

Dit onderzoek is uitgevoerd binnen de onderzoeksschool WIMEK-SENSE.

Effects of climate variability and land use change on the water budget of large river basins

Ruud T.W.L. Hurkmans

Proefschrift
ter verkrijging van de graad van doctor
op gezag van de rector magnificus
van Wageningen Universiteit,
Prof. dr. M.J. Kropff,
in het openbaar te verdedigen
op maandag 15 juni 2009
des namiddags te half twee in de Aula.

Hurkmans, R.T.W.L.

Effects of climate variability and land use change on the water budget of large river basins [Ph.D. thesis, Wageningen University, 2009, xviii+174 pp.]

In Dutch: Effecten van klimaatvariabiliteit en landgebruiksverandering op de waterhuishouding van stroomgebieden van grote rivieren. [proefschrift, Wageningen Universiteit, 2009, xviii+174 pp.]

ISBN 978-90-8585-398-5

Abstract

Due to global warming, the hydrologic behavior of the Rhine basin is expected to shift from a combined snowmelt and rainfall driven regime to a more rainfall dominated regime. Land use changes may reinforce the effects of this shift through urbanization, or counteract them through, for example, afforestation. One of the objectives of this thesis is to investigate and quantify these changes in the hydrological regime of the Rhine basin using hydrological modeling studies. The Variable Infiltration Capacity (VIC) model is used throughout this thesis as the hydrological model. Designed as a land surface model, the VIC model's physically-based formulation for land-atmosphere interactions offers the potential to more accurately simulate the partitioning of precipitation into evapotranspiration and streamflow compared to more simple water balance models. This potential is investigated by comparing the accuracy of streamflow simulations of the water balance model (STREAM) and the VIC model. Both models are applied to the Rhine river basin using downscaled re-analysis data as atmospheric forcing, and evaluated using observed streamflow and lysimeter data. We find that VIC is more robust and less dependent on model calibration. Whereas STREAM more effectively compensated for erroneous forcing data in the calibration period, VIC performed better than STREAM in the validation period, except for the Alpine part where both models have difficulties due to the complex terrain and surface reservoirs.

Subsequently, the VIC model is used to investigate the effects of projected land use change scenarios on mean and extreme river discharge in the Rhine basin at various spatial scales. Atmospheric forcing is kept constant and consists of the downscaled re-analysis data mentioned before. To simulate differences between vegetation types realistically, the model is modified to allow for bare soil evaporation and canopy evapotranspiration simultaneously in sparsely vegetated areas, as this is more appropriate to simulate seasonal effects. All projected land use change scenarios lead to an increase in streamflow. Streamflow at the basin outlet proved rather insensitive to land use changes, because over the entire basin affected areas are relatively small. Moreover, projected land use changes (urbanization and conversion of cropland into (semi-)natural land or forest) have opposite effects. At smaller scales, however, the effects can be considerable. In addition, the effects of climate change on Rhine river discharge are evaluated, keeping the land use constant. High-resolution (0.088°) regional climate scenarios are used to force the VIC model. These climate scenarios are based on model output from the ECHAM5-OM global climate model, which is in turn forced by three SRES emission scenar-

ios: A2, A1B and B1. Average streamflow, peak flows, low flows and several water balance terms are evaluated for both the first and second half of the 21st century. The first half of the century appears to be dominated by increased precipitation and streamflow throughout the year. During the second half of the century, a streamflow increase in winter/spring and a decrease in summer is found, similar to previous studies. Magnitudes of peak flows increase during both periods, that of streamflow droughts only during the second half of the century.

Another source of climate variability are interannual cycles of sea surface temperature, which influence the global climate through teleconnections. In the Colorado river basin, which has been experiencing extremely dry conditions during recent years, such teleconnections have been shown to have a significant influence on precipitation and streamflow. Time series of terrestrial water storage components, precipitation and discharge spanning 74 years are extracted from a simulation using the VIC model and related to climate indices that describe the variability of sea surface temperature and sea level pressure in the tropical and extra-tropical Pacific Ocean. Especially the low-frequency mode of the Pacific Decadal Oscillation (PDO) appears to be strongly correlated with deep soil moisture storage and surface water reservoir storage. During the negative PDO phase, these storage anomalies tend to be negative, and the “amplitudes” (mean absolute anomalies) of soil moisture, snow and discharge are lower compared to periods having positive PDO phases. If indeed a shift to a cool PDO phase occurred in at the end of the nineties, as data suggest, the current dry conditions in the Colorado basin may persist.

Finally, a distinguishing feature of the VIC model, its parameterization for small-scale heterogeneity in soil moisture variability is compared with alternative parameterizations in a small, Alpine sub-catchment of the Rhine, the Rietholzbach. As an alternative for the VIC parameterization, a hillslope-based parameterization is developed and compared to TOPMODEL and the VIC model. The effect of hillslope exposure on the resulting discharge is generally larger than that of spatial aggregation, although differences do occur in the generation of surface runoff. These are, however, generally compensated by decreasing baseflow. The changes in discharge are, therefore, small. Reduction of the amount of hillslopes in the catchment by classification based on hillslope similarity parameters yields similar results as when modeling individual hillslopes explicitly, which is much less the case when the catchment is modeled as an “open-book” or one large hillslope. Because the slopes in the Rietholzbach are generally steep, the influence of groundwater on soil moisture variability is relatively small and the VIC model is found to be able to accurately model catchment-averaged evapotranspiration and discharge.

Voorwoord / Preface

Voor u ligt het resultaat van ruim vier jaar promotie-onderzoek. Bij het tot stand komen van een proefschrift zijn natuurlijk veel meer mensen betrokken dan alleen ik, vandaar een woord van dank. Allereerst wil ik Peter Troch bedanken voor het mij er toe aanzetten überhaupt met promoveren te beginnen. Het eindgesprek van mijn afstudeervak (over een totaal ander onderwerp) eindigde met “en misschien kunnen we later nog eens wat samen onderzoeken”. Enkele jaren later was het dan zover; in september 2004 begon ik als AIO bij de leerstoelgroep Hydrologie & Kwantitatief Waterbeheer. Toen ik eenmaal op gang gekomen was nam Peter eind 2005 helaas de benen om naar Tucson, Arizona, te verhuizen. Ondanks het feit dat begeleiding via email en telefoon toch niet altijd even efficiënt bleek als “live” met elkaar te kunnen praten, pakte het allemaal goed uit. Ook bood het een mooie kans om een tijdje in Tucson te verblijven, waar ik twee keer enkele maanden dankbaar gebruik van heb gemaakt. Peter, bedankt voor dat alles, en ook de gastvrijheid waarmee ik in Tucson ontvangen werd. Also the people in Peter’s group: Maite, Steve, Matt: thanks for all your help in finding apartments, the lunches, the discussions and the fun. Matej, thanks for your help while I was in Tucson and for always promptly sending all kinds of data when requested.

Weer terug in Nederland werd Remko Uijlenhoet de nieuwe hoogleraar. Remko, ik ben erg blij dat je mij als enigszins “verweesde” AIO onder je hoede hebt genomen. Ondanks de grote hoeveelheid andere AIO’s maakte je tijd; bedankt voor de inspirerende gesprekken en voor de (wanneer dat nodig was) pragmatische manier van beslissingen nemen. Ook de andere collega’s bij de leerstoelgroepen Hydrologie en Kwantitatief Waterbeheer en Bodemfysica, Ecohydrologie en Grondwaterbeheer: bedankt voor de gezellige en inspirerende lunches en koffiepauzes, en het elk jaar weer erg geslaagde weekje EGU in Wenen. In het bijzonder Hidde, Patrick en Paul: bedankt voor het altijd klaarstaan om allerlei Matlab-, LaTeX- of willekeurige andere probleempjes te helpen oplossen. Eind 2007 werd Wilco Terink aangesteld op een sterk gerelateerd project, waardoor hij ook nauw betrokken was bij enkele hoofdstukken van dit proefschrift. Wilco, bedankt voor de prettige samenwerking! Verder ben ik Eddy Moors van de leerstoelgroep Aardsysteemkunde, die betrokken was via hetzelfde project, erg dankbaar voor de waardevolle discussies en suggesties. Ook Peter Verburg van de leerstoelgroep Landdynamiek wil ik graag bedanken voor het beschikbaarstellen van de landgebruiksveranderingsscenario’s en de waardevolle feedback op Hoofdstuk 3.

Ook buiten de universiteit zijn er veel mensen die hun data voor mij beschikbaar stelden, en/of met wie ik mocht samenwerken. Hoofdstuk 2 is voor een belangrijk deel tot stand gekomen met de hulp van Jeroen Aerts en Hans de Moel van de Vrije Universiteit Amsterdam: bedankt daarvoor! De atmosferische data die in vrijwel het hele proefschrift werd gebruikt is afkomstig van het Max Planck Institut für Meteorologie in Hamburg. From MPI-M, I'd like to thank Daniela Jacob for making available the climate model data and for the very nice and useful discussions we had in Hamburg, and Eva Starke for helping in using the data. Hendrik Buiteveld en Rita Lammersen van (tegenwoordig) Rijkswaterstaat Waterdienst, bedankt voor het beschikbaar stellen van alle geobserveerde data. Furthermore, I would like to thank Irene Lehner and Reto Stöckli from ETH Zürich for providing data from the Rietholzbach catchment.

In 2006 kreeg ik samen met Ryan Teuling, dankzij een reisbeurs van NWO, de kans om deel te nemen aan een veld-experiment in Australië. Ondanks het feit dat de resulterende data uiteindelijk niet in dit proefschrift terecht gekomen zijn was het een fantastische ervaring. Jeff, Rocco, Olivier and all the other participants of the NAFE campaign, thanks for the great time!

Tegen het einde van mijn AIO-periode kreeg ik de gelegenheid twee studenten (mede) te begeleiden. Marcel en Tjeerd, het was een genoegen om jullie te begeleiden en ik heb er zelf ook veel van geleerd. Tot slot, voor iedereen die heeft bijgedragen aan dit boekje maar hierboven niet genoemd is: hartelijk bedankt!

Het is natuurlijk onmogelijk om almaar aan een proefschrift te werken; de ontspanning tussendoor is ook erg belangrijk. Ik heb altijd met veel plezier bij de Ontzetting gespeeld, en later ook bij allerlei andere orkesten in de buurt. (oud)-Ontzeters, bedankt voor alle gezelligheid! In hetzelfde kader wil ik ook de (ex-)bewoners van Haarweg 217, waar ik altijd erg prettig gewoond heb, en het clubje van oud-roeiërs bedanken. Bart en Pieter, leuk dat jullie mijn paranimfen willen zijn! Rest mij nog mijn ouders, Carin en Paul te bedanken voor alle kansen die zij mij geboden hebben. Tenslotte, Rinske: voor mij zit het er bijna op, voor jou breken de laatste loodjes nu aan. Hopelijk heb jij in de komende tijd net zoveel aan mij als ik aan jou heb gehad!

Ruud

Acronyms and abbreviations used in this thesis

A1	SRES scenario type: “global economy”
A1B	SRES scenario type: “global economy with balanced energy sources”
A2	SRES scenario type: “continental market”
B1	SRES scenario type: “global cooperation”
B2	SRES scenario type: “regional communities”
CATHY	Catchment Hydrological model
CHR	International Commission for the Hydrology of the Rhine
CRB	Colorado River Basin
DEM	Digital Elevation Model
E	Nash-Sutcliffe modeling efficiency
ECHAM5-OM	Global climate model developed by MPI-M
ECMWF	European Centre for Medium-range Weather Forecasting
ENSO	El Niño Southern Oscillation
ERA	ECMWF re-analysis
ERA15	ECMWF re-analysis dataset (1979-1993)
ERA15d	Downscaled ERA15-data
ESMA	Explicit Soil Moisture Accounting models
FAO	United Nations Food and Agriculture Organisation
GEV	Generalized Extreme Value distribution
GCM	Global Climate Model
GHG	Greenhouse gas
GIS	Geographical Information System
GP	Generalized Pareto distribution
HBV	Hydrologiska Byråns Vattenbalansavdelning model
hsB	hillslope-storage Boussinesq model
hsB-LATS	hsB, coupled to an unsaturated zone model
IPCC	Intergovernmental Panel on Climate Change
LAI	Leaf Area Index
LPJ	Lund-Potsdam-Jena global vegetation model
LSM	Land surface model

MEI	Multi-variate ENSO index
MPI-M	Max Planck Institut für Meteorologie, Hamburg, Germany
NINO34	Index describing ENSO variability
NINO3	Index describing ENSO variability
NINO4	Index describing ENSO variability
NINO12	Index describing ENSO variability
PDM	Probability Distributed Model
PDO	Pacific Decadal Oscillation
PDV	Pacific Decadal Variability
PELCOM	Pan-European Land Cover Monitoring and Mapping
PNA	Pacific North-American pattern
MAM Q	Average annual maximum streamflow
Max Q	Maximum river streamflow
Mean Q	Average river streamflow
RCM	Regional Climate Model
REMO	Regional climate model developed by MPI-M
RVE	Relative Volume Error
SHE	Système Hydrologique Européen; physically based hydrological model
SRES	Special Report on Emissions Scenarios
SST	Sea Surface Temperature
STREAM	Spatial tools for river basins and environment and analysis of management options model
SVAT	Soil-Vegetation-Atmosphere-Transfer
SWE	Snow Water Equivalent
TOPMODEL	Topographic-index based hydrological model
TOPLATS	Land surface model based on TOPMODEL
TWS	Terrestrial Water Storage
USDA	United States Department of Agriculture
VIC	Variable Infiltration Capacity model

Contents

1	General introduction	1
1.1	Background	3
1.1.1	Hydrological modeling	3
1.1.2	Climate variability and climate change	5
1.1.3	Greenhouse gas emission scenarios	8
1.2	Study area	9
1.3	The Variable Infiltration Capacity model	12
1.3.1	Streamflow generation	12
1.3.2	Evapotranspiration	14
1.3.3	Streamflow routing	15
1.4	Problem description and thesis outline	15
2	Water balance versus land surface model in the simulation of Rhine river discharges	19
2.1	Introduction	21
2.2	Study area and data	22
2.3	Description of models	25
2.4	Model calibration	28
2.5	Model validation	30
2.6	Discussion and conclusions	38
3	Effects of land use changes on streamflow generation in the Rhine basin	41
3.1	Introduction	43
3.2	Study area, model and data	44
3.3	VIC model simulations of a single pixel	49
3.4	VIC model simulations for the entire basin	55
3.5	Summary and conclusions	61

4	Changes in streamflow in the Rhine basin under climate scenarios	65
4.1	Introduction	67
4.2	Data and model	68
4.2.1	Study area	68
4.2.2	Hydrological model	69
4.2.3	Atmospheric data	69
4.3	Methodology	71
4.3.1	Bias correction	71
4.3.2	Model calibration	74
4.4	Results	75
4.4.1	Spatial patterns of atmospheric variables	76
4.4.2	Mean streamflow	79
4.4.3	Water balance components	80
4.4.4	Extreme streamflow	83
4.5	Discussion	87
4.6	Conclusions	90
5	Effects of climate variability on water storage in the Colorado River Basin	91
5.1	Introduction	93
5.2	Study area and datasets	94
5.3	Results	98
5.3.1	Analysis of spatial averages	98
5.3.2	Analysis of distributed data	104
5.4	Summary and conclusions	107
6	A hillslope-based parameterization for sub-grid variability of topography	109
6.1	Introduction	111
6.2	Study area and data	112
6.3	Hydrological models	113
6.3.1	TOPMODEL	115
6.3.2	The hillslope-storage Boussinesq model	116
6.3.3	Unsaturated zone formulation	116
6.4	Methodology	119
6.4.1	Correction for hillslope exposure	120
6.4.2	Hillslope delineation and classification	122
6.5	Results	124
6.6	Summary and conclusions	132
7	General discussion	135
7.1	Introduction	137
7.2	Discussion of the hydrological model	137

7.3	Discussion of the climate and land use change scenarios	138
7.4	General conclusions	139
7.4.1	Effects of land use change	140
7.4.2	Effects of climate change	140
7.4.3	Effects of oscillations in ocean temperature	141
7.4.4	An alternative parameterization for small-scale variability of soil moisture	142
7.5	Directions for further research	142
8	Nederlandse samenvatting	145
8.1	Inleiding	147
8.2	Het hydrologisch model in perspectief	147
8.3	De landgebruiks- en klimaatveranderingsscenarios in perspectief	148
8.4	Algemene conclusies	150
8.4.1	Effecten van landgebruiksveranderingen	150
8.4.2	Effecten van klimaatveranderingen	151
8.4.3	Effecten van oscillaties in oceaantemperaturen	152
8.4.4	Een alternatieve parametrisatie voor kleinschalige bodemvochtvariabiliteit	153
	Appendix: Extreme value distributions	155
	Bibliography	157
	Curriculum Vitae	171
	List of publications	173

List of Figures

1.1	Schematic overview of global hydrological fluxes and stores.	3
1.2	Observed trends in global temperature, sea level and snow cover.	6
1.3	The greenhouse gas emission scenario families as defined by IPCC in the SRES-report.	8
1.4	GHG emission and global temperature evolution according to SRES scenarios.	9
1.5	The Rhine basin and its sub-basins.	11
1.6	Schematic description of the VIC model.	13
2.1	The Rhine basin and locations of streamflow gauges and lysimeters.	23
2.2	Climatologies of atmospheric input variables.	24
2.3	ERA15d versus CHR precipitation, aggregated over different periods.	25
2.4	Comparison of spatial patterns of temperature and precipitation.	26
2.5	Relation between soil moisture and baseflow in the VIC model.	27
2.6	Observed and simulated daily streamflow at Lobith for the calibration period.	30
2.7	Simulated discharge by VIC and STREAM forced by two precipitation sources.	31
2.8	Observed and simulated monthly discharge at eight locations in the Rhine basin.	33
2.9	Observed and simulated discharge at Lobith for three extreme events.	35
2.10	Extreme peak flows versus their return periods.	37
2.11	Monthly timeseries of observed and simulated evaporation.	38
3.1	Observed and simulated hydrographs at Lobith for the period 1994–2003.	46
3.2	Land use maps for the current situation and the four Eururalis scenarios in 2030.	48
3.3	Climatologies of water balance terms using the water balance mode.	50
3.4	Climatology of relative differences in streamflow for the modified model.	54
3.5	Climatology of relative differences in streamflow for the original model.	56
3.6	Annual maximum streamflow versus their return periods.	57
3.7	Annual maximum cumulative streamflow deficit.	58
3.8	Spatial pattern of differences in average surface runoff.	61
3.9	Spatial pattern of differences in average soil moisture content.	62

4.1	Schematic representation of the employed datasets and their use.	71
4.2	Bias correction results: mean monthly values.	73
4.3	Bias correction results: spatial patterns.	74
4.4	Time series of annual streamflow.	76
4.5	Difference in spatial patterns of precipitation.	77
4.6	Difference in spatial patterns of evapotranspiration.	78
4.7	Difference in spatial patterns of temperature.	79
4.8	Climatologies of streamflow differences.	81
4.9	Climatologies of water balance components.	82
4.10	Climatologies of differences in water balance components.	84
4.11	Contribution of snowmelt to streamflow.	84
4.12	Extreme peak flows.	85
4.13	Extreme streamflow droughts.	86
5.1	The Colorado River Basin.	95
5.2	Time series of hydrologic anomalies and climate indices.	96
5.3	Autocorrelation functions and power spectra.	97
5.4	Monthly correlations between hydrologic anomalies and climate indices.	99
5.5	Time series of specific months for soil moisture, NINO3.4 and PDO.	100
5.6	Time series of 24-month running means.	101
5.7	Correlation maps between hydrologic anomalies and NINO3.4.	105
5.8	Correlation maps between hydrologic anomalies and PDO.	106
5.9	Maps of standard deviations of anomalies.	107
6.1	Characteristics of the Rietholzbach catchment.	113
6.2	Observed time series of atmospheric forcing.	114
6.3	Hillslopes and topographic indices in the Rietholzbach.	118
6.4	Modeling of snow water equivalent.	120
6.5	Calibration and validation results for VIC and TOPMODEL.	121
6.6	Correction of potential evapotranspiration for slope and aspect.	122
6.7	Distributions of hillslope similarity parameters.	123
6.8	Monthly time series of evaporation and discharge for all models.	126
6.9	Monthly time series of water balance terms for all models.	127
6.10	Differences between aggregation levels for TOPMODEL.	129
6.11	Differences between aggregation levels for hsB.	130
6.12	Differences between aggregation levels for hsB-LATS.	131
6.13	Differences between aggregation levels for TOPLATS.	132

List of Tables

1.1	Tributaries of the Rhine basin and their characteristics.	10
2.1	Statistics of calibration and validation results at Lobith.	31
2.2	Performance of streamflow simulation at different locations in the Rhine basin.	32
2.3	Extreme peak flows and low flows in all model simulations and observations.	34
2.4	Simulated water balance terms and lysimeter observations.	36
3.1	Areal coverage of land use types in the Lahn sub-basin and the entire Rhine basin.	47
3.2	Classification of land use types in the different datasets and main parameter values.	49
3.3	Mean annual values of water balance terms in the original and modified VIC model.	52
3.4	Extreme flood peaks and low flows for the Lahn sub-basin.	59
3.5	Extreme flood peaks and low flows for the entire Rhine basin.	60
4.1	Overview of the employed atmospheric datasets.	70
4.2	Observed streamflow characteristics and calibration results.	75
4.3	Mean annual values of water balance components.	83
4.4	Streamflow drought statistics.	88
5.1	Average amplitudes of hydrologic anomalies during each PDO phase.	103
5.2	Correlation coefficients calculated separately for each PDO phase.	104
6.1	Classification of hillslopes.	124
6.2	Statistics of discharge simulation for all models.	125

Chapter 1

General introduction



1.1 Background

1.1.1 Hydrological modeling

The water cycle is of major importance to the global climate system. Water vapor in the atmosphere, for example, is the most important greenhouse gas. Liquid water in the atmosphere, on the other hand, reflects radiation through clouds and has a cooling effect (*Chahine*, 1992). Because evaporation of water requires a significant portion of incoming solar radiation, it also plays a role in the energy balance at the land surface (e.g. *Brutsaert*, 2005). Moreover, all major life forms, including human life, depend on water to sustain (*Oki and Kanae*, 2006). Figure 1.1 shows a schematic overview of the fluxes and storages in the hydrological cycle. A vast majority of liquid water is stored in the oceans: only about 2.5% of all water on earth is fresh water, and only a fraction of that is available to humans (*Oki and Kanae*, 2006). An important part of the terrestrial part of the hydrologic cycle is the partitioning of precipitation (falling as rain or snow) into evapotranspiration, infiltration and surface runoff. To a large extent, this partitioning is determined by the characteristics of the land surface: vegetation, soils, geology and topography (*Beven*, 2001). The amount of water that infiltrates and drains as surface runoff is of paramount importance because it determines peak flows (floodings) and groundwater discharge (baseflow), and therefore water scarcity during dry spells.

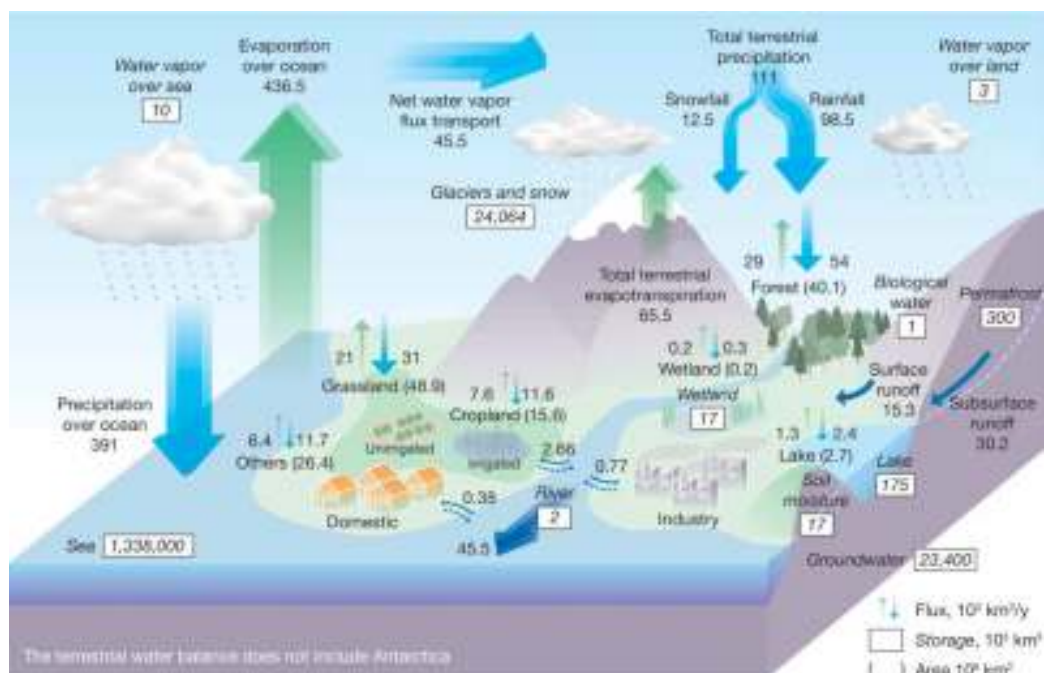


Figure 1.1: Schematic overview of global hydrological fluxes and stores in 1000 km^3 per year (for fluxes). Source: *Oki and Kanae* (2006).

How a catchment (i.e., an area of land that drains to one river and its tributaries) reacts to precip-

itation is still not fully understood, in spite of many advances in the science of hydrology (*Beven, 2001*). This has several reasons. Hydrological systems often behave highly non-linearly, and essential characteristics of the catchment, such as the hydraulic conductivity of the soil, are highly heterogeneous in space. Measurements of such characteristics are all too often only representative for a very small area (often a point), whereas usually the area of interest is much larger. To provide information about the behavior of a catchment, hydrological models have been developed using effective values of catchment characteristics. These effective values are often determined from model calibration using observations of the quantity that is being simulated. A hydrological model then offers a means for quantitative extrapolation or prediction into the future.

Generally, two types of hydrological models that are relevant to this thesis can be distinguished. One type is the rainfall-runoff model, which is designed to translate precipitation input to discharge output for a given catchment. The other type is the land surface model (LSM), which is designed to provide land surface boundary conditions for atmospheric models (Section 1.1.2).

Different rainfall-runoff models have been developed over the past decades (see Chapter 2 of *Beven (2001)* for an overview). Their main difference is the level of complexity that is involved. Some are physically-based and attempt to take into account as many as (sub)surface flow processes as possible. Examples are the SHE model (système Hydrologique Européen; *Abbott et al., 1986*) and CATHY (*Paniconi and Wood, 1993*). However, often they require (calibration of) many parameters and spatially detailed input data, and they are numerically so demanding that their application is barely feasible for large catchments (*te Linde et al., 2008*). On the other hand, more simplistic and conceptual models have been developed that require calibration of less parameters. These models are usually of the ESMA (explicit soil moisture accounting) type (*O'Connell, 1991*) and consist of some storage reservoirs with different delay functions to represent fast and slow runoff. Examples are the HBV model (*Bergström and Forsman, 1973*) and Rhineflow (*Kwadijk, 1993*). Because they are relatively easy to parameterize, they often perform as good as or better than complex, physically-based models in reproducing an observed hydrograph (*te Linde et al., 2008*). An intermediate type of rainfall-runoff models is basically of the ESMA type, but incorporates some statistical distribution that describes the spatial variability of runoff generation. Examples of this type are the Probability Distributed Model (PDM; *Moore and Clarke, 1981*), TOPMODEL (*Beven and Kirkby, 1979*) and also the Variable Infiltration Capacity model (VIC; *Liang et al., 1994*), although the latter was originally designed as a land surface model. Related to model complexity is the spatial discretization of the model, or whether the model is spatially distributed or lumped. The input data and parameters of complex-physically based models require them to be spatially distributed, whereas more simple, conceptual models can also be applied in a lumped way, further reducing computation time. This choice, of course, depends on the availability of atmospheric forcing data and the objectives of the modeling exercise.

The development of “interactive” LSMs started from a simple bucket type model developed by (*Manabe, 1969*). Before that, moisture conditions were prescribed to climate models, preventing important

soil moisture feedbacks to be captured by the models (Koster *et al.*, 2000). Advances in LSMs have mainly focused on their vertical structure with the inclusion of multiple soil layers (Hansen *et al.*, 1983), and a complex vegetation structure (Sellers *et al.*, 1986; Dickinson *et al.*, 1986). The description of the hydrological processes, however, long remained relatively simplistic due to the one-dimensional model structure. The influence of shallow groundwater tables on soil moisture contents was only incorporated recently (e.g. Liang *et al.*, 2003; Maxwell and Miller, 2005; Bierkens and van den Hurk, 2007; Fan *et al.*, 2007; Maxwell and Kollet, 2008), and in most cases this is still too computationally demanding for large-scale applications. Some LSMs have been developed, however, that incorporate a statistical parameterization for variability of runoff generation (see the previous paragraph). Examples are TOPLATS (Famiglietti and Wood, 1994), which is based on the TOPMODEL concept, and the VIC model. LSMs thus typically have a detailed and physically-based formulation for the calculation of evapotranspiration, because this is their main output to the climate model. Because evapotranspiration is inherently coupled to runoff and streamflow through the water balance, LSMs potentially simulate the amount of streamflow more accurately than models with a conceptual formulation for evapotranspiration as well. For example, the VIC model is in essence an LSM, but when it is coupled to an algorithm for streamflow routing it can and has been used for hydrological purposes as well (e.g. Hamlet *et al.*, 2007; Nijssen *et al.*, 1997; Sheffield and Wood, 2007). The VIC model is described in detail in Section 1.3.

1.1.2 Climate variability and climate change

Climate is defined as the “average weather”, where weather consists of surface variables such as precipitation, temperature and wind, and the averaging period is classically 30 years (see Appendix 1: “Glossary” of IPCC (2007)). The climate is not constant, but is changing constantly. Climate change is defined by the Intergovernmental Panel on Climate Change (IPCC) as follows:

“Climate change in IPCC usage refers to a change in the state of the climate that can be identified (e.g. using statistical tests) by changes in the mean and/or the variability of its properties, and that persists for an extended period, typically decades or longer. It refers to any change in climate over time, whether due to natural variability or as a result of human activity.” (IPCC, 2007)

Figure 1.2 shows observed trends in global average temperature, sea level and snow cover over the past 150 years. The global warming that can be seen in Figure 1.2a, can have major consequences for the global climate system (IPCC, 2007), and it is accelerated or inhibited by numerous feedbacks that are not yet fully understood. One important aspect is that warm air can contain more water vapor because its saturated vapor pressure is higher compared to colder air. Research indicates that this can accelerate the hydrological cycle (e.g. Trenberth, 1997a; Chahine, 1992). More precipitation will fall as rain instead of snow, and it is believed that precipitation will fall in more extreme events (Trenberth, 1997a). Hydrologically, this will have important consequences for river discharge, both in terms of extreme peak flows and low flows. Specifically for the Rhine basin (Section 1.2), average temperature

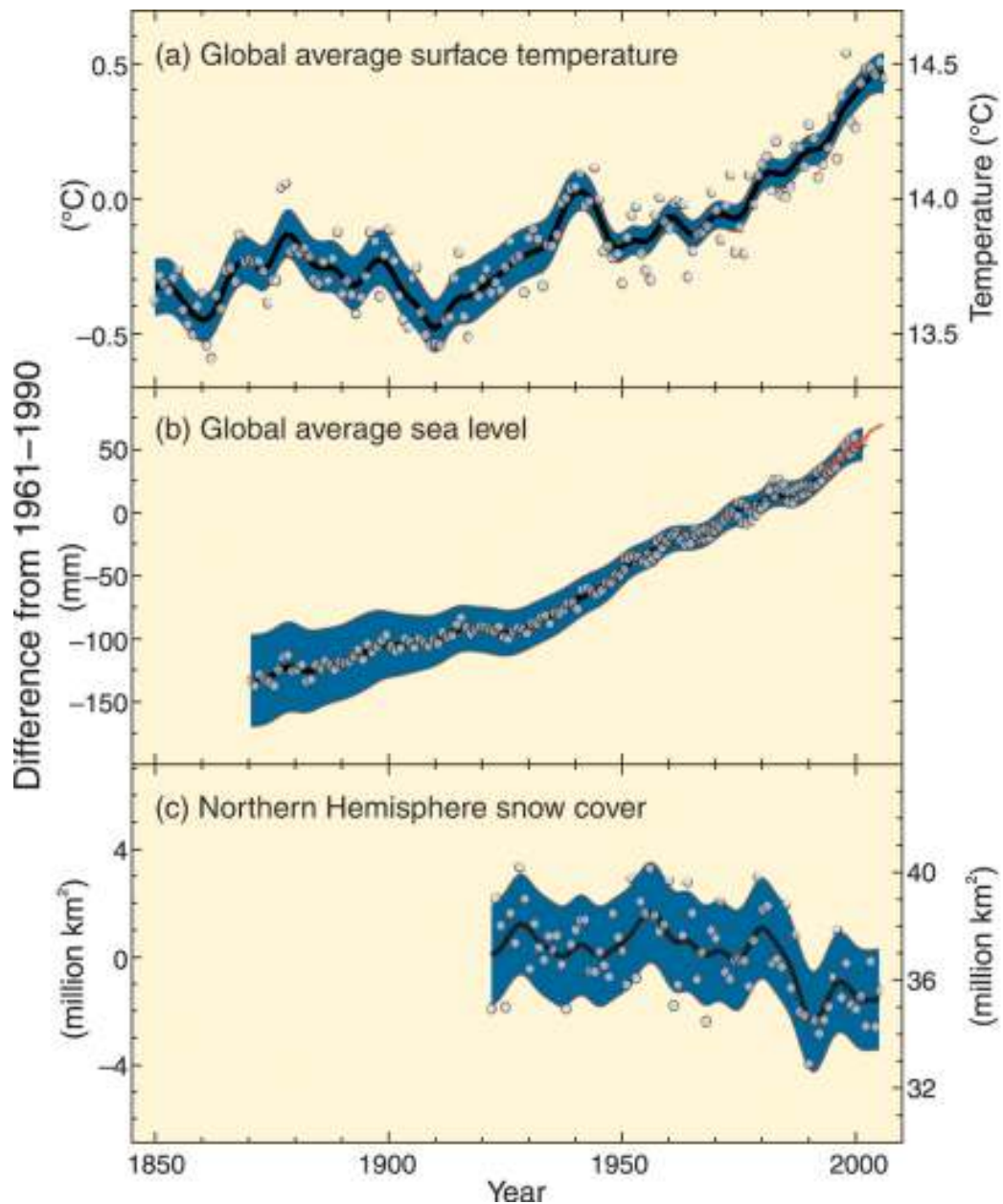


Figure 1.2: Observed trends in global temperature, sea level and snow cover over the past 150 years. Source: *IPCC (2007)*.

is expected to increase with 1.0°C to 2.4°C by 2050. This will cause the hydrological regime of the Rhine to shift from a combined rainfall-snowmelt system to a more rainfall-dominated system.

Global Climate Models (GCMs) are used to model the climate system and predict how the trends

shown in Figure 1.2 will develop in the future. Many different GCMs have been developed (e.g. Covey *et al.*, 2003; Reichler and Kim, 2008; IPCC, 2007), and the variability of their predictions is large. However, when observed trends are reproduced by such a model, the reliability of its predictions increases (Covey *et al.*, 2003). Because the spatial resolution of GCMs is too low for hydrological applications (hundreds of square kilometers) regional climate models (RCMs) have been developed to downscale GCM output. A RCM is typically nested in a GCM over the domain of interest (e.g. Jacob, 2001; Lorenz and Jacob, 2005).

On geological time scales, the global climate is mainly driven by cycles in the amount of solar radiation that reaches the earth. This, in turn, is controlled by various cycles in the activity of the sun, such as the amount of sunspots, and the distance between the sun and the earth (Milanković-cycles). However, experiments with GCMs suggest that the driving factor behind recent global warming are rising concentrations of CO₂ and other greenhouse gasses (GHGs), i.e., observed trends are only reproduced when trends in GHG-emissions are included (Arpe and Roeckner, 1999; Covey *et al.*, 2003). As a result, there is not only uncertainty related to the climate models themselves, but also to their forcing, which consists of greenhouse gas emissions and solar radiation, although the latter can be predicted relatively accurately. To ensure consistent model comparisons using identical forcing, a consistent set of GHG emission scenarios has been developed by the IPCC. These scenarios are described in more detail in Section 1.1.3. Climate scenarios that are based on these GHG emission scenarios have been widely used in climate studies since 2000, for climate model intercomparisons (e.g. Jacob *et al.*, 2007; Déqué *et al.*, 2007) and climate change impact assessments (e.g. Lenderink *et al.*, 2007; Ekström *et al.*, 2007). In addition to climate scenarios, scenarios of land use change have been developed, based on the same GHG-emission scenarios and the socio-economic developments that are associated with them (Verburg *et al.*, 2006a; Rounsevell *et al.*, 2006). An example of resulting land use maps can be found in Figure 3.2.

In addition to the above, climate variability is also driven by natural cycles with sometimes very long periods, in the order of decades. These cycles are related to sea surface temperature or sea level pressure in certain regions of the Pacific and Atlantic oceans. The physical processes behind these cycles is to date poorly understood, hence their predictability is low (e.g. Newman, 2007). A well-known example, with a relatively high frequency, is ENSO (El Niño Southern Oscillation), of which the positive and negative phases are called El Niño and La Niña respectively (Trenberth, 1997b). Less well known examples are the Pacific Decadal Oscillation (PDO; Mantua *et al.*, 1997) and the North Atlantic Oscillation (NAO; e.g., Johansson (2007)). In Europe, the influence of these cycles is relatively small (Bouwer *et al.*, 2006, 2008). In other parts of the world, however, their influence can be much bigger (e.g. Redmond and Koch, 1991; Andersen Jr. and Emanuel, 2008; Mason and Goddard, 2001). For example, in the Colorado River Basin (CRB), ENSO and PDO have been linked to precipitation and streamflow (Hidalgo and Dracup, 2003; Cañon *et al.*, 2007). Therefore, the CRB is the area of interest in Chapter 5, where the impact of low-frequency climate variability on different hydrologic variables is explored.

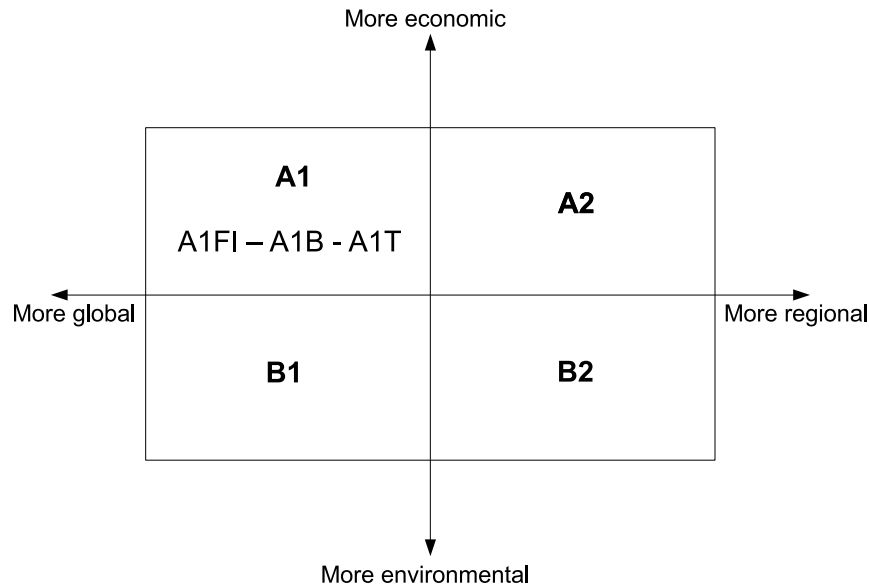


Figure 1.3: The greenhouse gas emission scenario families as defined by IPCC in the SRES-report.

1.1.3 Greenhouse gas emission scenarios

In 2000 the IPCC defined a group of consistent greenhouse gas (GHG) emission scenarios in the Special Report on Emission Scenarios (SRES; IPCC, 2000). Based on different alternative developments of energy and technology, about 40 different scenarios were created, which can be grouped in scenario “families”. Figure 1.3 schematically shows the main SRES-scenario families. Each family is based on a different storyline. The storylines for the different families are as follows:

- A1 family: a future world of very rapid economic growth, global population that peaks in mid-century and declines thereafter, and rapid introduction of new and more efficient technologies. The A1 family is further divided into three groups representing alternative developments of energy technology:
 - A1FI: fossil fuel intensive
 - A1B: balanced use of energy
 - A1T: predominantly non-fossil fuel
- A2 family: a very heterogeneous world with continuously increasing global population and regionally oriented economic growth that is more fragmented and slower than in other storylines.

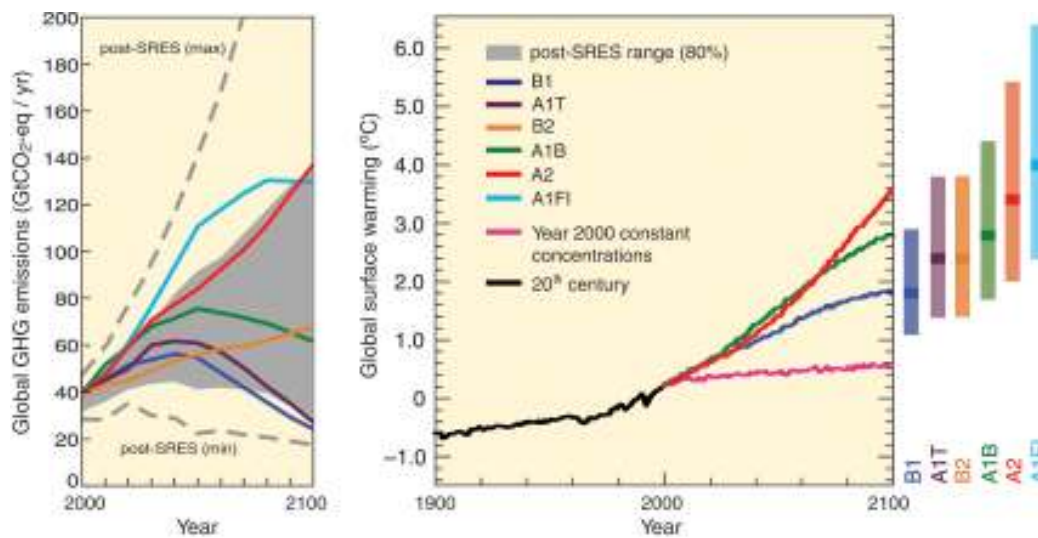


Figure 1.4: CO₂ emission and associated surface temperature rise according to the SRES greenhouse gas emission scenarios (IPCC, 2000). Source: IPCC (2007).

- B1 family: a convergent world with the same global population as in the A1 storyline but with rapid changes in economic structures toward a service and information economy, with reductions in material intensity, and the introduction of clean and resource-efficient technologies.
- B2 family: a world in which the emphasis is on local solutions to economic, social, and environmental sustainability, with continuously increasing population (lower than A2) and intermediate economic development.

By forcing several GCMs with each SRES scenario, projections of global temperature rise are obtained (IPCC, 2007). Figure 1.4 shows the development of GHG emissions and associated global temperature increase for the SRES scenario families. As can be seen in Figure 1.4, the scenarios represent a wide range in temperature increases, but all of them project global warming.

1.2 Study area

The Rhine basin is major river basin in western Europe and covers large parts of Germany, Switzerland, France, Luxembourg and The Netherlands. It originates in the Swiss Alps and drains in the North Sea in the Netherlands. Figure 1.5 shows the location of and elevations in the Rhine basin. It covers a wide range of elevations: from minus 6 meters in the Netherlands to 4275 meters in the Swiss Alps (Pfister *et al.*, 2004). After leaving the Alps it forms one of the largest lakes of Europe, Lake Constance, also known as Bodensee. Further downstream, the Rhine forms the border between France and Germany and receives on its way the water of several important tributaries such as the

Table 1.1: Tributaries of the Rhine basin and their characteristics. Mean, maximum and mean annual maximum discharge (MAM Q) are calculated over the period 1993-2003. The same numbers are also shown for the basin outlet Lobith. Areas are taken from *Lammersen (2004)*.

Tributary	Gauge	Area [km ²]	Mean Q [m ³ s ⁻¹]	Max Q [m ³ s ⁻¹]	MAM Q [m ³ s ⁻¹]
Lippe	Schermbeck	4,783	43	442	249
Sieg	Menden	2,825	50	806	518
Nahe	Grolsheim	4,013	32	809	468
Lahn	Kalkofen	5,304	48	587	394
Main	Raunheim	24,764	187	1991	1177
Mosel	Cochem	27,088	364	4009	2650
Neckar	Rockenau	12,710	154	2105	1396
Ruhr	Hattingen	4,118	75	867	611
Rhine	Lobith	185,000	2395	11775	8340

rivers Neckar, Main and Mosel. After crossing the German-Dutch border, the Rhine bifurcates into three branches (Waal, Nederrijn/Lek and IJssel) and finally mouths in the North Sea. The Rhine has a length of 1320 km and a catchment area of 185,000 km². Water discharge at Basel (just after the Alps) is around 1000 m³ s⁻¹ and at the German-Dutch border (Lobith) it is ~2400 m³ s⁻¹ on average.

Based on its geographical and climatological characteristics, the Rhine can be divided into three parts: the Alpine area (upstream of Basel), the middle mountain area (between Basel and Cologne) and the lowland area (downstream of Cologne). The Alpine area exists of roughly 16.000 km², with maximum heights of 4000 m a.s.l. About 400 km² of that area is covered with glaciers. The upper stretch, from the source to the Bodensee, is called the Alpenrhein; the part between the Bodensee and Basel is called the Hochrhein. Main tributaries draining in the Hochrhein are the Aare, Rheus and Limmat. In the middle part of the basin, maximum elevations range from more than 1000 m a.s.l. in the south to about 600 m a.s.l. in the north. Between Basel and Bingen, the river stretch is called the Oberrhein, while between Bingen and Cologne it is called the Mittlerrhein. The main tributaries in the middle part of the basin are the Neckar, Main, Lahn, Mosel and Sieg. The lower part of the basin, in which the river stretch is called the Niederrhein, includes extensive sedimentary areas: (fluvio)glacial deposits, loess, cover sands and fluvial deposits. The main tributaries are the Lippe, Ruhr and Vecht (*Daamen et al., 1997*). Table 1.1 shows characteristics of the major tributaries of the Rhine and the Rhine itself.

The Rhine basin is a densely populated basin: around 50 million people live in the catchment area (*Daamen et al., 1997*). Around 30 million of the inhabitants receive drinking water, which is directly,

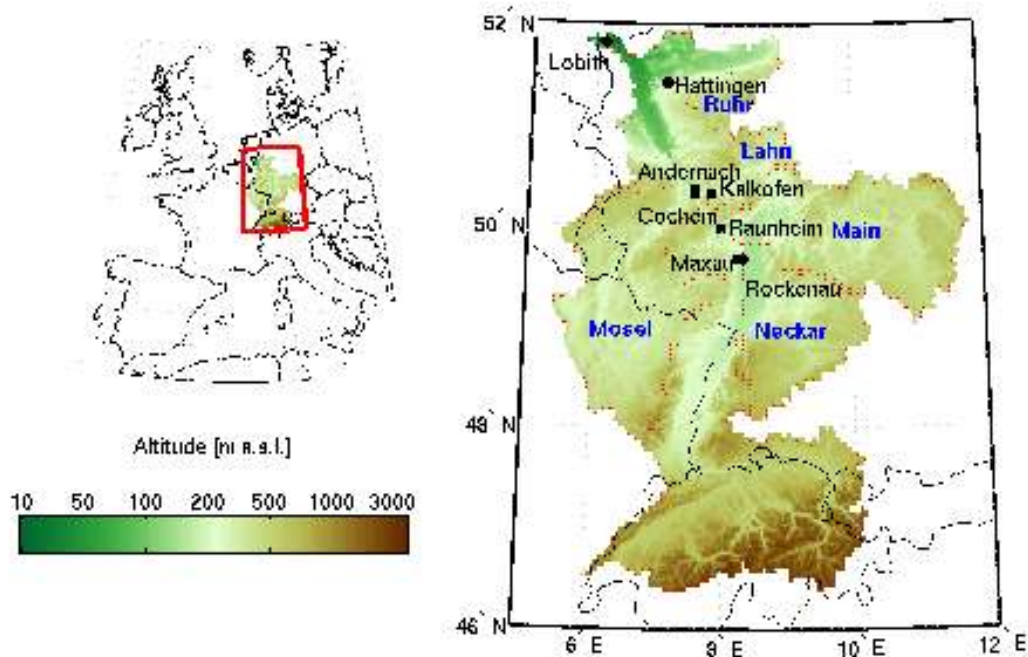


Figure 1.5: Location of and elevations in the Rhine basin. Note that the color scale is logarithmic for better visibility. The discretisation of the basin in the hydrological model and the various sub-basins that are used in the analyses are shown by small black dots. The location of the eight streamflow gauges that are used in the thesis are shown in black text, whereas the corresponding tributaries are shown in white text (see also Table 1.1). Source: *Hurkmans et al. (2009a)*.

or indirectly prepared from river water. It is a heavily industrialized area in which almost 2/3 of the chemical and pharmaceutical companies of the world can be found. It is also a very busy river with one of the largest seaports of the world (Rotterdam) and the largest inland harbor of the world (Duisburg). Due to these ports, it has one of the highest traffic densities in the world (*Kwadijk and Rotmans, 1995*). Because of the large economical and industrial value that is concentrated in the basin, it is very vulnerable to damage by extreme peak flows and low flows occurring in the river (e.g. *Kleinn et al., 2005*). The extreme streamflow drought in 2003 caused problems with inland navigation due to low water levels, and energy plants suffered from lack of cooling water due to low discharges and high water temperatures. Because of global warming (see Section 1.1.2), such problems are expected to increase (*IPCC, 2007*).

The Rhine basin is the area of interest for most of the research presented in this thesis: Chapters 2, 3, 4. In Chapter 5, however, the Colorado river basin will be studied and described in more detail. In Chapter 6, finally, a very small Alpine sub-basin of the Rhine is investigated, the Rietholzbach.

1.3 The Variable Infiltration Capacity model

The Variable Infiltration Capacity (VIC) model (*Liang et al., 1994, 1996; Wood et al., 1992*) was designed to provide boundary conditions at the land surface for global and regional climate models. In the model concept, therefore, the emphasis is put on the correct calculation of evaporation and energy balance fluxes since they are the most important variables to return to the atmospheric model. Hydrologic processes below the subsurface are represented in a conceptual and relatively simplistic manner. Figure 1.6 shows a schematic representation of the most important fluxes and stores in the VIC model. In most applications the model is applied in a distributed sense; the catchment under consideration is divided into pixels, that are resolved separately. The model can also be applied in a lumped sense, in that case the entire catchment is considered as one pixel. Variability within a pixel (sub-grid variability) is accounted for by further dividing the pixels into tiles for different land use types based on their fractional coverage (Figure 1.6). In addition, similar tiles are created based on the variability of elevation within a pixel. Evapotranspiration is calculated for each tile separately by solving the coupled water and energy balance. This is explained in more detail in Section 1.3.2. Streamflow generation and the separation between fast and slow discharge is described in Section 1.3.1.

1.3.1 Streamflow generation

As can be seen in Figure 1.6, the soil is divided into three layers. The upper layer is typically very thin and used for calculation of bare soil evaporation and infiltration. Moisture transport between the layers is driven by gravity only and is described by the Brooks-Corey equations (*Brooks and Corey, 1964*). No horizontal transport of soil moisture is allowed. The lowest layer represents the groundwater reservoir. It drains according to the Arno model formulation (*Todini, 1996*), representing baseflow. The relationship between soil moisture in the lowest layer and baseflow consists of a linear and a non-linear segment (see graph “Baseflow Curve” in Figure 1.6). The latter is intended to represent relatively fast groundwater runoff when the moisture content is high. The thickness of the root zone is not dependent on the thickness of the model layers, but is specified for each vegetation type. The moisture content in the root zone for each vegetation type is then calculated by taking the weighted average over the moisture content(s) of the soil layer(s) that the root zone (partly) coincides with.

The feature that most distinguishes the VIC model from other macro-scale models is its function to allow for heterogeneity of fast runoff production and soil moisture storage (*Beven, 2001*). This function consists of a relation between the soil moisture content in the upper two layers (layers 0 and 1 in Figure 1.6) and the infiltration capacity, hence the model’s name. The concept is shown in the “Variable Infiltration Curve” in Figure 1.6. The variability of the infiltration capacity i over an area can be described by:

$$i = i_m \left[1 - (1 - A)^{1/b} \right], \quad (1.1)$$

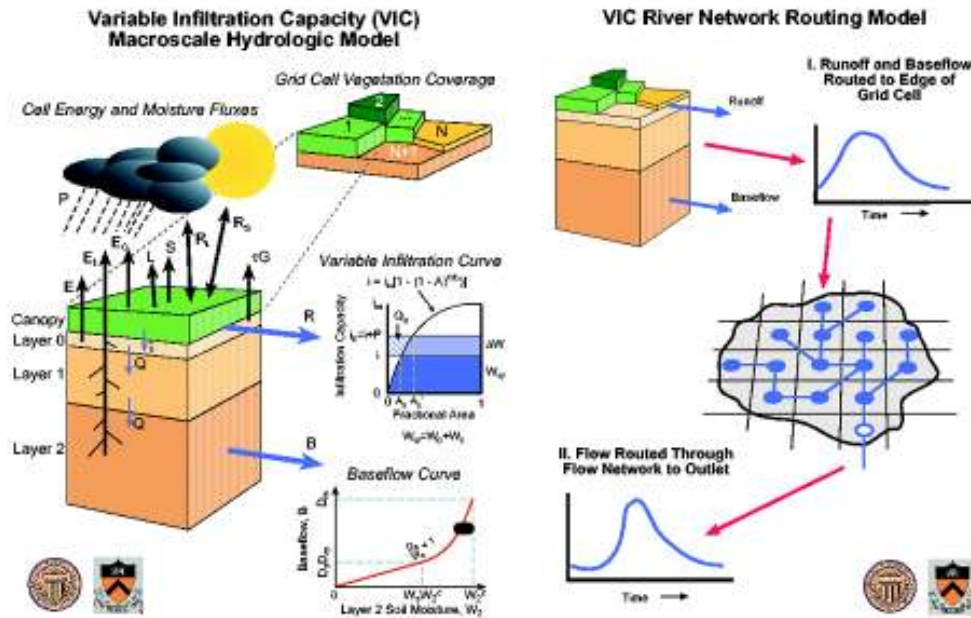


Figure 1.6: Schematic description of hydrological processes as they are represented in the VIC-model. Source: <http://www.hydro.washington.edu/Lettenmaier/Models/VIC/VIChome.html>.

where i is the infiltration capacity up to which the soil is filled, and i_m is the maximum infiltration capacity of the soil, which depends on the soil moisture storage capacity W_{max} by $i_m = (1 + b)W_{max}$. A represents the fraction of the grid cell that has an infiltration capacity less than i and is derived from the soil moisture contents in the upper layers W by:

$$A = 1 - \left(1 - \frac{W}{W_{max}}\right)^{b/(1+b)}, \quad (1.2)$$

Equation 1.1 basically describes the dynamics of runoff contributing areas as a function of the mean soil water content (Lohmann et al., 1998a). The shape parameter b is thus a measure for the amount of variability in topography within a grid cell. For $b = 1$ therefore, the distribution is uniform and there is no heterogeneity present in streamflow generation. In Figure 1.6, A_s is that fraction of the grid cell area that is saturated at the beginning of the time step, corresponding with initial soil moisture depth W_0 . For a precipitation amount P , the amount of water that infiltrates is the areally integrated infiltration capacity $\int_{i_0}^{i_0+P} A(i)di$, indicated as ΔW in Figure 1.6. The remainder $P - \int_{i_0}^{i_0+P} A(i)di$,

indicated as Q_d , contributes to surface runoff (Wood *et al.*, 1992).

1.3.2 Evapotranspiration

VIC solves the coupled energy and water balance to calculate the actual evapotranspiration and the associated turbulent fluxes, i.e. the calculation of evapotranspiration (and the latent heat flux) is iterated until the energy balance closes:

$$R_{net} = \lambda E + H + G, \quad (1.3)$$

where R_{net} is the net radiation, λ is the latent heat of vaporization of water, E is the evapotranspiration flux, H is the sensible heat flux and G is the ground heat flux. R_{net} , λE , H and G all depend on the surface temperature T_s . As an initial guess, T_s is set equal to the air temperature. All energy fluxes are calculated using this initial temperature. λE is the connection to the water balance, therefore its calculation is explained in more detail. First, potential evaporation E_p is calculated using the Penman-Monteith equation (Penman, 1948; Monteith, 1965):

$$\lambda E_p = \frac{\Delta R_{net} + \rho_a c_p \frac{[e_s(z) - e(z)]}{r_a}}{\Delta + \gamma \left(1 + \frac{r_c}{r_a}\right)}, \quad (1.4)$$

where $e_s(z)$ and $e(z)$ are the saturated and actual vapor pressure at height z (the height where the wind speed is measured) respectively, Δ is the rate of change of e_s with temperature, ρ_a and c_p are respectively the density and specific heat capacity of air, γ is the psychrometric constant, r_a is the aerodynamic resistance and r_c is the canopy resistance. r_a depends on vegetation properties such as surface roughness and trunk height. For the equations to calculate r_a , H , and G , see for example Liang *et al.* (1994).

From E_p and the contents of the upper soil moisture layer an actual evaporation E_a is calculated, according to:

$$E_a = E_p \left(\int_0^{A_s} dA + \int_{A_s}^1 \frac{i_0}{i_m [1 - (1 - A)^{1/b}]} dA \right), \quad (1.5)$$

Note that in Equation 1.5, the area is divided in a saturated part, which evaporates at the potential rate, and an unsaturated part, which evaporates at a rate that is reduced by the storage deficit. Equation 1.5 provides a new λE and the energy balance is solved again, yielding updated energy fluxes and T_s . Except for the bare soil evaporation described by Equation 1.5, transpiration and canopy interception evaporation are calculated. If the surface is vegetated, vegetation is divided in a wet and a dry fraction: from the wet fraction canopy evaporation occurs ($r_c = 0$) and from the dry fraction

transpiration occurs.

1.3.3 Streamflow routing

The sum of surface runoff and baseflow from each grid cell is routed to the basin outlet (or any other user defined location in the river basin) using an algorithm developed by *Lohmann et al.* (1996). The algorithm is used “stand-alone”, i.e., output of the VIC model is post-processed to obtain streamflow. Therefore, no river bed infiltration or feedbacks due to flooding are taken into account. The concept is shown in the right panel of Figure 1.6. Based on digital elevation data, the river basin is divided in grid cells at the same spatial resolution as the VIC model, each with an average elevation. Each grid cell then drains to its lowest neighbour. It is assumed that each grid cell drains directly in the channel network. River routing is then carried out with the linearized St.Venant equation:

$$\frac{\delta Q}{\delta t} = D \frac{\delta^2 Q}{\delta x^2} - C \frac{\delta Q}{\delta x}, \quad (1.6)$$

where D and C are diffusivity and celerity respectively. Equation 1.6 can be solved by convolution integrals:

$$Q(x, t) = \int_0^t U(t - s)h(x, s)ds, \quad (1.7)$$

where U is the sum of surface runoff and baseflow from the VIC model, and $h(x, s)$ is the impulse response function of Equation 1.6 (*Lohmann et al.*, 1996, 1998a):

$$h(x, t) = \frac{x}{2t\sqrt{\pi t D}} \exp\left(\frac{-(Ct - x)^2}{4Dt}\right), \quad (1.8)$$

where x is the total channel length running through a grid cell.

1.4 Problem description and thesis outline

In the first part of this thesis, Chapters 2, 3 and 4, the VIC model and the Rhine river basin will play a central role. In Chapter 2, the VIC model is first applied to the Rhine basin, and compared to a more simple and conceptual water balance model. The latter model is representative for models that have been used in climate change impact assessments before (e.g. *Middelkoop et al.*, 2001; *Kwadijk and Middelkoop*, 1994; *Shabalova et al.*, 2003; *Lenderink et al.*, 2007). The VIC model has several advantages compared to these models. First, evapotranspiration is calculated in a more physically based manner (see Section 1.3.2), whereas in the more simple water balance models it is often based on temperature only. Second, small-scale heterogeneity in land use, elevation and topography is taken into account

in the VIC model, whereas it is not in simpler water balance models. Third, water balance models use precipitation and temperature as input, while the VIC model can employ additional climate model output where this is available, such as radiation, humidity and wind speed. Water balance models thus rely very much on calibrated parameter values to reproduce historical streamflow. The physical basis behind these parameters is often limited, and it is highly questionable whether the values for these parameters remain stable under changing climate conditions. Although the VIC model also relies on model calibration of certain parameters, they are more physically based, thus reducing the sensitivity to calibrated parameter values.

Another advantage of the physical basis of the calculation of evapotranspiration for different vegetation types, is the possibility to evaluate scenarios of land use change. This is done in Chapter 3. Land use change can have significant effects on rainfall-runoff processes. For example, research indicated that deforestation can amplify flood risk (e.g. *Laurance, 2007; Bradshaw et al., 2007*) through decreasing infiltration capacity, transpiration and interception (*Clark, 1987*). Urbanization decreases the infiltration capacity and transpiration as well through the removal of vegetation and the creation of impervious surfaces (e.g. *Dow and DeWalle, 2000; DeWalle et al., 2000*). In the Eururalis project (*Verburg et al., 2006a*), four land use change scenarios for Europe were developed, which are based on the story lines described by the SRES scenario families (Section 1.1.3). Based on socio-economic and demographic developments, and a model that allocates resulting land use types to individual pixels (*Verburg et al., 2008*), four high-resolution (1 km²) land use scenarios for the year 2030 were obtained. These scenarios, as well as two hypothetical scenarios in which all agricultural land in the Rhine basin is replaced by either forest or grassland, are evaluated in terms of streamflow using the VIC model. Climate conditions are kept constant for all land use scenarios.

In Chapter 4, the land cover is kept constant and the influence of climate change is investigated. To this end, three climate scenarios are used to force the VIC model. All scenarios consist of model output from a GCM, downscaled using an RCM. Each scenario is based on one of three SRES-emission scenarios (A2, A1B and B1; see Section 1.1.3). Compared to previous studies, the spatial resolution of the climate scenarios that are employed here is relatively high (~ 10 km), whereas resolutions of 25 or 50 km were typically used in other studies (e.g. *Shabalova et al., 2003; Lenderink et al., 2007*). This high resolution enables precipitation events that typically cause extreme peak flows to be simulated more accurately, because such events are often convective in nature and their spatial extent is relatively small. There are many uncertainties involved in such a climate change impact assessment: even in the reproduction of the current climate, there is a large range of model outcomes, both from GCMs and RCMs (*Covey et al., 2003; Jacob et al., 2007*). Apart from that, there is uncertainty involved in the hydrological model and its parameterization, and in the GCM forcings (emission scenarios). In Chapter 4, three plausible climate scenarios are analyzed in terms of their effects on average and extreme streamflow (both peak flows and low flows), while the uncertainties involved are acknowledged and discussed.

As was mentioned in Section 1.1.2, in the Colorado River Basin (CRB) low-frequency (interannual to interdecadal) climate variability has an important influence on the hydrologic system. It thus presents an excellent study area to investigate and quantify this influence, which is done in Chapter 5. The CRB recently experienced a severe multi-year drought (Seager *et al.*, 2007). Water availability is an important issue in the Colorado basin: population grows explosively, while climate models predict severely dry conditions (Barnett and Pierce, 2008; Cook *et al.*, 2004). Previously, precipitation and streamflow in the CRB have been linked to ENSO (e.g. Cañon *et al.*, 2007; Hidalgo and Dracup, 2003) and PDO (e.g. Gershunov and Barnett, 1998). Total terrestrial water storage (TWS) has received relatively little attention. It is, however, an important variable because it integrates hydrological processes in the catchment, such as snow accumulation, evapotranspiration and recharge. Different approaches exist to estimate TWS, several of which have been compared by Troch *et al.* (2007). In the latter study, storage dynamics as simulated by VIC proved to be similar to that of other methods. In Chapter 5, anomalies of TWS and its components as they are simulated by VIC are used to investigate the effects of low-frequency cycles of Pacific ocean temperature on the hydrology of the Colorado basin.

As was described in Section 1.3, the representation of subsurface hydrological processes in the VIC model is relatively simplistic compared to the representation of land-atmosphere interactions (evapotranspiration and vegetation). At a large spatial scale, such as that of the Rhine basin, it is not possible to explicitly model all existing heterogeneity in topography, vegetation and soil. It, therefore, needs to be parameterized. Chapter 6 focusses on different approaches to do this. The area of interest is a small Alpine sub-catchment of the Rhine basin: the Rietholzbach in Switzerland. Three approaches to parameterize small-scale variability of topography are investigated: (1) the statistical approach of VIC, described in Section 1.3.1; (2) the TOPMODEL approach (Beven and Kirkby, 1979; Famiglietti and Wood, 1994), in which from a high-resolution digital elevation model areas of hydrologically similar behavior are identified; and (3) the hillslope approach, in which the hydrological behavior of a hillslope is modeled and upscaled to a larger spatial scale using hillslope similarity parameters. Streamflow and spatially averaged evapotranspiration resulting from all model approaches are compared to each other and to observed values.

In Chapter 7, finally, the most important conclusions from this thesis are summarized and possible directions for further research are discussed.

Chapter 2

Water balance versus land surface model in the simulation of Rhine river discharges



This chapter is a modified version of: R. T. W. L. Hurkmans, H. de Moel, J. C. J. H. Aerts and P. A. Troch (2008), "Water balance versus land surface model in the simulation of Rhine river discharges," *Water Resour. Res.*, 44, W01418, doi:10.1029/2007WR006168

Abstract

Accurate streamflow simulations in large river basins are crucial to predict timing and magnitude of floods and droughts and to assess the hydrological impacts of climate change. Water balance models have been used frequently for these purposes. Compared to water balance models, however, land surface models carry the potential to more accurately estimate hydrological partitioning and thus streamflow, because they solve the coupled water and energy balance and are able to exploit a larger part of the information provided by regional climate model output than water balance models. Due to increased model complexity, however, they are also more difficult to parameterize. The purpose of this study is to investigate and compare the accuracy of streamflow simulations of a water balance approach (STREAM) and a land surface model (VIC) approach. Both models are applied to the Rhine river basin using regional climate model output as atmospheric forcing, and evaluated using observed streamflow and lysimeter data. We find that VIC is more robust and less dependent on model calibration. Although STREAM performs better during the calibration period (Nash-Sutcliffe efficiency (E) of 0.47 versus $E = 0.29$ for VIC), VIC more accurately simulates discharge during the validation period, including peak flows ($E = 0.31$ versus $E = 0.21$ for STREAM). This is the case for most locations throughout the basin, except for the Alpine part where both models have difficulties due to the complex terrain and surface reservoirs. In addition, the annual evaporation cycle at the lysimeters is more realistically simulated by VIC.

2.1 Introduction

River discharge integrates hydrological processes at the catchment scale and can be measured directly, as opposed to many other catchment fluxes (e.g., evaporation, precipitation). Streamflow is thus a suitable variable to validate and/or compare hydrological model performances. In Central Europe, recent floods in the Rhine (1993 and 1995), Elbe (2002) and Danube (2002), as well as droughts (e.g., the summer of 2003) caused billions of euros of damage (Kleinn *et al.*, 2005). Improving streamflow simulations in these densely populated large river basins is important to accurately predict timing and magnitude of floods and droughts (Nijssen *et al.*, 1997). Climate change is believed to affect streamflow characteristics mainly because of two reasons: first, the warming-related shift from snow to rainfall will change the seasonal streamflow cycle in rivers which have their source region in the Alps (including the Rhine). Second, there is increasing evidence for an acceleration of the hydrological cycle and an associated increase in precipitation intensity during winter (Kleinn *et al.*, 2005). Numerous studies have been carried out to quantify the impact of climate change on extreme value distributions of river streamflow, indicating a projected increase in extreme winter floods and more droughts in summer (Middelkoop *et al.*, 2001; Milly *et al.*, 2005; Aerts *et al.*, 2006; de Wit *et al.*, 2007; Kwadijk, 1993; Buishand and Lenderink, 2004). In these studies, future climate data were obtained from climate models, down-scaled either using statistical weather generators (Beersma *et al.*, 2001; Eberle *et al.*, 2002; Dibike and Coulibaly, 2005), or regional climate models (RCMs) (e.g., Christensen *et al.*, 2004; Kleinn *et al.*, 2005). Although the latter have the advantage to supply a sufficient number of meteorological variables at a high enough spatial and temporal resolution to force more sophisticated models, often conceptual water balance models have been used to simulate future streamflow. Examples of water balance models for the Rhine include HBV (Hydrologiska Byråns Vattenbalansavdelning; (Bergström and Forsman, 1973; Lindström *et al.*, 1997)), Rhineflow (Kwadijk, 1993) and STREAM (Spatial Tools for River basins and Environment and Analysis of Management options; (Aerts *et al.*, 1999, 2006)).

To accurately simulate streamflow, it is essential to have a realistic description of all relevant land surface processes, including the partitioning of available energy. Errors in estimates of evaporation propagate into similar errors in other terms of the energy and water balance and ultimately affect streamflow prediction (Koster *et al.*, 2000). Water balance models typically use empirical or statistical methods to estimate potential evaporation based on temperature. For example, Rhineflow and STREAM use an approach developed by Thornthwaite and Mather (1957) that is based on daily temperature measurements. Present day land surface models (LSMs) on the other hand, derive evapotranspiration from coupled water and energy balance simulations (Liang *et al.*, 1994; Famiglietti and Wood, 1994), and are able to utilize additional information provided by RCM output, such as solar radiation, wind speed, specific humidity and atmospheric pressure. Therefore, LSMs carry the potential to more accurately estimate hydrological partitioning (evaporation, soil moisture, surface runoff and streamflow). Because of the complex model structure and the large number of parameters in LSMs, they are generally more difficult to parameterize. LSM intercomparison experiments have demonstrated large variability in simulated land surface-atmosphere fluxes and streamflow using different LSMs

(e.g., Pitman *et al.*, 1999; Wood *et al.*, 1998; Lohmann *et al.*, 2004). The original purpose of LSMs was to represent the land surface in (regional) climate simulations used for climate models and numerical weather prediction (e.g., Liang *et al.*, 1994; Koster *et al.*, 2000; Zeng *et al.*, 2002; Dai *et al.*, 2003). Recently, LSMs have been used for (experimental) streamflow forecasting as well (e.g., Wood *et al.*, 2005). However, many studies assessing climate change impacts use water balance models, as well as short-term flood forecasting systems (e.g., in The Netherlands, Sprokkereef, 2001a).

To our knowledge, no direct comparison between a water balance model and a LSM in such application has yet been carried out. The purpose of this study is to investigate and compare the accuracy of streamflow simulations of a water balance approach and a more detailed land surface modeling approach, including the energy balance. We use a state of the art LSM (the Variable Infiltration Capacity (VIC) model, version 4.0.5) and a water balance model (STREAM) to simulate hydrological partitioning in the Rhine river basin. STREAM is a distributed water balance model that has been adapted to simulate streamflow at the basin outlet. Previous applications of VIC to a range of catchment scales have used streamflow indicators for verifying simulations and have demonstrated satisfactory results (Nijssen *et al.*, 1997, 2001; Lohmann *et al.*, 1998b). In addition to solving the coupled water and energy balance, we applied VIC in the water balance mode (VIC-WB): instead of obtaining surface temperature by solving the energy balance, it is assumed equal to air temperature, thereby avoiding iterative solution of the energy balance. VIC-WB is an intermediate between VIC and STREAM in that it does not solve the coupled water and energy balance but does account for, for example, sub-grid variability. In this way the influence of solving the energy balance is separated from that of other differences in the formulation of the models, such as the sub-grid variability parameterization in VIC (see Section 2.3), and investigated more specifically. All models are calibrated to a similar extent (as is further explained in Section 2.4) and subsequently applied to the Rhine basin in the period between 1993 and 2003 using RCM output as meteorological forcing (Jacob, 2001). Within this period, the Rhine basin experienced the near-floods in 1993 and 1995, as well as a severe low flow period during the summer of 2003. We compare model simulations for these extreme flows. To evaluate streamflow simulations from all three models, we use observed streamflow data from main tributaries, as well as data from several locations along the main Rhine branch. In addition, lysimeter data is employed to evaluate the simulation of evaporation at specific locations within the basin.

2.2 Study area and data

The river Rhine originates in the Swiss Alps and drains large parts of Switzerland, Germany and The Netherlands. After crossing the German-Dutch border near Lobith, the river splits into three distributaries before discharging in the North sea. Therefore, only the area upstream of Lobith is considered here, which measures about 185,000 km². Streamflow gauges at the mouths of five major tributaries (Lahn, Mosel, Main, Neckar and Ruhr) and at three locations along the main branch (Maxau, Andernach and Lobith) were used to compare the models. The Rhine basin is described in more detail in

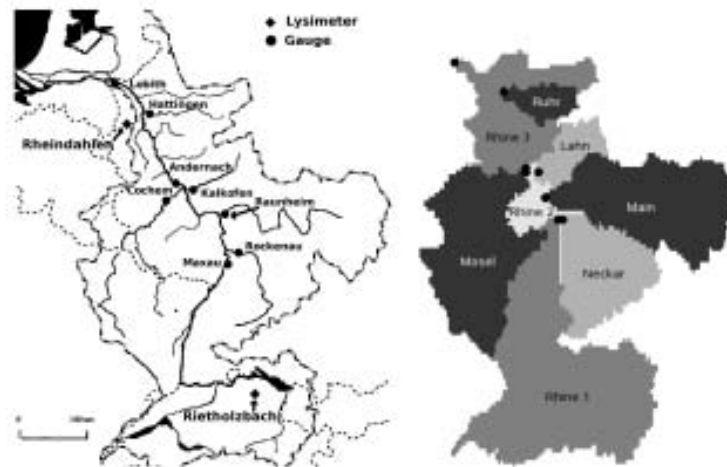


Figure 2.1: Location of Rhine basin and streamflow gauges (left) and the discretization of the basin for routing purposes (right). In the left plot, also lysimeter locations are shown.

Section 1.2, and in Table 1.1 streamflow gauges and main streamflow characteristics of the main Rhine tributaries are listed. The Rhine basin and the location of the gauging stations are shown in Figure 2.1.

All three models are forced using downscaled ECMWF ERA15 reanalysis data (<http://www.ecmwf.int/research/era/>), provided by the Max Planck Institut für Meteorologie, Hamburg, Germany (MPI). Downscaling was carried out at MPI using the regional climate model REMO (Jacob, 2001). This dataset will be referred to as ERA15d hereafter. The dataset comprises the years 1993 through 2003, with data available every three hours at a spatial resolution of 0.088 degrees (about 9 km). In Figure 2.2 monthly climatologies of the seven variables that were used to force VIC and VIC-WB, i.e., precipitation, temperature, specific humidity, surface pressure, incoming longwave and shortwave radiation and windspeed, are shown. To compare this data to observations, an additional meteorological dataset is used from the International Commission for the Hydrology of the Rhine basin (CHR), referred to as CHR hereafter. This dataset contains daily values of precipitation and temperature and is based on observations from 36 stations throughout the basin (Sprokkereef, 2001b). Temperature and precipitation for the years present in both datasets (1993 through 1995) are compared. In Figures 2.3 and 2.4, the results are shown. Monthly values of precipitation match reasonably well ($R^2 = 0.73$), however at daily and weekly scales, correlations are very low. Temperatures are structurally about 1.5°C higher for ERA15d (Figures 2.2 and 2.4). This difference is occurring throughout the basin, but it is smallest in the relatively flat areas. In summer, the difference is maximal (about 2°C). Precipitation differs greatly between both datasets during winter (DJF) in the Alpine area, in some areas up to 200 mm, probably due to significant amounts of snow that are not measured by the observation network used in the CHR dataset. In summer, differences in precipitation are small.

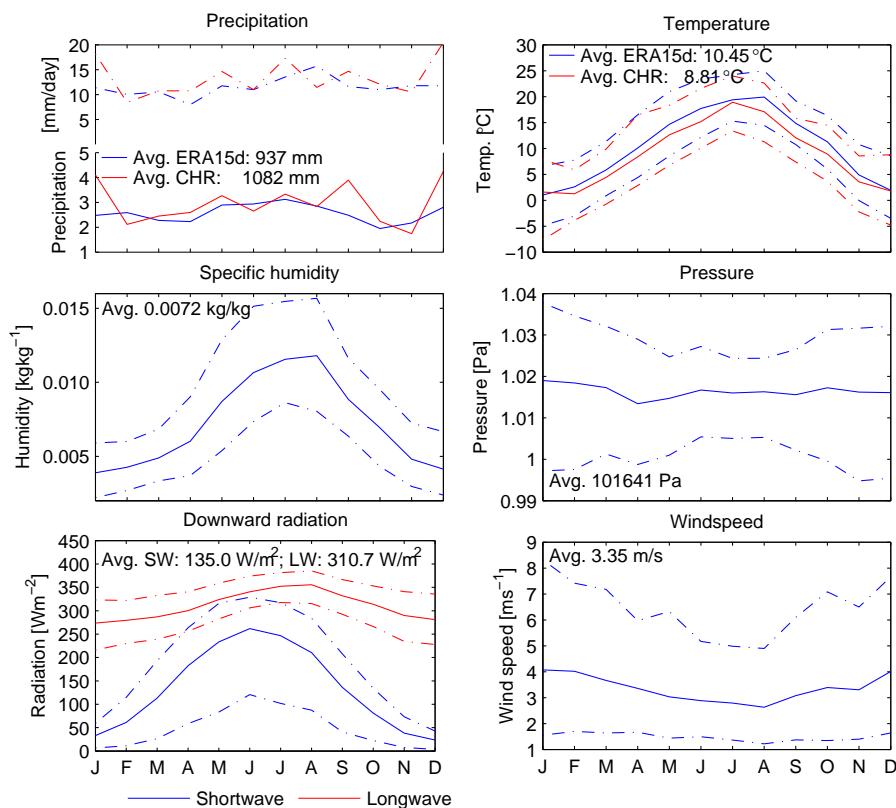


Figure 2.2: Monthly averages (solid), maxima and minima (dash-dotted) of forcing variables in the ERA15d dataset. For precipitation (top left) and temperature (top right) also the CHR dataset is shown. Also annual averages (sums for precipitation) are shown. Note that for the CHR dataset, only 3 years of data are used because only three years were overlapping in the datasets.

It is clear that both datasets have their shortcomings. However, in the remainder of this paper we use the ERA15d because a) CHR does not contain all input fields to run VIC, b) only three years of overlapping data (i.e., 1993-1995) are available and c) the re-analysis data is similar to RCM output that is generally used to assess the hydrological impacts of climate change.

For land use, the Pan-European Land Cover Monitoring and Mapping-database (Mücher *et al.*, 2000) was used. Soil data were taken from the global FAO dataset (Reynolds *et al.*, 2000). Lysimeter data were available for two stations located in very different parts of the basin. Rheindahlen (51.16N, 6.33, elevation about 75 m.a.s.l.) is close to the basin outlet and Rietholzbach (47.38N, 8.99, elevation about 700 m.a.s.l.) is located in the Alpine part of the basin (Figure 2.1). At both lysimeter sites, the dominant vegetation type is grass. More information about the lysimeter station at Rheindahlen can be found in Xu and Chen (2005). Of the four available lysimeters at Rheindahlen, we used

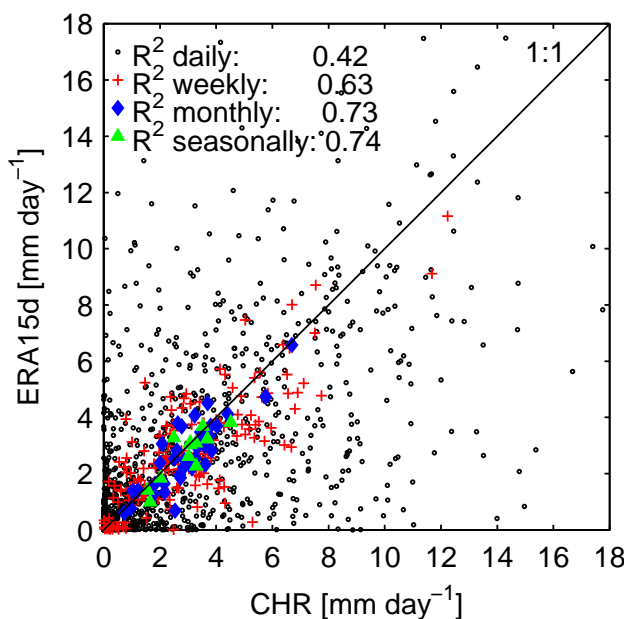


Figure 2.3: ERA15d versus CHR precipitation. The period 1993-1995 was used for the comparison. Average precipitation amounts of both datasets are plotted against each other, aggregated over 1, 7, 30 and 90 days. For every aggregation period, the resulting square of the correlation coefficient (R^2) is displayed in the upper left corner.

lysimeter nr. 3, in accordance with *Xu and Chen (2005)*. The lysimeter at Rietholzbach is described at <http://www.iac.ethz.ch/research/rietholzbach/instruments/>.

2.3 Description of models

STREAM (Spatial Tools for River basins and Environment and Analysis of Management options), is a distributed, grid based water-balance model (*Aerts et al., 1999, 2006*), based on the Rhineflow approach (*Kwadijk, 1993*). The water balance is solved for every grid cell in the basin at a daily timestep. The model consists of three storage reservoirs: snow storage, soil moisture storage and groundwater storage, dividing outflow into a fast and a slow component. The fast component is affected by soil moisture storage and the slow component by ground water storage, both behaving as linear reservoirs. Potential evapotranspiration is derived from surface temperature, following the approach of *Thornthwaite and Mather (1957)*. Actual evapotranspiration is calculated using the soil moisture storage and the so-called 'accumulated potential water loss', see *Thornthwaite and Mather (1957)*. Snow accumulation is equal to precipitation when temperature is below zero degrees Celsius, snow melt linearly depends on temperature. Both fast and slow flow are routed to the basin outlet by flow ac-

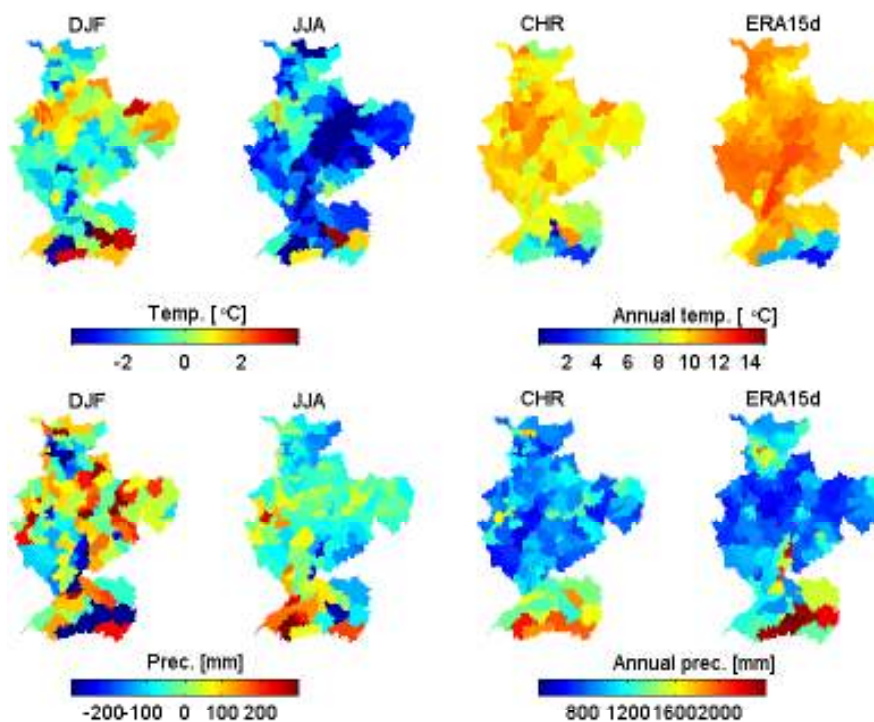


Figure 2.4: Spatial patterns of temperature and precipitation from the CHR and ERA15d datasets. The upper four maps show temperature, the lower four maps precipitation. In the right four maps, annual mean temperature and annual cumulative precipitation are plotted. In the left four maps, average differences between the datasets are shown for two seasons: winter (DJF) and summer (JJA). Positive values indicate an overestimation of ERA15d, with respect to CHR. Averages are computed from the years 1993 through 1995.

cumulation under the assumption of a constant flow velocity. An overview of parameters typically used for calibration is given in Section 2.4. Because STREAM only needs precipitation and temperature as dynamic input variables, its application is relatively simple. STREAM has been applied to various river basins, including the Krishna river in India (*Bouwer et al.*, 2006) and many of the major catchments in the world in a study on Holocene and future discharges (*Aerts et al.*, 2006; *Ward et al.*, 2007).

The Variable Infiltration Capacity (VIC) model (*Liang et al.*, 1994, 1996; *Liang and Xie*, 2001), is a variable-layer soil-vegetation-atmosphere transfer (SVAT) scheme for general and regional circulation and weather prediction models. Its most distinguishing aspect in comparison with other LSM is its variable infiltration capacity curve, which is described by:

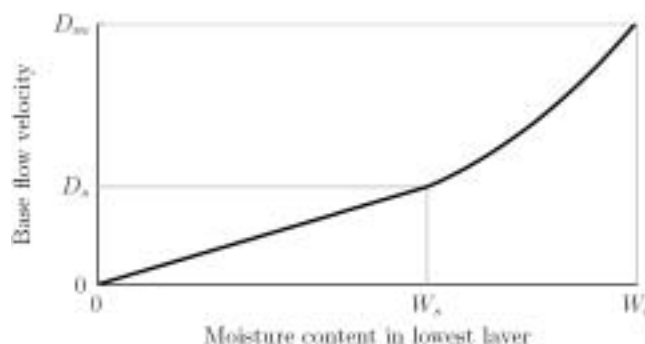


Figure 2.5: Relationship between soil moisture content in the lowest layer W_c and base flow D . D_m represents maximum base flow velocity, D_s is a fraction of D_m and W_s is a fraction of W_c . The point (W_s, D_s) represents the point where the curve becomes nonlinear.

$$I = I_m \left[1 - (1 - A)^{1/\beta} \right] \quad (2.1)$$

where I and I_m are the infiltration capacity and maximum infiltration capacity, respectively. A is the fraction of an area for which the infiltration capacity is less than I and β is a shape parameter. Drainage from the upper to the lower layers is assumed to be driven by gravity only, using the *Brooks and Corey* (1964) relationship to estimate hydraulic conductivity. Baseflow is modeled following the ARNO model formulation (*Todini*, 1996). The relation between soil moisture in the lowest layer and base flow is shown in Figure 2.5. These concepts, as well as the calculation of evapotranspiration is described in more detail in Section 1.3 and shown in Figure 1.6. The parameters in Figure 2.5 and β , as well as depths of the soil layers, are typically used for model calibration (e.g., *Lohmann et al.*, 1998a). See Section 2.4 for more details about model calibration. When snow is present on the ground, the model is coupled with a two layer energy- and mass-balance model. Snow can also be intercepted by the canopy, melt from the canopy snowpack is simulated using a simplified energy balance model. More details about the VIC model can be found in Section 1.3. The VIC model can operate in two modes: in the energy balance mode, the energy balance is solved iteratively to obtain the surface temperature, whereas in the water balance mode, surface temperature is assumed equal to air temperature. In both modes, potential evapotranspiration is calculated using the Penman-Monteith equation. In the energy balance mode, a time step of 3 hours is used, in correspondence with availability of forcing data, whereas in water balance mode the model is integrated at a daily time step. Therefore simulation times are drastically reduced compared to the full mode.

Routing of surface runoff and base flow from all models is done by the algorithm developed by *Lohmann et al.* (1996), which has been applied in combination with VIC by *Lohmann et al.* (1998a,b). The sum of base flow and runoff from the models is convoluted with a normalized impulse response

function, based on the linearized St. Venant equation (e.g., Troch *et al.*, 1994), assuming that water from each grid cell flows into the channel in the steepest direction to one of its eight neighbors.

2.4 Model calibration

All three models were calibrated using daily observed streamflow at Lobith for the year 1993. Only one year was used to limit the amount of calibration time. Because 1993 contains a relatively dry summer, as well as a near flood event, it was considered representative for the total period. Because no data were available before 1993 and, based on preceding streamflow observations, conditions and model storages in October 1993 were assumed to be similar to January 1993, the model states (i.e., moisture contents, snow pack) of October 1993 were used to initialize all model simulations in January 1993. STREAM was calibrated using a built-in optimization routine, iteratively changing the parameters one-at-a-time and minimizing the mean absolute difference between observed and simulated streamflow, and then fine-tuned manually. Four parameters were optimized following e.g., Aerts *et al.* (2006): a factor C to adjust the land use dependent crop factor that defines potential evapotranspiration for different land use types, a depletion factor D for the groundwater reservoir, a factor X to separate between direct runoff and groundwater recharge, and finally a parameter H that defines the relation between temperature and reference evapotranspiration. To calibrate VIC, seven parameters influencing the shape of the hydrograph and the total outflow volume were subjected to a sensitivity analysis. Based on this analysis, the depth of the (very thin) upper layer and the baseflow parameter W_s (see Figure 2.5) appeared to have no influence on the resulting hydrograph and were therefore left out of the calibration procedure to save computation time. Parameters influencing potential evapotranspiration, differing per vegetation type, were left at their default values. The resulting parameters for optimization are, similar to former applications (Lohmann *et al.*, 1998a; Liang *et al.*, 1994): D_m and D_s to define the relation between baseflow and soil moisture in the lowest layer (see Figure 2.5), the shape parameter β in Eq. 2.1 and the depths of the lower two layers d_2 and d_3 . Because these parameters are not transferable between the full and energy modes, VIC was re-calibrated for the water balance mode, using the same parameters. For optimizing the objective function O a power transformation was used to balance sensitivity to peak flows and low flows. The objective function can be written as:

$$O = \frac{1}{N} \sum_{i=1}^N \frac{(Q_{obs,i}^\lambda - Q_{sim,i}^\lambda)}{\lambda} \quad (2.2)$$

where N is the number of time steps and Q_{obs} and Q_{sim} are observed and simulated discharge respectively. Both are raised to the power λ which is taken as 0.3 in this study because this gives an optimal balance between sensitivity to peak and low flows (Misirli *et al.*, 2003).

To calibrate the models to a comparable level, all parameters were kept uniform in space. To enable streamflow comparison at other streamflow gauges than Lobith only, STREAM surface runoff and base flow were routed using the VIC routing algorithm. Figure 2.6 shows daily streamflow in 1993 for VIC (both modes) and STREAM compared to observations. For STREAM, two hydrographs are plotted: one obtained by routing using the original STREAM routing scheme (STREAM1) and one obtained by routing using the VIC algorithm (STREAM2). The VIC routing algorithm tends to slightly delay runoff peaks compared to the original STREAM routing scheme. Varying celerity and diffusivity in the VIC routing algorithm did not change this behavior. To remove the influence of the routing algorithm that was used, hereafter 10-daily averaged streamflow values are evaluated at gauging stations other than Lobith. For analyses at the Lobith gauging station that require daily streamflow (such as peak flow analyses), daily discharge obtained by the original STREAM routing algorithm is used for the STREAM simulations.

In Table 2.1, correlation coefficients (ρ), Nash-Sutcliffe modeling efficiencies (E ; Nash and Sutcliffe, 1970) and relative volume errors (RVE) for both the calibration and validation period are shown for daily discharge at Lobith. During the calibration period, STREAM performs better: $E = 0.47$ for STREAM, whereas $E = 0.29$ for VIC. Also ρ for STREAM is higher (0.77) than for VIC (0.67). As mentioned before and can be seen in Table 2.2, routing STREAM output with the VIC algorithm reduces STREAM's performance drastically for daily discharge. The performance of VIC-WB is in between VIC and STREAM with $E = 0.39$ and $\rho = 0.71$. Changing parameters in STREAM has a more direct effect on the resulting hydrograph, whereas in VIC a more extensive calibration including more parameters would have been necessary to obtain similar results. For VIC-WB, changing the calibration parameters has a larger effect compared to VIC yielding better results. The rather poor results in the calibration period in terms of Nash-Sutcliffe values are partly explained by an overestimation of streamflow in summer. The inset of Figure 2.6 shows that this was mainly caused by too high precipitation in the ERA15d dataset.

To investigate the influence of this biased forcing data, VIC and STREAM were also forced by precipitation from CHR. The other required forcing variables are from ERA15d, because they were not available in the CHR dataset. Figure 2.7 shows daily simulated discharges at Lobith for VIC and STREAM, where precipitation from both ERA15d and CHR is used, for the period 1993 through 1995, i.e., the period where both forcing datasets overlap. Note that the models were not recalibrated for the CHR dataset. It appears that both models improve drastically when forced with the CHR precipitation: for VIC, E increases from 0.45 to 0.59, for STREAM from 0.47 to 0.56. The correlation coefficient on the other hand increases especially for STREAM; from 0.81 to 0.92, whereas for VIC this increase is much less: from 0.79 to 0.83. In the summer of 1993, VIC with CHR precipitation now simulates discharge very well, while STREAM underestimates discharge, as was to be expected because the model was not recalibrated.

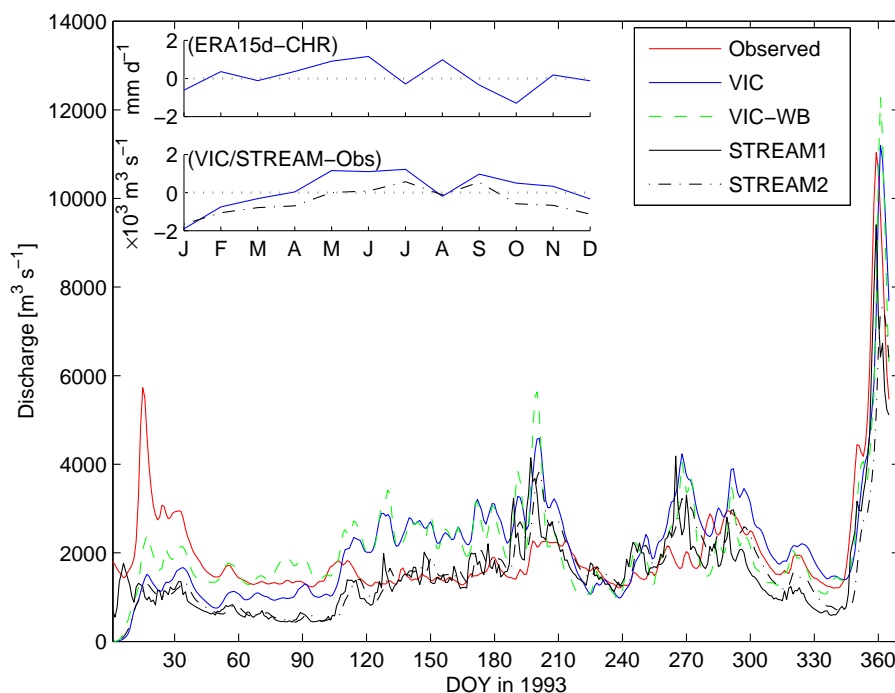


Figure 2.6: Simulated and observed daily streamflow at Lobith for the calibration period (1993). VIC-WB represents the VIC simulation in the water balance mode, STREAM1 represents the results of STREAM internal routing used for calibration and STREAM2 represents result of STREAM output routed by the VIC algorithm. The upper panel of the inset shows the difference between ERA15d and CHR precipitation (positive shows higher ERA15d), the lower panel shows simulated minus observed monthly discharge for VIC (solid line) and STREAM1 (dash-dotted line).

2.5 Model validation

The calibrated models are evaluated using data from the remaining period, i.e., 1994 to 2003. Table 2.2 shows ρ , E and RVE for 10-daily averaged discharge for all streamflow gauges in this period. During the validation period, VIC ($\rho = 0.74$, $E = 0.31$) and VIC-WB ($\rho = 0.70$, $E = 0.40$) slightly improve with respect to the calibration period, whereas ρ (0.63) and E (0.14) for STREAM decrease. When considering all streamflow gauges, correlation coefficients and most E values are higher for VIC, although the latter are higher for STREAM at Maxau and Rockenau. For VIC-WB, correlation coefficients are mostly intermediate. E , however, is often higher for VIC-WB compared to VIC, suggesting a more efficient calibration procedure when VIC is run in water balance mode. For Maxau and Rockenau, E values for all models are negative. The mountainous nature of these areas, where complex terrain and snow processes play a larger role than in other parts of the basin, make these ar-

Table 2.1: Statistics of daily streamflow at the basin outlet (Lobith) for both the calibration period (1993) and the validation period (1994-2003). Correlation coefficients ρ , Nash-Sutcliffe modeling efficiencies (E) and volumetric errors of simulated discharge relative to observed discharge (RVE) are shown.

Calibration period				
	VIC	VIC-WB	STREAM1	STREAM2
ρ	0.68	0.71	0.77	0.66
E	0.29	0.39	0.47	0.31
RVE [%]	7.49	6.82	-22.77	-21.36
Validation period				
	VIC	VIC-WB	STREAM1	STREAM2
ρ	0.74	0.70	0.73	0.63
E	0.31	0.40	0.21	0.14
RVE [%]	8.04	-1.35	29.09	-25.05

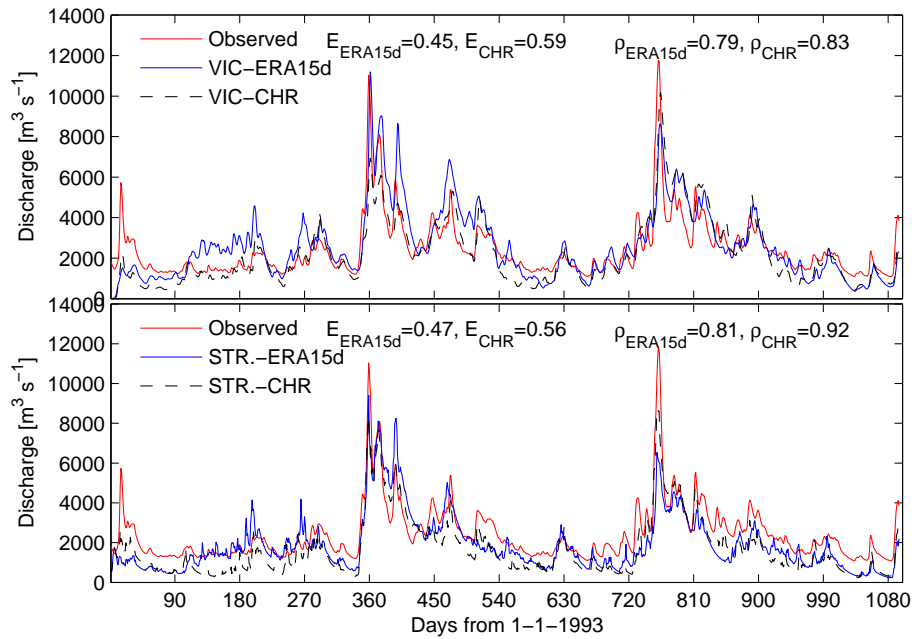


Figure 2.7: Discharge as simulated by VIC (upper panel) and STREAM (lower panel), with both ERA15d and CHR precipitation, for the period 1993 through 1995. Also model efficiencies (E) and correlation coefficients (ρ) are shown.

Table 2.2: Statistics of 10-day streamflow for five tributaries of the Rhine (Lahn, Main, Mosel, Neckar and Ruhr) and three locations along the main Rhine branch (Maxau, Andernach and Lobith). For gauge locations, see Figure 2.1. Correlation coefficients ρ , Nash-Suthcliffe modeling efficiencies (E) and volumetric errors of simulated discharge relative to observed discharge (RVE) are shown for the full (with energy balance) VIC simulation, the water balance mode simulation (VIC-WB) and STREAM.

	ρ			E			RVE [%]		
	VIC	VIC-WB	STREAM	VIC	VIC-WB	STREAM	VIC	VIC-WB	STREAM
Ruhr	0.74	0.71	0.67	0.52	0.49	0.38	0.80	-7.37	-26.28
Lahn	0.69	0.68	0.62	0.35	0.45	0.19	-35.23	2.06	-47.17
Mosel	0.74	0.78	0.67	0.47	0.53	0.28	-26.67	-19.89	-39.10
Main	0.76	0.75	0.66	0.41	0.27	0.24	-2.88	34.66	-8.00
Neckar	0.73	0.74	0.63	-0.80	-0.33	-0.13	17.89	26.67	-22.13
Maxau	0.70	0.67	0.53	-0.34	-0.02	-0.32	16.42	-5.71	-23.21
Andernach	0.76	0.71	0.63	0.39	0.42	0.03	2.34	-4.58	-27.82
Lobith	0.79	0.75	0.68	0.39	0.49	0.18	8.14	-1.24	-24.87

was difficult to simulate for all models. It is assumed, however, that applying distributed parameters in all models would probably significantly improve their performances. From Figure 2.8, it appears that these are also the areas where peak flows are most severely overestimated by VIC, which is surprising given the topography of the area where layer thicknesses are most likely overestimated by VIC, because of the uniform layer depths. There are three possible explanations for these overestimations. First, some large surface reservoirs are present in the area, of which Lake Constance (north east Switzerland, see also Figure 2.1) is the largest with a storage volume of 55 km³. These reservoirs can have a dampening effect on discharge and are not taken into account in the models. Second, the snow model in VIC (see Section 2.3) is not calibrated because no snowpack data was available, leading to a possible overestimation of snow melt. Third, the ERA15d dataset may overestimate precipitation in the periods corresponding to these peak flows, but no additional precipitation data is available to verify this. The fact that VIC also overestimates peak flows at other gauges to a lesser degree, which can be seen in Figure 2.8 for a peak in early 1999, supports this explanation. In the STREAM simulation these peaks are much less distinct (Figure 2.8), which may be explained by the fact that STREAM is known to slightly underestimate snow melt because at pixels with very high elevations temperature does not exceed 0°C, causing snow to constantly accumulate without melting. During low flow periods, all models underestimate streamflow frequently, although for STREAM this is slightly more the case than for VIC and VIC-WB.

For Lobith, daily values are analyzed more closely through a peak flow analysis. Because 1993 was a near flood year in the Rhine basin, both the calibration and validation periods are taken into account

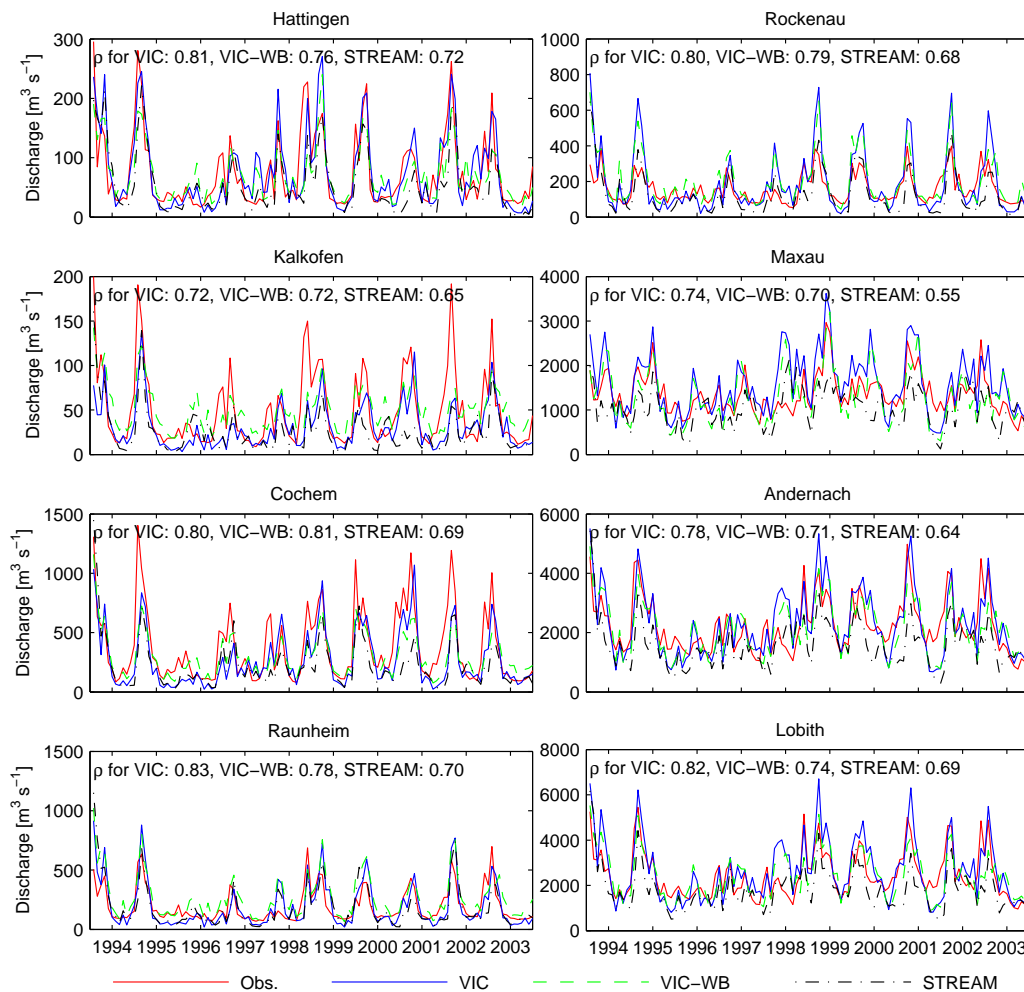


Figure 2.8: Timeseries of monthly discharge as observed, and simulated by VIC, VIC-WB and STREAM at eight gauges in the Rhine basin. Also monthly correlation coefficients ρ with respect to observations are shown in each plot.

for this analysis. Table 2.3 shows the five highest daily discharges and the five lowest monthly discharges, as observed and simulated at Lobith. In addition, two near-floods (1993 and 1995) and the extreme low flow period of 2003 are plotted in Figure 2.9. In this Figure, a time window of 20 days before and after the day of the peaks in 1993 and 1995 is shown. For the low flow period of 2003 the detailed window is 180 days. Also the average discharge during those periods is displayed. The magnitude of the 1993 event is simulated accurately by VIC with a difference of only 1.5% in the peak flow, but the peak is delayed by about 2 days, as is the case for nearly all peaks shown in Table 2.3. All models significantly underestimate the magnitude of the 1995 event, especially STREAM with more than 40%. Because the 1993 event is the only significant peak in the calibration period, it influenced the calibration procedure. The accurate simulation of this event is, therefore, not surprising. For the

Table 2.3: Peak and low flows at the outlet of the basin (Lobith). The five highest daily peaks and the five lowest monthly flows from both the calibration and validation period are shown. From top to bottom: observed peak discharge, simulated peak discharge by VIC, VIC-WB and STREAM, relative difference between simulations and observations for VIC, VIC-WB and STREAM (positive values denote higher simulated values), and, only for peak flows, the time lag (τ) of the peaks for all models. A positive time lag denotes a delay in the simulation of the peak.

Peak flows	31-1-95	25-12-93	4-11-98	7-1-03	28-3-01
Max Q_{obs} [m ³ /s]	11775	11034	9410	9366	8666
Δ_{vic} [%]	-26.7	1.5	-35.1	-15.5	12.5
Δ_{vic-wb} [%]	-21.6	11.2	-41.2	-41.4	-13.9
Δ_{stream} [%]	-44.5	-14.8	-53.2	-55.2	-38.6
τ_{vic} [days]	2	2	6	6	4
τ_{vic-wb} [days]	1	2	1	3	3
τ_{stream} [days]	-2	0	-1	4	0
Low flows	9-2003	11-1997	8-1998	9-1996	3-1993
Max Q_{obs} [m ³ /s]	958	1153	1158	1297	1338
Δ_{vic} [%]	38.8	51.4	37.9	6.1	-23.8
Δ_{vic-wb} [%]	46.6	4.9	41.0	-6.7	17.8
Δ_{stream} [%]	40.7	-10.7	32.8	2.0	-59.0

low flow period in the summer of 2003, all models, especially VIC-WB, overestimate average flow levels and show more variability than the observations. Because all models show a similar pattern this is most likely caused by overestimated precipitation events in the forcing data, although in this period no additional precipitation data is available to verify this possible explanation.

In Figure 2.10 extreme flows are further analyzed through their return periods. A log-Pearson type III distribution (see Appendix 1) is fitted based on peak discharges to compare and extrapolate extreme peak flows more easily. To fit the distribution, frequency factors were taken from Table 7.7 in *Haan* (1977). Peaks were selected using the Peak-Over-Threshold (POT) approach, where the threshold was defined as the double of the long-term mean, with the constraint that peaks should be at least 20 days apart from each other to maintain independency. This resulted in, on average per simulation, just below two peaks per year. Return periods and Pearson fits were based on maximum 10-day discharges for the eight evaluated streamflow gauges, to remove the influence of streamflow routing, as was discussed in Section 2.4. For Lobith, the same is shown for maximum daily discharges. As can also be seen in Figure 2.8, VIC overestimates peak flows especially for Maxau and Rockenau, while for small tributaries, Kalkofen and Hattingen, all models underestimate them. For the most downstream gauging stations, Andernach and Lobith, both data and Pearson fits differ strongly for lower return

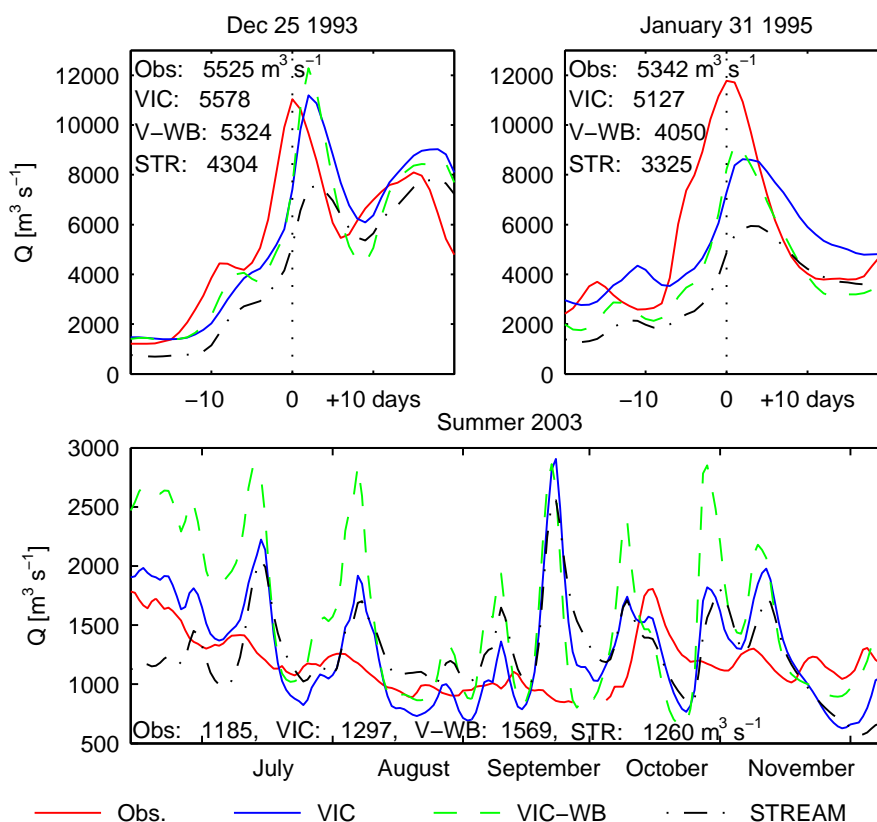


Figure 2.9: Observed and simulated daily hydrographs at Lobith, zoomed in to three extreme events in the Rhine basin. The upper panels show the near-floods of 1993 (left) and 1995 (right), the lower panel shows the low flow period of 2003. For the peak flows a time window of 20 days before and after the observed maximum is shown, for the low flow the detailed window is 180 days. The text within the panels displays the average discharge over the displayed period for all simulations.

times, whereas for high return times (up to 11 years in case of data points), models and observations agree quite well. For Maxau, however, the range in simulated and fitted discharges keeps increasing towards higher return times, although for VIC-WB the fit almost coincides with the fit based on observations for Maxau. However, modeling efficiencies for all models including VIC-WB are negative, as was mentioned before. Correlations are also relatively low at this gauge: 0.70, 0.67 and 0.53 for VIC, VIC-WB and STREAM respectively (see Table 2.2). Neither of the models performs very well for this part of the basin, mainly because of three reasons: first, the terrain is very complex, leading to local differences in precipitation and radiation that are not taken into account in the models. Second, although all models account for snow storage and melt to some degree, snow (melt) and glaciers play

Table 2.4: Average summer (S), winter (W) and annual (A) totals of precipitation, evaporation, lysimeter (observations) or pixel (models) outflow for the two lysimeters at Rheindahlen and Rietholzbach. Data from the period 1993-1998 are used and results from the models VIC, VIC-WB, STREAM are shown.

Rheindahlen	Precip.			ETP			Outflow		
	S	W	A	S	W	A	S	W	A
Lysi.	198	198	766	251	85	659	4	112	231
VIC	221	205	851	264	16	541	18	66	242
VIC-WB	221	204	851	209	84	657	24	49	188
STREAM	221	204	849	209	130	686	5	8	37
Rietholzbach	Precip.			ETP			Outflow		
	S	W	A	S	W	A	S	W	A
Lysi.	487	386	1578	269	31	541	199	340	1035
VIC	248	160	748	298	6	574	25	43	140
VIC-WB	248	160	748	217	33	509	42	55	230
STREAM	248	160	747	216	78	591	8	8	36

an important role in this area, which further complicates the situation. Third, there are surface water reservoirs present in this area that are not accounted for in the models. These surface reservoirs explain the fact that VIC overestimates peak flows for this area, especially peaks in 1998 and 1999 that are overestimated by VIC originate in the part upstream of Maxau. For gauges near the outlet of the basin (Lobith and Andernach), STREAM, and to a lesser degree also VIC-WB, underestimate the relatively low maxima. The fitted lines converge towards higher return periods, however. For these gauges, VIC simulates the extremes quite well: the fitted lines practically coincide, only for very high return times the fitted lines slightly diverge.

Figure 2.11 shows monthly evaporation as observed at the two lysimeters at Rheindahlen and Rietholzbach and simulated by VIC and STREAM. VIC accurately mimics the annual cycle at both lysimeters, hence the high correlations compared to STREAM: 0.97 and 0.80 vs. 0.71 and 0.42 for Rietholzbach and Rheindahlen respectively. Again, VIC-WB performs intermediate with 0.63 (Rheindahlen) and 0.83 (Rietholzbach). VIC simulates summer evaporation quite well for both locations, but underestimates winter evaporation, especially for Rheindahlen. For STREAM, modeled evaporation shows more variability and in winter evaporation is mostly overestimated. VIC-WB also shows more variability but simulates average winter evaporation very well at both lysimeters (Table 2.4). Both STREAM and VIC-WB underestimate summer evaporation. The smaller amplitude in evaporation cycle for VIC-WB and STREAM can be explained by the fact both models assume the surface temperature to be equal to the air temperature, while VIC computes the surface temperature from the energy balance. In summer, the surface is warmer than the air (giving higher evaporation than when air temperature is used) while in winter the opposite is true. This difference is captured by VIC but neglected

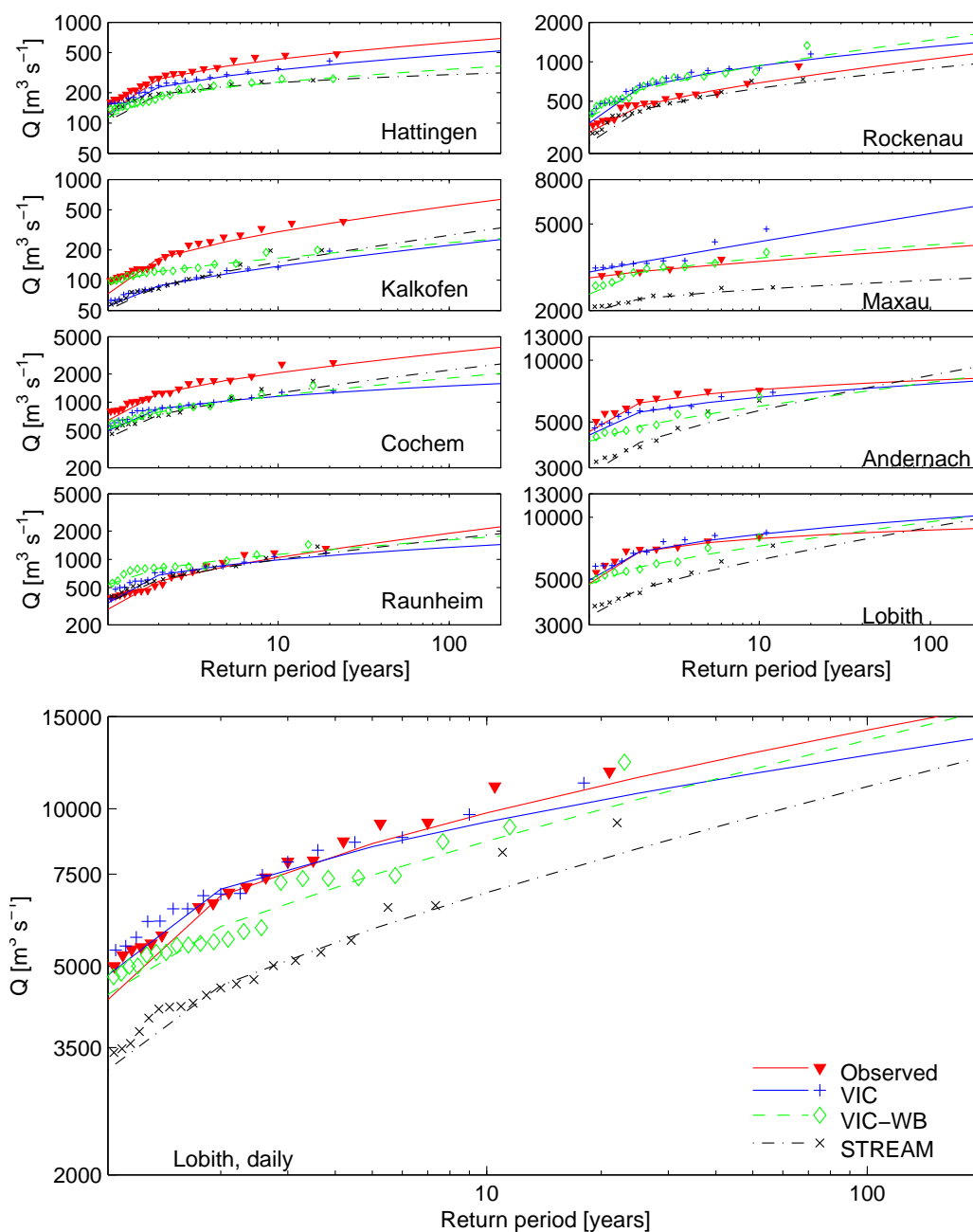


Figure 2.10: Peak flows selected using a peak-over-threshold approach and their return periods, as well as a log-Pearson type III distribution fitted through the data points. The upper eight panels show the fits at the eight evaluated stream-flow gauges, where STREAM is routed using the VIC routing algorithm, based on annual maximum 10-day discharges. The lower, larger panel shows the same only for Lobith, based on annual maximum daily flows, where STREAM is routed using the original STREAM algorithm.

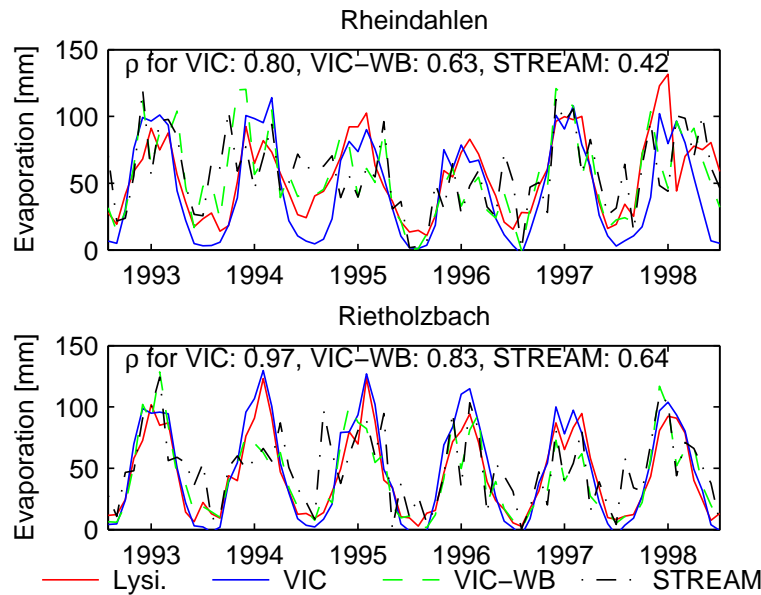


Figure 2.11: Monthly evaporation for lysimeters Rheindahlen (upper panel) and Rietholzbach (lower panel) as observed by lysimeters and modeled by VIC, VIC-WB and STREAM. Correlation coefficients are displayed in the left upper corners.

by VIC-WB and STREAM. When total annual evaporation is considered, VIC simulated evaporation in Rheindahlen is too low, mainly due to the underestimation in winter, while evaporation simulated by STREAM and VIC-WB is comparable to observations. VIC's underestimation in winter may partly be explained by vegetation parameters that do not completely correspond to the exact conditions at the lysimeter location, an effect that is masked by the 'dampened' annual cycle in the other models that was mentioned before. Another partial explanation can be in VIC's snow model that was not specifically calibrated and may contribute to the underestimated evaporation in winter. In addition, in Table 2.4 it can be seen that observed precipitation in Rietholzbach is higher than it is at the corresponding location in the ERA15d dataset, however, practically all extra rainfall leaves the lysimeter as outflow, hence evaporation is still similar to simulated values.

2.6 Discussion and conclusions

We applied three models (VIC, VIC-WB and STREAM) with the same meteorological forcing to the Rhine basin and evaluated them using observed streamflow and measured evaporation data from two lysimeters. All models were calibrated to a similar level, using data from only one representative year and keeping calibration parameters uniform over the catchment. STREAM is a simple, relatively easy to calibrate model, needing only temperature and precipitation as input, while VIC is more phys-

ically based and requires more parameters and computation time. VIC-WB is an intermediate in that it does not solve the coupled water and energy balance but does account for, for example, sub-grid variability. Streamflow at Lobith was simulated best by STREAM during the calibration period. During the validation period, however, the performance of STREAM decreased while VIC and VIC-WB improved, indicating a smaller dependence on calibration for VIC: while only calibrated to a limited extent, results in the validation period were still acceptable. It should be kept in mind that this relatively simple calibration process still was much more computationally demanding than the STREAM calibration. Especially for the calibration period, most of the difference between observed and simulated discharge for all models were explained by differences between meteorological (re-analysis) forcing data and observed data for the same period. Because only three years of overlapping data and not all the input fields required to run VIC were available as observations, and because the re-analysis data is similar to RCM outputs that are generally used to assess the hydrological impacts of climate change, we used the re-analysis dataset to drive the models. This should be kept in mind while interpreting the results described before. Simulated evaporation was compared to lysimeter observations at two very different locations in the catchment. It appeared that VIC quite accurately mimicked the annual cycle at both locations, but, especially at Rheindahlen, underestimated evaporation in winter. STREAM produced acceptable annual values but poorly reproduced the annual cycle and showed a large short term variability. Both STREAM and VIC-WB significantly underestimated summer evaporation. This can be explained by the assumption in VIC-WB (and STREAM) that surface temperature is equal to air temperature, whereas VIC derives surface temperature from the energy balance. Because in summer surface temperature is usually higher than air temperature, potential evaporation is underestimated. In this case, the impact of this assumption appears to be significant. In interpreting the lysimeter results, however, it should be kept in mind that vegetation parameters were defined for the most dominant vegetation types in 25 square kilometer grid cells, which do not necessarily have to be the same as these particular lysimeter locations. Besides that, we did not optimize vegetation and evapotranspiration parameters in this study.

Streamflow from various tributaries and the catchment as a whole was generally modeled best by VIC during the validation period. The Alpine part (upstream of Maxau) was not modeled very well by either of the models, STREAM underestimated streamflow especially in spring, indicating underestimation of snow melt by its simple snow melt algorithm. VIC underestimated snow melt much less, and tends to overestimate winter peak flows, due to reservoirs in this area that are not taken into account in VIC. The extreme events investigated in this study were generally modeled better by VIC when peak flow height was considered, but the timing of peaks was slightly delayed, in spite of varying parameters (celerity, diffusivity) in the routing algorithm. STREAM underestimated especially peak flows with lower return times in the simulated period, although for the most downstream gauging stations fitted log-Pearson curves and data points converged with the observations at higher return periods.

Overall, STREAM systematically underestimated peak flows. Because in the low flow part of the cal-

ibration period streamflow was simulated well, even though input precipitation was partly too high, this suggests that the high precipitation was compensated by the calibration, increasing infiltration capacity and/or evapotranspiration. In this particular period, streamflow simulated by VIC was too high, whereas over the whole period, peak flows were better predicted by VIC. This indicates that VIC is less sensitive to the model calibration and more robust. Overall, performance of all models would most likely be improved by calibrating them in a distributed way, however, especially for VIC this would be computationally very intensive.

Application of STREAM is easier because it requires only precipitation and temperature as input data, and only little computation and calibration time. VIC in full mode, on the other hand, requires more atmospheric input data and relatively long computation times. Therefore, when assessment of the effects of climate change is the objective, involving simulations over long periods (e.g., hundreds of years), running VIC in the full mode at this scale quickly becomes infeasible and one is obliged to use a less complex model. Running VIC in water balance mode significantly reduces computation time (almost by a factor 5) and also reduces the forcing data requirements. The sub-grid variability that is accounted for in VIC-WB, as opposed to STREAM, results in improved streamflow simulation compared to STREAM. Similar to STREAM, however, VIC-WB then becomes relatively sensitive to model calibration, the validity of which can be questionable when carried out under current climatic conditions. Including the energy balance further improves extreme streamflow simulation, significantly improves simulation of evapotranspiration and increases the model's robustness. However, long computation times when running VIC in the full mode oblige one to, for example, only simulate the most extreme parts of long climate scenario time series.

Acknowledgements

This research was supported by the European Commission through the FP6 Integrated Project NeWater (<http://www.newater.info>) and the BSIK ACER project under the Dutch Climate Changes Spatial Planning programme. Daniela Jacob and Eva Starke from the Max Planck Institut für Meteorologie are kindly acknowledged for providing meteorological data and we gratefully acknowledge Reto Stöckli from ETH, Zürich for providing the lysimeter data. Finally, we thank Rita Lammersen and Hendrik Buiteveld from Rijkswaterstaat Waterdienst, The Netherlands, for providing the streamflow observations and the two anonymous reviewers for their constructive and helpful comments.

Chapter 3

Effects of land use changes on streamflow generation in the Rhine basin



This chapter is a modified version of: R. T. W. L. Hurkmans, W. Terink, R. Uijlenhoet, E. J. Moors, P. A. Troch and P. Verburg (2009), *“Effects of land use changes on streamflow generation in the Rhine basin”*, Water Resour. Res., in press.

Abstract

The hydrological regime of the Rhine basin is expected to shift from a combined snowmelt-rainfall regime to a more rainfall-dominated regime because of climate change, leading to more extreme flood peaks and low flows. Land use changes may reinforce the effects of this shift through urbanization, or counteract them through, for example, afforestation. In this study, we investigate the effect of projected land use change scenarios on river discharge. Sensitivity of mean and extreme discharge in the Rhine basin to land use changes is investigated at various spatial scales. The Variable Infiltration Capacity (VIC; version 4.0.5) model is used for hydrological modeling forced by a high-resolution atmospheric dataset spanning the period 1993 to 2003. The model is modified to allow for bare soil evaporation and canopy evapotranspiration simultaneously in sparsely vegetated areas, as this is more appropriate to simulate seasonal effects. All projected land use change scenarios lead to an increase in streamflow. The magnitude of the increase, however, varies among sub-basins of different scales from about 2% in the upstream part of the Rhine (about 60,000 km²) to about 30% in the Lahn basin (about 7,000 km²). Streamflow at the basin outlet proved rather insensitive to land use changes, because over the entire basin affected areas are relatively small. Moreover, projected land use changes (urbanization and conversion of cropland into (semi-)natural land or forest) have opposite effects. At smaller scales, however, the effects can be considerable.

3.1 Introduction

The Rhine basin is a densely populated and industrialized river basin in Western Europe. Therefore, floods and droughts occurring in the basin can have vast consequences (*Middelkoop et al.*, 2001; *Kleinn et al.*, 2005). For example, the near-floods in 1993 and 1995 caused severe damage (only in Germany about 900 million USD; see also *Kleinn et al.* (2005)). The drought period of 2003 affected a wide range of sectors, from inland navigation to hydropower generation (*Middelkoop et al.*, 2001). Climate change scenarios project temperatures to increase by 1.0-2.4°C over the Rhine basin by 2050 (*Barnett et al.*, 2005; *IPCC*, 2007), as a result of which the hydrological cycle is expected to intensify, causing more extreme precipitation events (*Trenberth et al.*, 2003). Both factors will have major impacts on the hydrological regime: the temperature increase will cause more precipitation to fall as rain instead of snow, and the winter snow pack will melt earlier in spring (*Barnett et al.*, 2005). The Rhine basin hydrology, therefore, will shift from a combined rainfall-snowmelt regime to a more rainfall-dominated regime, resulting in increased flood risk in winter and a higher probability of extensive droughts in summer.

In addition to climate change, land use changes can also have a profound influence on hydrological processes. For example, recent research by *Laurance* (2007) and *Bradshaw et al.* (2007) indicated that deforestation can increase flood risk, because deforestation causes canopy interception storage, transpiration, and infiltration capacity to decrease (*Clark*, 1987). In addition, forests strongly affect snow accumulation and melt processes relative to other land use types (*Matheussen et al.*, 2000). Counteracting the effects of afforestation, the fraction of urbanized area in Europe is increasing strongly and expected to continue increasing (e.g. *Rounsevell et al.*, 2006). Urban land possesses the opposite hydrological properties of forest, i.e., less infiltration capacity through creation of impervious surface, removal of vegetation and thus transpiration, and less possibilities for snow storage. Therefore, urbanization increases flood risk both because of altering flood frequency distributions and the increase in economic damage (*DeWalle et al.*, 2000; *Dow and DeWalle*, 2000). When careful land use planning is applied, land use changes could help to mitigate the impact of climate change. Therefore, it is worthwhile to investigate whether afforestation (e.g. of agricultural land), can decrease the magnitude of flood peaks and alleviate extensive drought periods.

Recently, two European-wide studies, i.e. ATEAM (*Rounsevell et al.*, 2006) and Eururalis (*Verburg et al.*, 2006a, 2008), have provided scenarios for land use development in Europe (*Verburg et al.*, 2006b). These scenarios offer possibilities for a hydrological assessment of the projected land use changes. Several studies have investigated the impact of land use change on streamflow generation. For example, *Hundecha and Bárdossy* (2004) used a conceptual rainfall-runoff model with regionalized parameters to assess the impact of hypothetical land use changes. *Quilbe et al.* (2008) used past land use evolution determined from satellite images, hypothetical future changes and an integrated, GIS based modeling system. *DeWalle et al.* (2000) and *Claessens et al.* (2006) investigated effects of urbanization on streamflow in urbanizing watersheds in the U.S. Many of these studies, however, use statistical methods and historical land use data, and/or relatively simple, conceptual models. These models

have the disadvantage that land use specific parameters often do not have a physical meaning and can be used to calibrate the model, for example by tuning a crop factor, making it difficult to assign parameters to differentiate land use classes. A straightforward solution is the application of a distributed, more physically based model, as was done by *Matheussen et al.* (2000). These researchers used the Variable Infiltration Capacity (VIC) model (*Liang et al.*, 1994) to assess the effect of land cover change between 1900 and present on streamflow in the Columbia river basin. Very recently, *Saurral et al.* (2008) used the VIC model to assess land use impacts in the Uruguay river basin. The VIC model has the advantages that it solves the coupled water- and energy balance to calculate evapotranspiration and assigns physically based parameters, such as albedo and leaf area index, to each land use type. In addition, it accounts for sub-grid variability by dividing each grid cell into land use fractions. When the physically based parameters are assumed realistic, therefore, no calibration parameters are needed in the calculation of transpiration, snow accumulation and melt.

To our knowledge, land use change scenarios as provided by projects like Eururalis have not been used for hydrological impact studies of land use change at this large river-basin scale. At smaller scales, however, for example *Niehoff et al.* (2002), *Bronstert et al.* (2002), and *Bronstert et al.* (2007) employed land use change scenarios from a land use change model to investigate their hydrological impact on storm-runoff. In this study, we use the VIC model in combination with the Eururalis land cover change scenarios to investigate the effect of land use change on streamflow generation in the Rhine basin. To verify model processes for different land use types, we first simulate evapotranspiration and runoff generation in a single model grid cell. A slightly modified version of the model is then used to simulate land use change scenarios for the entire Rhine basin. In addition, we evaluate some extreme, hypothetical scenarios where cropland is converted to forest or grassland to explore possibilities of afforestation to mitigate effects of climate change. To evaluate up to which spatial scale land cover change can affect streamflow generation, streamflow from sub-basins of various sizes are analyzed. The remainder of this paper is structured as follows: after a short overview of study area, datasets and the VIC model in Section 3.2, results of the simulations of a single pixel are discussed in Section 3.3. Simulations covering the entire basin are discussed in Section 3.4. Finally, in Section 3.5, we provide a short summary and draw conclusions from our simulation results.

3.2 Study area, model and data

The Rhine River is a major river in Western Europe. It originates in the Swiss Alps and drains to the North Sea after passing through the delta area in The Netherlands (Figure 1.5). Because of the various bifurcations in the lower Rhine, only the part upstream of Lobith (the point where the river crosses the German-Dutch border) is considered in this study. Table 1.1 shows the main tributaries of the Rhine with their size and streamflow characteristics. The area of the Rhine upstream of Lobith is about 185,000 km². The Rhine is a mixed river, i.e., in part snow dependent (melt water from the Alps) and in part rain dependent. For a more extensive description of the Rhine basin, see Section 1.2.

The Variable Infiltration Capacity (VIC) model is a distributed Soil-Vegetation-Atmosphere Transfer (SVAT) model developed for general and regional circulation models (Liang *et al.*, 1994, 1996). It solves the coupled water-and energy balances, and sub-grid heterogeneity is included through a statistical parameterization for infiltration capacity and a division of each grid cell into tiles based on land use types and elevation zones. The VIC model can operate in two modes. The energy balance mode solves the coupled water and energy balance iteratively to calculate the available energy for evapotranspiration. In the water balance mode, on the other hand, surface temperature is assumed equal to air temperature, thus considerably saving computation time. Routing of surface runoff and baseflow was done using the algorithm developed by Lohmann *et al.* (1996). The VIC model is described in more detail in Section 1.3.

For atmospheric forcing, a downscaled re-analysis dataset is used, which is described in detail in Hurkmans *et al.* (2008). It consists of re-analysis data from ECMWF (ERA15¹, extended with operational ECMWF analysis data. Downscaling of the data was done dynamically by the regional climate model REMO (Jacob, 2001). The dataset consists of precipitation, temperature, wind speed, short- and longwave incoming radiation, air pressure and vapor pressure. All data are available at a temporal resolution of 3 hours and a spatial resolution of 0.088 degrees for the entire Rhine basin over the period 1993-2003. For all simulations in this study, 1993 is used to initialize the model and the remaining 10 years (1994-2003) are used in the analyses. Soil data are obtained from the global FAO dataset (Reynolds *et al.*, 2000). Based on sand and clay percentages from this dataset, soil textures are classified into twelve soil texture types as defined by USDA². For each type, the associated hydraulic parameters are used as given on the VIC-website³. Land use information to represent the current situation is obtained from the Pan-European Land Cover Monitoring and Mapping (PELCOM) database (Mücher *et al.*, 2000), providing a high-resolution (1x1 km) land cover map of Europe.

The VIC model (version 4.0.5) was applied to the Rhine basin as described in Hurkmans *et al.* (2008), at a spatial resolution of 0.05 degrees and a temporal resolution of three hours. In the present study we use the same set-up as Hurkmans *et al.* (2008), except for the following changes. First, in Hurkmans *et al.* (2008) a spatially uniform calibration was used for model comparison purposes. This was considered to be a cause for the modest modeling efficiencies of simulated Rhine discharges. Therefore, instead of a spatially uniform calibration, five sub-basins (the Ruhr, Lahn, Main, Mosel and Neckar; shown in Figure 1.5) were calibrated separately in the current study. Apart from these five sub-basins, two areas along the main Rhine branch (upstream of Maxau, and the stretch Maxau-Lobith), are used for calibration. For every sub-basin, the same calibration method was used as in Hurkmans *et al.* (2008). Results of the model calibration are shown in Figure 3.1. Here, hydrographs are shown for observed and simulated streamflow at Lobith, the basin outlet. The Nash-Sutcliffe modeling efficiency E (Nash

¹<http://www.ecmwf.int/research/era/ERA-15/>

²<http://soils.usda.gov/technical/handbook/>

³<http://www.hydro.washington.edu/Lettenmaier/Models/VIC/Documentation/Info/soiltext.html>

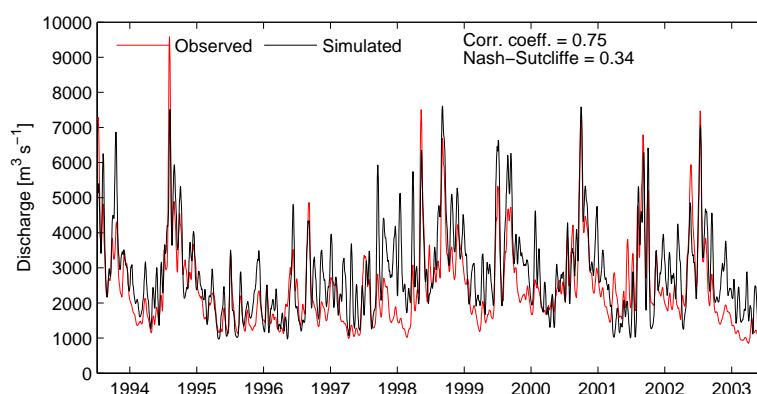


Figure 3.1: Simulated discharge at the basin outlet, Lobith, compared with observations. The entire period that is used in this study is shown (i.e. 1994–2003). Correlation coefficient and Nash-Sutcliffe modeling efficiency are shown in text. For visibility, 10-day running averages are plotted.

and Sutcliffe, 1970) and the correlation coefficient ρ are also shown in Figure 3.1. They are not particularly high (0.34 and 0.75 resp.), mainly because of two reasons. First, the entire period from 1994–2003 is used to calculate ρ and E , whereas only the period October 1993 to December 1994 was used for calibration (the first part of 1993 was used for model initialization). The remaining period is used for validation. Second, as was pointed out in *Hurkmans et al.* (2008), the atmospheric forcing that was used is not always consistent with observations, causing big differences between observed and modeled precipitation. The re-analysis data were used because available observed datasets are of insufficient spatial and temporal resolution to force the model. In Figure 3.1, however, it can be seen that overall peak flows are simulated quite well, although some peaks are over- or underestimated.

Land use scenarios are obtained from the Eururalis⁴ project (*Verburg et al.*, 2006a). Changes in demand for agricultural land use were determined at the national level for the European states using a combination of two global scale models: the integrated assessment model (IMAGE) and a global economy model (GTAP) that were used to describe the influences of global changes in demography, economy, policy and climate on European land use (*van Meijl et al.*, 2006; *Eickhout et al.*, 2004). A land use change model (Dyna-CLUE; *Verburg et al.* (2008)) was used to allocate land use types to individual grid cells of 1 km² for the European Union. From the various results provided by this project, four land cover maps as projected for 2030 are extracted. These four land use change scenarios were developed based on four emission scenarios that were defined by the IPCC in the Special Report on Emission Scenarios (SRES; *IPCC* (2000)): A1 (“Global economy”), A2 (“Continental market”), B1 (“Global cooperation”) and B2 (“Regional communities”). The A-scenarios thus refer to a more economically oriented society with low regulation, the B-scenarios to a more environmentally aware society with high regulation.

⁴<http://www.eururalis.eu>

Table 3.1: Land use types in all scenarios as percentages of area, for the entire basin and the Lahn tributary.

Entire basin									
Scenario	Forest	Crops	Grass	Urban	Water	Snow/Ice	Shrubs	Wetlands	Bare soil
Current	42.17	39.61	10.63	4.76	1.01	0.59	0.20	0.00	1.03
Eururalis A1	40.49	25.21	11.82	10.62	1.34	0.59	8.79	0.06	1.09
Eururalis A2	38.38	33.44	13.34	8.64	1.32	0.58	3.14	0.06	1.09
Eururalis B1	40.92	24.43	11.79	8.56	1.31	0.58	11.26	0.06	1.10
Eururalis B2	41.11	26.06	12.51	8.47	1.35	0.59	8.76	0.06	1.09
Lahn									
Scenario	Forest	Crops	Grass	Urban	Water	Snow/Ice	Shrubs	Wetlands	Bare soil
Current	42.19	50.16	4.72	2.93	0.00	0.00	0.00	0.00	0.00
Eururalis A1	45.01	17.53	16.07	9.82	0.06	0.00	11.50	0.00	0.00
Eururalis A2	43.39	29.84	17.28	7.34	0.07	0.00	2.07	0.00	0.00
Eururalis B1	45.17	18.48	15.61	7.20	0.06	0.00	13.49	0.00	0.00
Eururalis B2	44.98	22.03	16.82	7.50	0.07	0.00	8.60	0.00	0.00

Similarly, the A1 and B1 scenarios refer to a more globalized and the A2 and B2 scenarios to a more regional society. For further details about these four scenarios we refer to Section 1.1.3 and IPCC (2000). For the specific elaboration of the land use change scenarios to the European context and land use policies we refer to *Westhoek et al.* (2006). The resulting land cover maps, as well as the current situation, are shown in Figure 3.2. In addition, the main land cover types as fraction of total area are tabulated in Table 3.1 for the Rhine basin and the Lahn sub-basin (on which most analyses will focus in the remainder of this study).

It is important to mention that the Eururalis scenarios do not take into account changes in land management, such as tillage practices or timing of crop planting. In this paper, therefore, only effects of changes in land cover are taken into account, not in land management. A drawback of the Eururalis data is that the project was only carried out for the 27 countries of the European Union. Therefore, no data is available for Switzerland. Most of Switzerland has an alpine character and consequently the amount of agricultural areas is relatively small. Therefore, changes in land use will probably be relatively small compared to changes in other parts of the Rhine basin, as is also indicated by the national level scenario results of Eururalis that include Switzerland (*Eickhout et al.*, 2007). In the remainder of this study, therefore, land use changes in Switzerland are ignored and the PELCOM land cover map is adopted over Switzerland for all scenarios. In addition, in Eururalis there is only one class for forest, whereas in PELCOM, three types of forest are differentiated: deciduous, coniferous and mixed. To account for this, all types of forest in the reference situation, as well as the forest type in Eururalis, are assigned parameters of the “mixed” type. Furthermore, we added the vegetation class “urban area” to the parameterization in the VIC model because this did not exist yet; usually urban areas are clas-

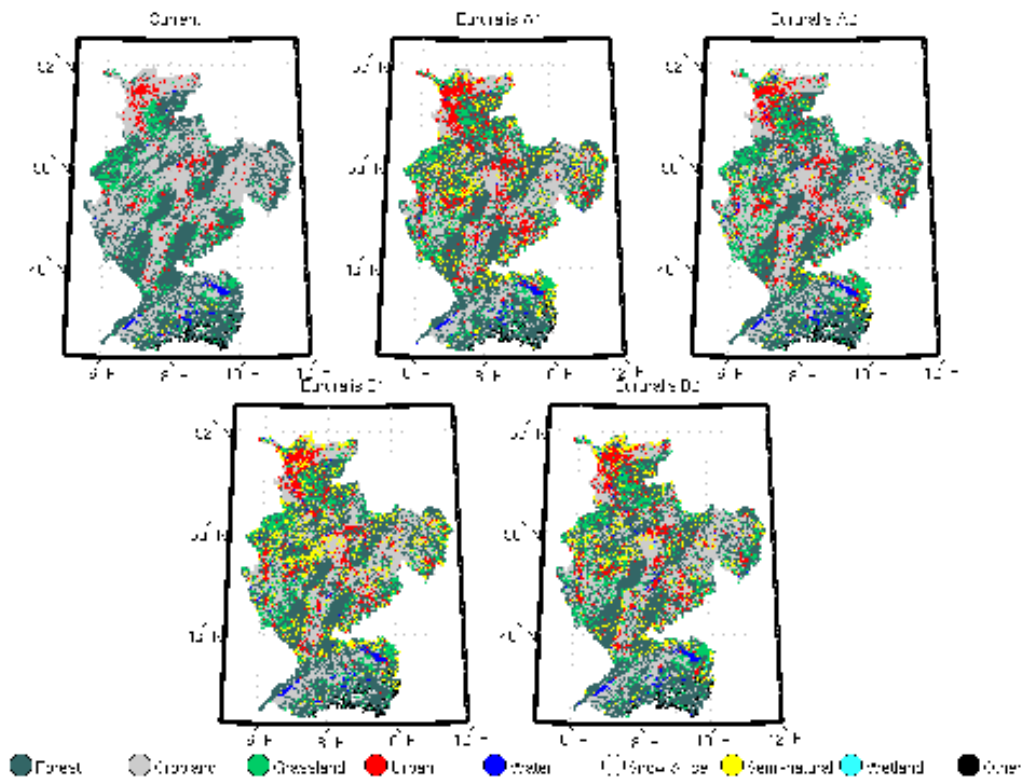


Figure 3.2: Land cover maps of the Rhine basin for the current situation and the four Eururalis scenarios (A1, A2, B1 and B2). Scenarios are projected for 2030.

sified as bare soil. By assigning such a vegetation class, it is possible to define specific settings of soil and vegetation parameters for urban areas. The advantage of adjustable parameter values for urban areas is that the effects of management measures that often take place in urban areas, such as local storage reservoirs, parks, and so-called “green roofs” can be evaluated. This is planned for further research. Because land cover types in Eururalis differ from those in PELCOM, multiple Eururalis types are grouped and given identical parameters. This classification and the most important parameters, in terms of sensitivity, are shown in Table 3.2. These parameters, which include maximum and minimum leaf area index (LAI is prescribed to the model as monthly values), architectural resistance and the minimum stomatal resistance, are based on parameter values available from the VIC website⁵. To explore the effects of (de)forestation, some more extreme, hypothetical scenarios were created by replacing all cropland by either forest or grassland in addition to the Eururalis scenarios.

⁵<http://www.hydro.washington.edu/Lettenmaier/Models/VIC>

Table 3.2: Classification of Eururalis land cover types and the main vegetation parameters for each land use type: annual minimum/maximum leaf area index (LAI), architectural resistance (R_{arc}) and minimum stomatal resistance (R_{min}).

PELCOM	Eururalis	Min. LAI [-]	Max. LAI [-]	R_{arc} [s m ⁻¹]	R_{min} [s m ⁻¹]
Water	Salines	0.00	0.00	0.00	0.00
	Water and coastal flats				
Coniferous forest	-	3.40	4.40	50.0	50.0
Deciduous forest	-	1.52	5.00	40.0	30.0
Mixed forest	Forest	2.46	4.7	45.0	40.0
Grassland	Grassland	2.00	3.85	2.0	90.0
Rainfed crop	Non-irrigated arable	0.018	4.50	2.0	90.0
	Annual biofuel crop				
Irrigated crop	Irrigated arable	0.018	4.5	2.0	90.0
Permanent crop	Permanent arable	0.018	4.50	2.0	90.0
	Perennial biofuel crop				
Shrubland	(Semi-)natural vegetation	2.00	3.85	3.0	110.0
	Abandoned arable land				
	Abandoned grassland				
	Heather and moorlands				
Wetlands	Inland wetland	2.00	3.85	2.5	110.0
Ice & Snow	Glaciers & snow	0.00	0.00	0.00	0.00
Urban land	Built-up area	0.00	0.00	5.00	0.00
Bare soil	Sparsely vegetated	0.00	0.00	0.00	0.00
	Beaches, dunes and sands				

3.3 VIC model simulations of a single pixel

To verify how the VIC model treats different land use types, a single grid cell was simulated for six land cover types, each completely covering the grid cell. A grid cell in the northern part of the basin (51.15 °N / 6.35 °E) was chosen because of the availability of lysimeter data. Atmospheric data for the period spanning 1994 through 2003 was used for all simulations, and data from 1993 was used to initialize the model. Because the model can operate in two modes, simulations were carried out for both the water and energy balance modes to check whether the differences in water balance terms between the land use types are similar in each mode. In both the water and energy balance mode, a model time step of three hours was used. In general, evapotranspiration tends to be lower in the energy balance mode compared to the water balance mode, and thus streamflow tends to be slightly higher. The surface temperature, which is iteratively solved in the energy balance mode, is higher than the air temperature most of the time. In the water balance mode, both are assumed to be equal.

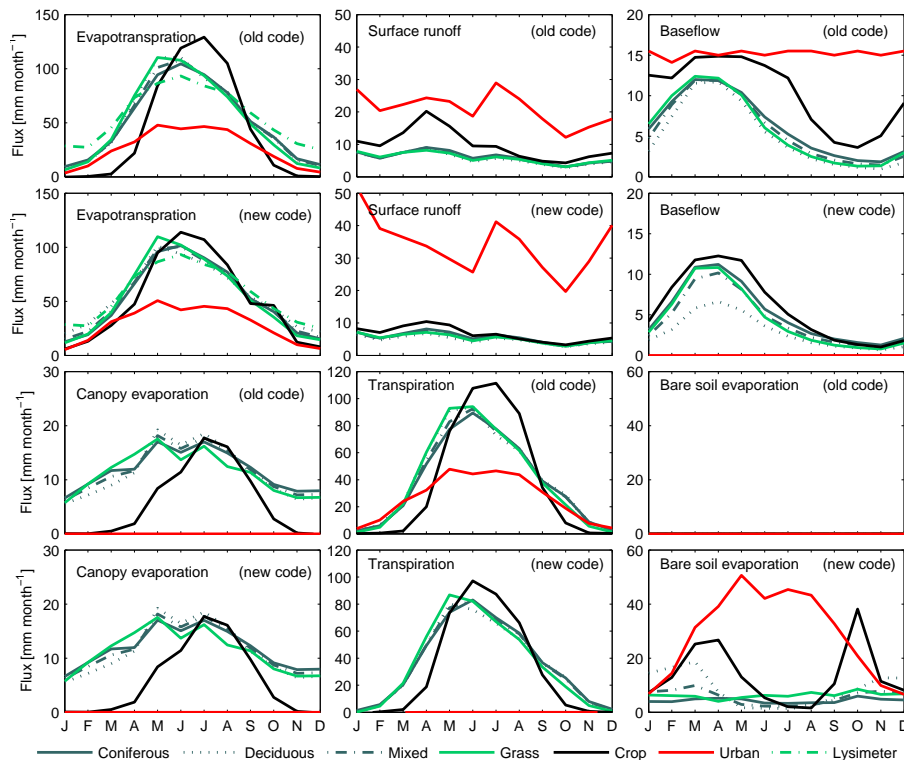


Figure 3.3: Climatology of total evapotranspiration, runoff and baseflow for different land use types, according to the original VIC model (upper row) and the modified VIC model (second row from the top). The lower rows show evapotranspiration components: canopy (interception) evaporation, transpiration and bare soil evaporation, according to the original (third row from the top) and modified code (lower row). All VIC model simulations are carried out using the water balance mode. In the plots for evapotranspiration (left upper panel and the one below), the dash-dotted line in the same color as grassland shows the climatology of lysimeter observations (lysimeter is covered by grass).

The higher temperature in the energy balance mode leads to a higher outgoing longwave radiation and sensible heat flux, lower net radiation available for evapotranspiration, and thus higher streamflow. These effects are similar across land use types, although they are less strong in forests. The difference is smaller than 1% for forest, whereas for other land use types it is about 7% (Table 3.3). In Figure 3.3, the climatology of several fluxes are shown for different land use types using the water balance mode. In the energy balance mode, the fluxes are almost entirely similar and are therefore not shown. Only in some months (e.g. surface runoff in April), differences between land use types are slightly larger in the energy balance mode compared to the water balance mode.

From Figure 3.3, it becomes clear that our original application of the VIC model, denoted as VIC_{org}

hereafter, is not fully suitable to simulate vegetation and land use changes. This was also noticed in an earlier study (Hurkmans *et al.*, 2008), which compared lysimeter data to evapotranspiration as modeled by the VIC model (VIC_{org}) for the same pixel that was used here, and found an underestimation of about 100 mm per year by the VIC model (their Table 5), mainly originating from the winter half year. Mean monthly values of evapotranspiration as measured by this lysimeter are also shown in Figure 3.3. The underestimation of evapotranspiration in winter also shows in this figure: especially for crop land there is no evapotranspiration in winter whatsoever. Even though the LAI in winter for cropland is very low (0.02; Table 3.2), there is no bare soil evaporation. This can be explained by the way evapotranspiration is conceptualized in the VIC model: when a vegetation tile is classified as vegetation during model initialization, only the canopy evaporation and transpiration routines are called in the model. The VIC model has been modified to accommodate for this by implementing in each vegetation tile a fraction of bare soil, F_b , which can be exponentially related to the Leaf Area Index (LAI; see for example Teuling *et al.* (2007); Gilabert *et al.* (2000)):

$$F_b = \exp(-C * LAI) \quad (3.1)$$

where C is a light extinction coefficient. LAI is prescribed to the model on a monthly base. For the fraction F_b , an extra call to the bare soil evaporation routine is implemented and the bare soil evaporation from fraction F_b is added to transpiration. Incoming radiation available for bare soil evaporation is also multiplied by the factor F_b . Values for the light extinction coefficient C were taken from the literature (e.g. Teuling and Troch, 2005) where possible. Verstraeten *et al.* (2005) investigated evapotranspiration in ten different forests and croplands in the same climate zone (Flanders, Belgium) and calculated mean annual values for forest and cropland for total evapotranspiration, bare soil evaporation, interception evaporation and transpiration for the period 1971–2000. These values (shown in Table 3.3), as well as the annual total evapotranspiration value for grass from the lysimeter described above and in Hurkmans *et al.* (2008) are used as a reference to validate our modifications to the VIC model.

Table 3.3 shows that evaporation from bare soil is a significant part of total evapotranspiration: about 10% on average for forests and up to 30% for cropland. The fact that in winter the total evapotranspiration for grass as observed by the lysimeter is much higher than the simulated values (Figure 3.3) also suggests that bare soil evaporation is of importance. Because the coverage of grass is relatively high year-round, the contribution of bare soil will be smaller than for deciduous forest and cropland. To realistically simulate the seasonal cycle of evapotranspiration, therefore, bare soil evaporation should be included for vegetated surface as well. In VIC_{mod} , annual evapotranspiration is higher for all land use types compared to the old situation, due to the inclusion of bare soil evaporation. The amount of transpiration, however, significantly decreased in VIC_{mod} compared to VIC_{org} . The higher annual total evapotranspiration is in accordance with the lysimeter data for this location, which is shown in Table 3.3 for grass. As can be seen in Figure 3.3, the annual cycle for grass is also represented more realistically due to higher evapotranspiration values in winter and spring because of the inclusion of

Table 3.3: Mean annual values for total evapotranspiration (ET), surface runoff (R), baseflow (B), canopy evaporation (E_c), transpiration (T) and bare soil evaporation (E_b) for 6 land use classes, for the original version of the VIC model (O), the modified version of the VIC model (N) and other sources (literature, observations) where possible (D). Data for cropland and forest are from *Verstraeten et al.* (2005). They represent average annual values of 10 forests and 10 croplands over the period 1971–2000. Data for grass are average annual values (1993–1998) from the lysimeter described in *Hurkmans et al.* (2008), which is covered by grass. Simulation of both the water and energy balance modes of the VIC model are shown. Mean annual precipitation is 750 mm.

Water balance mode																
Type	ET			R		B		E_c			T			E_b		
	N	O	D	N	O	N	O	N	O	D	N	O	D	N	O	D
Conif.	629	608		67	73	60	75	141	141		434	466		52	0	
Decid.	663	628	491	57	67	34	60	136	136	126	422	491	315	103	0	47
Mixed	640	616		63	71	52	69	139	139		431	475		68	0	
Grass	639	614	659	63	70	53	71	135	135	-	429	480	-	75	0	-
Crop	608	518	398	79	118	70	124	69	69	0	378	450	261	162	0	131
Urban	341	314	-	409	252	0	183	0	0	-	-2	314	-	343	0	-
Energy balance mode																
Type	ET			R		B		E_c			T			E_b		
	N	O	D	N	O	N	O	N	O	D	N	O	D	N	O	D
Conif.	634	604		64	73	57	79	143	143		402	458		86	0	
Decid.	665	623	491	56	68	33	64	139	139	126	387	482	315	137	0	47
Mixed.	644	611		61	72	50	73	142	142		397	466		102	0	
Grass	628	598	659	66	75	62	84	141	142	-	404	458	-	84	0	-
Crop	589	486	398	86	136	84	139	73	75	0	356	412	261	162	0	131
Urban	323	290	-	427	278	0	183	0	0	-	-6	291	-	330	0	-

bare soil evaporation. In comparing the data from *Verstraeten et al.* (2005) to our results, it should be noted that the data from *Verstraeten et al.* (2005) are from a different area and were calculated over a different (much longer) time period. In addition, *Verstraeten et al.* (2005) assumed an interception evaporation of zero for cropland, although they state that this can amount to 25 to 82 mm year⁻¹. Their total evapotranspiration for cropland is thus probably underestimated.

From the values in Table 3.3, it appears that the total evapotranspiration values for grass are about as high as for forest in both versions of the code. This is not realistic compared to measured data from catchment studies where usually forest yields higher evapotranspiration than other land use types (*Bosch and Hewlett, 1982*). An overestimation of canopy interception evaporation (E_c) seems to be the

main cause for this. In the VIC model, however, E_c is mainly a function of the LAI (Table 3.2) and the aerodynamic and architectural resistances. As can be seen in Table 3.2, these parameters do not differ very much across land use types. As was mentioned before, these parameter values were obtained from the VIC website. A review of plant parameter values by Breuer *et al.* (2003), however, indicates a large range in values of canopy resistance and LAI. This range exists not only across land use types; for LAI also significant differences between similar land use types in North America and Europe were found. In addition, the size of the interception reservoir is assumed proportional to the LAI with a factor of 0.2 for all land use types in the VIC model (Liang *et al.*, 1994). However, this factor is also highly variable across land use types according to measurements (Breuer *et al.*, 2003). The small differences in parameter values thus seem to explain the small differences in evapotranspiration between the land use types. Therefore, appropriate parameter values that are specific to the area of interest should be selected. In the remainder of this study, however, the default parameters are used, because we do not have sufficient observations available for all different land use types to properly determine the correct values for all parameters.

In Figure 3.3, it also appears that in VIC_{org}, all evaporation from urban areas is counted as transpiration instead of bare soil evaporation, even though there is no vegetation present. This is an artifact of our choice to assign a vegetation class to urban areas: because the urban land use tile is now classified as vegetated, all bare soil evaporation is classified as transpiration in VIC_{org} (hence the high transpiration values for urban land in Table 3.3). In the modified model, hereafter denoted as VIC_{mod}, however, urban area is a “vegetation” type with $LAI = 0.0$. Therefore F_b is 1 and all evapotranspiration consists of bare soil evaporation. LAI may, of course, be increased in urban areas to parameterize vegetation. In that case, bare soil evaporation, interception evaporation and transpiration occur simultaneously. In this study, however, we assume urban area to consist of bare soil only.

Furthermore, in Figure 3.3, the amount of baseflow according to the original VIC model is surprisingly high for urban areas. This can be explained by the fact that no transpiration is taking place, so no water is extracted from the lowest soil moisture reservoir, keeping baseflow at its maximum level. By imposing the saturated conductivity in layer two to be very low, only small amounts of moisture percolate to the lowest layer. The saturated conductivity of layer two was selected based on a sensitivity analysis: adjusting for example the conductivity of the first layer yielded no effect because its thickness is too small with respect to the other layers. The high baseflow is thus reduced, and surface runoff increased due to the higher soil moisture contents in the upper layers. Adjusting the value of the saturated conductivity of the second layer provides the opportunity to parameterize the effects of urban management measures mentioned above (i.e, delaying runoff) in a very crude manner. In the remainder of this paper, however, an extreme case is considered, where urban areas are considered to be completely impervious. Therefore, the saturated conductivity in layer two is set to a value of zero. For this study, therefore, our relatively crude approach suffices. When urban management measures need to be evaluated in detail, a more appropriate parameterization, such a recently proposed by Cuo *et al.* (2008), could be thought of. For urban areas, transpiration is now indicated as bare soil

evaporation. In addition, total outflow is slightly higher and total evapotranspiration lower, which is consistent with *Dow and DeWalle (2000)*, who found decreased annual evaporation and increased mean streamflow in urbanizing watersheds in Pennsylvania, and *DeWalle et al. (2000)* who found a mean increase in mean annual streamflow of about 15% in urbanizing watersheds, based on data from 39 watersheds throughout the United States. In our case the difference in streamflow between an urbanized and a rural pixel is much higher than 15% (about 25% for grassland). Because the urbanizing watersheds used by *DeWalle et al. (2000)* are not 100% urbanized and in a different climate, these values cannot be compared quantitatively. The proposed set of modifications seems to be an improvement of the model and is adopted for the remainder of this study. It is important to mention, however, that these modifications are intended to enable the land use change simulations described in this paper only; it is not our intention to present an improved version of the VIC model.

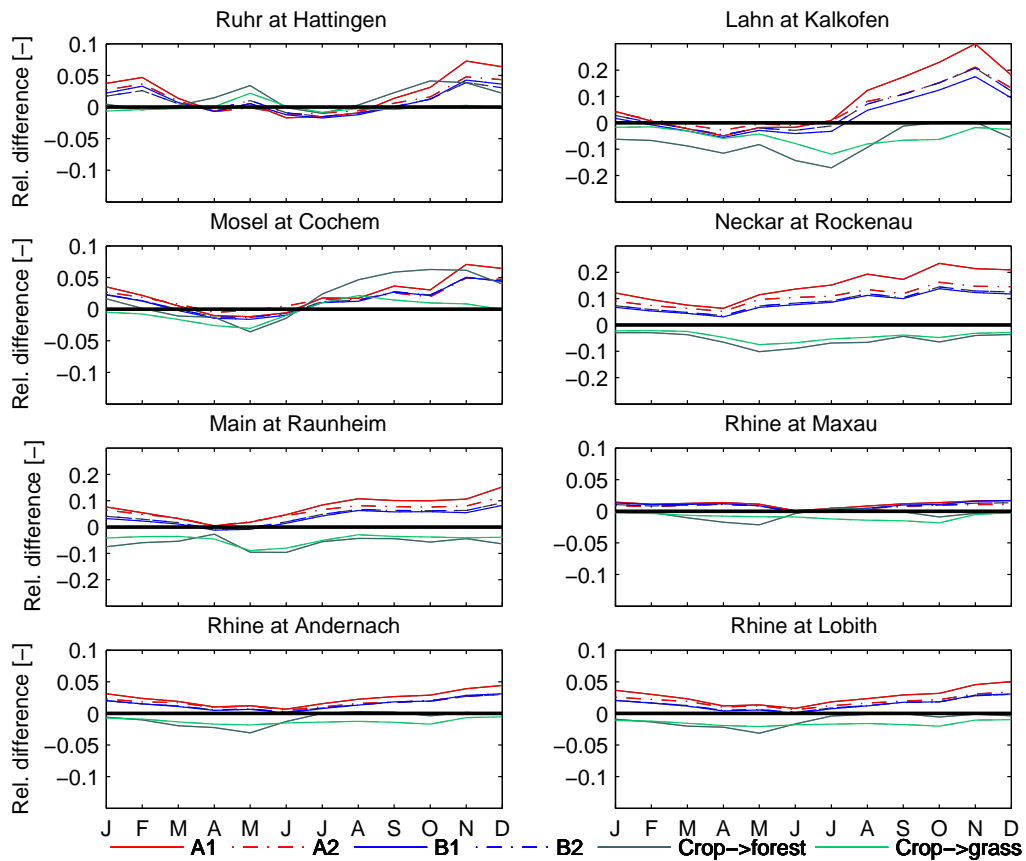


Figure 3.4: Climatology of relative streamflow differences, computed as (Scenario - Current)/Current, at eight locations (Figure 1.5) in the Rhine basin, and six land use scenarios (4 Eururalis scenarios, and crop replaced by resp. forest and grass) using VIC_{mod} . Note the different scale for the Lahn, Main and Neckar.

3.4 VIC model simulations for the entire basin

VIC_{mod} is used to simulate the entire Rhine basin, again for the period spanning 1994 through 2003, where data from 1993 is used for model initialization. Because running the model in water balance mode greatly reduces computation time, all simulations covering the entire basin (which are computationally quite demanding) are carried out in water balance mode. This is justified because differences between water balance and energy balance modes are relatively small and similar across land use types, as was pointed out in Section 3.3. As an additional check, a VIC model simulation over the entire basin in the energy balance mode pointed out that the effect over all sub-basins and the entire basin was similar, i.e. a small increase in streamflow of about 4%. A consequence of using the water balance mode (see Section 3.3) is that the difference between forest versus other land use types is slightly underestimated. This should be taken into account when interpreting the results. Figure 3.4 shows relative differences in streamflow between the various scenarios at eight locations in the Rhine basin (Figure 1.5). Relative differences are calculated as $(\text{Scenario} - \text{Current})/\text{Current}$, where Current is the VIC model output under the current land use conditions. For comparison purposes, Figure 3.5 shows the same, but here all simulations are based on VIC_{org} .

Comparing the two figures, it appears that the effects of different land use types are similar in either version of the code. The modifications have, however, reduced the differences in the hypothetical scenarios and enhanced the effects in the Eururalis scenarios. In case where the differences due to land use change are small, the relative change in streamflow can have a different sign in VIC_{org} and VIC_{mod} . Relative changes, however, remain small (within a few percent). In the small tributaries, the Lahn and the Ruhr, differences between VIC_{org} and VIC_{mod} are larger. In the Ruhr, all scenarios cause a small decrease in streamflow in VIC_{org} for most of the year, whereas in VIC_{mod} these scenarios cause a small increase. The Lahn appears to be very sensitive to land use changes, especially for the Eururalis scenarios. The Lahn is the only basin where the difference between VIC_{org} and VIC_{mod} is quite large: the maximum increase in streamflow (November) is 30% in VIC_{mod} whereas it is only 8% in VIC_{org} .

In general, conversion of cropland to grassland and forest tends to decrease streamflow (increased evapotranspiration), while in the Eururalis scenarios of land use change an increasing streamflow is observed. Although the conversion of arable land to pasture and forest is an important process in most of the scenarios, this effect is offset by the urbanization that occurs at the same time. Considered over the entire basin (locations Andernach and Lobith), relative differences are small (within 5%). However, on smaller scales they can be larger. For example, maximum streamflow increases in the Lahn basin with 30% for the Eururalis A1 scenario, and also in the Neckar changes are substantial. This, of course, largely depends on the current land use in these sub-basins. For example, the Neckar has a high urbanization rate according to the Eururalis scenarios (from 6.7% in the current situation to 15.3% in the A1 scenario), hence the increases in streamflow. The Lahn contains a lot of cropland in the current situation, which leads to large changes in the scenarios where cropland is replaced by

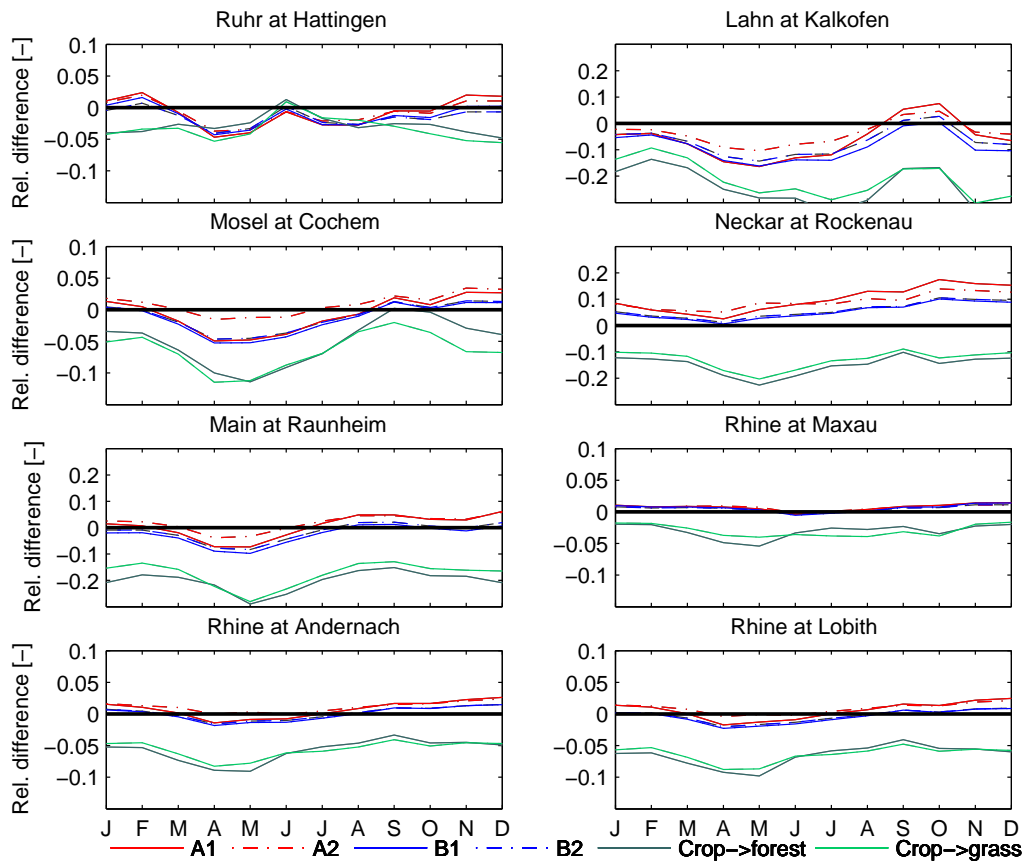


Figure 3.5: As Figure 3.4, but for simulations based on VIC_{org} .

forest or grass. Differences between the four Eururalis scenarios are relatively small for the area under consideration, as can also be seen in Figure 3.2. The largest increase in streamflow corresponds to the scenario with the highest urbanization rate and the strongest growing economy (A1). Especially in the Rhine upstream of Maxau, changes are extremely small. This is largely caused by the assumption that no land use changes take place in Switzerland: the percentage of streamflow at Maxau that originates in Switzerland amounts to about 75% in winter to 97% in early summer (Alpine snow melt). The fact that in the hypothetical scenarios (which do include Switzerland) changes are just as small supports the assumption that land use changes in this area will be relatively small compared to other parts of the basin. Because changes in most of the sub-basins are small or similar, and to have a contrast between a large and a small basin, we focus on one small sub-basin, which is most sensitive to land use changes. Subsequent analyses will thus be shown for the Lahn sub-basin and the entire Rhine basin.

To investigate extreme events, annual maxima of daily streamflow are plotted versus their recurrence times in Figure 3.6. To improve comparison, Generalized Extreme Value (GEV; Appendix 1) distribu-

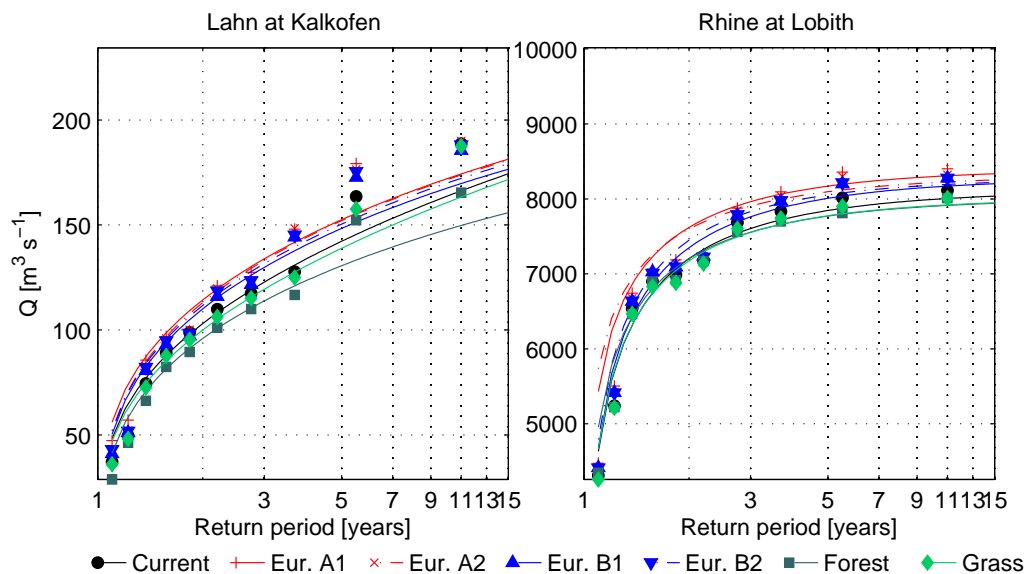


Figure 3.6: Annual maximum streamflow versus their recurrence time for the Lahn sub-basin and the entire Rhine basin. A Generalized Extreme Value (GEV) distribution is fitted through the data points. Six scenarios are plotted (4 Eururalis scenarios, and crop replaced by resp. forest and grass, as well as the current situation).

tions are fitted through the data points using maximum likelihood estimation. However, considering the short period, they are not extrapolated to higher recurrence times. A similar analysis for low flows is presented in Figure 3.7. Here, a low-flow event is defined as the cumulative deficit volume of streamflow below a threshold (i.e. the event stops at the moment the threshold is exceeded; *Fleig et al. (2006)*). The annual maximum values of the cumulative deficit volume are then plotted versus their recurrence times. As a threshold, the 30th percentile of streamflow is selected. This value is a trade-off between the amount of years without any event and the number of multi-year events, which both affect the analysis (*Fleig et al., 2006*). A suitable and widely used limit distribution for excesses over a threshold is the Generalized Pareto distribution (see *Fleig et al. (2006)*, and Appendix 1). Therefore, this distribution is fitted to the data points in Figure 3.7, again using maximum likelihood estimation. Similar to Figure 3.4, the difference between peak magnitudes across the scenarios is small over the entire basin (within a few percent). Over the entire range of return periods, the Eururalis scenarios slightly increase the magnitude of the peak flows (especially A1 and A2). Conversion to forest and grass slightly decreases this magnitude. Differences between extreme low flow periods are barely visible when the entire basin is considered. At the sub-basin scale, differences in peak magnitudes are slightly larger: all Eururalis scenarios increase peak flows, whereas afforestation leads to a small decrease. Conversion to grassland hardly makes a difference. For extreme low flows in the Eururalis scenarios a very small reduction in deficit volume (i.e., some alleviation of the low flow event) ap-

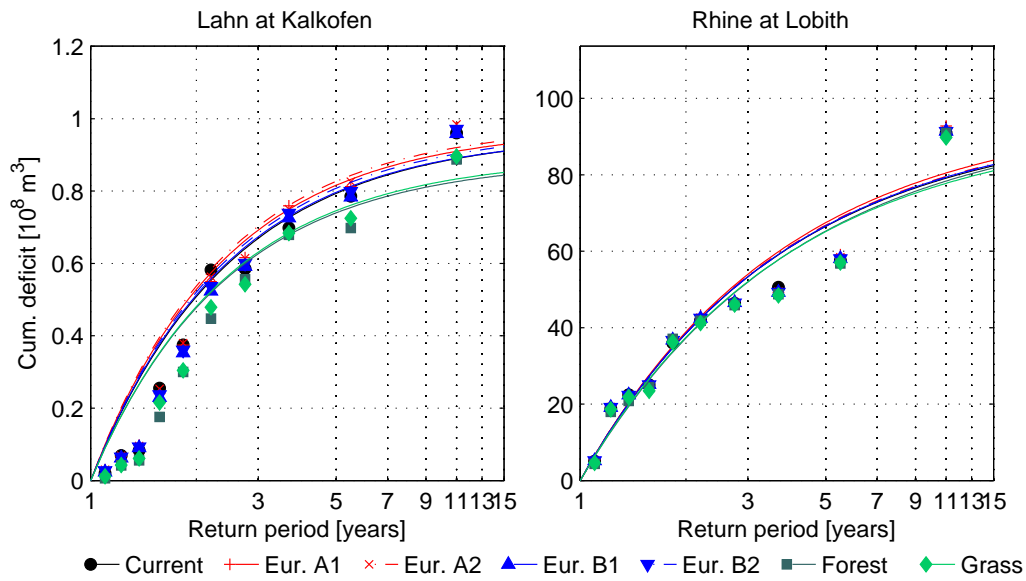


Figure 3.7: Annual maximum cumulative non-exceedances of the 30th percentile of streamflow versus their recurrence time for the Lahn sub-basin and the entire Rhine basin. A Generalized Pareto (GP) distribution is fitted through the data points. Six scenarios are plotted (4 Eururalis scenarios, and crop replaced by resp. forest and grass, as well as the current situation).

pears for the low return times. Towards longer return times, on the other hand, low flows are slightly enhanced. Conversion to cropland and grassland, on the other hand, reduces the deficit volume especially toward longer return periods. This can be explained by the fact that a large portion of the extra streamflow in the Eururalis scenarios is surface runoff, which is absent in dry periods. Forest, and to a smaller degree grass, sustain more baseflow in late summer, which is when most extreme low flows occur. The same analyses were also carried out for the original VIC model source-code, however, they are not shown here because they produced to a large extent the same results. Only for the conversion to grassland results differed in a similar way to the mean streamflow differences described above (Figure 3.5), i.e., grassland reduced extreme events even more than afforestation.

As can be seen from the data points in Figures 3.6 and 3.7, not all individual extremes behave the same. This is further illustrated in Tables 3.4 and 3.5, which shows differences between the scenarios for the five most extreme peak flows and low flows at Kalkofen and Lobith. Peak flows were selected from the daily streamflow record of the reference simulation, under the constraint that peaks should be two weeks apart to ensure independence, whereas low flows were selected based on the lowest monthly means, which are selected to be 5 months apart. From Tables 3.4 and 3.5, it appears that at a smaller scale (the Lahn basin), land use changes have varying effects on individual peak flows: there is a wide range of differences in magnitude of the changes, from none at all to about 12% and even

Table 3.4: Five most extreme flood peaks and low flows at Kalkofen (outlet of the Lahn basin), selected according to the reference situation, and the relative difference between six scenarios (Eururalis A1, A2, B1, B2, and cropland replaced by forest and grass) and the reference situation for each event. Positive values denote an increase with respect to the reference situation. For peak flows the magnitude of the peak is considered. Low flow periods were selected based on the minimum monthly discharge value. the mean discharge over a 5-month window centered around this minimum monthly mean discharge is then used to compare the land use scenarios. Simulations are based on the modified VIC model.

Lahn at Kalkofen: peak flows					
Date of max.	10-04-94	31-01-95	29-01-94	19-02-95	22-03-94
Magnitude [m^3s^{-1}]	188.70	163.59	162.25	150.22	148.16
A1 [%]	0.10	9.55	2.40	-2.98	0.08
A2 [%]	0.71	7.88	3.14	-1.81	1.46
B1 [%]	-1.69	5.57	2.20	-3.90	-0.73
B2 [%]	-0.25	7.25	2.18	-3.13	0.08
Forest [%]	-12.34	-6.94	-2.26	-7.82	-11.89
Grass [%]	-0.63	-3.64	-0.74	-2.82	-1.61
Lahn at Kalkofen: low flow periods					
Month of min.	11-95	10-97	11-96	10-01	09-03
Monthly min. [m^3s^{-1}]	2.20	3.27	3.38	3.40	3.96
5-month mean [m^3s^{-1}]	3.66	4.58	6.74	6.20	6.33
A1 [%]	20.49	30.68	24.80	23.49	15.71
A2 [%]	14.33	19.07	17.16	16.78	10.24
B1 [%]	7.08	15.22	11.89	14.56	4.97
B2 [%]	11.45	19.05	15.80	17.35	8.61
Forest [%]	-26.31	-6.68	-9.97	-1.04	-19.95
Grass [%]	-19.78	-9.87	-7.27	-2.57	-15.32

directions are not consistent. Low flows, on the other hand, are relieved by the Eururalis scenarios to some extent because of increasing streamflow. However, discharge in the Lahn nearly disappears during extreme low flows (e.g. about $3.5 \text{ m}^3\text{s}^{-1}$ in November 1995). Therefore, in an absolute sense differences are still very small. Conversion to forest or grassland mainly reduces streamflow due to enhanced evapotranspiration. When the entire basin is considered, the same effects can be seen as in the Lahn, although changes are much smaller, mainly within 5%.

Finally, spatial patterns of differences in surface runoff and soil moisture between all six scenarios are displayed in Figures 3.8 and 3.9. For the Eururalis scenarios, surface runoff mainly increases in the areas that show the highest urbanization (Figure 3.2), i.e., the Ruhr area close to Lobith, along

Table 3.5: As Table 3.4, but for Lobith, the outlet of the entire Rhine basin.

Rhine at Lobith: peak flows					
Date of max.	27-02-99	02-02-95	29-03-01	28-03-02	03-02-94
Magnitude [m^3s^{-1}]	8111	8015	7834	7685	7173
A1 [%]	3.56	4.27	3.34	2.49	1.18
A2 [%]	2.58	3.54	2.58	2.05	0.90
B1 [%]	2.04	2.30	1.72	1.27	0.85
B2 [%]	2.04	2.52	1.83	1.35	0.73
Forest [%]	-1.27	-2.55	-1.71	-1.61	-0.04
Grass [%]	-1.23	-1.43	-1.19	-1.09	-0.51
Rhine at Lobith: low flow periods					
Month of min.	10-95	09-01	01-97	02-98	03-96
Monthly min. [m^3s^{-1}]	1123	1130	1149	1190	1231
5-month mean [m^3s^{-1}]	1512	1617	1984	2150	1529
A1 [%]	2.77	3.56	4.91	3.64	3.14
A2 [%]	2.06	2.45	3.45	2.60	2.46
B1 [%]	1.72	2.00	3.02	1.90	1.80
B2 [%]	1.63	2.02	3.01	1.95	1.79
Forest [%]	-1.46	-0.03	-1.50	-1.50	-2.49
Grass [%]	-1.83	-0.99	-1.43	-2.12	-1.97

the main Rhine branch and in the Neckar sub-basin. In the scenarios where cropland was replaced by forest or grass, changes in surface runoff occur only locally at a few distinct spots, although in both scenarios land cover over an extensive area is changed. This, of course, is very much related to soil type and topography: surface runoff decreases in most of the basin, especially in the more sandy parts, whereas it increases in the mountainous southern part. When cropland is converted to grass, the same can be seen to a smaller extent. Because surface runoff is only caused by saturation in the VIC model, increases in surface runoff are correlated with increases in soil moisture. As can be seen in Figures 3.9 and 3.8, increases in both soil moisture and surface runoff are concentrated in the western part of the basin for the hypothetical scenarios. This area has a more loamy soil texture than many other areas covered with cropland, delaying the discharge of water through baseflow and increasing soil moisture contents. Apart from the western part, soil moisture contents mainly decrease in the remaining zones where cropland was converted to (semi-)natural land. Also in the Eururalis scenarios, the increases in surface runoff are associated with increases in soil moisture, which in turn correspond to urbanizing areas.

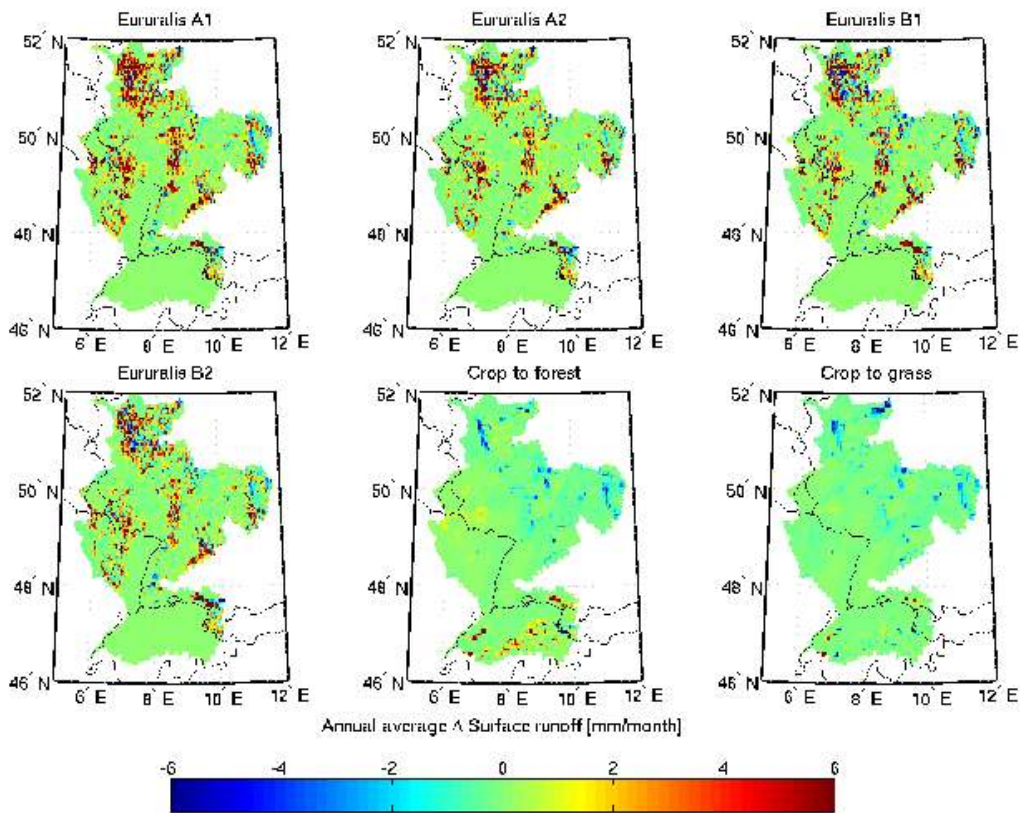


Figure 3.8: Spatial pattern of absolute differences in surface runoff between the six scenarios and the current situation. Positive values indicate an increase with respect to the current situation. Results for VIC_{mod} are shown.

3.5 Summary and conclusions

In this study, we have investigated the effects of land use changes on average streamflow, as well as extreme floods and low flows for various locations in the Rhine basin. Land use projections for the year 2030 were used, according to four IPCC emission-scenarios. In addition, to investigate the sensitivity of streamflow to land use change, some extreme, hypothetical scenarios were devised, where all cropland throughout the basin was replaced by either forest or grass. All land use change scenarios were simulated using the VIC model, which has the advantage that the evapotranspiration routine is physically based and does not require specific calibration parameters. All simulations were carried out using the same atmospheric forcing dataset, which spans the period of 1994 through 2003. Effects of climate change are not taken into account in this study. In later research, therefore, it would be interesting to investigate whether land use change effects are different under a different climate regime. Besides the simulations covering the entire Rhine basin, another set of simulations was carried out covering a single VIC pixel completely covered with six different land use types.

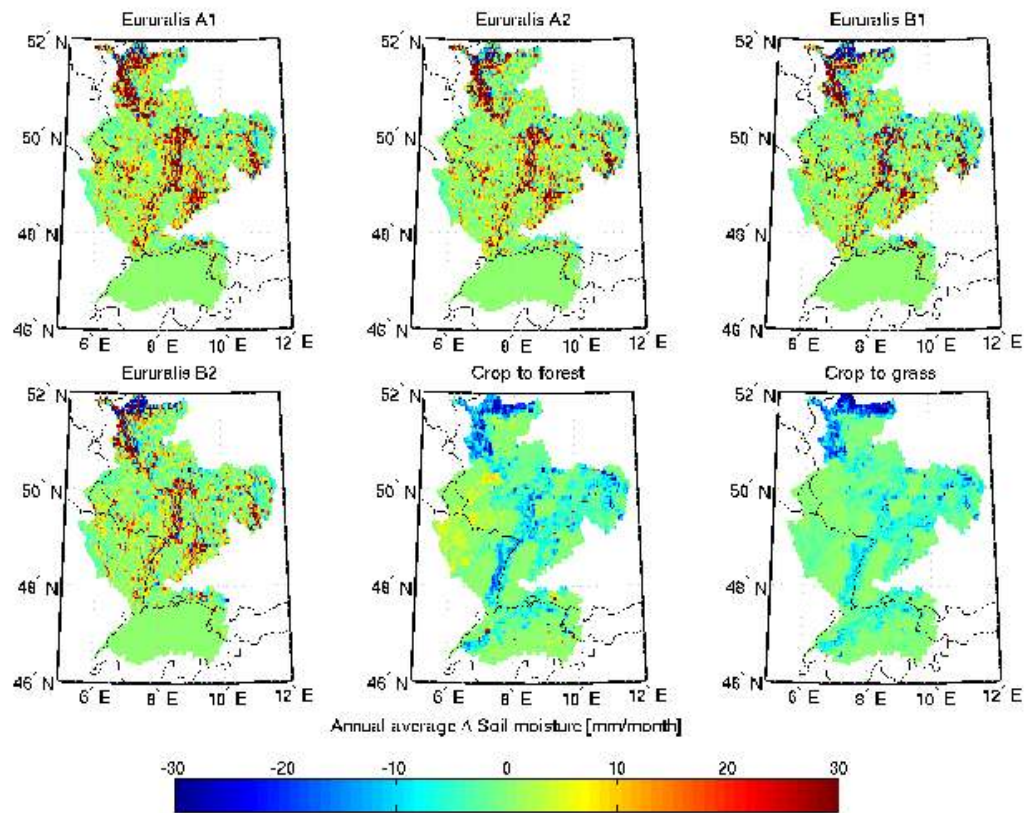


Figure 3.9: As Figure 3.8, but now differences in total soil moisture storage are plotted.

From the latter simulations, it appears that the current version of the VIC model is not completely suitable to simulate differences in land use types, mainly because of the fact that no bare soil evaporation is allowed when a land use tile is classified as vegetated. Especially in winter this leads to underestimations of evapotranspiration, which is confirmed by *Hurkmans et al. (2008)*, where a comparison between evapotranspiration from a VIC pixel and a lysimeter (their Figure 11) indeed shows severe underestimations by the VIC model in winter. By introducing a fractional bare soil evaporation in vegetated areas, the representation of bare soil evaporation and transpiration is more realistic and the annual cycle for grass is represented more accurately compared to the lysimeter data. The total amount of evapotranspiration is slightly higher but not unrealistic (see *Verstraeten et al. (e.g. 2005)* and the lysimeter data mentioned before).

From the simulations covering the entire Rhine basin, the effects of different land use change scenarios on mean streamflow are similar for both the original and modified VIC model, suggesting that they are fairly robust and independent on the model formulation of the VIC model. The effects are

small when considering streamflow at the basin outlet (within 5%, both in mean and extreme streamflow), because in the Eururalis scenarios the affected areas are relatively small and the contribution from Switzerland can be considerable, especially in spring season. In general, the future land use scenarios (Eururalis) indicate an increase in streamflow, mainly due to urbanization. Effects of urbanization are quite small, however, because they are partly compensated by a decrease of cropland and small increases in grassland, forest and natural area (e.g. shrubs). The more extreme, hypothetical scenarios, on the other hand, indicate a decrease of streamflow. Conversion of cropland to grass reduces streamflow nearly as much as conversion to forest. This, however, is partly caused by an overestimation of interception evaporation for grass in the model that was discussed in Section 3.3.

For management purposes, i.e., mitigating extreme floods and low flows, land use changes can have local effects and can affect streamflow from small tributaries significantly. As far as influencing the magnitude and timing of peaks arriving at Lobith are concerned, however, effects are small. In different areas, different types of land use changes would be necessary. For example, only the relatively small Lahn basin proved relatively sensitive to afforestation, because in the current situation the dominant land use type is cropland. Therefore, afforestation has a relatively large influence. For each area, specific land use changes, depending on the current dominant cover could be designed. In further research, therefore, alternative scenarios should be taken into account for each sub-basin separately, or for even smaller sub-basins. An effective combination of different land use changes in different parts of the basin could be able to significantly alter the magnitude of low flows and/or the timing of flood peaks at the basin outlet.

Acknowledgements

This research was supported by the European Commission through the FP6 Integrated Project NeWater and the BSIK ACER project of the Dutch Climate Changes Spatial Planning Programme. We thank Daniela Jacob and Eva Starke from the Max Planck Institut für Meteorologie, Hamburg, Germany for providing the atmospheric forcing data. Rita Lammersen and Hendrik Buiteveld from Rijkswaterstaat Waterdienst, The Netherlands are kindly acknowledged for providing streamflow observations and we thank the three anonymous reviewers for their constructive comments.

Chapter 4

Changes in streamflow dynamics in the Rhine basin during the 21st century under different climate scenarios



This chapter is a modified version of: R. T. W. L. Hurkmans, W. Terink, R. Uijlenhoet, P. J. J. F. Torfs, D. Jacob and P. A. Troch (2009), *“Changes in streamflow dynamics in the Rhine basin during the 21st century under different climate scenarios”*, submitted to J. Clim.

Abstract

Due to global warming, the hydrologic behavior of the Rhine basin is expected to shift from a combined snowmelt and rainfall driven regime to a more rainfall dominated regime. Previous impact assessments have indicated that this leads, on average, to increasing streamflow by ~30% in winter and spring, and decreasing streamflow by a similar value in summer. In this study, high-resolution (0.088°) regional climate scenarios for the Rhine basin are used to force a macro-scale hydrological model. These climate scenarios are based on model output from the ECHAM5-OM global climate model, which is in turn forced by three SRES emission scenarios: A2, A1B and B1. The Variable Infiltration Capacity model (VIC; version 4.0.5) is used to examine changes in streamflow at various locations throughout the Rhine basin. Average streamflow, peak flows, low flows and several water balance terms are evaluated for both the first and second half of the 21st century. The results reveal a distinct contrast between those periods. The first half is dominated by increased precipitation, causing increased streamflow throughout the year. During the second half of the century, a streamflow increase in winter/spring and a decrease in summer is found, similar to previous studies. This is caused by (1) temperature and evapotranspiration, which are considerably higher during the second half of the century, (2) decreased precipitation in summer and (3) an earlier start of the snowmelt season. Magnitudes of peak flows increase during both periods, that of streamflow droughts only during the second half of the century.

4.1 Introduction

According to the latest IPCC assessment report (IPCC, 2007), all currently available global climate models agree on an increase in global mean temperature of 1.1°C to 6.4°C over the 21st century. Associated with this global warming, the hydrological cycle is expected to intensify, causing precipitation to fall in more extreme events (Trenberth, 1997a). In addition, higher air temperatures will cause more precipitation to fall as rain instead of snow, and the snow melt season to start earlier in the year (Barnett et al., 2005). As far as the Rhine basin is concerned, this amounts to an increase in temperature of 1.0°C to 2.4°C by 2050, causing the hydrological regime of the Rhine to shift from a combined rainfall and snowmelt driven system to a more rainfall dominated system (Barnett et al., 2005; IPCC, 2007).

The Rhine basin is densely populated and heavily industrialized, and the river Rhine has the highest traffic density in Europe as an inland waterway. Its water is used for many purposes, e.g. agriculture, industry, domestic water supply and (hydro)power generation (Kwadijk and Rotmans, 1995; Middelkoop et al., 2001). Because of all the economic value that is concentrated in the basin, it is very vulnerable to hydrologic extremes, both floods and droughts (Kleinn et al., 2005). It is therefore not surprising that many climate change impact assessments have been carried out for the Rhine basin in recent years (e.g. Kwadijk and Middelkoop, 1994; Kwadijk and Rotmans, 1995; Middelkoop et al., 2001; Shabalova et al., 2003; Pfister et al., 2004; Zierl and Bugmann, 2005; Lenderink et al., 2007). Most of these studies are based on climate model output, which are based on scenarios describing greenhouse gas emissions. Emission scenarios range from a simple doubling of CO₂ concentrations (e.g. Middelkoop et al., 2001) or a gradual increase of CO₂ (for example 1% per year in Shabalova et al. (2003)) to the more complex scenarios developed by IPCC in the Special Report on Emission Scenarios (SRES; IPCC, 2000). SRES-scenarios are based on several alternative developments of energy technology and contain not only CO₂, but also other greenhouse gases and aerosols. Because the spatial resolution of global climate models (GCM) is generally too low for hydrological applications (> 100 km), downscaling occurs either by statistical methods (as was done for example by Kwadijk and Middelkoop (1994); Kwadijk and Rotmans (1995)), or by nesting a regional climate model (RCM) in the GCM over the domain of interest (e.g. Shabalova et al., 2003; Middelkoop et al., 2001; Kleinn et al., 2005). The downscaled climate data are then fed to some hydrological model to obtain river discharges. All the assessments mentioned above qualitatively agree in their results. More discharge is projected in winter and spring because of increased precipitation and snow melt (+30% according to Lenderink et al. (2007) and Shabalova et al. (2003)), and less discharge in summer because of increased evapotranspiration, less snow buffering and decreased precipitation (−30% to −40% according to the same studies).

In the studies described above, most of the employed regional climate scenarios have spatial resolutions of 25 to 50 km. By means of a second downscaling step higher spatial resolutions can be obtained. From the Max Planck Institut für Meteorologie (MPI-M) in Hamburg, Germany, climate scenarios are available for the Rhine basin at a spatial resolution of 0.088° (~ 10 km). These scenarios are based on the GCM ECHAM5-OM and downscaled in two steps by the regional climate model

REMO (Jacob, 2001). To capture extreme precipitation events, and thus also extreme peak flow events, a high spatial resolution is important because extreme precipitation is usually convective in nature and its spatial extent relatively small. Moreover, as part of the catchment is very mountainous, orography is relatively complex and a high model resolution allows more of this complexity to be resolved explicitly. An additional advantage of the climate scenarios used in this study is the fact that they are transient, spanning the entire 21st century. The studies that were mentioned above typically used a timeslice of 30 years, often the period 2071–2100.

In this study, we employ three high-resolution climate change scenarios, according to three SRES scenarios: B1, A1B and A2. We compare the scenarios with results of a reference model run spanning the period 1950–2000. All atmospheric time series are corrected for their model bias based on observations of precipitation and temperature (Section 4.3.1). As a macro-scale hydrological model, we use the Variable Infiltration Capacity (VIC; Liang *et al.*, 1994). This model was applied to the Rhine basin at a spatial resolution of 0.05° (~ 5.5 km), as described by Hurkmans *et al.* (2008). Compared to other models that are typically used for climate change impact studies and which are generally more simple, VIC has the advantages that (1) its parameterization of evapotranspiration is physically based, (2) it has a detailed description of snow accumulation and melt processes and (3) sub-grid variability of land use, elevation and infiltration is taken into account. For these reasons, VIC was found to be less sensitive to parameter settings than the more simple water balance models mentioned above (Hurkmans *et al.*, 2008). This is an important advantage because it is questionable whether conceptual model parameters determined under current climate conditions will be valid throughout the 21st century under a changing climate. From the model results, we investigate the effect of climate change on average and extreme streamflow, both in terms of peak flows and streamflow droughts. By analyzing streamflow at several locations throughout the river basin and the distributed model results, the spatial pattern of the effects of climate changes is investigated. Finally, changes in various components of the water balance, such as evapotranspiration, snow melt and baseflow, are analyzed.

4.2 Data and model

4.2.1 Study area

The Rhine basin is a major river in western Europe. It originates in the Swiss Alps and drains portions of Switzerland, Germany, France and The Netherlands before draining in the North Sea. The total area covered is about 185,000 km². After crossing the German-Dutch border at Lobith, the river splits into three branches. Therefore, we only take into account the area upstream of Lobith (Figure 1.5). As was mentioned before, the discharge of the Rhine is a combination of rainfall and snowmelt. Snow is concentrated in the Alpine part of the area, where elevations range up to about 4000 m.a.s.l. For more information about the Rhine basin, see Section 1.2.

4.2.2 Hydrological model

The Variable Infiltration Capacity model (VIC; *Liang et al.*, 1994) is a distributed, macro-scale hydrological model. It is developed to provide land surface boundary conditions for climate models, and therefore solves evapotranspiration and the associated turbulent fluxes in a physically based way. The coupled water- and energy balances are solved, in combination with the Penman-Monteith equation (*Penman*, 1948; *Monteith*, 1965), to calculate evapotranspiration. Sub-grid variability in land use and elevation is accounted for by dividing each grid cell in tiles based on fractional areal coverage. Sub-grid variability of topography is accounted for by means of an exponential relation between the fraction of the grid cell that is saturated and the infiltration capacity. The soil column is divided in three soil layers. Drainage from the surface to the lowest layer is gravity-driven and downwards only. Baseflow depends on the soil moisture content of the lowest soil layer through a function that consists of a linear and a non-linear segment. Routing of baseflow and surface runoff occurs through a simple algorithm developed by *Lohmann et al.* (1996), which was applied in combination with VIC before (e.g. *Lohmann et al.*, 1998a,b). The VIC model is described more extensively in Section 1.3. The VIC model has been used in previous studies as a land surface parameterization in climate models (e.g. *Lohmann et al.*, 1998c; *Pitman et al.*, 1999; *Liang et al.*, 1998), but also for hydrological purposes. For example, *Hamlet et al.* (2007) used the model for climate variability impact assessments and *Matheussen et al.* (2000) and *Hurkmans et al.* (2009a) investigated land use changes using VIC. Also *Nijssen et al.* (1997) and *Nijssen et al.* (2001) successfully applied VIC for streamflow simulation in large river basins.

The VIC model was applied to the Rhine basin in a previous study (*Hurkmans et al.*, 2008), at a spatial resolution of 0.05° and a temporal resolution of 3 hours. Two modifications of the VIC model that were introduced in a recent study dealing with land use changes (*Hurkmans et al.*, 2009a), are used in this study as well. First, in sparsely vegetated areas bare soil evaporation is allowed to occur simultaneous to transpiration and canopy evaporation. Second, a parameter is introduced in urban areas to increase the amount of surface runoff relative to baseflow. For more details about these modifications, we refer to *Hurkmans et al.* (2009a). Atmospheric forcing for the model is described in Section 4.2.3. Land use data were obtained from the PELCOM project (*Mücher et al.*, 2000) at a spatial resolution of 1 km, and soil data are taken from the global FAO dataset described by *Reynolds et al.* (2000). Based on percentages of sand and clay from this dataset soil textures are classified and the default parameters from the VIC website¹ are assigned to each class.

4.2.3 Atmospheric data

All atmospheric datasets that are used in this study are model output from the Regional climate model REMO (*Jacob*, 2001) as provided by the Max Planck Institut für Meteorologie (MPI-M) in Hamburg, Germany. A validation dataset, a reference dataset and three scenarios datasets were available. The main characteristics of all datasets are shown in Table 4.1, and the way they are used in this study is

¹<http://www.hydro.washington.edu/Lettenmaier/Models/VIC/VIChome.html>

Table 4.1: Overview of atmospheric datasets used in this study.

Dataset	Driving model	Spatial res.	Time res.	Period
Validation	ECMWF	0.088	hourly	1979–2003
Reference	ECHAM5-OM	0.088	hourly	1950–2000
Scenarios	ECHAM5-OM	0.088	hourly	2001–2100
Observations	-	sub-basin	daily	1961–1995

shown schematically in Figure 4.1. The validation dataset is an extended version of the atmospheric dataset that was used in *Hurkmans et al. (2008)* and *Hurkmans et al. (2009a)*. It is based on the global ERA15 re-analysis dataset (ECMWF Re-Analysis², 1979–1993), extended up to 2003 using operational ECMWF analysis data. Because the ERA data are (partly) based on observations, this data can be used to calibrate the hydrological model, as was done in *Hurkmans et al. (2008)*. The reference dataset is based on a REMO model run driven by the general circulation model ECHAM5-OM, as are the three scenario datasets. Because the reference dataset is not constraint by observations, it only resembles the current climate in a statistical sense. It can, therefore, not be used for hydrological model calibration. Because it is based on the same models as the scenarios, it can be compared with the scenarios to obtain a climate change signal. This is not the case for the validation dataset because it is based on a different driving model (i.e. ERA-data).

The spatial resolutions of both ERA and ECHAM5-OM data is too low for hydrological applications (> 100 km). They are, therefore, dynamically downscaled using the REMO model in two steps. First, intermediate REMO output with a resolution of 0.44° (about 50 km) is obtained, which is downscaled using a second step to 0.088° (about 10 km; *Jacob et al., 2008*) and personal communication with S. Kotlarski, (MPI-M).

Both driving “models”, ERA-data and ECHAM5-OM, have structural modeling errors compared with observations. Prior to using the data, this model bias needs to be corrected for using observations. Interpolated observations were available over the Rhine basin (*Sprokkereef, 2001a*) for this purpose. Because the spatial and temporal resolutions of these observations are too low, they cannot be used to force the VIC model. Therefore, we use the validation and reference datasets described above to represent the current climate conditions. The bias corrections are described in detail in Section 4.3.1. For both driving models a separate bias correction is needed. Because the three scenario datasets are based on the same modeling chain as the reference dataset, we assume that the model bias is similar for both the reference dataset and the scenarios and apply the same correction to both.

The three scenarios are based on three different CO₂ emission scenarios as defined by the IPCC in the Special Report on Emission Scenarios (SRES; *IPCC, 2000*): the A2, A1B and B1 scenarios. Each of those scenarios is based on a storyline of energy and technology development. The A2 scenario refers

²<http://www.ecmwf.int>

to a world with continuously growing population and very regionally oriented economic growth. A1B refers to a globalized, very rapidly growing economy with fast introduction of new technologies that are balanced between fossil fuel-intensive and sustainable and clean. Population in A1B grows rapidly until the middle of the century and declines thereafter. B1, finally, refers to a globalized, rapidly growing population, but with changes in economic structure with an environmental emphasis, and fast introduction of clean and efficient technologies. For more details about these storylines, see Section 1.1.3 and IPCC (2000).

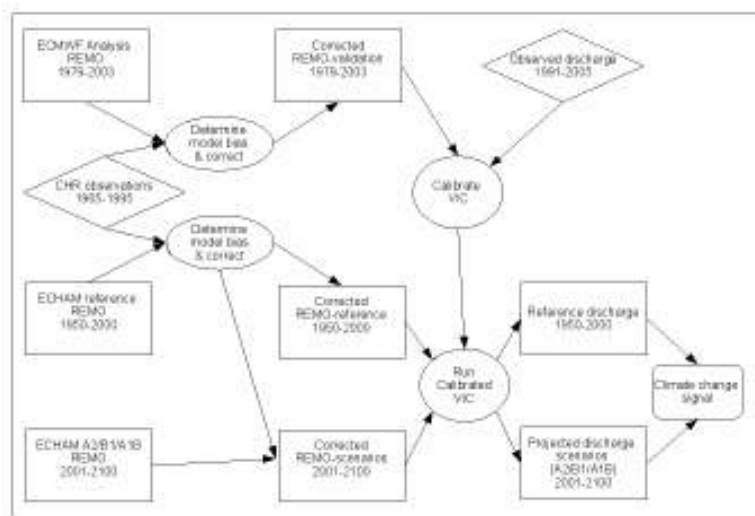


Figure 4.1: Schematic representation of all datasets used in this study and how they are used.

4.3 Methodology

4.3.1 Bias correction

A problem with the use of RCM output is the fact that simulated precipitation and temperature differ systematically from observed values (*Christensen et al.*, 2008). These biases can vary among RCMs and are also geographically dependent (*Jacob et al.*, 2007), and to obtain realistic streamflow simulations in the present climate, they should be corrected (*Lenderink et al.*, 2007). Different methods exist to correct for these biases. For example, *Lenderink et al.* (2007) used a spatially and seasonally varying correction factor, and *Hay et al.* (2002) used the Gamma distribution to match observed and simulated precipitation values. In this study, we use a relatively simple method that was applied to the Meuse basin by *Leander and Buishand* (2007). In addition, *Shabalova et al.* (2003) applied it to the Rhine basin to

obtain a plausible climate scenario. An advantage of this method is that not only the mean, but also the temporal variability is corrected. The method corrects precipitation and temperature separately, and leaves other input variables for VIC (i.e., radiation, humidity, wind speed and air pressure) unaffected. Because no observations are available for these variables at this scale and resolution, it is not possible to correct for them. Moreover, the effect on the resulting streamflow of errors occurring in these variables are relatively small compared to biases in precipitation and temperature. Observed precipitation and temperature for the period 1961–1995 are available on a daily basis for each of 134 sub-catchments in the Rhine basin (*Sprokkereef, 2001a*). Therefore, and because the model bias was found to vary spatially (in accordance with *Leander and Buishand (2007)* and *Lenderink et al. (2007)*), the bias correction is applied to daily average temperature and daily accumulated precipitation, for each sub-basin individually.

Because the reference dataset and validation datasets (Table 4.1) are based on different models, a bias correction is applied to both datasets separately. For both corrections, the maximum period of overlap between data and observations is used to estimate the correction parameters. For the validation dataset, this period is 1979–1995, whereas for the reference dataset it is 1961–1995. For both precipitation and temperature, a 5-day climatology is derived from observations and model output by calculating the average and standard deviation over all available years, i.e., 17 years for the validation and 35 years for the reference dataset. A window of 30 days before and 30 days after the considered 5-day period is used to calculate the “smoothed” average and standard deviation. The average and standard deviation are thus calculated over 65×17 (validation dataset), or 65×35 (reference dataset) data points. The correction is applied separately for each of the 73 5-day periods in the resulting climatology.

Precipitation is corrected according to a non-linear function (*Leander and Buishand, 2007*):

$$P^* = aP^b, \quad (4.1)$$

where P is the uncorrected precipitation, P^* the corrected precipitation and a and b are two parameters. First, b is fitted for the coefficient of variation (CV) of the modeled precipitation to match the CV of the observed precipitation. Second, a is fitted such that the average modeled precipitation fits the average of the observed precipitation (using the value of b obtained in the first step).

The correction of temperature is done in a linear way, based on the mean and standard deviation. For each sub-basin, the corrected daily temperature T_{mod}^* is calculated as:

$$T_{mod}^* = \bar{T}_{obs} + \frac{\sigma(T_{obs})}{\sigma(T_{basin})} (T_{mod} - \bar{T}_{obs}) + (\bar{T}_{obs} - \bar{T}_{basin}), \quad (4.2)$$

where T_{mod} is the uncorrected daily modeled temperature, T_{obs} is the observed daily average temperature for a sub-basin, and T_{basin} is the modeled sub-basin average temperature. In Equation 4.2 an

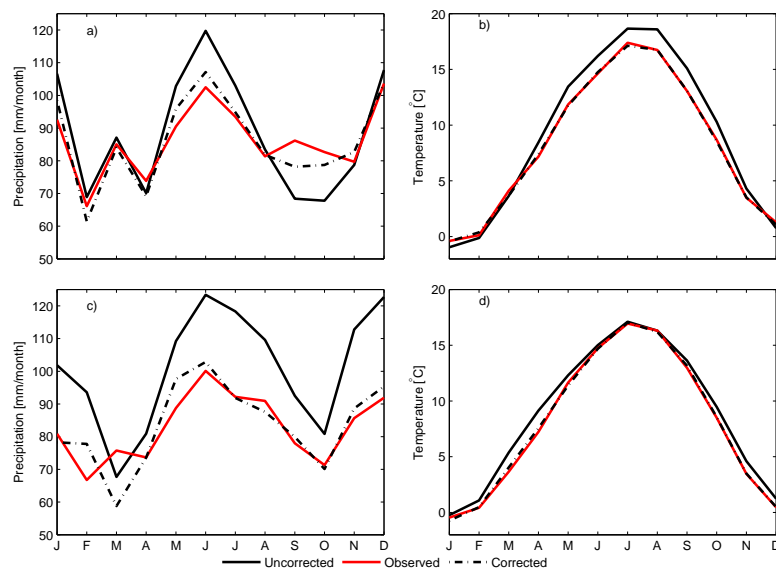


Figure 4.2: Results of the bias corrections for the validation (a and b) and reference (c and d) datasets. Monthly averaged precipitation (a and c) and temperature (weighted by sub-basin area; b and d) are shown for observed, uncorrected and corrected precipitation and temperature.

overbar denotes the average over the considered period (1979–1995 for the validation dataset; 1961–1995 for the reference dataset) and σ the standard deviation.

Results of the bias correction of the validation dataset, as well as the reference dataset, can be found in Figures 4.2 and 4.3. Figure 4.2 shows climatologies of corrected and uncorrected precipitation and temperatures for both the validation and the reference dataset. It appears that the correction works very well in terms of monthly averages. Especially for temperature, corrected values almost exactly match the observed ones. The mean absolute error (MAE) decreased from 1.15 to 0.15°C for the validation dataset and from 0.76 to 0.16°C for the reference dataset. For precipitation, the results are not as good as for temperature, but still the monthly means were improved significantly: for the validation dataset the MAE decreased from 8.5 to 3.6 mm month⁻¹ for the reference dataset from 19.5 to 4.6 mm month⁻¹. Figure 4.3 shows spatial patterns of the difference between modeled (corrected and uncorrected) and observed precipitation and temperature. Differences between uncorrected and observed precipitation are sometimes very large, especially in the Alps differences of more than 500 mm year⁻¹ exist. For all sub-basins, however, the correction performs well: the spatial MAE (weighted to area, for temporal averages) drops from 161 to 9 mm year⁻¹ for the validation dataset and from 276 to 12 mm year⁻¹ for the reference dataset. For temperature, the weighted MAE is also reduced significantly: for the validation dataset from 0.91 to 0.06°C and for the reference dataset from 0.85 to 0.06°C. Additional validation analyses (Terink *et al.*, 2008) showed that apart from these numbers, also

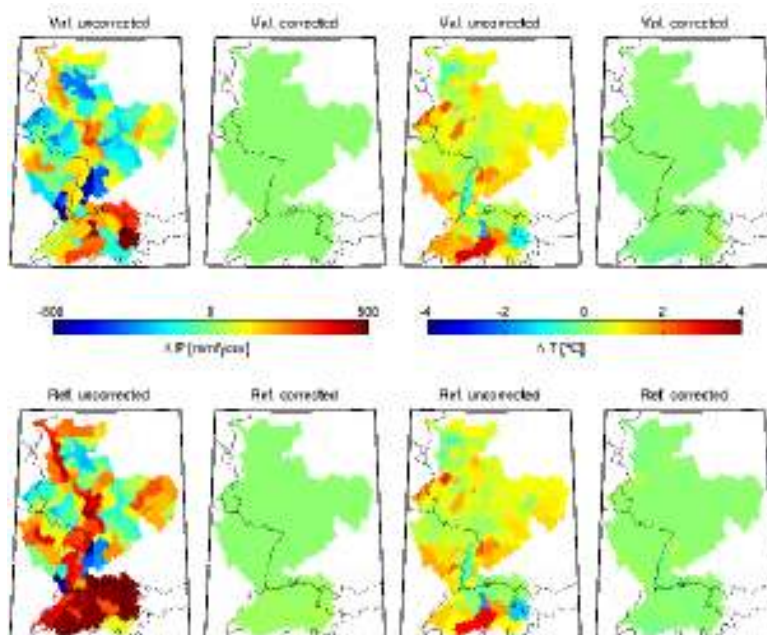


Figure 4.3: Results of the bias corrections in terms of spatial patterns. Each map shows the difference between corrected or uncorrected data versus observations. Differences in mean annual temperature and mean cumulative precipitation are shown, for both the validation (upper four panels) and reference datasets (lower four panels). Positive values indicate an overestimation with respect to the observations.

other statistics, such as the extreme values (low exceedence probabilities), the lag-1 autocorrelation and the number of wet days in the corrected datasets improved with respect to the uncorrected ones.

4.3.2 Model calibration

The bias-corrected validation dataset is used to calibrate VIC. Because the calibration process is computationally quite demanding, we calibrated the model on a relatively short period: 1994–1997. For each simulation, 1993 is used to initialize the model. The remainder of the validation dataset (1998–2003) is used to validate the model. The model was calibrated in a similar way as described in *Hurkmans et al. (2008)*, using 5 calibration parameters (for details, see *Hurkmans et al. (2008)*) and a numerically efficient algorithm to optimize them simultaneously, the Downhill-Simplex algorithm (*Nelder and Mead, 1965*). The Nash-Sutcliffe model efficiency (*Nash and Sutcliffe, 1970*) was used as objective function. A difference with the application described in *Hurkmans et al. (2008)* is the fact that in this study, the model was calibrated for each of seven zones separately, including five of the largest tributaries. These zones are shown in Figure 1.5. Calibration and validation results for the entire basin and

Table 4.2: Characteristics of observed streamflow and calibration and validation results for five of the main tributaries of the Rhine (Ruhr, Lahn, Main, Mosel and Neckar), and three locations along the main branch of the Rhine: Maxau, Andernach and Lobith. Mean, maximum, and mean annual maximum (Q_{mam}) streamflow are all calculated for the period 1990-2005 (the extent of the database that is available). For the calibration period (1994–1997) and the validation period (1998–2003), the correlation coefficient (ρ , Nash-Sutcliffe modeling efficiency (E), and the relative volume error (RVE) are shown.

Sub-catchment	Station	Observed			Calibration			Validation		
		Q_{mean} [m ³ s ⁻¹]	Q_{max} [m ³ s ⁻¹]	Q_{mam} [m ³ s ⁻¹]	ρ [-]	E [-]	RVE [%]	ρ [-]	E [-]	RVE [%]
Ruhr	Hattingen	72.6	867.0	579.4	0.58	0.22	34.57	0.61	0.30	27.58
Lahn	Kalkofen	46.0	587.4	373.0	0.80	0.59	-13.37	0.61	0.27	-7.31
Main	Raunheim	175.2	1990.8	1053.3	0.81	0.65	-7.25	0.69	0.42	-7.95
Mosel	Cochem	338.6	4008.9	2492.3	0.71	0.49	1.21	0.69	0.37	12.02
Neckar	Rockenau	142.6	2105.4	1326.0	0.54	0.07	23.14	0.61	-0.15	35.84
Rhine	Maxau	1278.3	4427.8	3269.5	0.59	0.10	11.20	0.50	-0.81	26.82
Rhine	Andernach	2076.0	10460.0	7274.3	0.75	0.55	5.03	0.62	0.17	15.72
Rhine	Lobith	2239.9	11774.6	7655.3	0.81	0.59	11.69	0.70	0.22	19.77

the main tributaries are shown in Table 4.2.

From Table 4.2, it appears that especially for mountainous areas such as the Rhine upstream of Maxau and the Neckar, performance indicators are relatively low. This can have several reasons: first, the model was forced by REMO model output, as was discussed previously. Differences between observations and this modeled data are at times quite large, as was also pointed out by *Hurkmans et al.* (2008), who compared the datasets extensively. Even though the structural error or bias was largely removed by the bias correction (see Section 4.3.1), the variation over time was not changed and significant differences between observed and modeled precipitation time series persisted. Second, the complex topography in the mountainous areas complicates hydrological modeling due to the high amount of small-scale heterogeneity. Third, there are some large surface reservoirs present in the Alpine part, such as the Bodensee, which are not included in the model but can damp peaks in the hydrograph considerably.

4.4 Results

The calibrated VIC model is now used to simulate streamflow for the reference period and the three climate scenarios described in Section 4.2.3 using the bias-corrected atmospheric data. Figure 4.4

shows annual time series of the annual mean, minimum and maximum streamflow at the basin outlet, Lobith. For the reference period and the A2-scenario also the 10th and 90th percentiles are shown. Thus, Figure 4.4 shows in a qualitative manner the trends in average, minimum and maximum streamflow during the 21st century for all scenarios and the reference period. A striking feature is the fact that there seems to be a decreasing trend both in minimum and maximum streamflow, particularly during the period 2052–2100. However, annual maxima are higher than they are during the reference period throughout the 21st century. From the simulated records, the years 1951 and 2001 are used to initialize the model for the reference period and the scenarios respectively. To be able to compare three periods of equal length, also 2051 is discarded, yielding three periods spanning 49 years each. In Sections 4.4.2 and 4.4.4 we investigate the differences between the periods 2002–2050 and 2052–2100 on one hand, and 1952–2000 on the other hand, in more detail.

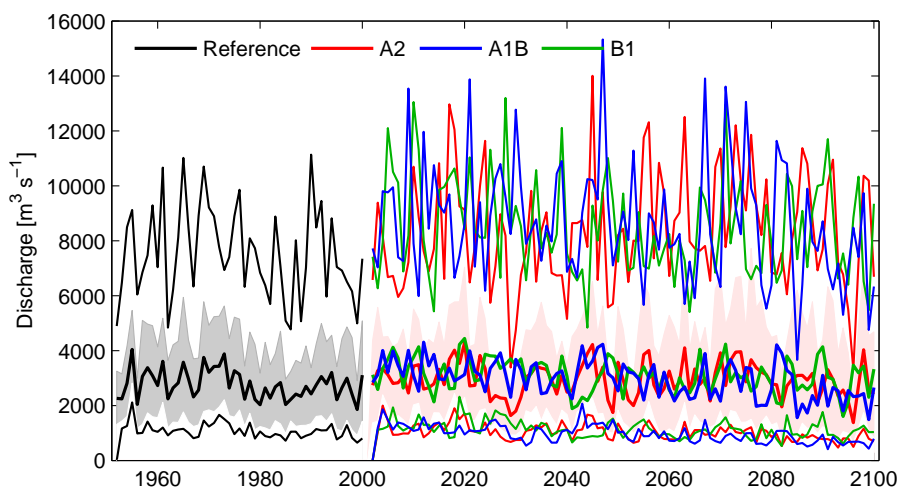


Figure 4.4: Time series of annual mean (middle solid lines), maximum (upper lines) and minimum (lowest lines) daily streamflow at Lobith for all datasets. For the A2-scenario and the reference situation, the shaded area represents area between the 10th and 90th percentiles.

4.4.1 Spatial patterns of atmospheric variables

To help interpreting the changes in streamflow that are discussed later in this paper, spatial patterns of the differences in precipitation, evapotranspiration and air temperature are plotted in Figures 4.5, 4.6 and 4.7 respectively. Temperature and precipitation are used to force the VIC model and are bias-corrected (Section 4.3.1), evapotranspiration is simulated by the model. Only differences between the period 2052–2100 and the reference period are shown, both for the winter (DJF) and summer season (JJA). Figure 4.5 shows precipitation increases in winter and decreases in summer for all scenarios. The largest increases in precipitation during the winter season are found in the northern and western

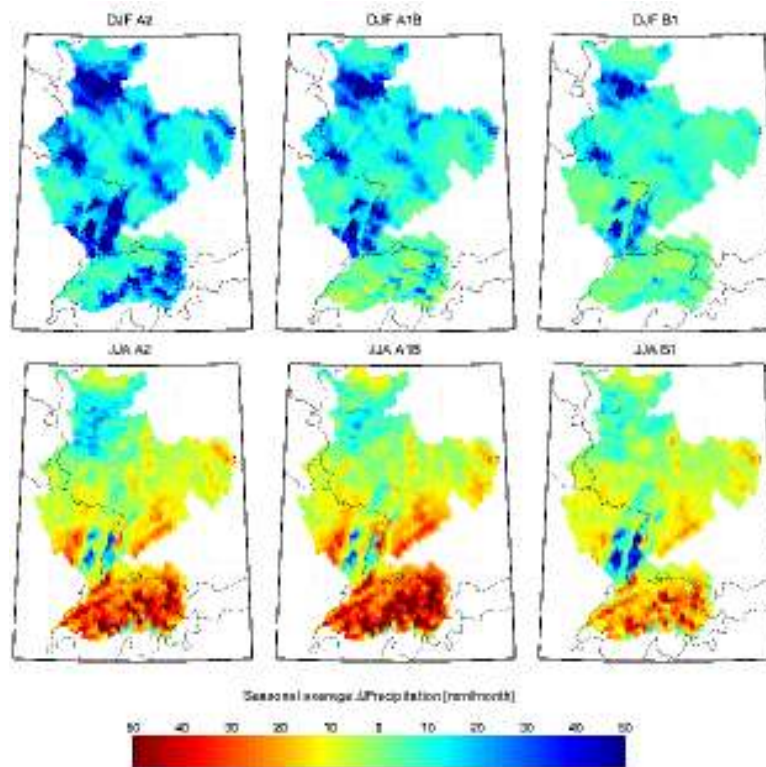


Figure 4.5: Difference in annual mean precipitation between three climate scenarios for the period 2052-2100 and the reference situation (1952–2000). The upper three panels show differences in the winter season (DJF), the lower three panels for the summer season (JJA).

part, as well as the mountainous area of the Black forest and the Vogues mountains, located along the southern part of the Rhine valley. The A2 scenario also shows increases in precipitation in the Alpine part and in some areas in the eastern Rhine basin, whereas the B1 scenario does not. The A1B scenario shows intermediate increases in those areas. In summer, the decrease in precipitation mainly occurs in the Alpine part of the basin, the Neckar sub-basin and the southern part of the Mosel. The northern part, the Black forest and the Vogues area still show small increases in precipitation. It should be noted that the spatial pattern of the applied precipitation is influenced by our bias correction. Because the correction was applied for each of 134 sub-basins separately, the overall spatial pattern is “drawn” towards that of the observations to some extent (see Figure 4.3). In addition, because the same exponent in Eq. 4.1 is applied to the reference dataset and the scenarios, differences between those can be amplified or reduced locally.

Changes in actual evapotranspiration (Figure 4.6) are quite homogeneous in space during the winter season: the entire basin, except the upper Alpine part experiences increases in evapotranspiration of

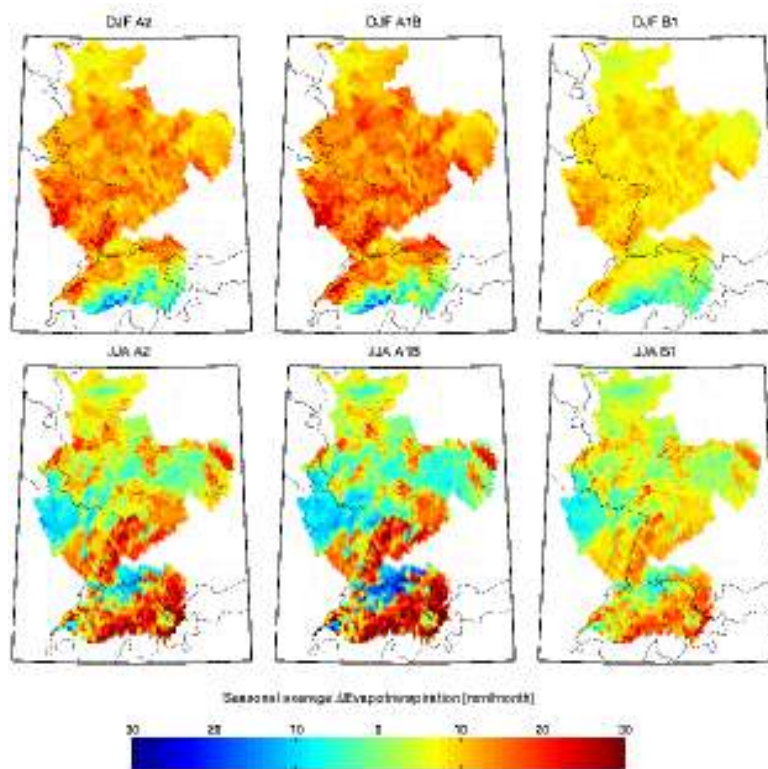


Figure 4.6: As Figure 4.5, but for actual evapotranspiration.

8 to 20 mm month⁻¹. In summer, however, there are large regional differences. Large parts of the western part (the Mosel area), as well as the eastern part (the Main) and a small area in northern Switzerland show small decreases in evapotranspiration. Ideally, to confirm that these decreases are caused by water limitation, one would want to see a similar plot of the potential evapotranspiration. This, however, does not belong to the standard VIC model output. Because of the parameterizations for sub-grid variability in the model (Section 4.2.2) it is not trivial to extract this information, therefore we used air temperature as a proxy for potential evapotranspiration (Figure 4.7). Radiation would be another option to use as a proxy but we do not expect the spatial pattern of incoming radiation to be very different from that of air temperature. The spatial pattern for temperature also looks quite homogeneous for both seasons, albeit that the warming is somewhat higher in the southern part, the valley of the upper Rhine and the higher areas on either side. Assuming that potential evapotranspiration follows a similar spatial pattern as temperature, this suggests that the decreasing evapotranspiration values in summer could indeed be caused by water limitation.

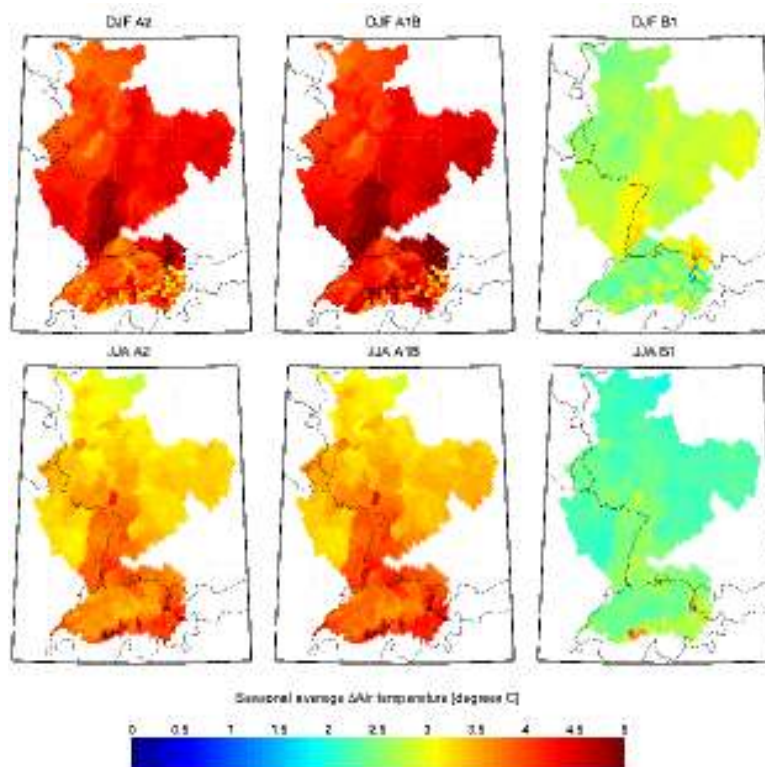


Figure 4.7: As Figure 4.5, but for air temperature.

4.4.2 Mean streamflow

Figure 4.8 shows the climatologies of relative differences in streamflow between each of the two future periods and the reference period, at four locations in the Rhine basin, representing a small (Ruhr) and a large (Main) tributary, the Alpine part (Maxau) and the entire basin (Lobith). The lower panel of Figure 4.8 shows the absolute streamflow climatology for Maxau, which is dominated by snowmelt. From this plot, it appears that during the period 2002-2050 the maximum monthly discharge at Maxau, which occurs in June, does not change or slightly increases (for the A1B scenario). The start of the melting season is slightly shifted to occur earlier in the year. During the second half of the 21st century, however, the melting season starts about 6 weeks to 8 weeks earlier and maximum discharge is significantly lower than during the reference period. In late summer (July to September), therefore, discharge is reduced considerably. The largest difference with the reference period is reached in August and amounts to about 40% less discharge at Maxau. The A1B scenario shows the most severe decrease in discharge. The earlier snow melt in combination with increased precipitation in winter and spring (Figures 4.9 and 4.10) causes increased discharge in these seasons. The increase in winter and spring nearly offsets the decrease in summer: annual streamflow slightly (<10%) increases for the A2 and B1 scenarios. For the A1B scenario the annual streamflow slightly decreases (~2%). The pronounced seasonal cycle that is visible at Maxau also dominates the signal at Lobith, al-

beit slightly damped. During the period 2052–2100, the maximum decrease in streamflow (in August) is about 30% for the A1B scenario, which is again the most extreme, whereas the A2 scenarios shows the strongest increase in April (also about 30%). Similar to Maxau, there is an increase in streamflow during the period 2002–2050 compared to the reference period, even in the summer months. In the tributaries, the Ruhr (Hattingen) and the Main (Raunheim), the seasonal cycle is less pronounced. In the Ruhr, streamflow increases throughout the year with 10 to 20% for both the first and second half of the 21st century. In the Main, finally, also an overall increase in streamflow can be seen for the period 2002–2050. Especially the B1 scenario shows a strong increase (up to 30%) in late summer. In the period 2052–2100, however, also the Main shows increasing streamflow in winter and spring, except February and March, and decreasing streamflow in summer and autumn. The overall increases in streamflow in the Ruhr and Main sub-basins is in accordance with Figure 4.5: the northern part of the Rhine basin, including the Main and Ruhr, is dominated by increasing precipitation throughout the year, although very little in summer. The severe decrease in precipitation in the summer season, therefore, only affects the southern tributaries, especially the Neckar and the Alpine part of the Rhine, as can be seen in the lower two panels of Figure 4.8.

4.4.3 Water balance components

Figure 4.9 shows average monthly values of some of the main water balance terms, averaged over the entire basin. To show the differences in more detail, the differences between the scenarios and the reference period are shown in Figure 4.10. In addition, Table 4.3 shows annual values of all water balance terms. As can be expected, precipitation shows a similar pattern as streamflow (Figure 4.8): overall increases during the period 2002–2050, and a decrease in the summer season during the period 2052–2100 with about 15%. This decrease in precipitation is amplified to the 30% decrease in streamflow (Figure 4.8) by increased evapotranspiration. This increases with about 8% for the A1B and A2 scenarios during the second half of the century. During the first half, this increase is still relatively modest with annual increases of about 2%. In both cases, evapotranspiration changes throughout the year, except for a short period in March and April. This pattern is similar to that of air temperature, indicating that on average evapotranspiration remains mainly energy limited, which is not surprising given the overall increases in streamflow and precipitation. The seasonal effect in precipitation seems to disappear to a large extent. Whereas during the reference period the highest monthly precipitation sums occur in summer and the lowest in March, precipitation is distributed more equally over the months in all scenarios. This causes the large seasonal differences (increase in spring, decrease in summer) that are observed in Figure 4.10.

Surface runoff, as expected, closely follows the climatology of precipitation and baseflow illustrates the transition to dryer circumstances during the second half of the century. Whereas there is still an increase in annual values of baseflow during the first half of the century, during the period 2052–2100 baseflow decreases throughout the year and most severely in (late) summer. This is related to the increase in evapotranspiration during the second half of the century, which reduces the amount of

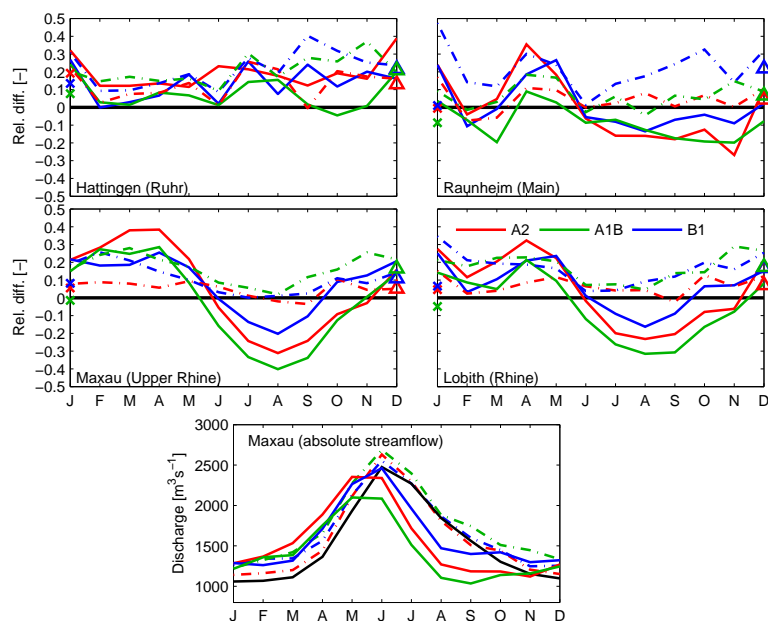


Figure 4.8: Climatologies of the difference in streamflow between three climate scenarios (A2, A1B and B1) and the reference situation at four locations in the Rhine basin: Hattingen (Ruhr), Raunheim (Main), Maxau (Upper Rhine) and Lobith (entire Rhine). Overall averages are indicated with crosses and triangles at the Y-axes. Dash-dotted lines and triangles indicate changes between the period 2002–2050 and the reference period, whereas solid lines and crosses indicate changes between the period 2052–2100 and the reference period. Positive values denote an increase in streamflow. The lowest panel shows the (absolute) climatology of streamflow at Maxau where the black line is the reference climatology.

water infiltrating and contributing to baseflow. Snowmelt is not a standard output variable of the VIC model. It is, therefore, estimated by taking the daily difference of the snow water equivalent. If this difference is positive, accumulation has occurred and melt is assumed to be zero. Note that in the VIC model snowmelt is added to precipitation before infiltration and runoff are calculated. It is, therefore, included in the baseflow and surface runoff fluxes. For the period 2002–2050, snowmelt increases in early summer compared with the reference period. SWE also increases in spring and early summer, but only for the A1B scenario. This is in accordance with higher precipitation during the spring season (Figure 4.10), as a portion of this precipitation falls as snow. Because the difference in air temperature is larger for summer than for spring during the period 2002–2050, the excess snow from the spring season melts in summer.

The annual values shown in Table 4.3 further illustrate the changes described above. In all scenarios precipitation increases quite drastically already during the period 2002–2050 (on average 88 mm,

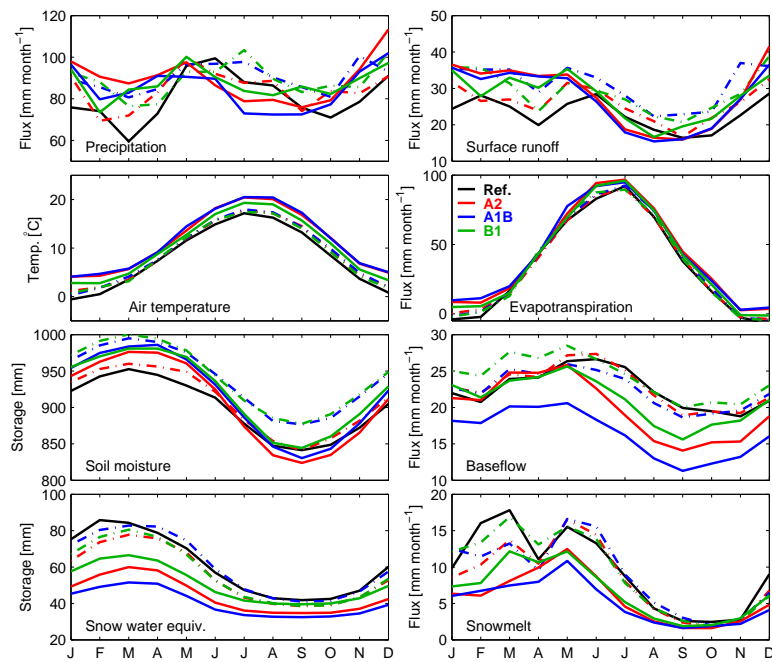


Figure 4.9: Climatologies of eight water balance components and air temperature, averaged over the entire basin. The reference period and three climate scenarios (A2, A1B and B1) are shown for the periods 2002–2050 (dash-dotted lines) and 2052–2100 (solid lines).

which is similar to the increase in the period 2052–2100), whereas evapotranspiration increases mainly during the second half of the century. This is correlated with air temperature, which also shows a modest increase during the first half of the century and a significantly larger increase during the second half. This can also be seen in the annual values for snow melt and SWE, which show a larger decrease during the second half of the century.

Figure 4.11, finally, shows the climatologies of snowmelt and total discharge averaged over the entire basin for the reference period, as well as for the three scenarios. It can be seen that during most of the snowmelt season (February–July), total streamflow increases, while snowmelt decreases, especially during the second half of the century. For the period 2002–2050, snowmelt increases for the A1B and B1 scenarios, as was mentioned before. Changes in the relative contribution of snowmelt to streamflow can thus be quantified. In March, the peak month for snowmelt, the relative contribution of snowmelt to streamflow decreases from 36% for the reference period to 27, 22 and 29% for A2, A1B and B1 respectively for the first half of the century. For the second half, these numbers are, for A2, A1B and B1, 14, 14 and 22% respectively. When the entire snowmelt season is considered, from February to July, the relative decrease in snowmelt is slightly smaller.

Table 4.3: Annual values of water balance fluxes (mm year^{-1}) and storages (mm) for the reference situation and 3 climate scenarios (A2, A1B, B1) for the first half of the 21st century (2002–2050) and the second half (2052–2100).

	1952–2000	2002–2050			2052–2100		
	Ref	A2	A1B	B1	A2	A1B	B1
Precipitation	968	1015	1082	1071	1073	1021	1050
Air temperature	8.06	8.89	8.99	8.75	11.34	11.52	10.21
Evapotranspiration	411	422	432	426	494	498	463
Interception evap.	16.8	12.4	12.5	16.3	12.2	12.5	11.0
Bare soil evap.	150	153	155	147	174	177	164
Transpiration	284	289	299	295	327	325	314
Surface runoff	277	313	373	349	339	327	332
Baseflow	271	274	269	290	238	197	253
Soil moisture	900	909	940	943	907	917	922
Snow water equiv.	61.1	55.7	60.7	56.6	44.5	40.3	50.6
Snow melt	113	100	107	110	69	62	80

4.4.4 Extreme streamflow

While the average changes in streamflow discussed in Section 4.4.2 provide useful information, extreme streamflow events are more relevant from a water management perspective. In this section, both peak flows and low flows are discussed. Figure 4.12 shows annual maxima as a function of their return times for streamflow at Lobith. The parameters of the Generalized Extreme Value (GEV; see Appendix 1) distribution are estimated using the maximum likelihood method. To put these results in some perspective, also the annual maxima from the observed record at Lobith³ are shown. For comparison, two different periods from the 20th century are displayed that each contain 49 years (1901–1949 and 1950–1998), similar to the other curves in the graph. For both the periods 2002–2050 and 2052–2100, annual maxima are higher than the reference situation for all three scenarios at nearly all return periods. During the first half of the century, the A1B and B1 scenarios are both higher than the A2 scenarios, whereas this reversed during the second half. During both periods the most extreme events are simulated under the A1B scenario, with the highest peak reaching nearly $16,000 \text{ m}^3 \text{ s}^{-1}$. The most extreme event in the reference simulation, about $11,000 \text{ m}^3 \text{ s}^{-1}$ (comparable to the near-floods in 1993 and 1995, which appear as the most extreme events in the “1950–1998” curve), will occur on average every 5 to 6 years during both halves of the 21st century for the most extreme scenarios. An event of the magnitude of 1926 (the most extreme event in the “1901–1949” curve) would occur every 10 to 20 years according to the climate scenarios. During the first half of the century the most extreme events seem to be larger than during the second half of the century, which is also suggested by Figure 4.4. In addition, it shows that either the hydrological model or the precipitation in

³Available from the KNMI website: <http://www.knmi.nl>

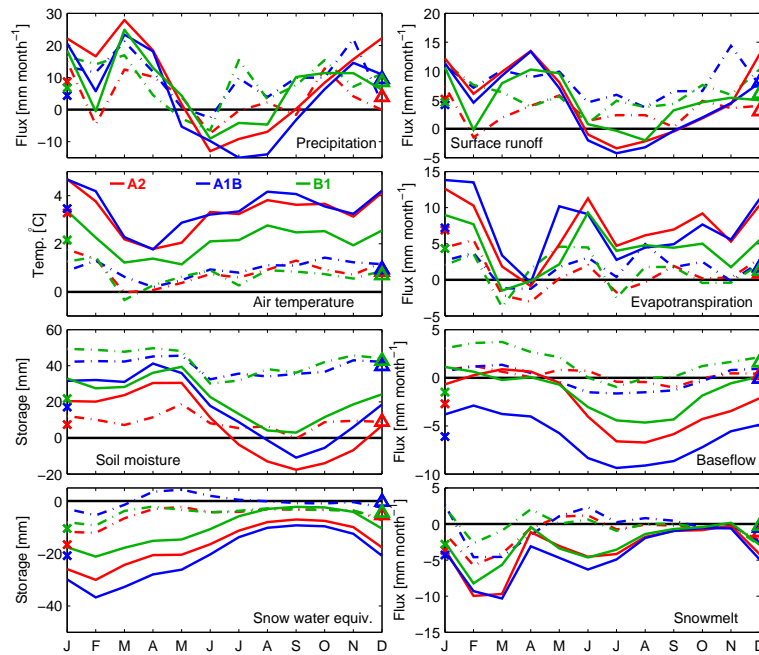


Figure 4.10: Climatology differences between the scenarios and the reference period and the scenarios for eight water balance components and temperature, averaged over the entire basin. Positive values denote increases. Differences between the period 2002–2050 and the reference period are indicated by dash-dotted lines and triangles (for annual means), differences between 2052–2100 and the reference by solid lines and crosses (for annual means).

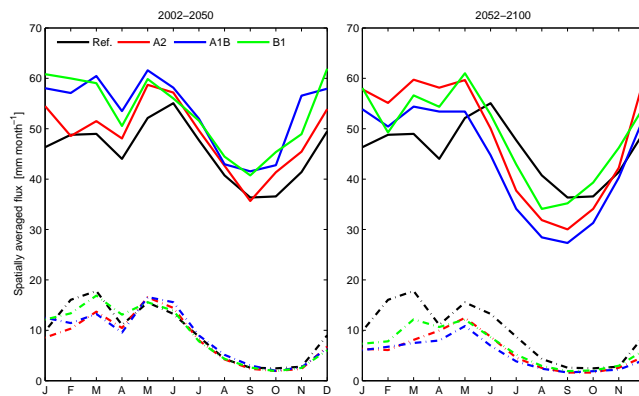


Figure 4.11: Climatology of streamflow (solid lines) and snowmelt (dash-dotted lines) for the reference period and the three climate scenarios. All values are in mm day^{-1} and averaged over the entire basin.

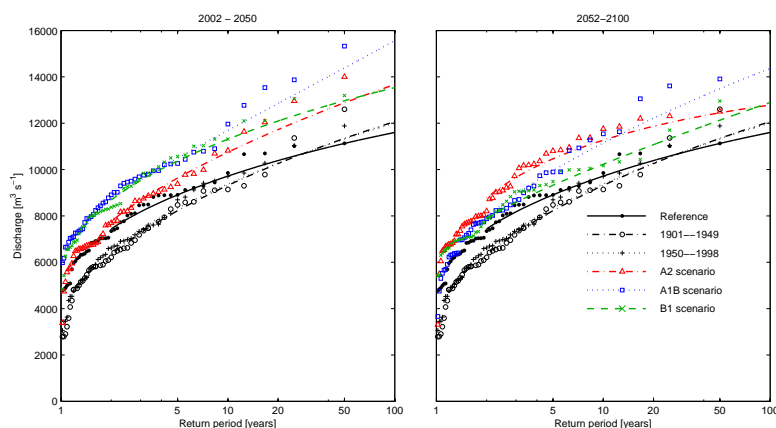


Figure 4.12: Annual maximum discharge at Lobith versus its return period for the reference period (1952–2000) and three climate scenarios. Both the periods 2002–2050 (left) and 2052–2100 (right) are displayed. A Generalized Extreme Value (GEV)-distribution is adjusted to the data. In addition, two periods of 49 years from the observed record are shown (1901–1949 and 1950–1998).

the reference dataset structurally overestimates events with low to medium return periods. For the extreme events, models and observations agree well.

A similar analysis is carried out for streamflow droughts. Several approaches exist to define a drought (e.g. Tallaksen and van Lanen, 2004; Fleig et al., 2006; Smakthin, 2001). Because not all annual low flow events reflect a drought, we define a streamflow drought as a cumulative deficit of streamflow below a threshold. At the moment the threshold is exceeded, the event ends (Hisdal et al., 2004). The threshold was selected to be the 75th percentile of streamflow (meaning the streamflow that is equaled or exceeded for 75% of the time) during the reference period (Hisdal et al., 2004). This value is a compromise between the number of years without any events and the number of multi-year events, which both can affect the results of the analysis (Fleig et al., 2006). Figure 4.13 shows the annual maximum deficit volume of such events, versus their return periods. A Generalized Pareto (GP; see Appendix 1) distribution is a suitable distribution to model such cumulative deficits (Tallaksen et al., 2004; Fleig et al., 2006). Therefore, such a distribution is adjusted to the data in Figure 4.13, again using maximum likelihood estimation. Additional streamflow drought statistics are shown in Table 4.4. Here, three statistics are selected: the average number of events per year, the average annual maximum duration, and the average annual maximum intensity. The intensity is defined as the deficit volume (of which the annual maxima are plotted in Figure 4.13), divided by the duration in seconds. The intensity (shown in $\text{m}^3 \text{s}^{-1}$) can thus be seen as the average streamflow deficit during the event.

Figure 4.13 shows that during the first half of the century, streamflow drought deficits are lower than the reference in all scenarios for small return periods. There are, however, some extreme events that

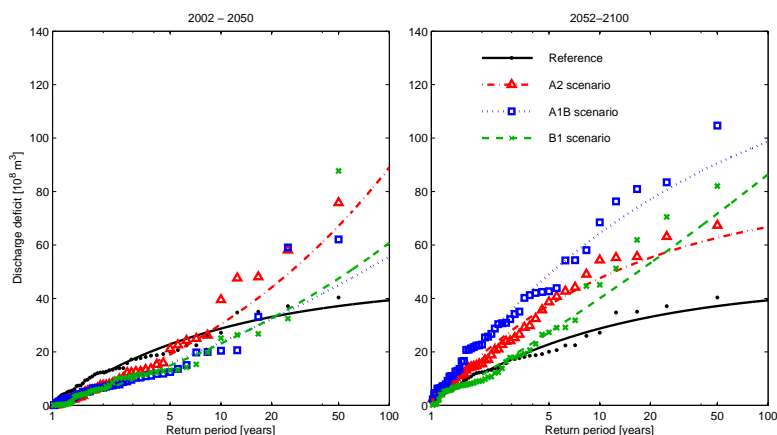


Figure 4.13: Annual maximum cumulative deficit of streamflow with respect to a threshold versus its return period for the reference period (1952-2000) and three climate scenarios. The periods 2002–2050 (left) and 2052–2100 (right) are displayed. The threshold is selected to be the 75th percentile at Lobith. A Generalized Pareto (GP) distribution is adjusted to the data.

are considerably higher than the extreme events during the reference period, especially in the A2 scenario. For the second half of the century the picture is entirely different: for nearly all return periods and all three scenarios streamflow drought deficits are larger than in the reference simulation. The most extreme streamflow drought deficit in the reference simulation, about $40 \times 10^8 \text{ m}^3$, occurs every 3 to 10 years depending on the scenario. The most extreme events during the period 2052–2100 occur in the A1B scenario and have a drought deficit volume that is more than double the volume during the reference period. Table 4.4 shows the streamflow drought events in more detail. Because statistics are shown for different locations in the basin (Figure 1.5), it also shows which regions are most susceptible to streamflow droughts. In Table 4.4, it can be seen that there are indeed significant regional differences within the basin. While the overall trend confirms the trends shown in Figure 4.13, there are some exceptions. For example, in the Mosel catchment, number, duration and intensity all keep decreasing during the 21st century. This seems in contradiction with Figure 4.6. Here it can be seen that a large part of the Mosel catchment experiences a decrease in summer evapotranspiration, supposedly due to water limitation. In winter however, there is also an increase in precipitation. An explanation for this contradiction is the fact that the winter precipitation rapidly percolates to the groundwater, where the water is out of reach for plants. Soil moisture droughts thus occur because evapotranspiration is water limited. However, the groundwater sustains relatively high baseflow levels, preventing streamflow droughts to occur (*Tallaksen and van Lanen, 2004*).

From Table 4.4, the Neckar basin appears to be the most susceptible to streamflow droughts: especially for the A1B scenario the average maximum duration increases from 29 to 81 days (the overall highest value), and the intensity rises from 29 to $60 \text{ m}^3 \text{ s}^{-1}$, which is also the highest value relative

to the threshold streamflow (which is only $108 \text{ m}^3\text{s}^{-1}$). The A1B scenario shows the highest values of drought statistics for most sub-basins and the entire basin, which corresponds to Figure 4.13. Figures 4.5 and 4.6 explain the fact that the Neckar sub-basin appears to be extremely vulnerable to streamflow drought events through the combination of strongly decreasing summer precipitation, only weakly increasing winter precipitation and increasing summer evapotranspiration. The same holds for the Alpine area, represented by Maxau. Because a large part of the Rhine discharge originates upstream of Maxau, this also has a strong influence at Lobith, the basin outlet.

4.5 Discussion

In this study we have investigated the effect of climate change on streamflow dynamics in the Rhine basin, by means of downscaled regional climate scenarios (0.088° spatial resolution) and a hydrological model. To represent the current climate two atmospheric datasets were available: a validation dataset based on re-analysis data that was used to calibrate the hydrological model, and a reference dataset based on a model run for the period 1050–2000 that was used for comparison with the scenarios. For each dataset, a bias correction was carried out to account for structural model errors. Three scenarios were available according to three SRES-emission scenarios: A2, A1B and B1. As a macro-scale hydrological model, the Variable Infiltration Capacity model was used, which is a land-surface model that has been applied in hydrological applications before. Changes in average streamflow were investigated, as well as changes in peak flow and streamflow droughts for different locations in the basin.

Data from a single GCM, RCM and hydrological model were used, whereas ideally one would use an ensemble for each model type. Model comparisons indicate a large range in model projections between GCMs. For example, the Coupled Model Inter comparison Project (CMIP) compared globally averaged air temperatures for the period 1961–1990s simulated by 18 GCMs and found a range of more than 4°C around the observed 14°C (Covey *et al.*, 2003). For precipitation, a similar range was found. Also the projected trend in global temperature structurally differs between GCMs. For example, the GCM used in this study, ECHAM5-OM, is known to give relatively strong temperature increases in the second half of the 21st century. As a model comparison in IPCC (2007) shows, ECHAM is relatively “cool” compared to the multi-model mean in the first half of the century, and relatively warm in the second half. The reason is a relatively high sensitivity of ECHAM to aerosol concentrations: in the first half of the century aerosol concentrations are high and their dimming effect is relatively strong. In the second half of the century, the model reacts strongly to the decline of aerosol concentrations, causing a strong temperature increase. This feature partly explains the contrast in our results between the periods 2001–2050 and 2051–2100 (relatively wet versus relatively dry), and further illustrates the need for a similar analysis with an ensemble of GCMs. The fact that in CMIP the ECHAM4-model is quite close to observed values for global mean temperature and precipitation (Figure 1 of Covey *et al.* (2003)), is encouraging. Also in model comparisons regarding other climate variables, ECHAM

Table 4.4: Statistics of streamflow drought events during the reference period and the 1st and 2nd half of the 21st century for the three climate scenarios (A2, A1B and B1), for seven streamflow gauges in the Rhine basin. For locations and corresponding sub-basins see Figure 1.5. Three statistics are shown, indicated by S1, S2 and S3. S1 is the average number of events (i.e., non-exceedence of the threshold) per year. S2 is the average of annual maximum durations in days. S3 is the average of annual maximum intensities, where the intensity is defined as deficit volume (plotted in Figure 4.13) divided by duration, in $\text{m}^3 \text{s}^{-1}$. For each station, the threshold value (75th percentile of the reference period) is shown between parentheses.

Period	Reference			A2 scenario			A1B scenario			B1 scenario		
	S1	S2	S3	S1	S2	S3	S1	S2	S3	S1	S2	S3
Hattingen (37.8 m^3s^{-1})												
2002–2050	5.7	33	16.8	6.5	33	17.6	5.0	27	15.6	4.6	26	12.9
2052–2100				7.1	35	19.7	6.7	39	19.9	6.0	33	18.9
Kalkofen (17.0 m^3s^{-1})												
2002–2050	7.5	33	5.6	8.1	30	5.8	7.3	25	5.5	6.0	22	4.6
2052–2100				8.7	32	7.1	9.0	34	7.1	7.3	28	6.2
Raunheim (92.9 m^3s^{-1})												
2002–2050	6.5	34	22.5	5.4	31	17.7	5.0	25	16.5	4.0	23	14.7
2052–2100				6.2	37	19.2	5.7	40	17.8	6.0	35	17.3
Cochem (165.9 m^3s^{-1})												
2002–2050	6.4	37	37.9	6.1	32	32.1	6.1	40	38.8	5.9	26	33.5
2052–2100				4.2	34	24.3	3.9	35	22.1	4.0	23	20.4
Rockenau (107.8 m^3s^{-1})												
2002–2050	7.0	29	29.1	5.5	26	23.5	7.4	25	27.2	4.1	24	21.6
2052–2100				9.5	44	40.0	11.8	81	60.1	8.4	42	36.8
Maxau (986.9 m^3s^{-1})												
2002–2050	4.8	33	209	4.1	30	217	4.1	20	204	4.1	23	173
2052–2100				7.2	33	334	8.7	38	420	5.8	28	259
Lobith (1801 m^3s^{-1})												
2002–2050	6.8	32	475	5.8	27	424	5.4	21	400	5.0	21	363
2052–2100				7.7	38	614	8.8	46	722	6.7	33	510

is ranked among the best performing GCMs (*van Ulden and van Oldenborgh, 2006*). In a recent model comparison, *Reichler and Kim (2008)* showed that ECHAM5-OM (which we use) performs very well compared to most other GCMs in simulating the current climate in terms of many different climate variables. The range of temperature changes that is projected by GCMs is further extended by the RCMs that are used for downscaling (e.g. *van den Hurk et al., 2005; Jacob et al., 2007; Déqué et al., 2007*).

In addition to the uncertainty in atmospheric models, there is also uncertainty involved in hydrological models and their parameterizations. However, given the fact that each GCM and RCM requires a specific bias correction (associated with different structural model errors), and each combination of a hydrological model with an atmospheric dataset would require a specific calibration, it was not feasible in the present study to use multiple models.

The bias correction that was applied to the meteorological data altered the spatial pattern of precipitation and temperature because the correction was applied to each of 134 sub-basins for which observations were available. As was noted in Section 4.4.1 and can be seen in Figure 4.3, the spatial pattern from the RCM is “drawn” towards that of the observations. In addition, the difference between the reference dataset and the scenarios can be amplified or reduced somewhat because the same exponent (Eq. 4.1) is applied to both. When the basin-wide spatial average is considered, this effect largely cancels out. This feature, however, is inherent to our correction for the model bias, which can be seasonally and geographically varying (e.g. *Christensen et al.*, 2008; *Leander and Buishand*, 2007). The above should be kept in mind when interpreting the spatial patterns as presented in this paper, or comparing them with uncorrected climate scenarios. Furthermore, while we assume that the model biases are similar for the current climate and the changing climate, *Christensen et al.* (2008) found that this is not always valid and biases tend to grow under warming conditions and depend on the amount of precipitation. This suggests an overestimation of the temperature increase, and should be kept in mind when interpreting the results.

The hydrological model that we used also presents some issues for discussion. While the VIC model has a physically-based approach for the calculation of evapotranspiration by solving the coupled water and energy balance, this is not the case for subsurface hydrological processes. No lateral soil moisture movement is included and the contribution of groundwater to evapotranspiration by capillary uprise is neglected as well. For an accurate modeling of streamflow drought events, ideally an explicit groundwater model should be included. However, at the scale of a large river basin, such as the Rhine, this is numerically not feasible. There has been some recent progress in including groundwater processes in land surface models like VIC (e.g. *Maxwell and Kollet*, 2008), although only for applications to small catchments. Because in the present study drought characteristics are not compared with observations but with a reference simulation, the presented results do provide valuable information on relative changes in drought characteristics as caused by climate change.

Finally, it is important to mention that the presented analysis of hydrological extremes is based on relatively short time series (3×100 years), whereas the Rhine discharge at Lobith that is relevant for safety purposes has a return period of 1250 years (*de Wit and Buishand*, 2007). The highest occurring streamflow in this study (about $16,000 \text{ m}^3\text{s}^{-1}$) is associated with much shorter return periods and therefore does not imply that higher values are not possible. Moreover, in this study river hydraulics and floodings are not taken into account, whereas floodings in Germany would have a significant impact on peak discharge at Lobith (*de Wit and Buishand*, 2007).

4.6 Conclusions

The present study differs from previous climate change impact assessments in the Rhine basin regarding the following points: the spatial resolution of the employed climate scenarios is higher; the hydrological model is more physically based and the entire 21st century was investigated as opposed to a timeslice of typically 30 years.

As far as streamflow at Lobith is concerned, this study confirms previous climate change impact assessments in the Rhine basin. By the end of the century, average streamflow at basin outlet is projected to increase with about 30% in winter and spring and to decrease with a similar value in summer and autumn. The majority of this effect originates in the alpine part of the catchment. It is caused for a large part by a decrease of the contribution of snowmelt to streamflow and by a shift of the timing of the snowmelt season to earlier in the year.

The high-resolution climate scenarios and the (distributed) hydrological model allow for a detailed analyses of spatial patterns. Results indicate that the projected decrease in summer discharge is concentrated in the southern part of the basin. The northern tributaries, where there is hardly any decrease in summer precipitation, are dominated by wetter conditions throughout the year.

The availability of data for the entire century allows the analysis of trends throughout the century, of which an overview is displayed in Figure 4.4. Towards the end of the 21st century, a gradually decreasing trend in annual maximum, minimum and mean streamflow appears. This trend causes an interesting contrast between the first half and the second half of the century. Because precipitation significantly increases in all three scenarios, the first half is dominated by relatively wet conditions. This also shows in our analysis of peak flows. During the second half of the century, temperature and evapotranspiration increase more drastically than during the first half, causing generally dryer conditions and more extreme droughts. Partly, this contrast originates from our choice of the GCM (see Section 4.5). It would be very interesting to repeat this analysis with another, or multiple, GCMs.

Acknowledgements

This research was financially supported by the European Commission through the FP6 Integrated Project NeWater and the BSIK ACER project of the Dutch Climate Changes Spatial Planning Programme. Rita Lammersen and Hendrik Buiteveld from Rijkswaterstaat Waterdienst, The Netherlands, are kindly acknowledged for providing observed data.

Chapter 5

Effects of climate variability on water storage in the Colorado River Basin



This chapter is a modified version of: R. T. W. L. Hurkmans, P. A. Troch, R. Uijlenhoet, P. J. J. F. Torfs and M. Durcik (2009), "*Effects of climate variability on water storage in the Colorado basin,*", submitted to J. Hydrometeorol.

Abstract

Understanding the long-term (interannual to decadal) variability of water availability in river basins is paramount for water resources management. Here, we analyze time series of simulated terrestrial water storage components, observed precipitation and discharge spanning 74 years in the Colorado River Basin and relate them to climate indices that describe variability of sea surface temperature and sea level pressure in the tropical and extra-tropical Pacific. El Niño-Southern Oscillation (ENSO) indices in winter (JFM) are related to winter precipitation, as well as to soil moisture and discharge in the Lower Colorado. The low-frequency mode of the Pacific Decadal Oscillation (PDO) appears to be strongly correlated with deep soil moisture. During the negative PDO phase, saturated storage anomalies tend to be negative, and the “amplitudes” (mean absolute anomalies) of shallow soil moisture, snow and discharge are slightly lower compared with periods of positive PDO phases. Predicting interannual variability, therefore, strongly depends on the capability of predicting PDO regime shifts. If indeed a shift to a cool PDO phase occurred in the mid-nineties, as data suggest, the current dry conditions in the Colorado basin may persist.

5.1 Introduction

Recently, the Colorado River Basin (CRB) experienced a severe multi-year drought that is unprecedented in the hydroclimatic record (Cook *et al.*, 2004). Due to temperature rise associated with climate change, similar drought episodes are predicted to occur more often (Seager *et al.*, 2007). For water management operations in the basin, understanding and predictive capacity of terrestrial water storage (TWS) dynamics and its associated hydrologic fluxes is crucial (Troch *et al.*, 2007). Precipitation in the southwestern U.S. has been linked to oceanic interannual variability (e.g. Redmond and Koch, 1991; Okin and Reheis, 2002; McCabe *et al.*, 2004; Hidalgo and Dracup, 2003), mostly involving El Niño-Southern Oscillation (ENSO; Trenberth (1997b)) and Pacific Decadal Oscillation (PDO; Mantua *et al.* (1997), a special case of Pacific Decadal Variability (PDV)). ENSO is considered the most important process of interannual variability of water availability in the southwestern U.S., and the most reliable one in terms of prediction (Cayan *et al.*, 1999). Warm (El Niño) and cold (La Niña) events typically occur every 3 to 7 years and last 8 to 16 months. These events have been linked to precipitation, floods and droughts across the western-United states (Cayan *et al.*, 1999; Cañon *et al.*, 2007; Hamlet *et al.*, 2007). La Niña conditions lead to wet conditions in the Northwest and dry conditions in the Southwest, and vice versa for El Niño conditions (Redmond and Koch, 1991). PDO shows similar effects in the southwestern U.S. (MacDonald and Case, 2005) and can, when in phase with ENSO, amplify El Niño or La Niña effects (Gershunov and Barnett, 1998; Hamlet *et al.*, 2007; Cole *et al.*, 2002). PDO regime shifts, however, are much less predictable than ENSO cycles. Although its power spectrum was shown to be most energetic at two ranges of return periods (one from 15-25 years and the other 50-70 years; Mantua and Hare (2002)), the physical processes driving PDV and PDO remain unclear. The abrupt changes between cool and warm phases (each lasting 20-30 years), therefore, are not yet predictable with sufficient lead times (Newman, 2007).

Much of previous research has focused on precipitation and, to a lesser degree, on streamflow (e.g., Maity and Kumar, 2008). Much less attention has been paid to regional water availability or terrestrial water storage (TWS; Troch *et al.* (2007)). Understanding the effects of climate variability on TWS is, however, relevant, since it is a hydrologic state variable and therefore integrates hydrologic processes such as snow accumulation, evapotranspiration, infiltration and recharge. There are several techniques available to estimate TWS, which are described in detail in Troch *et al.* (2007). Examples are the Basin-scale Water Balance (BSWB) method, used by Seneviratne *et al.* (2004) and Hirschi *et al.* (2006), which combines the atmospheric and terrestrial water balance to estimate changes in TWS from atmospheric moisture convergence, changes in atmospheric water vapor storage, and streamflow data. The GRACE satellite mission (Tapley *et al.*, 2004), has been also applied successfully to estimate water storage variability (e.g. Swenson and Milly, 2006; Han *et al.*, 2005). A third method is hydrological modeling of TWS-components. Among all these methods, estimated storage dynamics in the CRB agree reasonably well with each other and with in-situ data (Troch *et al.*, 2007; Hasan *et al.*, in prep.).

Here, we focus on TWS dynamics simulated using the Variable Infiltration Capacity hydrological

model (VIC; Liang *et al.* (1994)) forced by a meteorological dataset of interpolated observations, spanning the period 1915–2003. Hydrological modeling has several advantages compared to the other methods mentioned above. First, simulations are based on observed meteorological forcings (precipitation, temperature, air pressure, short- and longwave incoming radiation, vapor pressure, and wind speed), whereas for example the BSWB method applies model re-analysis data, which are constrained by radiosonde observations. Especially for hydrologic variables, balance problems can occur in such datasets (Seneviratne *et al.*, 2004). Second, TWS estimates from VIC span a longer period (1915–2003) compared to the other methods. Third, TWS can be investigated in a distributed manner. Finally, TWS can be analyzed for each of its components (such as soil moisture, snow, groundwater) separately. Troch *et al.* (2007) and Hasan *et al.* (in prep.) indicated that the amplitudes of modeled storage anomalies do not always agree well with that of other methods, and Niu and Yang (2006) found that they are generally too low in tropical regions and too high at high latitudes. Trends and variability, however, agree well (see also: <http://voda.hwr.arizona.edu/twsc/sahra/>, 2008).

We analyze the interannual variability of individual components of TWS: shallow and deep soil moisture, and snow water equivalent (SWE), as well as precipitation and discharge. Using several climate indices describing oceanic and atmospheric variability in the Pacific, we attempt to explain this variability. With enhanced understanding of this variability, predictability of hydrologic anomalies in the CRB may be improved. As already mentioned, an advantage of obtaining TWS from hydrological modeling, is its relatively high spatial resolution. Storage dynamics will, therefore, be analyzed both in a spatially averaged and a distributed way.

5.2 Study area and datasets

The Colorado River Basin (CRB) is located in the southwestern United States, and has a drainage area of about 637,000km² (Figure 5.1). Much of the basin is semi-arid, and in the southern part rainfall is generally concentrated in the summer monsoon. The high-elevation snow pack in the Rocky Mountains contributes about 70% of the total annual runoff.

The meteorological data used in this study were compiled by Hamlet and Lettenmaier (2005) and span the period from 1915 to 2005. Based on comparisons with observed streamflow and snow cover, Hamlet and Lettenmaier (2005) concluded that the dataset is temporally consistent and suitable for trend analysis of hydrologic variables at the macro-scale. The Hamlet and Lettenmaier (2005) dataset is thus used to force the Variable Infiltration Capacity (VIC, version 4.0.5; Liang *et al.* (1994)) model for the CRB at a spatial resolution of 0.25° and a temporal resolution of 3 hours. The VIC model is designed as a land surface model to provide the land surface boundary conditions for climate models. Evaporation is calculated by solving the coupled water and energy balance, and the soil column is represented by three layers. The soil moisture contents of the upper two, of which the upper is generally very thin (0.1m), determine the amounts of evaporation and infiltration. The soil moisture content of the lowest

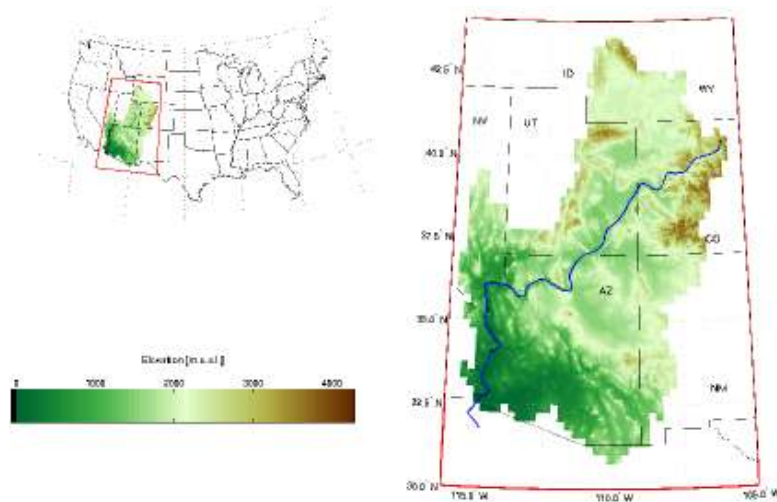


Figure 5.1: Location of and elevations in the Colorado River Basin. The basin outline represents the discretization of the basin in VIC at a resolution of 0.25 degrees. The Colorado river is shown as a black line.

layer determines the amount of baseflow, or groundwater discharge. Vertical transport of moisture through the soil column is assumed to be driven by gravity only and no lateral moisture transport is allowed. Calibration parameter values for the VIC model were obtained from A. Wood (University of Washington; personal communication). The model was calibrated to match naturalized streamflow at the basin outlet. Resulting modeling efficiencies at the outlet of the Upper Colorado and the entire CRB were respectively 0.88 and 0.85, where a value of 1 indicates a perfect match. From the modeling results the following variables were extracted: outflow (surface runoff plus baseflow), snow water equivalent (SWE), soil moisture in the lowest layer (hereafter denoted as deep soil moisture) and soil moisture in the upper two layers (hereafter denoted as shallow soil moisture). The latter three, as well as interception storage of the canopy (both snow and water), are summed to calculate total TWS. In addition, precipitation from the forcing dataset is included in the analyses. Due to the dominance of the summer monsoon and spring snow melt, all variables show a very strong annual cycle compared to the interannual variability. To remove seasonal influences, and because all climate indices are also based on a monthly time step, all time series are aggregated to monthly averages (sums for precipitation and outflow) and converted to anomalies by subtracting the mean annual cycle. Smoothed time series (12 month running means) of all anomalies are shown in Figure 5.2a and b, their autocorrelation functions are shown in Figure 5.3a and the corresponding power spectrum in Figure 5.3b. Because storage anomalies in the first 15 years were very high compared to the rest of the period, while precipitation anomalies were not, we discarded the first 15 years. The period of analysis is, therefore, 1930–2003 hereafter.

Precipitation over the CRB has been linked to both tropical (ENSO) and extratropical (PDO) Pacific

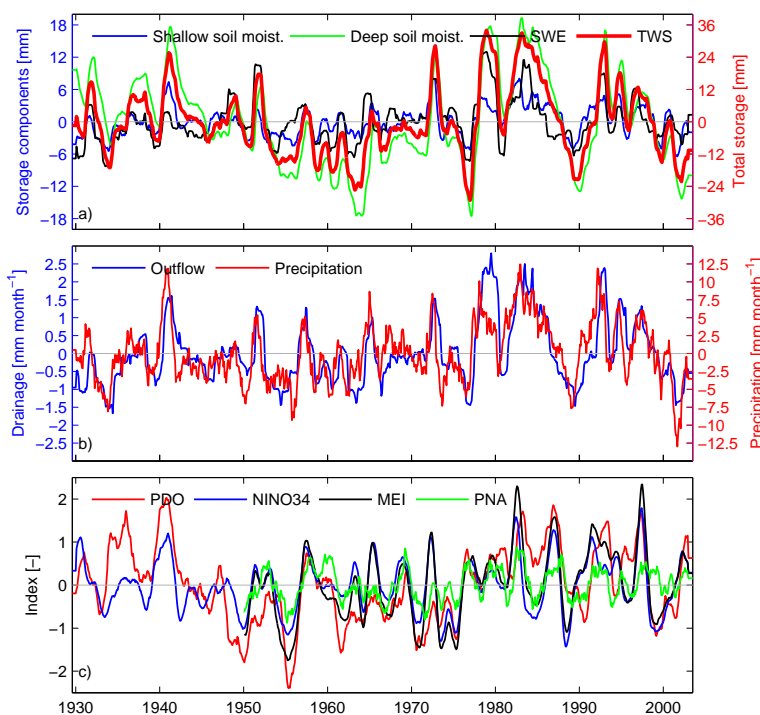


Figure 5.2: Time series of spatially averaged anomalies of (a) storage components and total storage in VIC, (b) outflow (surface runoff + baseflow) and precipitation, and (c) four climate indices (MEI, PDO, NINO3.4 and PNA). For clarity, 12 month running averages were calculated for each variable.

variability. Therefore, four indices that together represent both oceanic and atmospheric dynamics in the tropical and extratropical Pacific were selected. The Multivariate Enso Index (MEI; *Wolter and Timlin* (1998)) was selected because it is a composite of six variables over the tropical Pacific, and includes atmospheric anomalies in addition to sea surface temperatures (SST). Because MEI is only available from 1950, we use NINO3.4 (which is available for the entire period) as a proxy because it shows the highest correlation with MEI (0.90) compared with other ENSO indices (NINO1.2, NINO3 and NINO4). The difference between these ENSO indices is the area in the Pacific that is used to calculate them. NINO3.4 is calculated over the area bounded by 5°N–5°S in latitude, and 170°W–120°W in longitude. For NINO3 and NINO4, these bounding boxes have the same latitudes, but in longitude the ranges are 150°W–90°W for NINO3 and 160°E–150°W for NINO4. NINO1.2 is bounded by 0°–10°S latitude, and 90°W–80°W longitude. To represent PDO, the PDO index proposed by *Mantua et al.* (1997) is used, defined as the anomaly of sea surface temperature in the area of the Pacific north of 20°N. In addition, the Pacific North American pattern (PNA) is included because it is one of the most important modes of variability in the Northern Hemisphere extratropical atmosphere, and largely independent of ocean temperatures (*Johansson*, 2007). In addition, PNA was shown to have an influence on precipitation and discharge in the western United States by *Redmond and Koch* (1991). In this way

we cover both ocean and atmospheric dynamics in the tropics (MEI/NINO3.4) and the extratropics (PDO/PNA). Figure 5.2c shows 12-month running mean time series of all four indices and Figure 5.3b shows their autocorrelation functions (ACFs) and power spectra respectively. MEI and NINO3.4 have their most important spectral peaks at return periods of about 4 to 6 years, whereas PDO shares the peak at 6 years with ENSO, but has its most important peaks at 25 years and higher. However, the time series that is employed is too short (74 years) to capture this low-frequency behavior of PDO. Cross-correlations and cross-powerspectra between anomalies and climate indices were analyzed as well. Because in many signals there is significant autocorrelation (Figure 5.3a,c), they were found to provide little information and are therefore not shown in this article.

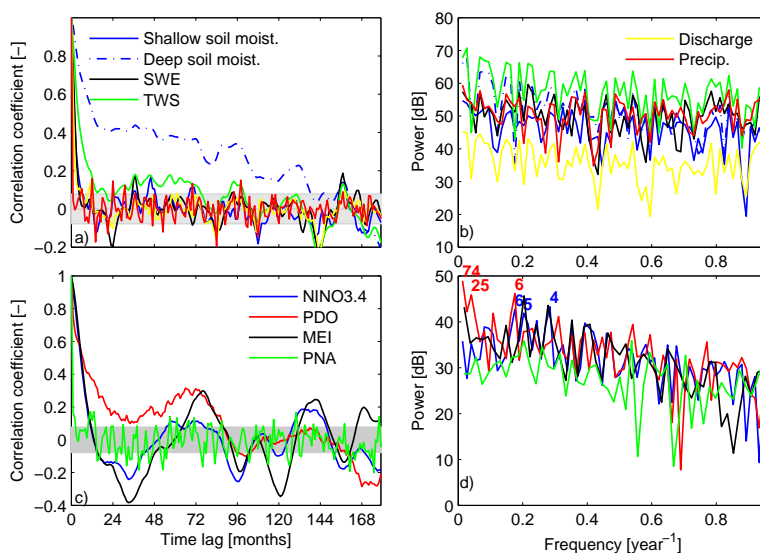


Figure 5.3: Autocorrelation functions for all anomalies (a) and indices (c) displayed in Figure 5.2, up to a time lag of 180 months (15 years). Gray shaded areas indicate autocorrelations not significantly different from zero. Power spectra are also shown for anomalies (b) and climate indices (d). Numbers in d) represent the return period in years of the strongest spectral peaks of NINO3.4 and PDO. Both (a) and (b) show six lines (shallow soil moisture, deep soil moisture, SWE, TWS, discharge, and precipitation) for which the legend is split between (a) and (b).

5.3 Results

5.3.1 Analysis of spatial averages

As can be seen in Figure 5.3, the autocorrelation function for deep soil moisture remains significant for very large time lags, up to about 11 years. The large autocorrelation propagates in the total TWS, causing the autocorrelation function for total TWS to be significant up to about 6 years, although small after 1 year. Therefore, in the analyses described hereafter, dynamics of total TWS are not examined as such, but storage dynamics for deep soil moisture, shallow soil moisture and SWE are investigated separately. For these latter variables, the autocorrelation function diminishes after a few months, so by calculating averages of 6 months, autocorrelation is almost filtered out and correlation patterns between climate indices and anomalies can be investigated, including time lags. Figure 5.4 shows a matrix of correlation coefficients between monthly values of the climate indices and 6 month moving averages of anomalies of shallow soil moisture, SWE, discharge and precipitation.

In Figure 5.4, correlation patterns are similar for precipitation, shallow soil moisture and discharge, although correlation coefficients are generally slightly lower for discharge. MEI and NINO3.4 show a nearly identical pattern, which is not surprising given their high mutual correlation (0.90). ENSO indices early in the year (January to May) give the highest correlations with hydrologic anomalies throughout the year, except for the period which is dominated by the summer monsoon. This is consistent with the findings of, for example, *Okin and Reheis* (2002) and *Gochis et al.* (2007), who found low correlations between winter ENSO and summer precipitation as well. ENSO indices in the second half of the year, on the other hand, seem to be correlated with the second half of the year (the monsoon and the period just after that). These findings are consistent with previously reported correlations. *Hidalgo and Dracup* (2003) report high correlations of warm season ENSO with warm season precipitation in the upper Colorado basin, whereas in the lower Colorado basin correlations are generally found to be higher between winter ENSO and winter precipitation (e.g. *Okin and Reheis*, 2002). PDO shows a slightly different pattern, with significant correlations for all but the winter months and generally slightly lower correlations. The amount of snow in the winter season, however, seems to be uncorrelated to any climate index. There is some correlation between SWE and MEI in summer, but that is only after the main snow melt season, when there is hardly any snow left. The lack of correlation between SWE and ENSO is consistent with the result that correlations between ENSO and winter precipitation are limited to the Lower Colorado basin, since SWE is concentrated in the Upper Colorado basin. The PNA index in some specific months (January and April) is also correlated with SWE, especially in the cold season. It should be noted, however, that due to limited availability of the climate indices, MEI and PNA only cover the period 1950-2003, while NINO3.4 and PDO cover the entire period from 1930.

By calculating the 6-month averages, the effect of autocorrelation should be filtered out. To further investigate the correlations that appear in Figure 5.4, the corresponding (scaled) time series to some of the pixels in Figure 5.4 are shown in Figure 5.5. Here, only PDO and NINO3.4 are shown because they

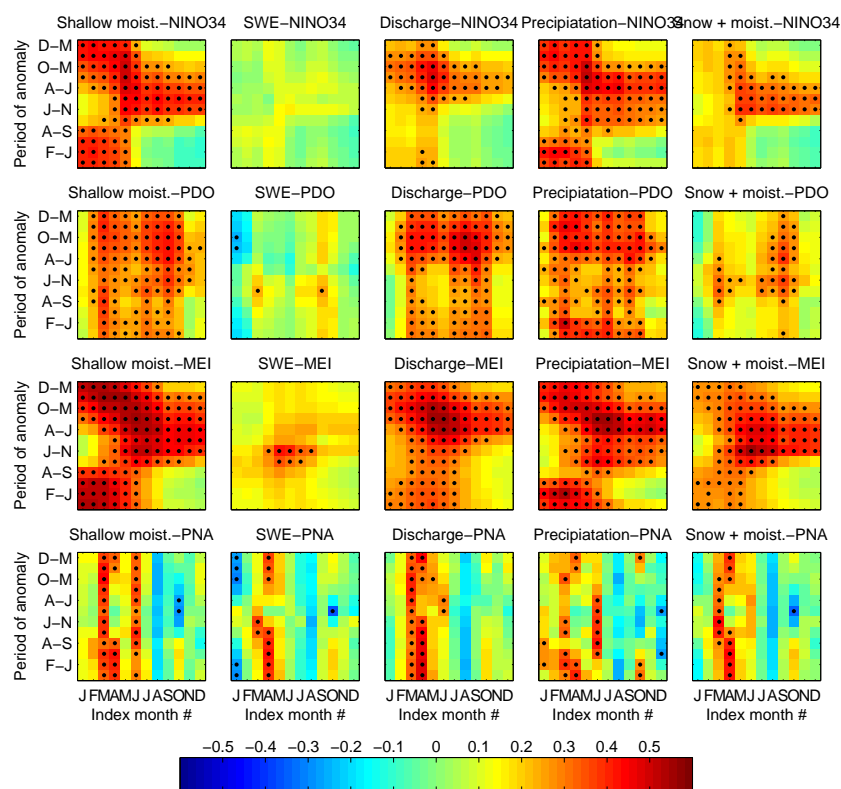


Figure 5.4: Correlation between 6-month moving averages of 5 hydrologic anomalies and monthly values of 4 climate indices (on the X-axes). The Y-axes, thus, represent from bottom to top 12 six-month moving averages: January-June, February-July (F-J)...December-May (D-M). Correlations that are significant at $\alpha = 0.05$ are denoted by a black dot.

cover the entire period, and only shallow soil moisture is shown because precipitation and discharge show a similar correlation pattern in Figure 5.4. Figure 5.5 shows that both the NINO3.4 and PDO indices are indeed related to anomalies of shallow soil moisture in winter and spring (Figure 5.5): nearly all the El Niño (La Niña) events (shaded in gray) correspond to a positive (negative) shallow soil moisture anomaly. Here, the definition of such events as given by *Trenberth* (1997b) is followed: an event is a consecutive period of 6 months in which the NINO3.4 index is higher than 0.4°C (for El Niño), or lower than -0.4°C (for La Niña). The same events are also visible for the PDO index, which explains the nearly identical correlation coefficients for both indices. Climate indices in March are correlated to shallow soil moisture throughout the year (Figures 5.5a-d), whereas the climate indices in September are only correlated with cold season shallow soil moisture (Figures 5.5g,h), and much less (not at all for NINO3.4) with warm season shallow soil moisture (Figures 5.5e,f). In all plots, it appears that especially the extreme El Niño and La Niña events are generally well correlated. For example, the El Niño event of 1940, which also shows a high PDO peak, is related to high shallow soil moisture

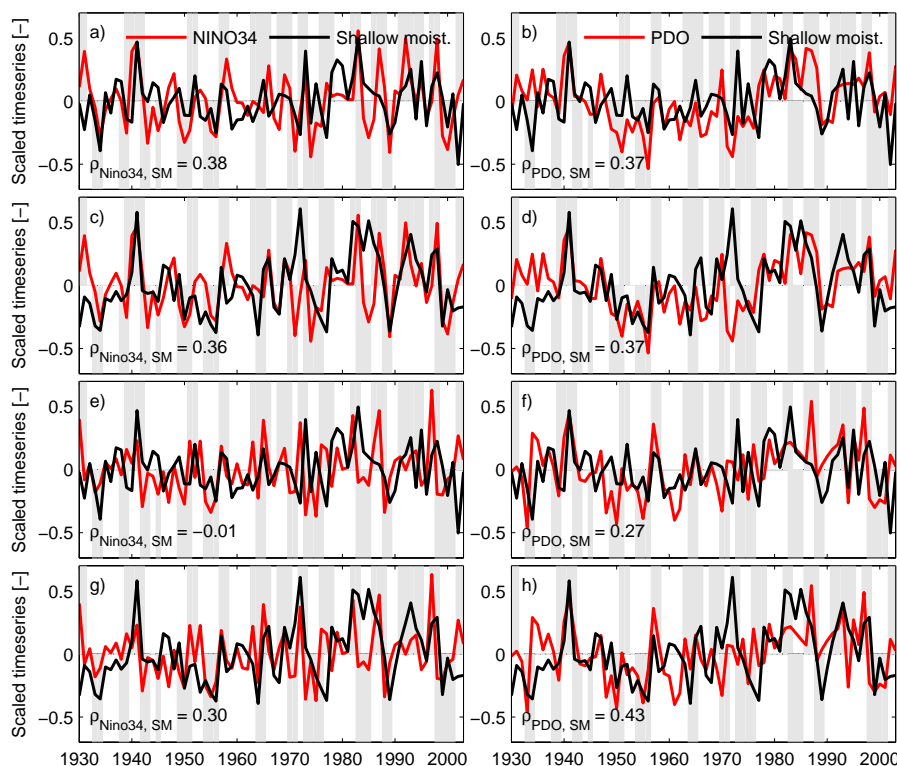


Figure 5.5: Time series of monthly NINO3.4 (a,c,e,g), PDO (b,d,f,h) and 6-month averaged shallow soil moisture, similar to the data used to create Figure 5.4. Four pixels from the matrices plotted in Figure 5.4 are used: a/b) the March indices versus March-September averaged shallow soil moisture; c/d) March indices versus September-February averaged shallow soil moisture; e/f) September indices versus March-September averaged shallow soil moisture and g/h) September indices versus September-February averaged shallow soil moisture. Also the cross-correlation coefficients (without time lag) are shown in every panel (SM indicates soil moisture). Gray shaded areas indicate El Niño events (positive) and La Niña events (negative).

anomalies throughout the year. Also the El Niño events of around 1972 and 1982 and the La Niña event of 1989 led to extremely wet (dry for La Niña) conditions. However, they were not so distinct throughout the year, i.e. they do not show up in all panels of Figure 5.5. It should be noted, however, that although Figure 5.5 shows the dynamics of climate indices and shallow soil moisture anomalies, the amplitudes of all signals (also with respect to each other) have no meaning because all time series were scaled by dividing each time series by the difference between its maximum and minimum value.

For some of the variables and indices in Figure 5.2, the 24-month running average is plotted in Fig-

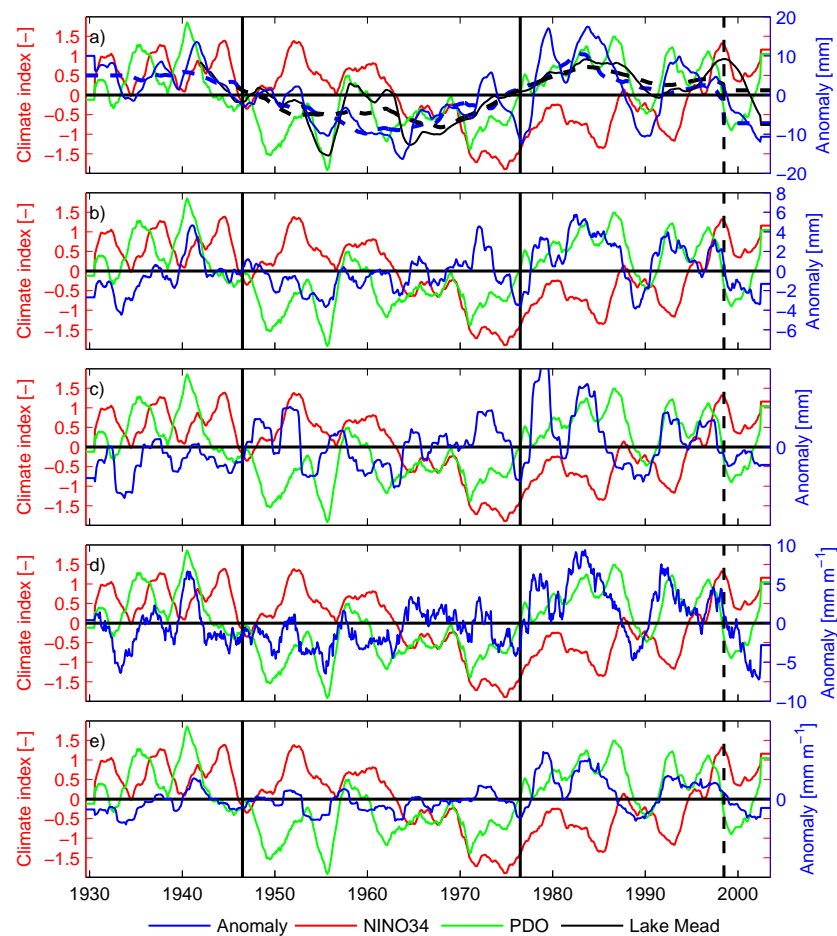


Figure 5.6: Interannual variability investigated through time series of 24-month running averages of a) deep soil moisture, b) shallow soil moisture, c) SWE, d) precipitation and e) discharge. In all plots, also NINO3.4 and PDO are plotted. In addition, the storage anomaly of Lake Mead is plotted in a). To illustrate the correlation between deep soil moisture and reservoir storage and PDO phases, the 10-year running means of the deep soil moisture anomaly (black) and that of the storage anomaly of Lake Mead (gray) are plotted as well in a) as thick dashed lines. Black vertical lines denote the shifts from warm to cool and again to warm PDO phase in all panels, and the dashed line at 1998 denotes a possible third phase change.

ure 5.6 in order to show interannual to decadal variability more clearly. The PDO phases, each about 30 years long, clearly stand out. PDO phases were identified by several independent studies (see *Mantua and Hare (2002)* for a review on PDO) as follows: warm (positive) PDO regimes dominated from 1925 to 1946 and from 1977 to about the mid-nineties, whereas cool (negative) regimes prevailed

between 1947-1976. The 74 years used in this study, therefore, only cover one complete PDO cycle. In Figure 5.6, regime shifts as they were indicated by Mantua *et al.* (1997) are indicated by vertical black lines.

In Figure 5.6a the sign of the anomaly of deep soil moisture is distinctly different between PDO phases. This is illustrated by the 10-year running mean (dash-dotted line in Figure 5.6a), of which the positive and negative episodes exactly coincide with the PDO phases. Apparently, during negative PDO episodes conditions are generally dryer, although this does not show that clearly in the other records. In addition, the storage anomaly of Lake Mead is plotted in Figure 5.6a. Lake Mead is a large surface water storage reservoir in the Lower Colorado, accounting for 45% of the total surface storage capacity in the CRB (Troch *et al.*, 2007), and data is available from 1941 onwards. Another large reservoir, Lake Powell (accounting for 42% of the total storage capacity), is only operational from 1963 and is therefore not included in the present analysis. The 24-month running average of the storage anomaly of Lake Mead follows the deep soil moisture anomaly with a time lag, although the signal is somewhat flattened. In addition, the 10-year running average of the storage anomaly of Lake Mead is shown. Again, the positive and negative episodes exactly coincide with the PDO regime phases as indicated in Figure 5.6. These findings are consistent with earlier research by McCabe *et al.* (2004), who find that a large part of the variability in drought frequency is explained by PDO. Some sources indicate that a shift of PDO to a new negative phase has occurred in the nineties (e.g. Mantua and Hare, 2002). If that is really the case and the length of the PDO phases would stay in the same order of magnitude as it has been throughout the 20th century, this implies that for the coming decades, dry conditions might prevail in the CRB.

Another striking feature in Figure 5.6 is the fact that the amplitude of the signal, or the size of the anomaly, seems to be larger in positive PDO phases for shallow soil moisture and precipitation. Table 5.1 shows the mean absolute anomaly over the entire period (A), positive (P) and negative (N) PDO-phases. A t-test was performed to test whether the averaged absolute anomalies between the PDO phases and the entire period are different. Results of two types of t-tests are displayed. First, a difference of means test for independent samples, because this test has the advantage that the time series do not need to be of equal length. This test was carried out to test the difference between A and P, A and N, and P and N. The test does assume independence, but not equal variance between the samples. For completeness, also a paired-samples test was carried out, which is more suitable for dependent samples. This test, however, needs samples of equal length, therefore a part of P was selected of similar length to N. In all tests, the length of the time series was corrected for autocorrelation by calculating an "effective sample size", which depends on the first-order autocorrelation (Cressie, 1991):

$$n_{eff} = \frac{n}{\left[1 + 2\left(\frac{\rho}{1-\rho}\right)\left(1 - \frac{1}{n}\right) - 2\left\{\frac{\rho}{1-\rho}\right\}^2 \frac{(1-\rho^{n-1})}{n} \right]}, \quad (5.1)$$

where n is the length of the time series, ρ is the first-order autocorrelation, and n_{eff} is the effective

Table 5.1: Average of the absolute values of hydrologic anomalies over the entire period (A), as well as positive (P) and negative (N) episodes of PDO. In the right four columns, p -values are given for a t-test which was performed to test whether averaged absolute anomalies are different between (1) the entire period and the positive episode (A vs. P), (2) the entire period and the negative episode (A vs. N), and the positive and negative episodes (P vs. N). A t-test for independent samples was used for differences between A vs P, A vs N, and P vs N. P vs N was also tested using a paired-samples (PS) test for dependent samples; results are displayed in the rightmost column. All values were calculated using an effective sample size, i.e., corrected for autocorrelation.

Variable	Mean A	Mean P	Mean N	A vs. P	A vs. N	P vs. N	PS P vs. N
Shallow soil moisture [mm]	3.507	3.720	3.194	0.694	0.221	0.137	0.029
Deep soil moisture [mm]	7.489	7.971	6.781	0.588	0.361	0.293	0.099
Discharge [mm month ⁻¹]	0.923	1.008	0.797	0.698	0.175	0.118	0.001
Precipitation [mm month ⁻¹]	9.146	9.151	9.140	0.504	0.495	0.492	0.580
SWE [mm]	4.190	4.568	3.636	0.653	0.286	0.209	0.017
SWE + Moisture [mm]	7.098	7.604	6.355	0.656	0.267	0.196	0.016

(corrected) length of the time series. It should be noted, however, that this method only corrects for linear correlation and does not take into account non-linear and higher order correlation effects and is therefore relatively crude. Results of the tests are displayed in Table 5.1 in terms of their p -values. We find differences between the PDO phases for shallow soil moisture, SWE and discharge, although it depends on the method of testing and correcting for auto-correlation whether they can be considered significant or insignificant, which is the reason for presenting the results in terms of p -values. The differences in amplitude (although small) seem consistent with previous research. *Gershunov and Barnett* (1998) found that ENSO is enhanced by PDO (or NPO as *Gershunov and Barnett* (1998) call it), i.e., during positive PDO phases El Niño patterns are stronger and more stable, whereas during negative PDO phases this is typically the case for La Niña patterns. More extreme and stable ENSO patterns could lead to more extreme hydrological conditions through the correlations displayed in Figure 5.4. This also explains the generally dryer conditions during the negative PDO phase. The higher amplitude for shallow soil moisture and discharge in positive PDO phases can also be explained by the higher saturated storage: more saturated storage means less buffering capacity. Runoff and shallow soil moisture content of the upper soil will, therefore, react faster and stronger to precipitation events, whereas during negative PDO-phases more water can percolate to the saturated storage reservoir and thus surface runoff and shallow soil moisture are buffered to some extent. In addition, *Cayan et al.* (1999) also found that the effect of climate variability is amplified in streamflow with respect to precipitation due to the non-linear response of surface runoff to precipitation. This is consistent with our finding that differences in the amplitudes of discharge and shallow soil moisture anomalies are significant where those of precipitation anomalies are not.

Table 5.2: Correlation coefficients between anomalies (shallow soil moisture, deep soil moisture, SWE, precipitation and discharge) and climate indices (PDO and NINO3.4), calculated for the entire period (All), and for positive (PDO+) and negative (PDO-) PDO phases separately, based on 24-month running averages of both data and indices. Significant values ($\alpha = 0.05$) are indicated in bold.

	NINO3.4			PDO		
	All	PDO+	PDO-	All	PDO+	PDO-
Shallow soil moist.	0.48	0.39	0.50	0.47	0.17	0.56
Deep soil moist.	0.20	-0.00	0.14	0.61	0.00	0.56
SWE	0.16	0.02	0.24	0.08	-0.18	0.30
Discharge	0.29	0.28	0.25	0.41	0.14	0.45
Precipitation	0.55	0.59	0.51	0.54	0.30	0.53

As Figure 5.5a, and to some degree also Figure 5.6a suggest, correlations between climate indices on one hand and hydrological anomalies on the other hand are stronger in some periods compared to others. Examples are the periods 1930-1950, and 1988-1999. Such periods of stronger and weaker correlations were also identified for summer precipitation by *Hu and Feng* (2001), and related to PDO-like variability. To investigate whether this is also the case in this study, Table 5.2 lists correlation coefficients as calculated over each PDO phase separately, based on 24-month running averages of both data and indices. In Table 5.2, we see that although correlation coefficients for NINO3.4 are nearly equal in both PDO phases (except perhaps for SWE, which does not show very strong correlations altogether), correlations with PDO during the negative PDO-phase are significantly stronger than during the positive PDO-phase. This is also visible to some extent in Figures 5.5b and 5.6. Correlation coefficients are relatively high because, as in Figure 5.6, correlation coefficients are based on 24-month running averages. Correlations based on monthly values (not shown) show the same pattern, but are less clear because overall correlation coefficients are lower.

5.3.2 Analysis of distributed data

A similar analysis as is shown in Figure 5.4, which represents spatial averages over the entire CRB, can be carried out in a distributed manner. For some of the data points in Figure 5.4, the corresponding map is shown in Figures 5.7 and 5.8. In these figures only PDO and NINO3.4 are shown, because these are available for the entire period. In addition, MEI and NINO3.4 are nearly identical. Because not much structural correlation was visible for SWE in Figure 5.4, SWE is not displayed in Figures 5.7 and 5.8. Moreover, if any significant correlations are present for SWE, the spatial pattern is rather predictable and limited to the mountainous areas (see Figure 5.1). For comparison purposes, standard deviations of the various anomalies are shown in Figure 5.9 to indicate the areas that show the highest

variability. Most of this variability seems to be related to orographic precipitation: the areas of highest variability in precipitation coincide with the areas with the most pronounced topography (Figure 5.1).

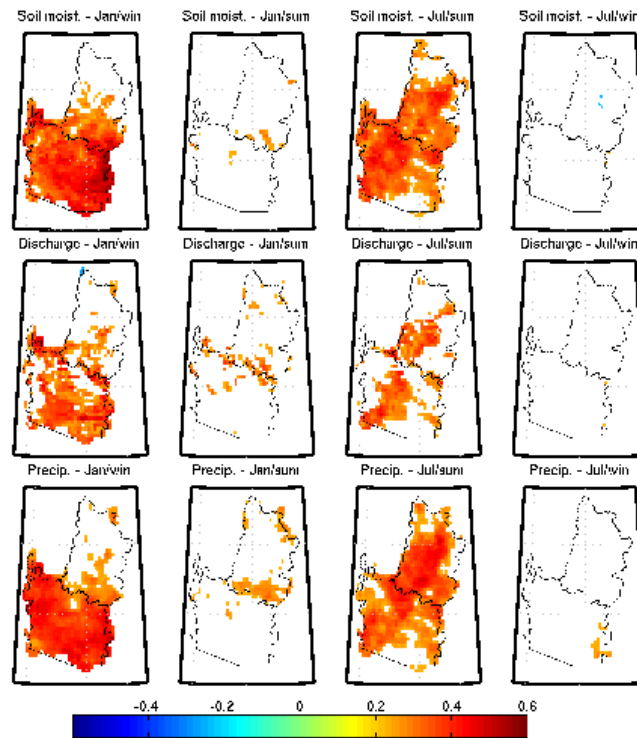


Figure 5.7: Maps of correlation coefficients between anomalies of 3 variables (shallow soil moisture, discharge and precipitation) and the climate index NINO3.4. Only significant correlations ($\alpha = 0.05$) are shown. Time series were aggregated similar to Figure 5.4; calendar months of climate indices are correlated with 6 month averages of anomalies. Here the climate index values for January (Jan) and July (Jul) are shown, correlated with anomaly values averaged over January-June (win), or July-December (sum).

Correlation coefficients between climate indices for January and July, and 6-month averages of shallow soil moisture, precipitation and discharge anomalies are plotted in Figures 5.7 and 5.8, each for a time lag of 0 and 6 months. As appeared from Figure 5.4 as well, NINO3.4 is mainly correlated to the hydrologic anomalies for time lags of 0 months, especially in the southern part of the basin. At time lags of 6 months, however, almost all correlation disappears except for a low mountain range along the northern rim of the Little Colorado basin (northeast Arizona; Figure 5.1). NINO3.4 values for July are correlated with summer anomalies over nearly the entire basin, except for two regions (far north and far south) in which very little variability is present according to Figure 5.9. This is consistent with *Hidalgo and Dracup (2003)*, who also find high correlations in summer throughout the basin. Especially

for precipitation, correlation coefficients are highest in the western part of the basin. It is not clear yet why this is the case. The PDO index for January is not correlated to any anomaly, which is consistent with Figure 5.4. The July PDO index, on the other hand, is highly correlated with winter/spring precipitation, shallow soil moisture and discharge anomalies, especially in the southern part of the basin. This suggests that, for this area, PDO could be used in prediction of precipitation anomalies in the next cool season, with about 6 months lead time. This as opposed to NINO3.4, which is more synchronously correlated in the southern part of the basin, i.e., without any lead time.

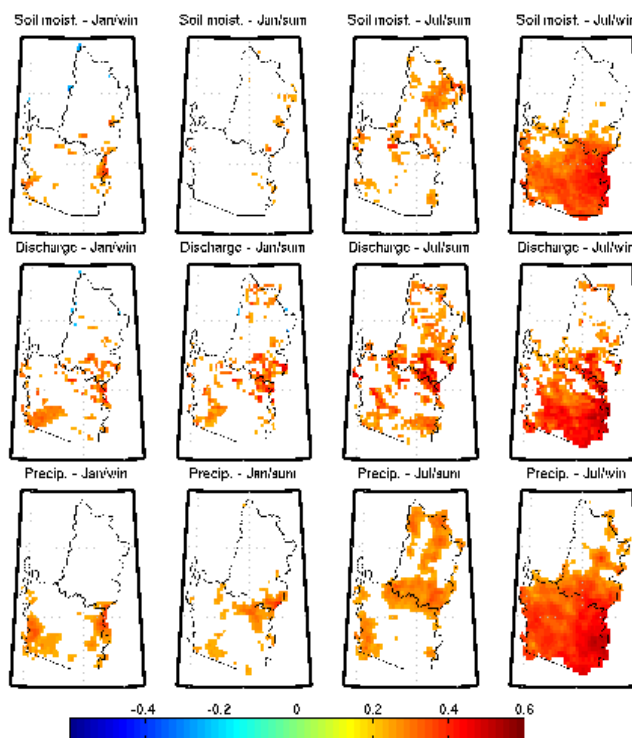


Figure 5.8: As Figure 5.7, but for the climate index PDO.

The spatial distribution of runoff and shallow soil moisture are to a large extent governed by soil properties, which in VIC depend strongly on model calibration. To correctly represent the spatial variability of hydrological states, separate parameter values should be assigned to every pixel in the VIC model. In the calibration that is employed in this study, however, the spatial variability in calibration parameters is relatively small, as is also pointed out by *Hasan et al.* (in prep.). Because discharge and shallow soil moisture show a similar pattern as precipitation, the spatial correlation pattern is most likely dominated by precipitation and not so much by calibration parameters. Moreover, the spatial distribution of the calibration parameter values is entirely different from these patterns, although not shown here.

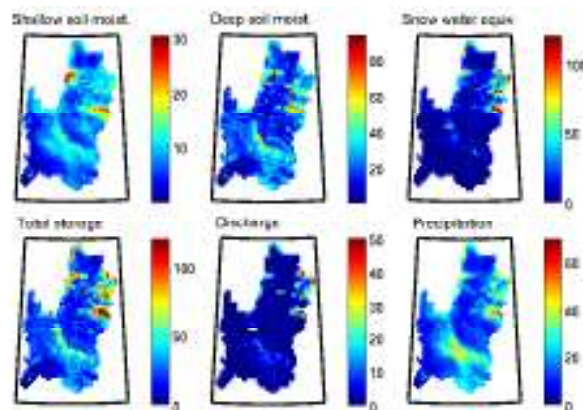


Figure 5.9: Maps of temporal standard deviations of anomalies of 3 storage components (shallow soil moisture, deep soil moisture, snow pack), total storage, outflow and precipitation. Storage components are in millimeters, fluxes in mm month^{-1} .

5.4 Summary and conclusions

In this study, we investigated the inter-annual to decadal variability of terrestrial water storage in the Colorado river basin. TWS data was obtained from modeling results of the Variable Infiltration Capacity (VIC) model, forced by a meteorological dataset of interpolated observations, spanning the period 1915–2003. The resulting TWS estimates have advantages compared to those obtained by other methods in that they (1) span a relatively long period (we analyze the period 1930–2003), (2) are spatially distributed and (3) offer the possibility to analyze the various storage components separately. As already mentioned, the model was forced by observations and calibrated to match naturalized streamflow at the basin outlet. The gridded observations that were used to force the model were, however, downscaled and interpolated (*Hamlet and Lettenmaier, 2005*). The hydrological variables that were analyzed should therefore be considered as “model re-analysis” data. We compare the time series of monthly anomalies (i.e. the mean climatologies are removed from the signals) of deep soil moisture, shallow soil moisture, precipitation, “discharge” (the sum of surface runoff and baseflow), and snow water equivalent (SWE), with four climate indices, describing the variability of ocean temperature and atmospheric pressure levels in the tropical and extra-tropical Pacific. Where previous studies in the CRB mainly investigated precipitation and discharge, we thus also take into account dynamics of deep and shallow soil moisture and snow.

Because autocorrelations extend over very large time lags for deep soil moisture and because this autocorrelation propagates in the TWS signal, cross-correlations with climate indices cannot be calculated reliably. Therefore, we focus on separate storage components, mainly shallow soil moisture and snow water equivalent. Precipitation, shallow soil moisture and discharge are all related to ENSO, mainly in winter and spring. For these seasons, correlations occur exclusively in the southern part

of the basin. ENSO in summer is also correlated to summer precipitation, moisture and discharge, as was also found by *Hidalgo and Dracup* (2003), throughout the CRB. The relation between these variables and NINO3.4 and PDO are strongest during extreme El Niño and La Niña events. PDO is correlated quite strongly with ENSO (0.58), showing the same extreme events. Apart from the PDO mode that is correlated with ENSO, PDO exhibits a periodicity at much lower frequencies (multiple decades), generally known as PDO phases, of which two (maybe three) transitions have taken place during the period of study. Deep soil moisture appeared to be closely related to these PDO phases. Because the time scales at which changes in deep soil moisture occur are much larger than those at which changes in for example shallow soil moisture or precipitation occur, the correlation between the low-frequency periodicity of PDO and deep soil moisture is more pronounced than the correlation with other variables. In addition, the high-frequency mode (which is related to ENSO) of the PDO index appeared to be more closely related to these anomalies during the negative episode of PDO.

This study aimed at improving the understanding of the interannual to decadal variability of the hydrologic state of the Colorado river basin. Although there is certainly some correlation with ENSO, as was found by many studies before, it is not always consistent and therefore difficult to employ for prediction purposes. The PDO index in summer, however, appears to be correlated with winter precipitation and shallow soil moisture for the Lower Colorado, and therefore offers potential for prediction with lead times of about 6 months. The low-frequency mode of PDO seems to have an important impact on the hydrological conditions: during the negative PDO phase (in the record of study this corresponds to 1946–1976), generally dryer conditions occurred. The physics behind the PDO and especially the (ir)regularity of this periodicity is not well understood to date. Prediction of PDO is, therefore, extremely difficult (*Newman, 2007; Mantua and Hare, 2002*). If the periodicity as it was seen throughout the 20th century continues, and if indeed a regime shift to a negative PDO phase occurred during the mid-nineties, which is still uncertain (*Mantua and Hare, 2002*), then the current dry conditions in the CRB may persist for several more years.

Acknowledgements

This research was financially supported by the Water Sustainability Program of the University of Arizona, the European Commission through the FP6 Integrated Project NeWater, and the BSIK ACER project of the Dutch Climate Changes Spatial Planning Programme. Andy Wood from the University of Washington is kindly acknowledged for sharing the calibration parameters for the hydrological model, and providing the observed dataset.

Chapter 6

A hillslope-based parameterization for sub-grid variability of topography



Abstract

Large-scale models typically operate at spatial resolutions of hundreds of square kilometers, while variability in soil, vegetation and topography occurs at much smaller length scales. Because this small-scale variability cannot be taken into account explicitly it needs to be parameterized. We use a hillslope-based approach to do this, where the hillslope-storage Boussinesq (hsB) model is used to simulate saturated zone dynamics. After coupling the hsB model to a formulation for the unsaturated zone we apply our model to a small, Alpine catchment, the Rietholzbach. Four levels of spatial aggregation are distinguished: (1) individual slopes, (2) classes of similar slopes, (3) two “open-book” slopes and (4) the catchment as one hillslope folded around the channel network. The hillslope-based approach is compared to the TOPMODEL approach, which is applied at similar levels of aggregation but represented by distributions of values for the topographic index, and the statistical approach of the Variable Infiltration Capacity (VIC) model. We find that for all models, changes in evaporation and discharge are dominated by the exposure of the hillslope and its land cover. Simulation of individual pixels or hillslopes results in increased surface runoff in both TOPMODEL and hsB. This increase is, however, largely offset by a decrease in baseflow. When the amount of hillslopes is reduced from 84 to 9 classes of similar hillslopes, catchment-averaged changes in runoff, baseflow and discharge, as well as the variability across hillslopes is preserved. This is not the case when the catchment is modeled as an “open-book” or one large hillslope.

6.1 Introduction

Macro-scale hydrological models such as land surface models (LSMs), which provide land surface boundary conditions for climate models, typically operate at spatial resolutions of multiple square kilometers. Variability in soil, vegetation and topography, however, usually occurs at much smaller scales (e.g., Wood, 1995; Koster *et al.*, 2000). This small-scale variability has an important influence on runoff generation in a catchment or macro-scale grid cell. It influences the spatially averaged infiltration and therefore the evapotranspiration as well. However, in the development of LSMs, emphasis has often been put on the formulations for evaporation and vegetation. The coupled water and energy balances are solved to compute the land surface fluxes (latent, sensible and ground heat), and canopy interception is modeled explicitly (e.g., Liang *et al.*, 1994; Eltahir and Bras, 1993). The formulation for runoff generation is often much less complex (Koster *et al.*, 2000), although Koster and Milly (1997) found that the formulation for surface runoff in an LSM is as important for the simulation of annual evaporation as the formulation of evaporation itself. Related to this small scale variability, the influence of groundwater on soil moisture variability through capillary uprise and lateral redistribution is often not taken into account (Liang *et al.*, 2003; Maxwell and Miller, 2005). Recently, studies have begun to model groundwater explicitly in an LSM (e.g. Maxwell and Miller, 2005; Miguez-Macho *et al.*, 2007; Maxwell and Kollet, 2008). Applications so far, however, have been limited to relatively small scales. Explicit groundwater modeling, therefore, is not (yet) feasible at the scale of large river basins. As sub-grid variability of soil moisture and its driving processes thus cannot be modeled explicitly in large-scale models, it needs to be parameterized.

Several approaches have been developed to do this. A relatively straightforward one is “tiling”, applied in for example MOSAIC (Koster and Suarez, 1996) and VIC (Liang *et al.*, 1994): a grid cell is divided into tiles of, for instance, similar vegetation based on high-resolution land use data (Avissar and Pielke, 1989). The model is then run for each tile and the area-weighted grid-cell average is computed. Entekhabi and Eagleson (1989) used a statistical-dynamical approach where a-priori reasonable spatial distributions of soil moisture and precipitation were introduced. Another statistical approach is used by the Variable Infiltration Capacity (VIC) model (Wood *et al.*, 1992; Liang *et al.*, 1994), where infiltration capacity is related to the fraction of the grid cell that is saturated. The TOPMODEL concept (Beven and Kirkby, 1979) makes use of hydrologic similarity by creating a distribution of so-called “wetness indices”, again based on high-resolution elevation data, assuming that hydrologic behavior at a point can be explained by the area draining to that point and the local slope. This concept has been used in various LSM applications: Famiglietti and Wood (1994) coupled TOPMODEL to a SVAT-scheme, Koster *et al.* (2000) divided a climate model grid cell into catchments and then parameterized heterogeneity within each catchment using the TOPMODEL approach, and Walko *et al.* (2000) incorporated TOPMODEL in the LSM LEAF-2.

In many catchments, hillslopes are the basic elements of the landscape (Troch *et al.*, 2003). Many studies have aimed at understanding hydrological processes within a hillslope, and to define similarity

parameters based on different hillslope geometries (e.g. Aryal *et al.*, 2002; Berne *et al.*, 2005; Wagener *et al.*, 2007). Hillslope similarity within a macro-scale grid cell or catchment could be employed to parameterize sub-grid scale variability of runoff generating processes. The hillslope-storage Boussinesq (hsB) model (Troch *et al.*, 2003; Paniconi *et al.*, 2003) simulates saturated storage dynamics in a hillslope in a computationally efficient way. When coupled to a formulation for the unsaturated zone and energy balance, it can provide the basis for a “hillslope-scale” LSM. The hsB approach relaxes some basic assumptions that are made in TOPMODEL: is not based on successive steady states and takes into account both advective and diffusive flow, which can be of importance in areas with modest topographic gradients.

In this study, we apply the hsB model, coupled to a formulation for the unsaturated zone and the energy balance, to a small alpine catchment, the Rietholzbach in Switzerland. Its performance is assessed using observed discharge and evaporation, and compared with simulations using TOPMODEL and VIC. The model is applied at different levels of spatial aggregation: the catchment as one big hillslope folded around the channel network, the catchment as an “open book”, enabling to investigate the effect of hillslope exposure, and the catchment divided into individual hillslopes. TOPMODEL is implemented in a similar way, by (1) explicitly taking into account all individual pixels, (2) grouping all pixels in one distribution of values of the topographic index, and (3) grouping all northfacing and southfacing pixels in separate distributions. For all models, the differences between aggregation levels in the various terms of the water budget will be evaluated.

6.2 Study area and data

The Rietholzbach is a small, mountainous catchment in northern Switzerland. It is located in the center of the Thur basin, which in turn is a tributary of the Rhine (Gurtz *et al.*, 2003). The catchment spans about 32.52 km², and the main flow direction is from west to east. Elevation ranges from approximately 650 to 930 m, and the main land use in the basin is pasture land, with an areal coverage of 76%. Observed soil types range from less permeable gley soils to more permeable brown soils and regosols with relatively large soil water storage capacities. The soil depth is generally between 0.50 and 2 meters. Elevation, land use and soil maps of the Rietholzbach basin are shown in Figure 6.1.

A meteorological station is present in the center of the basin in Bühl (Figure 6.1), from which precipitation, temperature, air pressure, wind speed, relative humidity, and incoming shortwave radiation are available at hourly timesteps. In the present study, we use data for the period 1999–2003, of which 1999 is characterized by some extreme precipitation events, and 2003 by a severe drought (see Figure 6.2). Unfortunately, air pressure has only been observed since December 2001, and there are many gaps in the measurements of shortwave incoming radiation. Therefore, additional data from a down-scaled re-analysis dataset is employed, which was also used in previous studies and is described in more detail in Hurkmans *et al.* (2008) and Hurkmans *et al.* (2009b). From the corresponding pixel in this

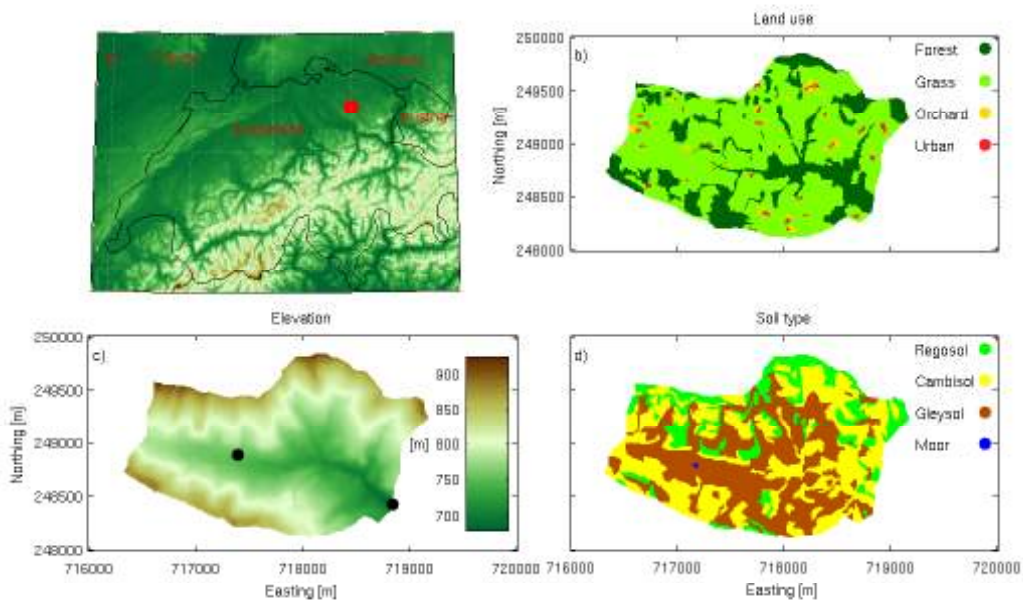


Figure 6.1: Main characteristics of the Rietholzbach catchment: from the upper left in clockwise direction the location of the basin, a land use map, an elevation map and a soil map are shown. Black dots in the elevation map indicate the locations of the meteorological station from which observations are used (Bühl, B) and the streamflow gauge at the basin outlet (Mosnang, M).

dataset, both incoming shortwave and longwave radiation were extracted, and air pressure was used after correcting for elevation: because air pressure in the re-analysis dataset is provided at sea level, it was corrected by subtracting the mean difference between the two datasets over the period of overlap.

In addition, data from a weighing lysimeter at the same location are available for the same period. Discharge is measured at the basin outlet (Mosnang), and soil moisture is measured at three depths (0.15, 0.25 and 0.55 m) at the same location as the meteorological station, as is the groundwater level. More information about the Rietholzbach and data availability can be found at

<http://www.iac.ethz.ch/research/riet/>.

6.3 Hydrological models

Three hydrological models are employed in this study, that use different approaches to parameterize sub-grid scale heterogeneity. In the next sections, TOPMODEL, and the hillslope-storage Boussinesq (hsB) model are described in more detail. The VIC model was described in detail in Section 1.3. Their application to the Rietholzbach is explained in Section 6.4. The three models have very different ap-

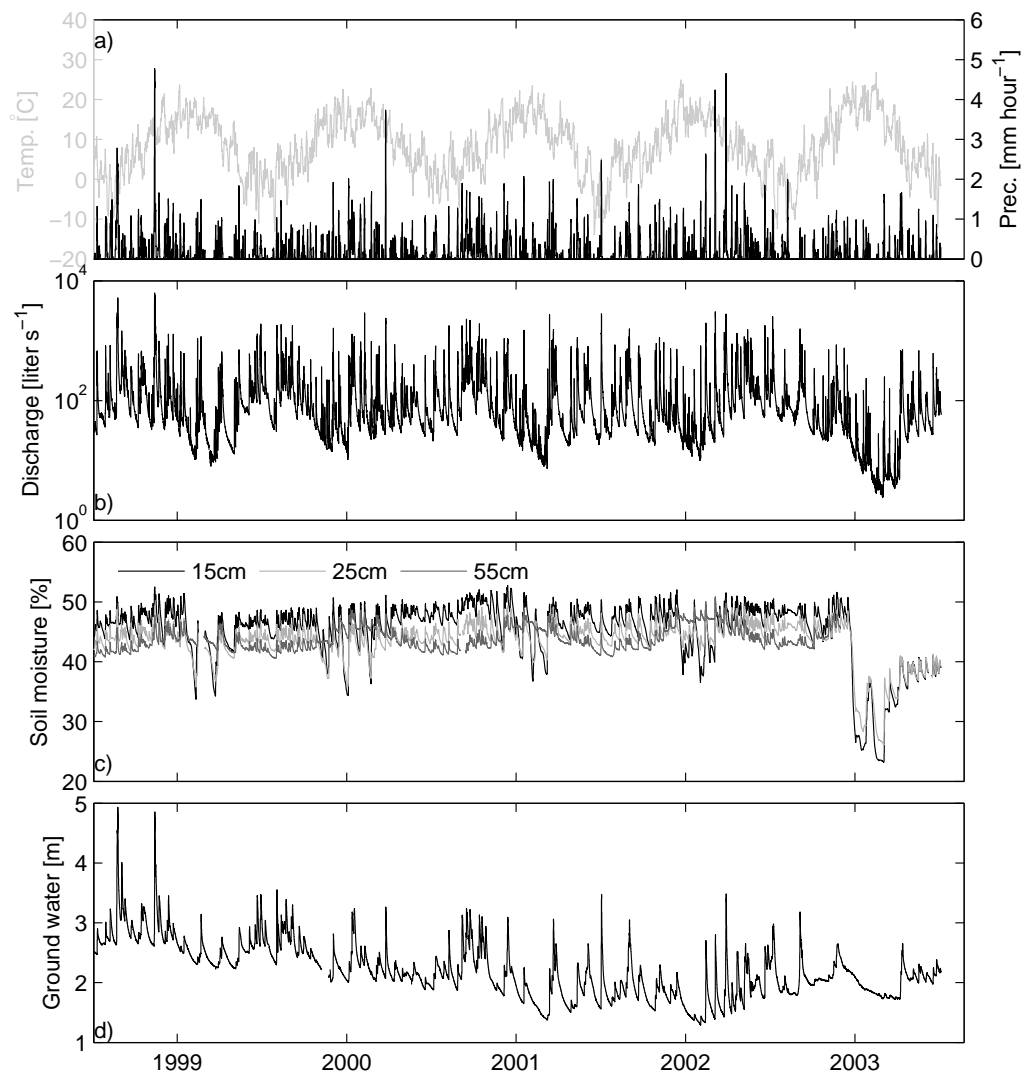


Figure 6.2: Time series of observations from the Rietholzbach catchment: a) precipitation and temperature from the meteorological station (temperature is smoothed using a 24-hour running average); b) discharge at the basin outlet (note the logarithmic scale); c) soil moisture content at the meteorological station at three depths; d) groundwater level at the meteorological station (the reference is 7.55 meter below the surface).

proaches to account for the unsaturated zone. VIC solves the fully coupled water and energy balance and the soil is modeled as three reservoirs. TOPMODEL employs two reservoirs and requires potential evaporation as atmospheric forcing, and the uncoupled version of hsB is forced with precipitation and potential evapotranspiration. To enable a fair comparison with VIC, both TOPMODEL and hsB

are coupled with a formulation for the unsaturated zone and the energy balance, which is based on the TOPLATS formulation of *Famiglietti and Wood* (1994). In the remainder of this paper, the coupled versions of TOPMODEL and hsB will be denoted as TOPLATS and hsB-LATS, respectively. For completeness, also the uncoupled models are taken into account in the comparisons.

6.3.1 TOPMODEL

TOPMODEL (*Beven and Kirkby*, 1979) is a semi-distributed model that has been widely used (e.g. *Franchini et al.*, 1996; *Beven*, 2001; *Warrach et al.*, 2002; *Famiglietti and Wood*, 1994; *Walko et al.*, 2000). It has been described extensively in these references but for completeness the main concept is repeated here. TOPMODEL is based on the assumptions that flow dynamics of the saturated zone can be represented by successive steady-states, and that the hydraulic gradient can be approximated by the topographic gradient, leading to the so-called topographic index $\ln(a/\tan\beta)$, where a is the area that drains to a point in the catchment per unit contour length [L], and β is the local slope [-]. This index can be seen as a similarity index for pixels in a digital elevation model (DEM). Another assumption is that of an exponential relationship between transmissivity T [$L^2 T^{-1}$] and storage deficit D [L]:

$$T = T_0 e^{-D/m}, \quad (6.1)$$

where T_0 [$L^2 T^{-1}$] is the horizontal transmissivity when the soil is completely saturated and m [L] is a model parameter controlling the decline of transmissivity in the soil profile. Given a catchment (or grid cell) averaged storage deficit \bar{D} , a local value can be calculated by:

$$D = \bar{D} + m \left[\gamma - \ln \left(\frac{a}{\tan\beta} \right) \right], \quad (6.2)$$

where γ is the mean value of the topographic index [L], and the baseflow Q_b [$L^3 T^{-1}$] is given by:

$$Q_b = T_0 e^{-\gamma} e^{-\bar{D}/m} \quad (6.3)$$

The unsaturated zone is represented by a root zone reservoir and an unsaturated zone reservoir for every class of the topographic index as described in *Beven* (2001). The root zone is depleted by evaporation, which is calculated by scaling the potential value (which is part of the input data) by the relative soil moisture content, and drains to the unsaturated zone reservoir when field capacity is reached. The recharge q_v [$L T^{-1}$] from the unsaturated zone reservoir to the saturated zone is given by:

$$q_v = \frac{S_{uz}}{Dt_d}, \quad (6.4)$$

where S_{uz} is the storage of the unsaturated zone reservoir [L] and t_d is a reservoir constant per unit of deficit [$T L^{-1}$]. If S_{uz} exceeds the available storage capacity (which is equal to D), overland flow

occurs.

6.3.2 The hillslope-storage Boussinesq model

The hillslope-storage Boussinesq (hsB) model (Troch *et al.*, 2003; Paniconi *et al.*, 2003) is a one-dimensional model that simulates saturated zone dynamics in a hillslope. The main equation is:

$$\frac{\partial h}{\partial t} = \frac{k \cos(\alpha)}{f} \left(\frac{h}{w} \frac{\partial h}{\partial x} \frac{\partial w}{\partial x} + \left(\frac{\partial h}{\partial x} \right)^2 + h \frac{\partial^2 h}{\partial x^2} \right) + \frac{k \sin(\alpha)}{f} \left(\frac{h}{w} \frac{\partial w}{\partial x} + \frac{\partial h}{\partial x} \right) + \frac{N}{f} \quad (6.5)$$

where h is the local water table height averaged over the width of the hillslope [L], α the slope [-], w the local hillslope width [L], N [$L T^{-1}$] is recharge and f drainable porosity [-]. The plan shape of the hillslope is taken into account using the hillslope width function w .

6.3.3 Unsaturated zone formulation

The formulation for the unsaturated zone and the energy balance that is coupled to TOPMODEL and hsB is based on the TOPLATS land surface scheme. Famiglietti and Wood (1994) give all relevant equations. For completeness, we mention here the most important.

The unsaturated zone consists of a root zone and a transition zone. The latter only exists if the water table depth H [L] is larger than the (fixed) depth of the rootzone d_{rz} [L]. Dependent on H (for each time step provided by hsB or TOPMODEL), therefore, three cases can occur:

1. The capillary fringe is located beneath the rootzone, i.e. $(H + \psi_{ae}) > d_{rz}$.
2. The capillary fringe is located in the rootzone, i.e. $(H + \psi_{ae}) \leq d_{rz}$.
3. The capillary fringe is located at the surface, i.e. total saturation takes place

Here, ψ_{ae} is the air entry pressure, expressed as a height of water [L]. Recharge is simulated as the net flux of drainage from the transition zone (rz , case 1) or the root zone (tz , case 2) to the water table and capillary uprise. Drainage $Q_{rz,tz}$ [$L T^{-1}$] is driven by gravity only and given by:

$$Q_{rz,tz} = K_s \left(\frac{\theta_{rz} - \theta_{res}}{\theta_{sat} - \theta_{res}} \right)^{2b+3}, \quad (6.6)$$

where θ_{rz} , θ_{tz} , θ_{res} and θ_{sat} are respectively the root zone, transition zone, residual and saturated moisture contents [-]. K_s is the saturated conductivity [$L T^{-1}$] and b is a pore size distribution index

[-], as used in the description by *Campbell* (1974). We employ K_{sat} , b and ψ_{ae} as given for different soil types by *Clapp and Hornberger* (1978). Capillary uprise Q_{cap} [L T⁻¹] takes place from the saturated zone directly to the root zone and is parameterized using the Gardner-Eagleson parameterization, similar to *Eagleson* (1978):

$$Q_{cap} = \alpha K_s \left(\frac{-\psi_{ae}}{H} \right)^{2b+3}, \quad (6.7)$$

where $\alpha = 1 + \frac{1.5}{\beta-1}$ and $\beta = 2 + 3/b$. Infiltration I [L T⁻¹] into the root zone is defined by *Milly* (1986) as follows:

$$I = \min [\max ((TF - ET_{pot}), 0), I_c] \quad (6.8)$$

where TF is throughfall [L T⁻¹], ET_{pot} is the potential evaporation [L T⁻¹], and I_c is infiltration capacity [L T⁻¹]:

$$I_c = 0.5K_u \left[1 + \left(-1 + \sqrt{1 + \frac{2K_s F_i}{S_o^2}} \right)^{-1} \right], \quad (6.9)$$

where K_u [L T⁻¹] is the hydraulic conductivity evaluated at the “rewetted moisture content” (porosity minus entrapped air fraction), F_i cumulative infiltration depth during a given storm period [L] and S_o is the sorptivity [L T^{-1/2}], also obtained from *Clapp and Hornberger* (1978).

Three types of evaporation are distinguished: canopy (interception) evaporation, transpiration and bare soil evaporation. Based on the interception storage w_c [L], vegetation is divided in a wet and a dry fraction by (*Deardorff*, 1978):

$$\omega_{wc} = \left(\frac{w_c}{w_{cmax}} \right)^{2/3}, \quad (6.10)$$

where ω_{wc} is the fraction of wet canopy [-] and w_{cmax} is the storage capacity [L], which is linearly related to the Leaf Area Index (LAI) with a coefficient of 0.2 mm. Actual canopy evaporation is then defined as the minimum of potential canopy evaporation and the w_c . For the calculation of actual transpiration we adopt the method described in *Teuling and Troch* (2005), using a stress function β :

$$\beta = \max \left[0; \min \left(1, \frac{(\theta_{rz} - \theta_w)}{(\theta_c - \theta_w)} \right) \right], \quad (6.11)$$

where θ_w is wilting point soil moisture [-] and θ_c is the critical soil moisture content above which there is no soil moisture stress [-]. Actual transpiration E_T [L T⁻¹] now is (*Teuling and Troch*, 2005):

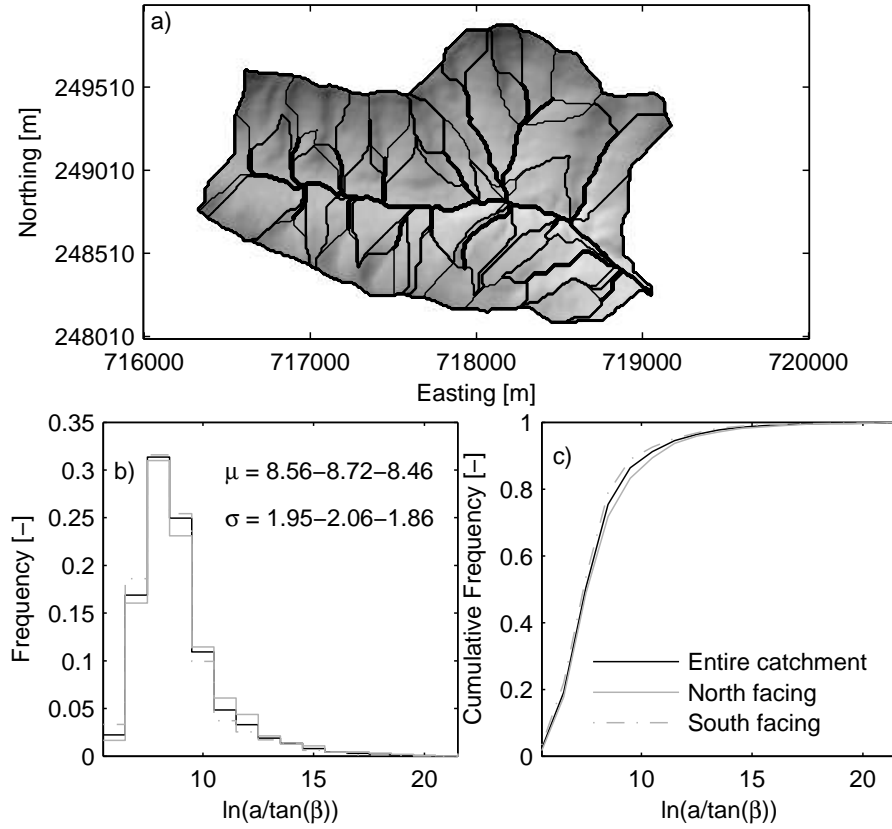


Figure 6.3: Partitioning of the catchment in (a) hillslopes and (b) three distributions of values for the topographic index $\ln(a/\tan\beta)$ representing respectively the entire catchment, all northfacing and all southfacing pixels. In (c), cumulative distributions are shown. In addition, in (b) the average values (μ) and standard deviations (σ) are shown for, from left to right, all pixels, all northfacing pixels and all southfacing pixels.

$$E_T = (1 - \omega_{wc})F_r\beta(1 - e^{-cLAI})E_{T_{pot}}, \quad (6.12)$$

where F_r is the root fraction in the root zone [-], c is a light use efficiency parameter [-], and $E_{T_{pot}}$ is potential transpiration [$L T^{-1}$]. Potential rates for transpiration and canopy evaporation are obtained from solving the energy balance. Using air temperature as an initial guess, latent (E) and sensible heat (H), as well as net radiation R_{net} are calculated and iterated until the energy balance ($R_{net} = E + H$) closes. Using the resulting temperature, re-calculating the latent heat flux yields the potential transpiration and canopy evaporation (in this case the stomatal resistance is set to zero). For further information we refer to *Famiglietti and Wood (1994)*.

6.4 Methodology

The models described in Section 6.3 are now applied to the Rietholzbach catchment at different spatial scales to investigate the effect of small-scale heterogeneity. We base our analysis on a DEM with a spatial resolution of 10 meters. Using software developed for terrain analysis by *Tarboton* (1997), we extract slope gradient, flow direction (hillslope aspect) and contributing area. We thus have a topographic index value for each DEM pixel. All values of the topographic indices are then binned in integer values of $\ln(a/\tan\beta)$. The resulting distribution is used as the “aggregated” case for TOPMODEL and TOPLATS. Because the Rietholzbach is flowing from west to east, thus dividing the catchment in a north-oriented and a south-oriented slope (Figure 6.1), an open book approach of two opposing hillslopes seems a proper approximation. All north- and southfacing DEM pixels are thus grouped to form two distributions of topographic indices, for which incoming radiation is corrected for slope and aspect separately. This is described in more detail in Section 6.4.1. Finally, TOPMODEL is applied in such a way that each individual pixel of the DEM is assigned a moisture deficit D (Equation 6.2). Figure 6.3 shows a map of the resulting hillslopes and the three (northfacing pixels, southfacing pixels and the entire catchment) distributions of topographic index values.

hsB and hsB-LATS are applied at four aggregation levels: (1) one aggregated hillslope folded around the channel network, (2) the catchment as an “open book”, i.e., a north- and a southfacing slope, (3) all hillslopes individually, and (4) classes of geometrically similar hillslopes. Again, incoming radiation is corrected for the slope and aspect of each hillslope (Section 6.4.1). Delineation and classification of hillslopes is described in Section 6.4.2.

Each hillslope or topographic index-class is assigned a dominant vegetation type (for coupled models only), a mean aspect (exposure) and slope. Vegetation parameters for the different vegetation types are similar to those used in the VIC-model and were obtained from the VIC-website¹. In winter, usually snow is present in the catchment. To account for this in a simple way, snowmelt is modeled using the degree-day method (*Martinec and Rango*, 1986; *Kustas et al.*, 1994), where the degree day factor is set to $0.0035 \text{ mK}^{-1}\text{d}^{-1}$ (*Martinec and Rango*, 1986). Figure 6.4 shows a comparison between SWE (snow water equivalent) as simulated by the degree-day method and the VIC model, which solves the energy balance for the snow pack. In addition, observed snow depths are shown.

To isolate the influence of the spatial scale of model application, the same sets of model parameters are used for all model simulations for each model. TOPMODEL and VIC were calibrated using the period 2000–2002, whereas 1999 was used for model initialization and 2003 for validation. Results of calibration and validation can be found in Figure 6.5. Because in the hsB model no unsaturated zone was taken into account, it is not directly comparable to TOPMODEL and VIC and its parameters are not transferable to the coupled version (hsB-LATS). Moreover, because running the coupled models (hsB-LATS and TOPLATS) is numerically more demanding and the models requires more parameters,

¹<http://www.hydro.washington.edu/Lettenmaier/Models/VIC/>

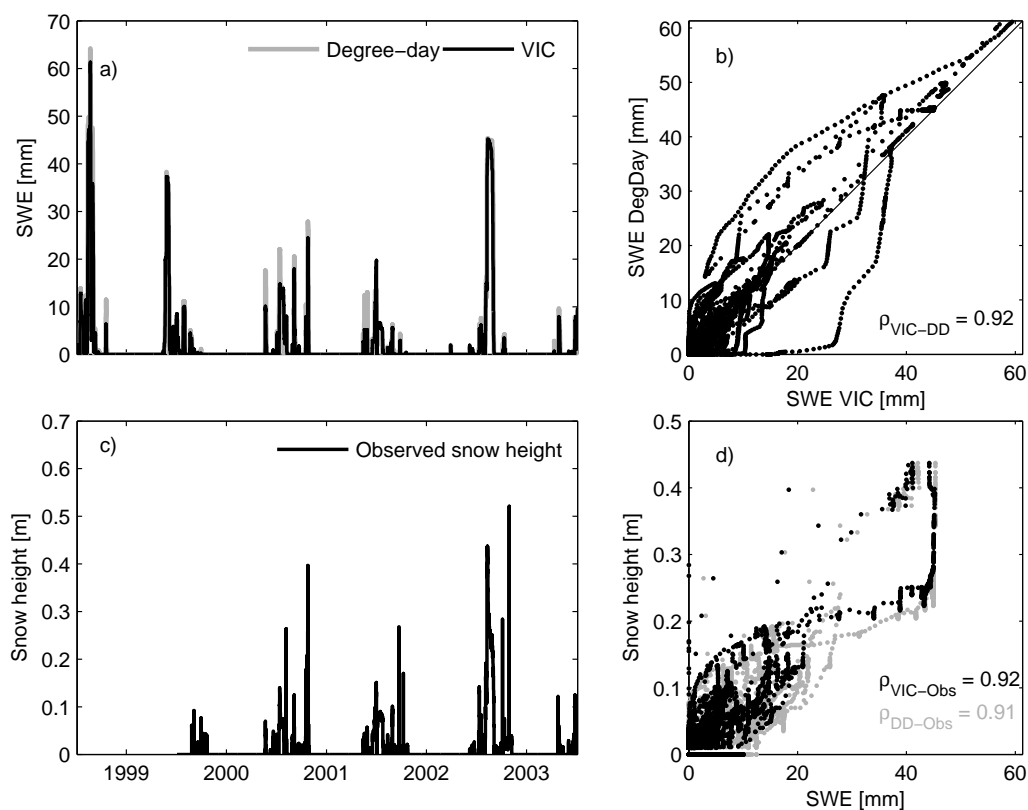


Figure 6.4: Time series (a) and scatter plot (b) of snow water equivalent as modeled by the VIC model and the degree day method that was implemented in the other models. Observed snow depths are shown in c), and a scatterplot between both modeled time series and the observations are shown in d). Note that observations do not cover the entire period of analysis.

it is not feasible to calibrate them in the current study. hsB and hsB-LATS are therefore not calibrated and the default parameter values are used. Because model parameters would mainly influence the timing of peaks and the relative contributions of surface runoff and baseflow, further analyses will focus on monthly values. The hsB model is forced by recharge, which is calculated as the difference between rainfall plus snow melt and potential evapotranspiration (i.e., no water-limited evaporation occurs).

6.4.1 Correction for hillslope exposure

Incoming long- and shortwave radiation are corrected for hillslope orientation using the “conversion factor” approach (Uijlenhoet, 1992). A correction factor is applied to direct insolation, based on (1) a binary factor that determines whether the slope is in the shadow or not, and (2) the ratio of the cosine

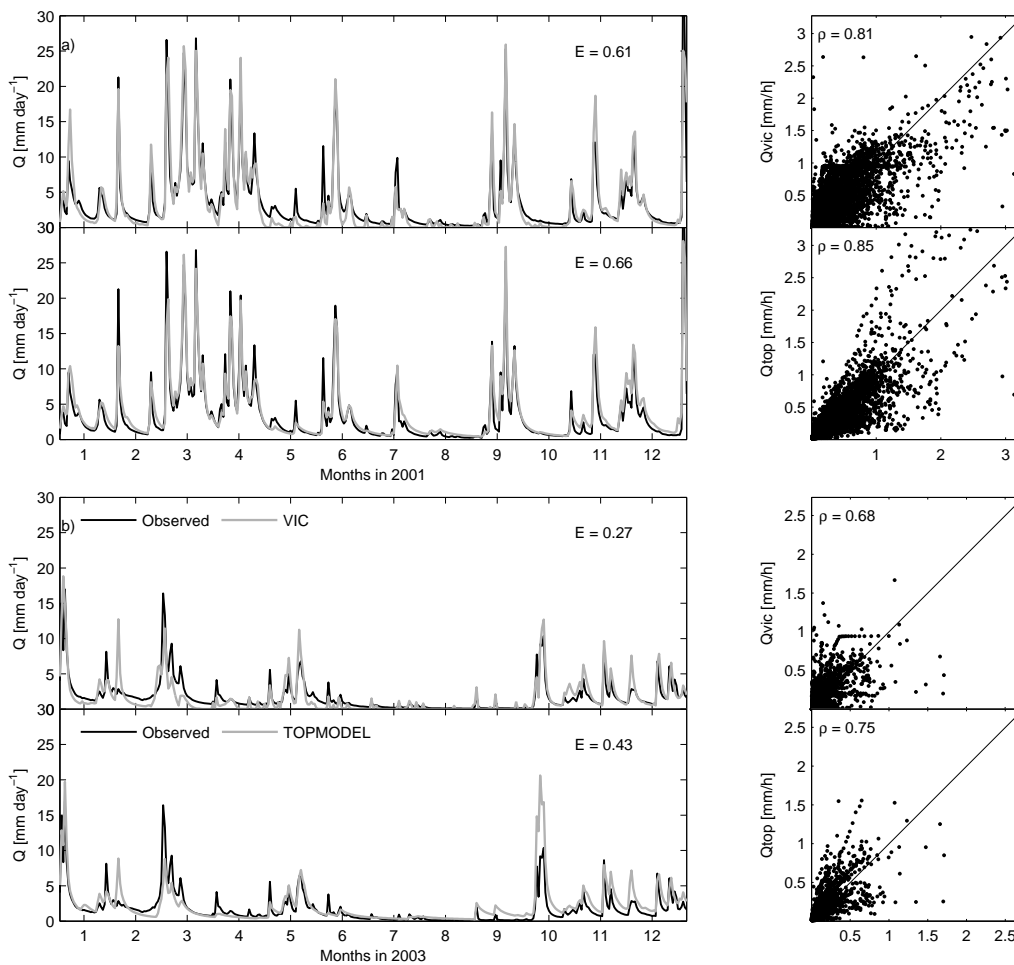


Figure 6.5: Calibration and validation results for part of the calibration period (a, 2001) and the validation period (b, 2003), for VIC (upper panels) and TOPMODEL (lower panels). Nash-Sutcliffe modeling efficiencies are displayed as E . Next to each time series, the corresponding scatterplot and correlation coefficient are shown. For visibility, the time series in a) and b) are plotted in terms of daily values.

of the incidence angle at the slope to that of the incidence angle at an imaginary horizontal surface at the same location. For diffuse radiation, the correction factor depends on the “sky view factor”, which is, analogous to the correction factor for direct insolation, the ratio of the integrated sky radiance at the slope to that of the sky radiance at an imaginary horizontal surface. This factor is calculated using the simplification that the catchment can be regarded as an infinitely long V-shaped valley, where the opposite slope has an inclination equal to that of the slope under consideration (Uijlenhoet, 1992). Given the shape of the catchment (Figure 6.1), this approximation seems reasonable. Figure 6.6 shows

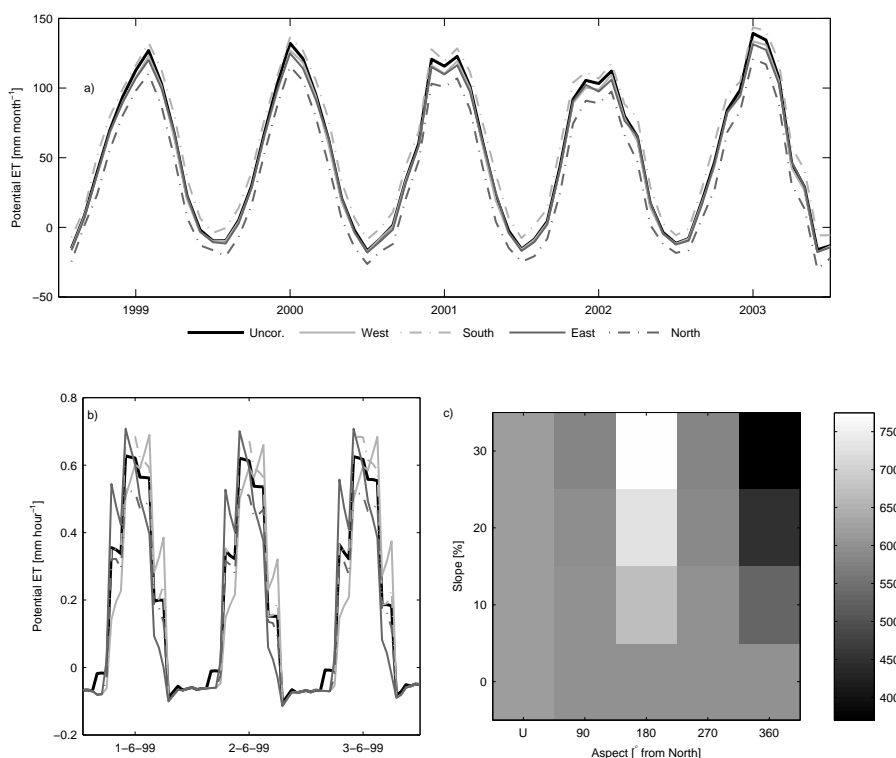


Figure 6.6: Correction of potential evaporation ET_p for hillslope exposure. Monthly ET_p without correction and with correction for four different aspects (north, south, east, west) and constant slope (20%) are shown in a). In b), the same is shown for hourly ET_p over three days. Note that radiation data was available at a temporal resolution of 3 hours. In c), finally, the influence of slope and aspect on average annual potential evaporation (in mm) is shown. In c), U denotes uncorrected evaporation.

the resulting corrected potential evaporation for various slopes and exposures.

6.4.2 Hillslope delineation and classification

From the digital elevation model, individual hillslopes were delineated using the algorithms developed by *Tarboton (1997)* and *Bogaart and Guardiola (2007)*. In this method, first the channel network is defined from the field of contributing areas, using a critical value of $50,000 \text{ m}^2$ (i.e., all values higher than that value are assumed to be part of the channel network). This value was chosen to visually match the channel network on a topographic map. Around the channel network, three kinds of “bank” pixels are defined: left banks, right banks and headwaters. Using a map of flow distances, all pixels draining to a specific bank are grouped as being a hillslope, of which then the corresponding

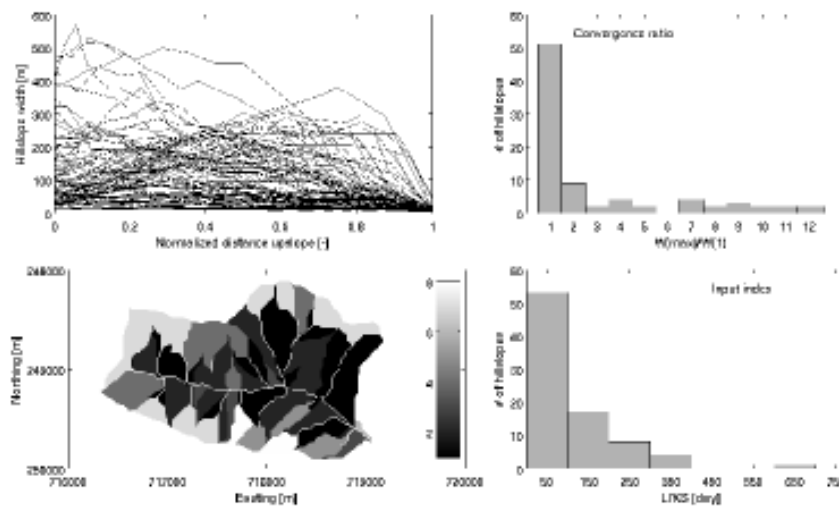


Figure 6.7: Distributions of the convergence ratio (CR) and input index (L/KS) as defined by *Aryal et al.* (2002). From the upper left are shown, in clockwise direction: the width functions of all hillslopes; the distribution of CR ; the distribution of L/KS and a map of all resulting hillslope types (see Table 6.1).

width function for modeling in hsB is calculated (*Bogaart and Troch, 2006*).

As was briefly mentioned in Section 6.1, different approaches to define similar hillslopes have been developed. For example, *Berne et al.* (2005) derived a relationship between the so-called Péclet number (representing the ratio between advective and diffusive flow, which depends on the hillslope's geometry) and the moments of the recession hydrograph. Because the slopes in the Rietholzbach are relatively steep and practically all flow will be advective, the Péclet number will probably not be the most suitable hillslope similarity index. *Aryal et al.* (2002) defined three dimensionless similarity parameters: a convergence ratio (CR), defined as the hillslope width at the ridge divided by the width at the outlet; a profile factor B , representing the degree of concavity or convexity; and a parameter $(q/Z)(L/KS)$ or input index. Because no information is available about net drainage (q) and soil depth (Z) for each specific hillslope, and each hillslope has a uniform slope, we discard the first factor of the latter parameter (q/Z) and B . We thus calculate two parameters for each slope: CR and L/KS , of which the latter is no longer dimensionless. In this parameter, L is the length of the hillslope, K is the saturated conductivity, and S is the slope. As can be seen in the upper left panel of Figure 6.7, all width functions, also the convergent ones, tend to decrease toward the ridge. Therefore, the calculation of CR is slightly modified: instead of the hillslope width at the ridge we use the maximum width. A value of CR close to one thus yields divergent or uniform hillslopes; a higher value indicates convergent hillslopes. The resulting distributions of CR and L/KS are shown in the right hand panels of Figure 6.7. As a (rather arbitrary) division we selected nine classes, based on different combinations of CR and L/KS . The classification can be found in Table 6.1. A map containing the

Table 6.1: Division of all 84 hillslopes in to 9 classes based on combinations of CR and L/KS (Figure 6.7).

	L/KS	100	L/KS
	\leq	$< L/KS \leq$	$>$
	100	300	300
$CR \leq 2$	1	2	3
$2 < CR \leq 7$	4	5	6
$CR > 7$	7	8	9

resulting classes can be found in the lower left panel of Figure 6.7.

6.5 Results

Figure 6.8 shows monthly values of actual evapotranspiration and discharge as simulated by all models in their aggregated version. In addition, the differences between the discharge simulations and the observations are shown. hsB and TOPMODEL both use potential evaporation as calculated by the Penman-Monteith equation (Penman, 1948; Monteith, 1965) as input. Due to an overestimation of the amount of dew this potential evaporation is too low in winter. In addition, they are identical for hsB and TOPMODEL because in winter no water limitation occurs. Because water limitation was assumed not to occur in hsB, summer evapotranspiration is slightly overestimated. This overestimation with respect to the lysimeter observations is relatively small (on average about 10 mm per month), indicating that evaporation is mainly energy limited. The VIC model also slightly overestimates summer evaporation, but winter evaporation is simulated accurately. The other models solving the energy balance (hsB-LATS and TOPLATS) accurately simulate winter evaporation as well. Summer evaporation as simulated by the latter models on the other hand is similar to that modeled by TOPMODEL and significantly lower than observed, suggesting that the soil moisture reservoir in these models is too small and water limited evaporation occurs too early.

Monthly values of discharge are reasonably close to the observed values, confirming that the model calibration does not have a large influence on monthly values. This is further illustrated by Table 6.2, where the performance of all models is summarized. Nash-Sutcliffe modeling efficiencies (E , Nash and Sutcliffe, 1970) at monthly time steps are high (close to 0.8) for nearly all models except TOPLATS, which appeared to have some initialization problems. In addition, Figure 6.9 shows the monthly dynamics of other relevant variables, together with observations (when available). Observations are available at one point (Bühl, Figure 6.1). Soil moisture observations were averaged over the three available depths (Figure 6.2), and for groundwater only the dynamics should be compared because the reference levels of the various water tables are different. For recharge and baseflow, all models agree quite well, the dynamics are practically the same. For comparison with recharge, the lysimeter

Table 6.2: Summary of model performances of all models employed in this study. The Nash-Sutcliffe modeling efficiency (E), correlation coefficient (ρ), and the relative volume error (RVE) are shown for hourly, daily and monthly timesteps. The uncoupled hsB model and TOPMODEL were run with (C) and without (U) correction for hillslope exposure.

			Hourly		Daily		Monthly		
			E	ρ	E	ρ	E	ρ	RVE
			[-]	[-]	[-]	[-]	[-]	[-]	[%]
VIC			0.61	0.80	0.74	0.87	0.83	0.93	-7.42
hsB	One slope	U	0.37	0.63	0.44	0.69	0.75	0.90	14.04
		C	0.35	0.63	0.41	0.68	0.64	0.89	24.99
	Two slopes	U	0.48	0.70	0.56	0.76	0.76	0.90	13.54
		C	0.46	0.70	0.54	0.76	0.66	0.90	24.40
	All slopes	U	0.53	0.74	0.64	0.81	0.76	0.90	14.64
		C	0.51	0.73	0.61	0.80	0.66	0.90	25.20
	Classes	U	0.48	0.70	0.57	0.77	0.76	0.90	14.19
		C	0.49	0.71	0.58	0.77	0.76	0.90	13.79
TOPMODEL	One distr.	U	0.72	0.87	0.80	0.91	0.81	0.92	8.71
		C	0.72	0.88	0.79	0.92	0.77	0.91	14.49
	Two distr.	U	0.72	0.87	0.80	0.91	0.81	0.92	8.71
		C	0.72	0.87	0.80	0.91	0.81	0.92	9.26
	All pixels	U	0.72	0.87	0.80	0.92	0.81	0.92	8.71
		C	0.72	0.88	0.79	0.92	0.77	0.91	14.49
TOP-LATS	One dist.	C	0.21	0.63	0.46	0.73	0.32	0.68	-14.24
	Two dist.	C	0.25	0.63	0.48	0.73	0.34	0.69	-14.77
hsB-LATS	One slope	C	0.30	0.55	0.37	0.61	0.76	0.87	-2.62
	Open book	C	0.34	0.59	0.42	0.65	0.77	0.88	-2.19
	All slopes	C	0.44	0.67	0.52	0.73	0.77	0.88	-5.18
	Classes	C	0.40	0.64	0.48	0.70	0.77	0.88	-6.01

drainage is plotted as well. Again the dynamics agree well, although simulated recharge is generally somewhat lower than the lysimeter drainage.

The volumetric soil moisture content for TOPMODEL is estimated from the root zone storage deficit assuming a porosity of 40%. Because the storage deficit is generally zero in winter, the moisture content is often equal to the porosity. This is in accordance with evaporation, which is at the potential rate in winter (Figure 6.8). VIC and TOPMODEL show similar dynamics, although more pronounced for TOPMODEL as explained above. The range in the observed soil moisture is much smaller, except for a sudden (and rather suspicious) decrease in the summer of 2003 (Figure 6.2). TOPMODEL and VIC

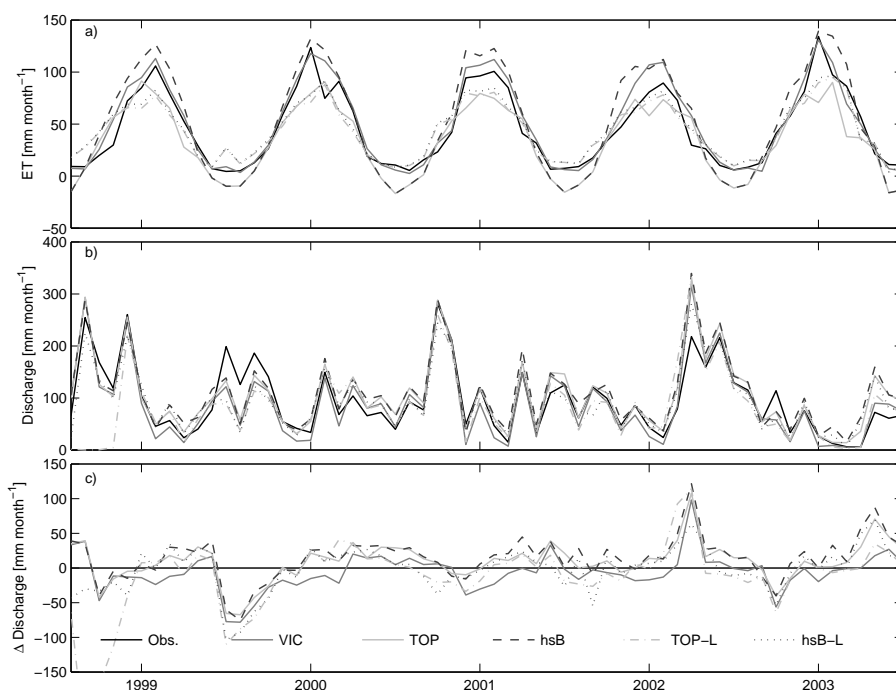


Figure 6.8: Monthly evapotranspiration (a) and discharge (b) as simulated by five models: hsB, hsB-LATS, TOPMODEL, TOPLATS and VIC. All models were used in their aggregated version, i.e., one hillslope for hsB(LATS) and one distribution of topographic indices for TOPMODEL/LATS. In c), differences between modeled and observed discharge are shown. Observed evaporation is measured by the lysimeter.

show this strong decrease as well, although slightly smoother. Soil moisture contents in TOPLATS and hsB-LATS stay rather constant and do not show any decrease in 2003. Observations of water table depth show an increasing trend until 2002, which is not captured by any of the models. Seasonal and intra-seasonal dynamics are similar for all models. Not surprisingly, the simulated water tables for hsB and hsB-LATS, and TOPMODEL and TOPLATS are very close together. Finally, for surface runoff the dynamics are similar across the models, only TOPLATS exhibits much stronger peaks for the extreme precipitation events.

Subsequently, the differences between the various levels of spatial aggregation for the different models are investigated, using the aggregated results that are shown in Figures 6.8 and 6.9 as the reference. Figures 6.10, 6.11, 6.12, and 6.13 show differences between the aggregation levels for respectively TOPMODEL, hsB, hsB-LATS and TOPLATS. Figure 6.10 shows differences for simulations with and without a correction for hillslope exposure, to isolate the effect of spatial aggregation. For TOPMODEL, it was not feasible to correct the potential evaporation for every individual DEM-pixel. Therefore, the simulations for every pixel and the distribution representing the entire catchment are both corrected

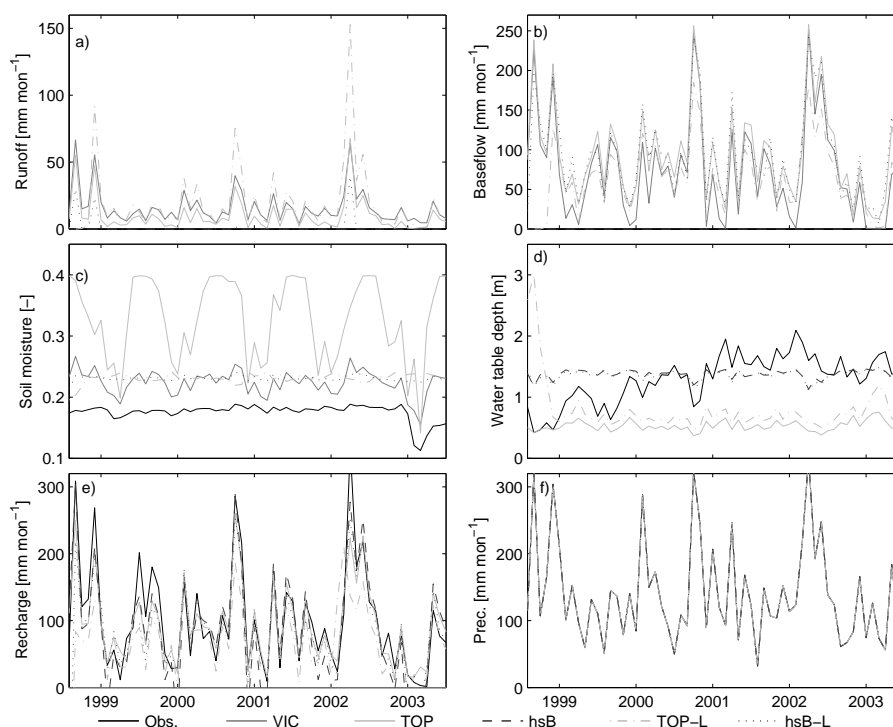


Figure 6.9: Monthly dynamics of other variables as simulated by five lumped models and observations (when available): surface runoff (a), baseflow (b), soil moisture (c), groundwater table (d), recharge (e) and precipitation (f). Note that not all variables are simulated by all models, and no observations are available for surface runoff and baseflow.

using the spatially averaged aspect. If no correction is applied, the changes in discharge appear to be very small (typically less than 1%). This was to be expected, because all distributions of topographic indices are very similar (Figure 6.3). When the correction for exposure is applied, overall evapotranspiration increases, causing an overall decrease of discharge. This, again, was to be expected given the larger area of the southfacing distribution compared to the northfacing one (Figure 6.3). The decrease in discharge can be attributed to similar decreases in both surface runoff and baseflow. Interestingly, even when no correction for exposure is applied, the ratio between surface runoff and baseflow is significantly different (up to 10%) between the simulation of one distribution and of all individual pixels. This difference is, however, much smaller compared to the differences that are caused by hill-slope exposure. This is caused by small-scale variability: the much larger variability of soil moisture contents in the unsaturated zone reservoirs in the simulation for individual DEM-pixels (over 33000 DEM pixels compared to only 17 classes in the distribution; Figure 6.3) apparently causes more local runoff, because this variability is “smoothed” in the lumped simulation. When aggregated to monthly values the increase in recharge and baseflow offsets this increase in runoff. It should be noted that relative differences are shown, so the large range in relative differences in surface runoff is compensated

by the (apparently) much smaller range in relative differences of baseflow. Also at hourly timesteps, however, the difference is too small to affect the hydrograph, because the statistics in Table 6.2 are identical for all TOPMODEL simulations.

Figure 6.11 shows the differences in monthly discharge for simulations of two hillslopes (“open book”), all 84 hillslopes, and the nine classes of similar hillslopes (Table 6.1) with respect to the aggregated reference case. Again, results are compared with and without correcting for hillslope exposure. In this case, each individual hillslope is corrected for its exposure, as opposed to the individual pixels in TOPMODEL. Similar to TOPMODEL, the changes in catchment-average discharge are small (typically within $\sim 5\%$) compared to the single hillslope-case. Only in very dry conditions, when there is barely any discharge, the relative difference increases. Examples are the late summer of 2003 and the early summer of 2000 (Figure 6.8). The catchment-averaged discharge for hillslope classes is generally lower than that of the other simulations, due to higher evaporation (not shown). The reason is that the majority of hillslopes that were taken as representative for their class were located at the southfacing side of the catchment. When no correction is applied, the average of the classes is similar to that of the open book and all hillslopes, illustrating the relatively large effect of hillslope exposure. Where the differences between spatially averaged discharges at a monthly scale are negligible, they are not at hourly and daily time steps, as can be seen in Table 6.2. Here, the resulting model efficiencies and correlation coefficients are significantly lower for the aggregated hillslope than for the other simulations ($E = 0.35$ vs. $E = 0.51$ for individual slopes). According to these statistics, the “open book”-simulation and the classes of similar hillslopes both proved to be better “aggregators”, with E values of 0.46 and 0.49 respectively. This is the case with and without the correction for hillslope exposure.

The coupled models (TOPLATS and hsB-LATS) were applied in a similar way as TOPMODEL and hsB. Results for hsB-LATS can be found in Figure 6.12. As opposed to the uncoupled models, absolute instead of relative differences are shown for better visibility. In addition to the weighted averages of discharge and evapotranspiration, the variability across individual hillslopes and classes of similar hillslopes is shown. This variability is highly asymmetrical towards higher values for evaporation and low values for discharge. This is caused by different land cover types, that were introduced in the coupled models. Forested hillslopes evaporate significantly more than hillslopes with pasture land. Because over the entire catchment the fraction of pasture land is much larger than that of forest (76% vs. about 20%; see Figure 6.1b), this effect is relatively small but still significant in the catchment averaged values. The inclusion of different land use types, therefore, causes structurally higher evapotranspiration and lower discharge in the simulations for individual hillslopes and classes compared to the open-book and aggregated hillslopes. The reduction of 84 to 9 hillslopes by our (although quite rude) classification yields practically the same results as the case where all individual hillslopes are compared, both in terms of the catchment average and the variability across hillslopes. The same holds for surface runoff, baseflow and the groundwater table, where the changes between the open book simulation and the aggregated case on one hand, and the individual hillslopes and classes on the other

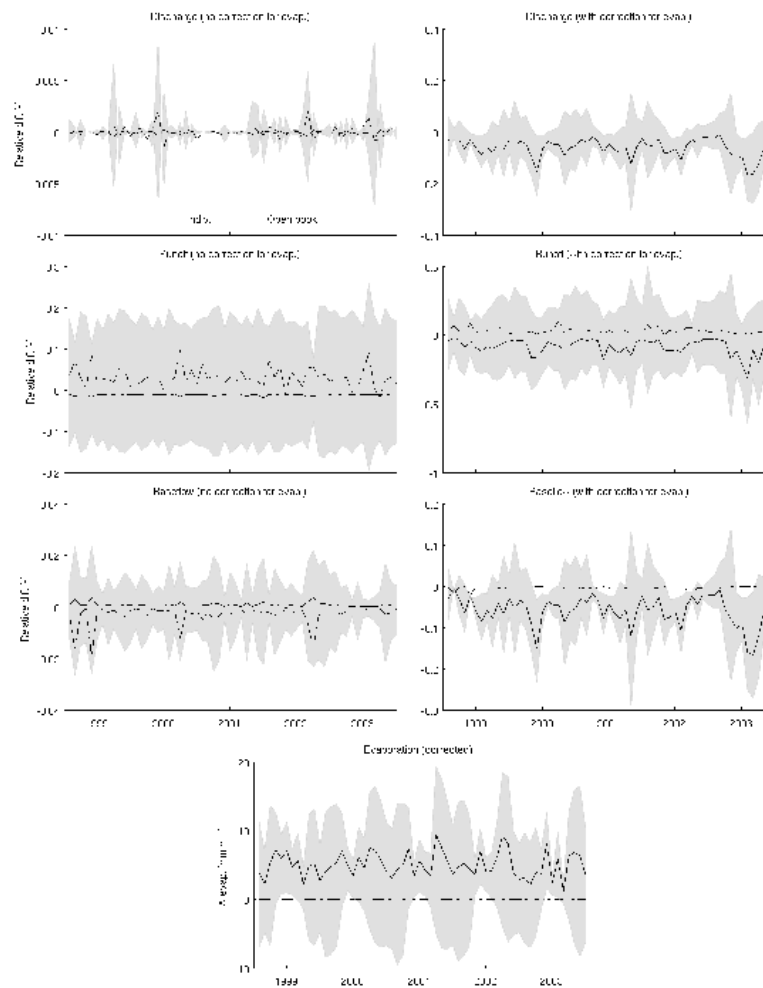


Figure 6.10: Differences in, from top to bottom, discharge, surface runoff, baseflow, and evaporation as simulated by TOPMODEL. In the left panels, evaporation is corrected for exposure, in the right panels this is not the case. The reference situation is the “aggregated” version (one distribution of topographic indices; Figure 6.8). Differences with respect to this reference are shown for the simulation where all DEM-pixels have their own unsaturated zone reservoir (dash-dotted lines), and the weighted average of the distributions containing north and southfacing pixels (solid lines). The shaded area indicates the difference between the simulated discharge for the distributions of northfacing and southfacing pixels. Negative values indicate lower values than the reference.

hand, show opposite signs. Surface runoff and baseflow for the open-book simulation only differ during extreme precipitation events (see Figure 6.8), so relative differences are negligible. However,

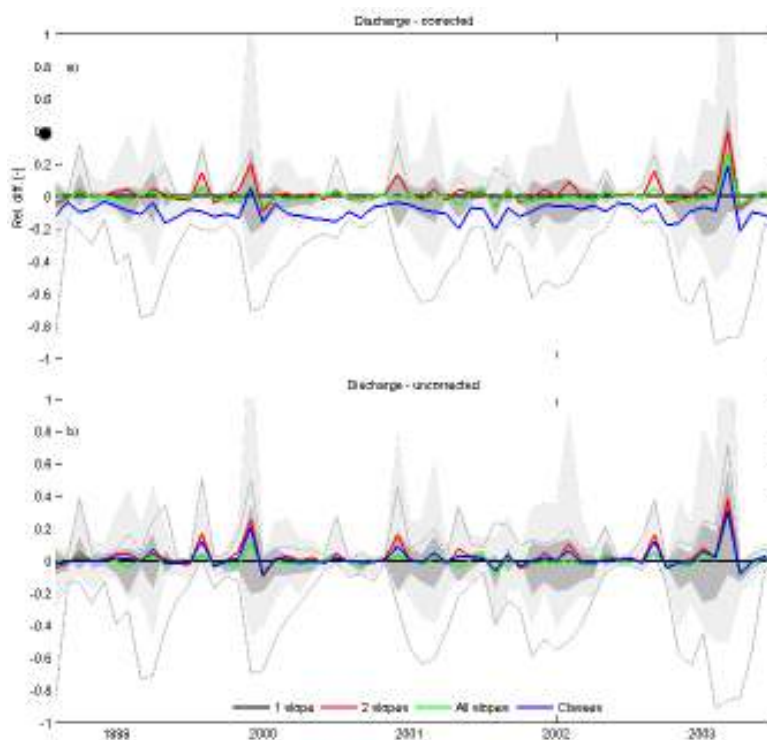


Figure 6.11: Differences in discharge as simulated by different versions of the hsB model. The reference is the hsB simulation of one aggregated hillslope (Figure 6.8). Differences are shown for the weighted average of the “open-book” simulations (north- and southfacing hillslopes), the weighted average of all individual hillslopes, and that of classes of similar hillslopes. Negative values indicate lower values than the reference. The light-shaded area represents the 10th and 90th percentiles of the individual hillslopes, the dark-shaded area indicates the range between the north- and southfacing slopes and the thin grey lines indicate the range of hillslope classes (see text for details).

simulation of individual hillslopes and classes yields more surface runoff, similar to TOPMODEL. Changes in surface runoff are offset by those in baseflow at monthly scales, again as was the case for the TOPMODEL simulations that were described before. These changes are practically identical for the simulations of individual hillslopes and the classes of hillslopes. The Nash-Sutcliffe values in Table 6.2 are, however, slightly higher for the open-book simulation (0.34 vs. 0.30 for the aggregated hillslope). For the individual slopes and classes, the Nash-Sutcliffe values are, similar to hsB, significantly higher: 0.44 and 0.40 respectively. Changes in moisture content and groundwater table are structural, but very small. It is not clear why the changes in soil moisture have opposite signs for individual hillslopes and hillslope classes. Similar results for TOPLATS can be found in Figure 6.13. For the coupled version of TOPMODEL, simulations where the unsaturated zone model is resolved

for each individual DEM pixel were not performed. Because the changes in discharge and evapotranspiration in the uncoupled TOPMODEL were very small, we expect that to be the case for the coupled model as well. Indeed, in Figure 6.13 a similar structural increase in evaporation and decrease in discharge can be seen as in Figure 6.10 when the open-book simulation is considered. For other variables, differences are again very small.

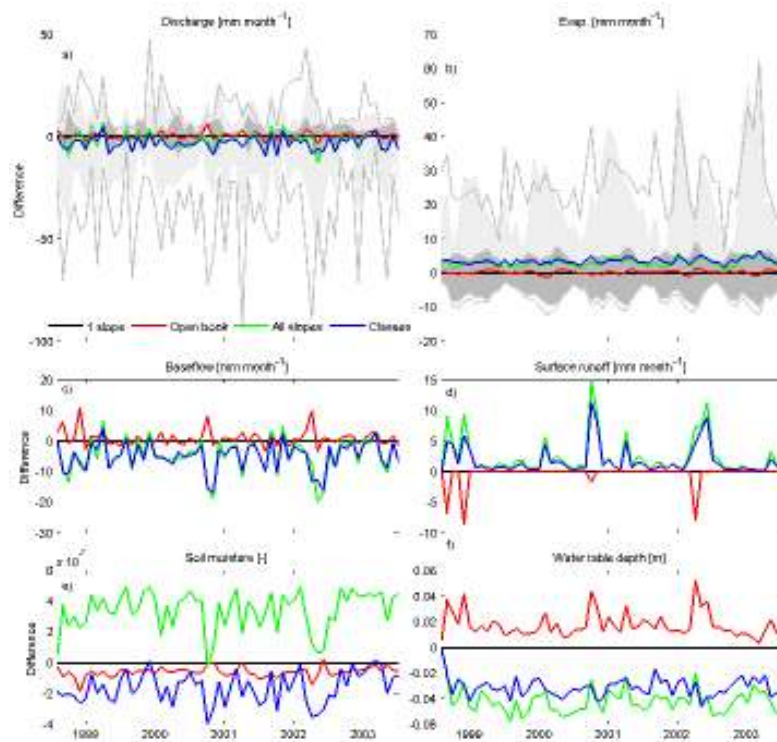


Figure 6.12: Differences in six variables as simulated by different versions of hsB-LATS. The reference is the simulation of one aggregated hillslope (Figure 6.8). Differences are shown for the weighted average of the “open-book” simulations (north- and southfacing hillslopes), the weighted average of all individual hillslopes, and that of classes of similar hillslopes. In a) and b), a light-gray shades represent the 10th and 90th percentiles of all individual hillslopes, and dark-gray shades represent the difference between the northfacing and southfacing slopes. Thin grey lines, finally, indicate the range of hillslope classes (Table 6.1 and Figure 6.7). Negative values indicate lower values than the reference.

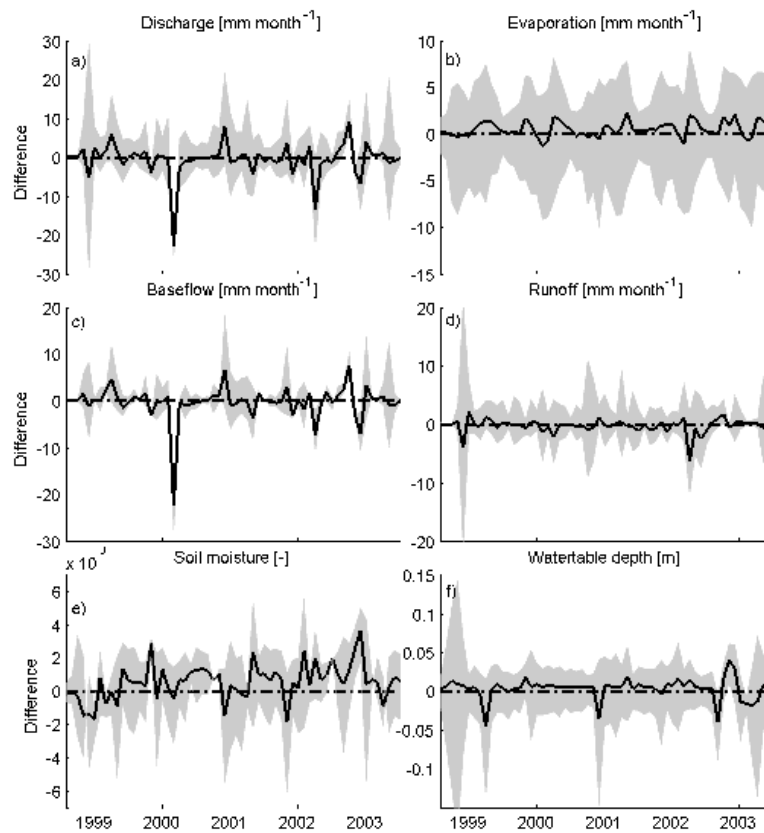


Figure 6.13: Differences in six variables as simulated by different versions of TOPLATS. The reference is the simulation of one distribution of values for the topographic index representing the entire catchment. The black line indicates the difference with the weighted average of the simulations for the distributions representing the northfacing and southfacing pixels. The shaded area represents the range between the latter two distributions. Negative values indicate lower values than the reference.

6.6 Summary and conclusions

In the present study, a hillslope-based parameterization of small-scale heterogeneity is developed and compared to other catchment parameterizations. The method is based on the hillslope-storage Boussinesq model, that simulates saturated zone dynamics in a numerically efficient way, and takes into account both advective and diffusive flow. The model is coupled to a similar formulation for the unsaturated zone and energy balance as the TOPLATS land surface scheme to make it appropriate for a land surface modeling context, and then applied to the small, alpine Rietholzbach catchment. To investigate the influence of spatial aggregation on the model results, the method was applied at four “aggregation levels”: (1) one large hillslope folded around the channel network; (2) two hillslopes

(“an open book”); (3) nine classes of similar hillslopes, based on similarity parameters as defined by *Aryal et al.* (2002), and (4) all individual hillslopes. This hillslope-based approach is compared with the TOPMODEL approach, where pixels with similar hydrologic behavior are classified from a DEM and the Variable Infiltration Capacity (VIC) approach, where a statistical relation between the fraction of saturated area and the infiltration capacity is employed. TOPMODEL is also applied at three levels of spatial aggregation: (1) one distribution of topographic indices; (2) two distributions, one representing all northfacing pixels and one representing all southfacing pixels, and (3) all individual DEM pixels.

The hsB approach relaxes some assumptions that TOPMODEL requires. First, TOPMODEL assumes that saturated zone dynamics can be described by successive steady-states. For small time steps this is reasonable, but for larger time steps this may introduce errors. In this study, however, a fixed time step of one hour was used for all models and the effect of this assumption was not investigated. Second, TOPMODEL only takes into account advective or kinematic, and not diffusive flow. In this study, however, this assumption is perfectly reasonable to make, because practically all hillslopes in the Rietholzbach are very steep (20 to 30%). It would, therefore, be interesting to repeat this analysis in another catchment with less steep, or even flat, slopes. In that case diffusive flow, which is taken into account by hsB, would be much more important.

There are some issues that would require more research to make a hillslope-based parameterization useful. Especially compared to numerically efficient approaches like VIC or TOPMODEL, the hsB-LATS model is numerically quite demanding in the current formulation (programmed in Matlab). Efficient programming in another computer language could significantly reduce run times. Furthermore, when the model is applied in areas such as the Rietholzbach with steep slopes, an analytical solution for the kinematic wave approximation as developed by *Troch et al.* (2002) would yield practically identical results. In addition, the amount of hillslope classes could probably be further reduced when carefully selecting similarity parameters. In less steep areas, for example, the Péclet number, which represents the ratio of diffusive and advective flow (*Berne et al.*, 2005; *Lyon and Troch*, 2007) could be used. In this study, a rather arbitrary classification based on parameters proposed by *Aryal et al.* (2002) was carried out. It would be worthwhile to further compare such similarity parameters in different areas and under different conditions.

When catchment-averaged streamflow is considered, the effect of hillslope exposure is larger than that of the level of spatial aggregation. When no correction for exposure is employed, the streamflow is practically the same for all aggregation levels. When surface runoff and baseflow are considered separately, however, it appears that there is more surface runoff when individual pixels are simulated than when they are grouped in distributions. The same holds for individual hillslopes versus aggregated hillslopes. At monthly time steps, this effect does not show up in the total discharge because it is offset by the lower baseflow. At hourly and daily time steps, however, model efficiencies and correlation coefficients suggest differences: the simulation of individual hillslopes achieves considerably

higher efficiencies than the simulation with one large hillslope (0.52 vs. 0.36 respectively, at hourly time steps). Inclusion of the unsaturated zone and energy balance enables more accurate simulation of monthly evaporation, but this does not show up in the resulting discharge: modeling efficiencies are quite low. Also in hsB-LATS, however, efficiencies are highest when all individual slopes are modeled. Obviously, the models should be recalibrated to some extent after introducing the unsaturated zone and energy balance formulations. Now, the model parameters obtained from calibrating the uncoupled models (Figure 6.5) were employed.

Based on these results, it cannot be concluded that one of the investigated approaches is better than the others. The VIC model, with its statistical representation of small-scale variability, captured catchment-averaged processes reasonably well; monthly evaporation was modeled accurately and also discharge was simulated well. Discharge simulations by hsB are comparable to others at monthly scales, but at hourly time steps model efficiencies are relatively low, which is not surprising given the fact that no unsaturated zone was taken into account. At hourly time steps TOPMODEL reached the highest model efficiencies; its low complexity makes it easy to parameterize and in this terrain its basic assumptions are valid. For both hsB and hsB-LATS modeling efficiencies were highest when the maximum amount of spatial detail was incorporated (i.e., hillslopes were modeled individually). For both models, reducing the number of hillslopes by grouping similar hillslopes together (from 84 to 9) yields very similar catchment-averaged fluxes and also the variability across hillslopes is similar compared to the simulation of all individual hillslopes. This is much less the case for aggregation of the catchment into one or two hillslopes. Given the steep slopes of this terrain, the advantage of hsB with respect to TOPMODEL (inclusion of diffusive flow) does not really play a role, and the effect of groundwater on soil moisture variability through capillary uprise will probably also be small, hence the small differences between the models. As mentioned before, it would be interesting to repeat the analysis for a different catchment with less steep slopes.

Acknowledgements

This research was supported by the European Commission through the FP6 Integrated Project NeWater (<http://www.newater.info>) and the BSIK ACER project under the Dutch Climate Changes Spatial Planning programme.

General discussion



7.1 Introduction

In this thesis, a land surface model, the Variable Infiltration Capacity (VIC; *Liang et al., 1994*) model, was employed to investigate and quantify the effects of land use change (Chapter 3), climate change (Chapter 4) and oscillations in ocean temperature (Chapter 5) on the hydrological system. To justify using the VIC model, its performance was assessed by comparing model results with those of a conceptual water balance model (STREAM; *Aerts et al., 1999*), and observations in the Rhine basin (Chapter 2). An important feature of the VIC model, its parameterization of small-scale heterogeneity of soil moisture within a model grid cell, was compared with alternative parameterizations in Chapter 6. In the remainder of this chapter, the advantages and disadvantages of the VIC model compared to other models are discussed in Section 7.2, whereas the uncertainties involved in the model input are discussed in Section 7.3. The main conclusions from the thesis are drawn in Section 7.4 and, finally, in Section 7.5, some directions for further research are suggested.

7.2 Discussion of the hydrological model

In the VIC model, the representation of land-atmosphere interactions (evapotranspiration) is relatively physically-based, whereas that of subsurface hydrological processes is more conceptual and simplistic (*Liang et al., 1994*). At the scale of large river basins such as the Rhine or the Colorado, however, it is not feasible to take into account these hydrological processes in detail, because there is simply too much heterogeneity. At this large scale, conceptual hydrological models often perform as good as or better than complex physically-based hydrological models (e.g., *Sivalapan, 2003; te Linde et al., 2008*), because the theory that physically-based models are based on is usually only valid at small scales (*McDonnell et al., 2007*). Models that have often been used to model the water budget in large river basins, such as HBV or STREAM (see Chapter 2 for details), simplify both subsurface hydrological processes and land-atmosphere interactions, making them relatively fast and easy to operate. The physically-based approach to calculate evapotranspiration in VIC, however, provides a potential for more accurate evapotranspiration and thus also streamflow simulations, since the two are closely linked through the water balance (e.g., *Koster et al., 2000*).

In Chapter 2, this potential is investigated by comparing streamflow simulations of the VIC and STREAM models in the Rhine basin. In addition, a model of intermediate complexity is introduced by applying the VIC model in the water balance mode (i.e., the energy balance is not resolved), denoted as VIC-WB. As atmospheric forcing for all models, downscaled re-analysis data (i.e., atmospheric model output combined with observations) was used. This dataset was shown to have a bias compared to observations, causing relatively poor modeling efficiencies for all models. Results showed that the STREAM model is more sensitive to calibrated parameter values, and thus more effectively compensated for erroneous forcing data in the calibration period, causing poor performance in the validation period. For the validation period, the sub-grid variability that is accounted for in VIC-WB,

as opposed to STREAM, results in improved streamflow simulation compared to STREAM. Similar to STREAM, however, VIC-WB is relatively sensitive to model calibration parameters.

Including the energy balance and reducing the model time step from 1 day to 3 hours (i.e., running the full VIC model) further improves extreme streamflow simulation, and significantly improves simulation of evapotranspiration. Furthermore, the model's robustness is increased, which is important for impact assessments of climate change and land use change, since it is highly questionable whether parameter values that were obtained from calibration under current conditions are valid under changing conditions. VIC's physically-based parameterization for evapotranspiration and vegetation provides an additional advantage: parameter values are physically-based as well and can be related to physical vegetation properties. This is much less the case for models such as STREAM, where evapotranspiration is estimated from temperature only.

7.3 Discussion of the climate and land use change scenarios

All land use change scenarios and climate scenarios that have been used in this thesis are based on storylines of socio-economic and technological developments and the associated CO₂-emissions that were composed by the Intergovernmental Panel on Climate Change (IPCC; IPCC, 2000). Four land use change scenarios were obtained from the Eururalis project (Verburg *et al.*, 2006b). They were created using a set of models that take into account economic and demographic developments, and allocate land use types to individual pixels of 1 km², resulting in land use maps for the year 2030. The effect of changing climate conditions is only taken into account through an increase in temperature, not precipitation. Many previous land use change impact assessments used historical data (e.g., Matheussen *et al.*, 2000), or hypothetical scenarios, for example a doubling of urban area (Hundechea and Bárdossy, 2004). The scenarios that were used in Chapter 3 are, therefore, among the most "realistic" scenarios available.

In Chapter 4, three climate scenarios were used that are based on the same IPCC storylines as the land use change scenarios. To obtain the actual changes in climate that are associated with each CO₂-emission scenario, Global Climate Models (GCMs) are used. Because their spatial resolution is too low for hydrological applications, Regional Climate Models (RCMs) are necessary to downscale the GCM-output to a higher resolution. Several GCMs and RCMs have been developed, and they generally give very different results, even in reproducing the current climate (e.g., Covey *et al.*, 2003; Reichler and Kim, 2008). Understandably, the range in projected scenarios is even larger. In addition, precipitation, which is the most critical variable for hydrological applications, is a very difficult variable to simulate in climate models. Most climate models, for example, tend to overestimate the amount of "drizzle" (Perkins *et al.*, 2007; Sun *et al.*, 2006). As a result, climate model output typically has a bias compared to observations that should be corrected for (Lenderink *et al.*, 2007).

Several ways exist to do this (e.g., *Leander and Buishand, 2007; Hay et al., 2002*). In Chapter 4, a relatively simple, non-linear correction is applied that corrects the bias, taking into account its spatial and temporal variations (*Leander and Buishand, 2007*). Not only the climate scenarios that were used in this thesis were found to be biased with respect to the observations, but also the re-analysis data that were used in Chapters 2 through 4. Their bias is, however, different than that of the scenarios, because the driving model behind it is different. It should be noted that the precipitation and temperature fields are strongly influenced by the bias correction in the sense that the spatial patterns of the model output are “drawn” towards those of the observations. Furthermore, because no information is available for the future, the model bias is generally assumed to be constant in time. Recent research by *Christensen et al. (2008)* indicated, however, that the bias tends to grow with increasing temperatures, resulting in an overestimation of the climate change signal. This should be kept in mind while interpreting the results of Chapter 4.

Ideally, ensembles of models, both of GCMs and RCMs, should be used, because the multi-model mean is generally a better predictor than individual models (*Lambert and Boer, 2001*). In this thesis, however, scenarios by only one GCM and one RCM were available at a high spatial resolution. Moreover, use of multiple models would not been feasible numerically. The GCM that was used in Chapter 4, ECHAM5-OM, does very well in reproducing the current climate (*Reichler and Kim, 2008*). It is, however, more sensitive to aerosol concentrations than most other GCMs, causing it to be relatively cool in the first half of the 21st century due to the “dimming” effect of the aerosols. After 2050, aerosol concentrations decline, causing a stronger temperature increase in ECHAM5-OM compared to other GCMs (*IPCC, 2007*). This feature partly explains the contrast between the first and second halves of the 21st century that was found in Chapter 4.

7.4 General conclusions

In Chapter 2, the VIC model was found to simulate extreme streamflow reasonably well, and to be less sensitive to calibrated parameter values than the STREAM model. In addition, the fact that its evapotranspiration parameters directly represent vegetation properties also makes it easier to investigate the impact of land use changes. Therefore, the VIC model was used for impact assessments of land use change and climate change, which are described in Chapter 3 and 4, respectively. To isolate the effects of both changes, in Chapter 3 the atmospheric forcing was kept constant, whereas in Chapter 4 the land use was kept constant. The atmospheric forcing in Chapter 3 was identical to that in Chapter 2, namely a downscaled re-analysis dataset.

7.4.1 Effects of land use change

Based on simulations of a single grid cell covered by different land use types, as described in Chapter 3, the VIC model's original formulation for evapotranspiration was slightly altered. In the original model, no bare soil evaporation is allowed when a land use tile is classified as vegetated. However, for sparsely vegetated areas, such as cropland in winter season, this causes underestimations of evapotranspiration. By introducing a fractional bare soil evaporation, which exponentially depends on the leaf area index, the representation of annual total evapotranspiration as well as its annual cycle is improved. In addition, a crude parameterization for water management in urban areas was introduced by changing the value of the hydraulic conductivity and thus tuning the amounts of surface runoff and baseflow in urban areas. The modified model was then used to investigate the effects on average and extreme streamflow of six land use change scenarios at various locations in the Rhine basin. Two scenarios were hypothetical and not very realistic: all agricultural land was turned into either forest or grass. The remaining four scenarios are realistic future scenarios (Section 7.3).

Results showed that the future land use scenarios (Eururalis) generally indicated an increase in streamflow, mainly due to urbanization. Effects of urbanization are quite small, however, because they are partly compensated by a decrease of cropland and small increases in grassland, forest and natural area (e.g., shrubs). Conversion of agricultural land to forest or grass yielded a decrease in streamflow in both cases because of increased evapotranspiration. When considering streamflow at the basin outlet, the effects are small, but the effects on streamflow from small tributaries can be significant. These results are consistent with previous studies; for example *Hundecha and Bárdossy* (2004) found considerable effects of land use changes on streamflow from small sub-basins in the Rhine. *Bronstert et al.* (2002), on the other hand, found that the effect of land use change on streamflow in the main branch of the Rhine is very small.

7.4.2 Effects of climate change

The effects of climate change on streamflow in the Rhine basin are much larger than those of land use changes, as demonstrated in Chapter 4. In previous studies, *Kwadijk and Rotmans* (1995) and *Shabalova et al.* (2003) found increases in winter streamflow of about 30%, and decreases in summer streamflow of 30 to 40% by the end of the 21st century. The study presented in Chapter 4 differs from previous studies in that the spatial resolution of the employed atmospheric data is higher, and that a time period spanning the entire 21st century was analyzed instead of a relatively small time slice. Simulations by the VIC model of three climate scenarios for the periods 2001–2050 and 2051–2100 were compared with a simulation of the reference period, 1951–2000. Each climate scenario was based on a different CO₂-emission scenario: A2, A1B and B1 (Section 1.1.3). All atmospheric data were dynamically downscaled by an RCM to a spatial resolution of 0.088 degrees, or ~10 km, and corrected for the bias with respect to the observations as discussed in Section 7.3. The downscaled and bias-corrected re-analysis dataset that was also used in Chapters 2 and 3 was then used to calibrate the hydrological

model. Results indicate average streamflow at the basin outlet to increase by 30% in winter and spring and to decrease with a similar value in summer and autumn at the end of the century. These results thus confirm previous studies (e.g., *Kwadijk and Rotmans, 1995; Shabalova et al., 2003*). The majority of this change originates in the Alpine part of the catchment, and is caused for a large part by a decrease of the contribution of snowmelt to streamflow and by a shift of the timing of the snowmelt season to earlier in the year. Furthermore, the high-resolution climate scenarios and the distributed hydrological model allow for a detailed analysis of spatial patterns. Results indicate that the projected decrease in summer discharge is concentrated in the southern part of the basin. The northern tributaries, where there is hardly any decrease in summer precipitation, are dominated by wetter conditions throughout the year. In addition, our results reveal an interesting contrast between the first and second half of the 21st century. In all three scenarios, the first half is dominated by relatively wet conditions and more extreme peak flows. During the second half of the century, temperature and evapotranspiration increase drastically, causing generally dryer conditions and more extreme streamflow droughts. To some extent, this contrast can be explained by the GCM that was employed, as discussed in Section 7.3.

7.4.3 Effects of oscillations in ocean temperature

In addition to the aspect of climate change discussed in Section 7.4.2, there is also climate variability originating from interannual to (inter)decadal cycles in Pacific and Atlantic ocean temperatures. In some areas of the world, these cycles affect the climate system and water resources through teleconnections (e.g. *Mason and Goddard, 2001; Power et al., 2006*). In the Colorado River Basin (CRB), precipitation and streamflow have been linked to ENSO (El Niño-Southern Oscillation) and PDO (Pacific Decadal Oscillation), for example by *Redmond and Koch (1991)* and *Cañon et al. (2007)*. In Chapter 5, the CRB is used as study area to assess the influence of Pacific ocean temperature variability on several hydrologic variables, such as precipitation, snow cover, soil moisture and groundwater. Data was extracted from a simulation by the VIC model spanning 74 years (1930–2003) and related to climate indices describing the variability of ocean temperatures in the tropical and extra-tropical Pacific ocean.

Results show that precipitation, soil moisture and discharge are all related to ENSO in the southern part of the basin, mainly in winter and spring. ENSO in summer is correlated to summer precipitation, moisture and discharge throughout the CRB, as was also found by *Hidalgo and Dracup (2003)*. The relation between these variables and ENSO and PDO are strongest during phases of extremely warm (cool) ocean temperatures, known as El Niño (La Niña).

The PDO has different cycles of variability. One with a relatively high frequency that is correlated with ENSO, and another spanning very long periods, even multiple decades, which are generally known as PDO phases. During the 74 years of study, two transitions to a different PDO phase have taken place, one in 1946 and one in 1976. Results show that a strong connection exists between hydrological conditions in the CRB and this low-frequency model of PDO. Smoothed storage anomalies of

groundwater and the surface reservoir of Lake Mead appeared to be strongly correlated with PDO, as were the amplitudes of the anomalies of soil moisture and runoff, indicating drier conditions during negative PDO phases. Although the mechanisms and exact periodicity behind PDO is not yet well understood (*Newman, 2007*), and its predictability is low, data indicates that a new regime shift to a negative phase may have occurred in the late nineties (*Mantua and Hare, 2002*). If that is the case, then the current dry conditions in the CRB may dominate for several more years or even decades.

7.4.4 An alternative parameterization for small-scale variability of soil moisture

The representation of (subsurface) hydrological processes in the VIC model is conceptual and, compared to the formulation for land-atmosphere interactions, relatively simplistic. As an alternative parameterization for small-scale variability of topography, a catchment, or large-scale grid cell, can be divided into hillslopes. Each class of hydrologically similar hillslopes can then be modeled using the hillslope-storage Boussinesq (hsB) model. The dynamics of the water table and its influence on soil moisture variability is then taken into account as well. This approach, along with the VIC model, was applied to a small, alpine catchment, the Rietholzbach. In addition, TOPMODEL was applied, which makes use of hydrologic similarity as well, but based on individual pixels from digital terrain information. The models were applied at different levels of spatial aggregation: individual hillslopes, classes of similar hillslopes, two opposite hillslopes and the catchment represented as one hillslope.

The larger variability of soil moisture contents that results from simulations of individual hillslopes yields more generation of surface runoff in all models. On monthly scales, however, this increase is compensated by decreasing baseflow. Therefore, changes in discharge are small. On daily and hourly time steps, this compensation does not take place. Therefore, the simulations with individual hillslopes achieve the highest modeling efficiencies when catchment-averaged streamflow is compared to observations. When the number of hillslopes is reduced from 84 to 9 classes of similar hillslopes, the simulation of catchment-averaged discharge, as well as the variability across hillslopes is similar to the case when all hillslopes are simulated explicitly. Division of hillslopes into such classes is a better way of aggregating then representing the catchment as one big hillslope. The statistical approach of VIC accurately simulated both discharge and evaporation. It is able to represent the processes associated with soil moisture variability in the Rietholzbach to a sufficient extent, although it is not physically-based and groundwater is not included.

7.5 Directions for further research

In this thesis, effects of land use change and climate change were assessed separately, i.e., climate conditions were kept constant for all land use scenarios and vice versa. It might well be that under extreme climate conditions such as predicted by climate scenarios, the land use affects streamflow in

a different way. Therefore, a logical next step would be to perform a combined analysis. For example, for each SRES storyline the associated climate scenarios and land use scenarios could be simulated simultaneously. Or, to limit computation time, extremely wet or dry episodes from the climate scenarios could be selected to evaluate the effects of land use changes under extreme conditions. Even better would be to represent vegetation dynamically and fully interactive, as is done for example at the global scale in the LPJ (Lund-Potsdam-Jena) model (Gerten *et al.*, 2004; Bondeau *et al.*, 2007).

The climate scenarios that were used in Chapter 4 were obtained from only one GCM, whereas ideally an ensemble of models should be used, as was already discussed in Section 7.3. According to GCM intercomparison experiments, multi-model means better represent current climate conditions and provide more realistic climate scenarios, because the specificities of individual models are averaged out (e.g. Covey *et al.*, 2003; Reichler and Kim, 2008). Furthermore, in this thesis the hydrological model is run “offline”. This causes inconsistencies, i.e., the evaporative fluxes from the land to the atmosphere as simulated by the VIC model may be (and probably are) different than those simulated by the original land component of the climate model. Ideally, one should carry out a similar experiment where the climate model and the hydrological model are coupled, to prevent inconsistencies and capture important feedbacks from soil moisture on precipitation and temperature (e.g. Seneviratne *et al.*, 2006).

Throughout this thesis, extreme peak flows and low flows have been analyzed. The length of the simulated time series used to obtain estimates of the extremes was relatively short (3 times 100 years at most). Flood peaks that are relevant for water management, for example the design discharge, have a return period of 1250 years for the Rhine basin (Eberle *et al.*, 2002). To make a statistically reasonable estimate of the design discharge, much longer time series spanning about 10.000 years would be necessary. It is obvious that such time series cannot be obtained from observations, and not (yet) from climate model simulations. A rainfall generator (Beersma, 2002; de Wit and Buishand, 2007), can create such time series by statistical resampling. In many applications, however, observed data are resampled. Maximum daily rainfall amounts are, therefore, not allowed to exceed those in the observed record, which is not very realistic under changing climate conditions. At the moment, applying such a rainfall generator to (bias corrected) climate model output seems to be the best option.

A relevant improvement of the hydrological model to simulate extreme streamflow droughts would be to improve the representation of groundwater. In many large-scale hydrological models, such as the VIC model, groundwater flows are not explicitly modeled and also the influence of groundwater on soil moisture through capillary uprise is not taken into account. Recently, these processes have been implemented in land-surface models (e.g. Maxwell and Kollet, 2008; Fan *et al.*, 2007; Miguez-Macho *et al.*, 2007), but at the scale of large river basins such as the Rhine or Colorado this is not feasible (yet).

In some parts of the world, large-scale climate oscillations have a significant influence on the hydrological system through teleconnections. However, the current level of understanding of the physics

behind these is limited, and often the frequency of oscillation is low (for example PDO), so only few “transitions” have occurred in the observed record. Accurately predicting these oscillations and the relations between them is still extremely difficult (*Newman, 2007*). To improve our understanding and their predictability more research is needed, because they are crucial for water management in, for example, the Colorado River Basin. To increase the length of the available time series, paleohydrological and -climatological records can be used for this research, as was already done by, for example, *MacDonald and Case (2005)* and *Rasmussen et al. (2006)*.

Because the effect of land use changes in the Rhine basin was shown to be quite small, it does not seem to be a relevant option for water managers to mitigate extreme floods or low flows. However, because effects in sub-basins can be significant, an effective combination of different land use changes in different parts of the basin could be able to alter the magnitude of low-flows and/or timing of flood peaks at the basin outlet. Other management options to locally mitigate hydrological extremes could take place in urban areas: so-called “green roofs” and ponds can help to increase storage capacity in upstream areas. In Chapter 3 a crude parameterization to evaluate the effects of such measures was implemented. A more refined parameterization was suggested by *Cuo et al. (2008)*, and it is part of ongoing research to implement such a parameterization in the VIC model and further investigate to what spatial extent these measures can influence streamflow.

For most of the additional simulation experiments that are suggested above, an important limiting factor is computation power. Simulating time series spanning hundreds of years at a high spatial and temporal resolution is very time consuming. The amount of time needed increases fast when multiple simulations are needed for model calibration or to get an idea of the uncertainty that is involved. As computing power keeps increasing and more and more multi-processor clusters get more readily available, the suggested simulations become easier to carry out.

Concerning the parameterization of small-scale variability that was discussed in Chapter 6, there are also some issues that would be interesting to investigate more in-depth. The hillslope-based approach, as opposed to the TOPMODEL-approach, takes into account both diffusive and advective flow. In the Rietholzbach, where slopes are generally steep, diffusive flow does not effectively play a role and this advantage is not of interest. Therefore, it would be interesting to repeat the analysis of Chapter 6 for a catchment with less steep slopes, or even no slopes at all. Moreover, the choice of similarity parameters to classify the hillslopes could be investigated further. Although our rather arbitrary method based on *Aryal et al. (2002)* yielded promising results, it would be interesting to see whether results change when all the parameters defined by *Aryal et al. (2002)* are taken into account instead of just two. In areas with less steep slopes, also the Péclet number, representing the ratio between advective and diffusive flow (*Berne et al., 2005*) could be used. These are just examples; a significant amount of research has recently been and will be devoted to this subject (e.g. *Sivalapan, 2003; Wagener et al., 2007; Tetzlaff et al., 2008*).

Chapter 8

Nederlandse samenvatting



8.1 Inleiding

De globaal gemiddelde temperatuur is de afgelopen tientallen jaren dusdanig gestegen, dat dit naar verwachting een grote invloed heeft op het klimaatsysteem en de hydrologische cyclus (IPCC, 2007). Omdat warme lucht een grotere verzadigde dampdruk heeft en meer waterdamp kan bevatten dan koude lucht wordt verwacht dat verdamping en neerslag verwacht toenemen. Ook kan de frequentie en omvang van extreme neerslaggebeurtenissen groter worden (Trenberth, 1997a). Bovendien kunnen de hydrologische effecten van deze veranderingen versterkt of verzwakt worden door landgebruiksveranderingen zoals bebossing en urbanisatie (bv. Bradshaw *et al.*, 2007). In dit proefschrift wordt een land-oppervlaktemodel, het Variable Infiltration Capacity model (VIC; Liang *et al.*, 1994), toegepast om de effecten van landgebruiksverandering (Hoofdstuk 3), klimaatverandering (Hoofdstuk 4) en oscillaties in oceaantemperatuur (Hoofdstuk 5) te onderzoeken en te kwantificeren. Om het gebruik van het VIC model te rechtvaardigen, zijn de prestaties ervan onderzocht door modelresultaten van het VIC model te vergelijken met die van een conceptueel waterbalansmodel (STREAM; Aerts *et al.*, 1999) en observaties in het Rijnstroomgebied (Hoofdstuk 2). Een belangrijk aspect van het VIC model, namelijk de parametrisatie van kleinschalige bodemvochtvariabiliteit binnen een modelgridcel, is vergeleken met soortgelijke parametrisaties in Hoofdstuk 6. Het vervolg van dit hoofdstuk is als volgt opgebouwd: in Sectie 8.2 worden de voor- en nadelen van het VIC model ten opzichte van andere modellen bediscussieerd; in Sectie 8.3 worden de onzekerheden omtrent de invoerdata voor het model beschreven, en in Sectie 8.4 tenslotte worden de belangrijkste conclusies van dit proefschrift samengevat en in perspectief geplaatst.

8.2 Het hydrologisch model in perspectief

In het VIC model is de berekening van de uitwisseling van vocht en warmte tussen land en atmosfeer, onder meer de verdamping, relatief complex en fysisch gebaseerd vergeleken met die van (ondergrondse) hydrologische stromingsprocessen, die relatief conceptueel en simplistisch is (Liang *et al.*, 1994). Op de schaal van grote rivierstroomgebieden zoals de Rijn of de Colorado, is het echter erg moeilijk om deze processen in detail en expliciet te modelleren omdat er simpelweg teveel heterogeniteit is in de eigenschappen van bodem, vegetatie en topografie die deze processen aansturen. Op deze schaal presteren conceptuele, simplistische modellen vaak even goed of zelfs beter dan complexe, fysisch gebaseerde modellen die wel proberen hydrologische processen in detail te simuleren (Sivalapan, 2003; te Linde *et al.*, 2008). Een van de redenen hiervoor is het feit dat de theorie die meestal ten grondslag ligt aan fysisch gebaseerde modellen alleen geldig is op kleine schaal of zelfs een punt (McDonnell *et al.*, 2007).

In studies die de invloed van klimaatverandering op de hydrologie onderzoeken, worden vaak modellen gebruikt die zowel de zojuist genoemde hydrologische stromingsprocessen als de uitwisseling met de atmosfeer via verdamping vereenvoudigen. Voorbeelden zijn HBV en STREAM (zie Hoofd-

stuk 2 voor meer details). Deze modellen zijn daarom vaak eenvoudig en snel toe te passen. De meer fysische gebaseerde berekening van verdamping in VIC kan mogelijk echter nauwkeurigere schattingen van de verdamping geven. Omdat afvoer en verdamping sterk gekoppeld zijn via de waterbalans, kan afvoer dus ook nauwkeuriger berekend worden (bv. *Koster et al.*, 2000). In Hoofdstuk 2 wordt dit nader onderzocht door afvoersimulaties van de VIC en STREAM modellen te vergelijken. Daarnaast wordt een model geïntroduceerd met een tussenliggende complexiteit door het VIC model toe te passen in de zogenaamde waterbalans-variant (VIC-WB), wat betekent dat de energiebalans niet wordt opgelost.

Als atmosferische invoerdata voor alle drie de modellen is her-analysedata gebruikt (dit is uitvoer van een atmosferisch model waarin waarnemingen zijn verwerkt), die vervolgens met een regionaal klimaatmodel zijn neergeschaald naar een hoge ruimtelijke resolutie (ongeveer 10 km). Deze her-analysedataset wijkt echter sterk af van geobserveerde neerslag en temperatuur, zo wezen de resultaten van een vergelijking uit, waardoor de kwaliteit van de gesimuleerde afvoer ten opzichte van de waargenomen afvoer voor alle drie de modellen relatief laag was. Het STREAM model bleek verder gevoeliger te zijn voor de gecalibreerde parameterwaarden dan het VIC model. Het compenseerde dus ook effectiever voor de afwijkingen in de neerslaginvoer ten opzichte van waarnemingen die aanwezig waren in delen van de calibratieperiode, hetgeen weer lagere modellerings efficiënties gedurende de validatieperiode veroorzaakte.

De parametrisatie van sub-pixel variabiliteit die wordt meegenomen in het VIC-WB model, in tegenstelling tot het STREAM model, resulteert in verbeterde afvoersimulaties vergeleken met het STREAM model voor de validatieperiode. Het VIC-WB model is echter, net als het STREAM model, gevoeliger voor gecalibreerde parameterwaarden. Het meenemen van de energiebalans en het verkleinen van de tijdstap van 1 dag naar 3 uur (zoals in het VIC model gebeurt) verbetert de afvoersimulaties nog verder, en levert ook een significante verbetering van de simulatie van verdamping op. Het VIC model blijkt robuuster te zijn vergeleken met de andere modellen (minder gevoelig voor calibratieparameters), hetgeen belangrijk is voor onderzoeken naar de effecten van klimaat- en landgebruiksveranderingen. Het is namelijk sterk de vraag of parameterwaarden die bepaald zijn door calibratie onder de huidige condities nog geldig blijven onder veranderende omstandigheden. De fysisch gebaseerde berekening van verdamping en vegetatie biedt bovendien een ander voordeel: de parameterwaarden hebben een fysische basis en kunnen gerelateerd worden aan fysische eigenschappen van de vegetatie. Dit is in veel mindere mate het geval voor STREAM, waar verdamping alleen uit temperatuurgegevens wordt geschat.

8.3 De landgebruiks- en klimaatveranderingsscenario's in perspectief

Alle landgebruiksveranderings- en klimaatscenario's die in dit proefschrift zijn gebruikt zijn gebaseerd op verhaallijnen die verschillende sociaal-economische en technologische ontwikkelingen en de

daarmee gepaard gaande CO₂-emissies beschrijven. Deze verhaallijnen zijn samengesteld door het Intergovernmental Panel on Climate Change (IPCC; IPCC, 2000). De vier gebruikte verhaallijnen worden weergegeven als A2 ("Continentale markten"), A1 ("Globale economie", waar bij het hier gebruikte subscenario A1B aangeeft dat er balans is tussen fossiele en duurzame energie), B1 ("Globale samenwerking") en B2 ("Regionale gemeenschappen"). Vier landgebruiksveranderingsscenario's, elk gebaseerd op één van deze vier verhaallijnen, zijn gebruikt zoals ze zijn samengesteld in het kader van het Eururalis project (Verburg *et al.*, 2006b). Deze werden gecreëerd met een modellen-set die economische en demografische ontwikkelingen gebruikt om ontwikkelingen in landgebruik te voorspellen, en de resulterende landgebruikstypen aan individuele pixels van 1 km² toewijst. Dit resulteerde in vier landgebruikskaarten voor het jaar 2030. Het effect van klimaatverandering op landgebruik is alleen meegenomen door een stijging van temperatuur, niet van neerslag. Eerdere effectstudies van landgebruiksveranderingen gebruikten historische data (bv. Matheussen *et al.*, 2000) of hypothetische scenario's zoals een verdubbeling van het stedelijk gebied (Hundecha and Bárdossy, 2004). De scenario's die zijn gebruikt in Hoofdstuk 3 behoren bij de meest realistische scenario's die beschikbaar zijn.

In Hoofdstuk 4 zijn drie klimaatscenario's gebruikt die elk zijn gebaseerd op een andere IPCC-verhaallijn, in volgorde van oplopende CO₂ emissies: B1, A1B en A2. Om de feitelijke verandering in klimaat te verkrijgen die gekoppeld is aan elk CO₂ emissiescenario worden globale klimaatmodellen (GCMs) gebruikt. Omdat de ruimtelijke resolutie daarvan veel te laag is voor hydrologische toepassingen zijn regionale klimaatmodellen (RCMs) nodig om de uitvoer van GCMs om te zetten naar een hogere resolutie. Er zijn verschillende GCMs en RCMs ontwikkeld en zij geven meestal erg verschillende resultaten, zelfs als zij het huidige klimaat proberen te reproduceren (bv. Covey *et al.*, 2003; Reichler and Kim, 2008). De bandbreedte van geprojecteerde klimaatscenario's is, zoals te begrijpen is, nog groter. Bovendien is neerslag, de meest kritieke variabele voor hydrologische toepassingen, voor klimaatmodellen erg moeilijk te simuleren. De meeste modellen hebben bijvoorbeeld de neiging om de hoeveelheid motregen te overschatten (Perkins *et al.*, 2007; Sun *et al.*, 2006). Klimaatmodellen hebben daarom bijna altijd een structurele fout ten opzichte van waarnemingen die gecorrigeerd moet worden (Lenderink *et al.*, 2007). Er bestaan verschillende manieren om dit te doen (bv. Leander and Buishand, 2007; Hay *et al.*, 2002).

In Hoofdstuk 4 is een relatief eenvoudige, niet-lineaire correctie toegepast die de structurele fout op een ruimtelijk en temporeel variabele manier corrigeert. Niet alleen de klimaatscenario's vertonen een structurele fout, maar ook de her-analyse data die zijn gebruikt in Hoofdstukken 2 tot en met 4. Deze fout is echter anders dan die van de scenario's omdat het model waar de her-analyses op gebaseerd zijn anders is. Belangrijk om te vermelden is dat de ruimtelijke patronen van neerslag en temperatuur door de correctie veranderen en naar die van de waarnemingen "getrokken" worden. Omdat er geen waarnemingen beschikbaar zijn voor de toekomst, wordt aangenomen dat de structurele fout constant blijft in de tijd. Recent onderzoek door Christensen *et al.* (2008) toont echter aan dat de structurele fout de neiging heeft te groeien bij stijgende temperatuur. Dit zou resulteren in een overschatting van het klimaatveranderingssignaal en is belangrijk om in het achterhoofd te houden

bij het interpreteren van de resultaten van Hoofdstuk 4.

Idealiter zouden verschillende modellen (zowel GCMs als RCMs) gebruikt moeten worden omdat het gemiddelde over meerdere modellen over het algemeen een betere voorspeller is dan individuele modellen (*Lambert and Boer, 2001*). Voor dit proefschrift was echter maar data van slechts één GCM en één RCM beschikbaar op de gebruikte hoge ruimtelijke resolutie. Bovendien is het erg (reken)tijdrovend om meerdere modellen te gebruiken. Het GCM dat in Hoofdstuk 4 gebruikt is, ECHAM5-OM, reproduceerde het huidige klimaat echter erg goed in vergelijkende tests (*Reichler and Kim, 2008*). Dit model is, vergeleken met andere modellen, echter gevoeliger voor veranderingen in aerosol-concentraties. Door het dimmende effect van de aerosolen zijn de klimaatscenario's uit ECHAM5-OM relatief "koel" in de eerste helft van de 21^{ste} eeuw. Na 2050 dalen de aerosol-concentraties en stijgt de temperatuur in ECHAM5-OM sterker dan in andere GCMs (*IPCC, 2007*). Dit feit verklaart gedeeltelijk het sterke contrast tussen de eerste en tweede helft van de 21^{ste} eeuw dat werd gevonden in Hoofdstuk 4.

8.4 Algemene conclusies

De resultaten in Hoofdstuk 2 wijzen uit dat het VIC model de afvoerpieken uit het Rijnstroomgebied redelijk simuleert, en dat het minder gevoelig voor de waarden van calibratieparameters is dan het STREAM model. Het feit dat in het VIC model de parameters voor de berekening van verdamping direct gerelateerd zijn aan eigenschappen van de vegetatie maakt het mogelijk om de invloed van landgebruiksveranderingen te onderzoeken. Dit is gedaan in Hoofdstuk 3. Daarnaast is in Hoofdstuk 4 de invloed van klimaatverandering onderzocht. Om beide effecten te isoleren, is in Hoofdstuk 3 de atmosferische forcering constant gehouden en in Hoofdstuk 4 het landgebruik.

8.4.1 Effecten van landgebruiksveranderingen

Als eerste is in Hoofdstuk 3 de simulatie van verschillende landgebruikstypen in het VIC model onderzocht door een enkele grid cel met verschillende landgebruikstypen te simuleren. De resultaten van deze simulaties wezen uit dat wanneer in het model een gebied is geclassificeerd als begroeid, er geen verdamping van de kale grond wordt uitgerekend. Voor schaarsbegroeide gebieden, bijvoorbeeld akkerland in de winter, leidt dit tot onderschattingen van de totale verdamping. Door een fractie "kale grond" te implementeren, die exponentieel afhangt van de bladoppervlakte-index (één van de vegetatieparameters), werd de simulatie van totale verdamping en ook de jaarlijkse gang realistischer.

Het aldus gewijzigde model is vervolgens gebruikt om de invloed van zes landgebruiksveranderingsscenario's op de gemiddelde en extreme afvoer op verschillende locaties in het Rijnstroomge-

bied te onderzoeken. Twee scenarios zijn hypothetisch en niet erg realistisch; alle landbouwgrond in het stroomgebied is vervangen door bos of grasland. De vier resterende scenarios zijn realistische toekomstscenarios zoals besproken in Sectie 8.3. Over het algemeen volgt uit de vier realistische scenarios een toename in de gemiddelde afvoer, die vooral wordt veroorzaakt door urbanisatie. Dit effect is tamelijk klein, onder andere omdat het wordt gecompenseerd door een afname van het areaal aan landbouwgrond en kleine toenames van het bos, grasland en natuurgebied. De twee hypothetische scenarios leidden tot een toename van de verdamping en dus tot een afname van de zowel gemiddelde als extreme afvoer. Over het algemeen zijn de effecten bij het uitlaatpunt van het stroomgebied, Lobith, tamelijk klein, maar de effecten op de afvoer uit kleine sub-stroomgebieden kunnen aanzienlijk zijn. Dit is consistent met voorgaande studies; *Hundecha and Bárdossy* (2004) vonden bijvoorbeeld ook aanzienlijke effecten van landgebruiksveranderingen in kleine stroomgebieden, terwijl *Bronstert et al.* (2002) slechts kleine effecten vonden van landgebruiksveranderingen op de afvoer in de hoofdtak van de Rijn.

8.4.2 Effecten van klimaatveranderingen

De effecten van klimaatverandering op de afvoer in het Rijnstroomgebied is veel groter dan die van landgebruiksveranderingen, zoals wordt gedemonstreerd in Hoofdstuk 4. In voorgaande studies vonden *Kwadijk and Rotmans* (1995) en *Shabalova et al.* (2003) al toenames van de gemiddelde afvoer in de winter aan het einde van de 21^{ste} eeuw met ongeveer 30%, en afnames in de zomer met eenzelfde hoeveelheid. De studie die wordt beschreven in Hoofdstuk 4 verschilt van voorgaande studies in die zin dat de ruimtelijke resolutie van de gebruikte klimaatscenarios hoger is (ongeveer 10 km, waar andere studies vaak 25 of 50 km gebruikten), en dat de gehele 21^{ste} eeuw wordt geanalyseerd in plaats van een relatief korte periode (vaak 30 jaar). Hydrologische simulaties door het VIC model van drie klimaatscenarios (zie Sectie 8.3) voor de periodes 2001–2050 en 2051–2100 zijn vergeleken met een simulatie van de referentieperiode, namelijk 1951–2000. Voor de calibratie van het VIC model is de eerder beschreven her-analysedataset gebruikt die ook al in de Hoofdstukken 2 en 3 is gebruikt. Alle datasets zijn gecorrigeerd voor hun structurele fout ten opzichte van de waarnemingen zoals kort beschreven in Sectie 8.3.

Uit de resultaten blijkt een toename van de gemiddelde afvoer bij Lobith, het uitlaatpunt van het Rijnstroomgebied, aan het eind van de 21^{ste} eeuw met ongeveer 30% in de winter en lente en een afname met eenzelfde waarde in de zomer. Dit bevestigt dus de resultaten van eerdere studies door (onder andere) *Kwadijk and Rotmans* (1995) en *Shabalova et al.* (2003). Het overgrote deel van deze verandering vindt zijn oorsprong in het alpiene gedeelte van het stroomgebied en wordt gedeeltelijk veroorzaakt door een sterke afname van de bijdrage van sneeuwsmelt aan de afvoer en doordat het sneeuwsmeltseizoen in de tijd verschuift naar eerder in het jaar. De hoge ruimtelijke resolutie van de klimaatscenarios en het gedistribueerde hydrologische model maken een gedetailleerde analyse van de ruimtelijke patronen mogelijk. Deze laten zien dat de geprojecteerde afname in zomerneerslag vooral in het zuidelijke deel van het stroomgebied optreedt. In de noordelijke deelstroomgebieden

neemt de zomerneerslag nauwelijks af, en neemt de totale jaarlijkse neerslag sterk toe.

Verder blijkt uit de resultaten een opvallend contrast tussen de eerste en tweede helft van de 21^{ste} eeuw. In alle drie de klimaatscenario's wordt de eerste helft van de eeuw gedomineerd door natte omstandigheden en meer extreme piekafvoeren. Tijdens de tweede helft van de eeuw vindt een drastische toename van temperatuur en verdamping plaats, die drogere omstandigheden veroorzaakt en meer en langere periodes van extreme afvoerdroogte. Zoals al bleek uit de discussie van de klimaatscenario's in Sectie 8.3, wordt dit contrast gedeeltelijk verklaard door de keuze van het klimaatmodel, dat door de relatief sterke gevoeligheid voor aerosolconcentraties een relatief groot verschil in temperatuur geeft tussen beide helften van de 21^{ste} eeuw.

8.4.3 Effecten van oscillaties in oceaantemperaturen

Een andere vorm van klimaatvariabiliteit is gerelateerd aan oscillaties in oceaantemperaturen in de Grote en Atlantische oceaan, met een golflengte van meerdere, soms zelfs tientallen jaren. In sommige delen van de wereld hebben deze oscillaties aanzienlijke effecten op het hydrologisch systeem in de vorm van zogenaamde teleconnecties (bv. *Mason and Goddard, 2001; Power et al., 2006*). In het stroomgebied van de Colorado zijn in voorgaand onderzoek (bv. *Redmond and Koch, 1991; Cañon et al., 2007*) neerslag en afvoer al gerelateerd aan het ENSO signaal (El Niño–Southern Oscillation) en de PDO (Pacific Decadal Oscillation).

In Hoofdstuk 5 is het stroomgebied van de Colorado gebruikt als studiegebied om de invloed van variabiliteit in Grote Oceaantemperatuur op verscheidene hydrologische variabelen zoals neerslag, sneeuwbedekking, bodemvocht en grondwater te onderzoeken. Deze variabelen zijn geëxtraheerd uit een simulatie door het VIC model die 74 jaar beslaat (1930–2003), en gerelateerd aan klimaatindices die de variabiliteit van oceaantemperatuur in zowel de tropische als de extra-tropische Grote oceaan beschrijven. De resultaten laten zien dat neerslag, bodemvocht en afvoer allemaal gecorreleerd zijn met ENSO in het zuidelijke deel van het stroomgebied, en dan vooral in de winter en lente. ENSO in de zomer is ook gecorreleerd met de neerslag, bodemvocht en afvoer in de zomer in het hele stroomgebied, zoals ook al is gevonden door *Hidalgo and Dracup (2003)*. De relaties tussen deze variabelen en ENSO en de PDO zijn het sterkst tijdens periodes van extreme warme of koude oceaantemperatuur, die bekend staan als respectievelijk El Niño of La Niña.

De PDO heeft verschillende cycli met verschillende frequenties. Een modus met een relatief hoge frequentie is gerelateerd aan ENSO. Een andere modus heeft een veel lagere frequentie en de verschillende fases ervan kunnen tientallen jaren duren. Tijdens de 74 jaren die bestudeerd zijn, hebben waarschijnlijk slechts twee transitieën plaatsgevonden; één rond 1946 en één rond 1976. Er is aangetoond dat er een sterke connectie bestaat tussen hydrologische condities in het stroomgebied van de Colorado en deze modus van de PDO met een lage frequentie. Anomalieën van grondwaterberging en berging in het stuwmeer Lake Mead zijn sterk gecorreleerd met deze

modus van PDO. Ook de amplitudes van de anomalieën van bodemvocht en afvoer zijn kleiner tijdens negatieve PDO-fases, hetgeen duidt op drogere condities. Hoewel de mechanismen achter en de exacte periodiciteit van de PDO nog niet goed begrepen worden, en lange-termijn voorspellingen dus nog erg moeilijk zijn (Newman, 2007), duidt recente data op een nieuwe overgang naar een negatieve PDO fase in de late jaren negentig (Mantua and Hare, 2002). Als dat inderdaad het geval is dan kunnen de huidige droge condities in het stroomgebied van de Colorado nog jaren of zelfs tientallen jaren aanhouden.

8.4.4 Een alternatieve parametrisatie voor kleinschalige bodemvochtvariabiliteit

De modellering van (ondergrondse) hydrologische stromingsprocessen in het VIC model is conceptueel en relatief eenvoudig vergeleken met die van land-atmosfeerinteracties. Als een alternatieve manier om de kleinschalige variabiliteit van de topografie binnen een stroomgebied of grootschalige model-pixel te parametriseren kan deze worden onderverdeeld in hellingen, omdat dit in veel stroomgebieden de “bouwstenen” van het landschap zijn. Elke klasse van hydrologisch soortgelijke hellingen kan dan worden gemodelleerd met het zogenaamde “hillslope-storage Boussinesq” (hsB) model. De grondwaterdynamiek en de invloed daarvan op bodemvochtvariabiliteit wordt dan ook meegenomen. Deze benadering, samen met die van het VIC model, is toegepast op een klein, alpien stroomgebied, de Rietholzbach. Daarnaast is ook TOPMODEL toegepast, een model dat ook gebruik maakt van hydrologische similariteit, maar dan gebaseerd op individuele pixels van een digitaal terreinmodel. De modellen zijn toegepast op verschillende ruimtelijke schalen: individuele hellingen, klassen van gelijkvormige hellingen, twee tegenoverliggende hellingen (“open boek”), en een helling die het hele stroomgebied weergeeft.

De grotere variabiliteit van bodemvochtgehalten die ontstaat als individuele hellingen worden doorerekend in plaats van ruimtelijk ge-aggregeerde hellingen zorgt voor meer oppervlakkige afvoer. In termen van maandelijks gemiddelde afvoeren wordt dit echter gecompenseerd door een lagere grondwaterafvoer; de verschillen in maandelijks totale afvoer zijn dus klein. Op uurlijkse of dagelijkse afvoeren treedt deze compensatie in mindere mate op, resulterend in verschillende modellerings efficiënties: hoe kleiner het aantal hellingen, hoe lager de efficiëntie. Dit is ook het geval wanneer, analoog aan de hellingen, verschillende distributies van de topografische index in TOPMODEL worden gebruikt. Als het aantal hellingen wordt gereduceerd van 84 naar 9 door de classificatie van gelijkvormige hellingen, blijft de gesimuleerde afvoer, en ook de variabiliteit tussen hellingen, praktisch gelijk aan de simulatie met 84 individuele hellingen. Deze classificatie is dus een betere manier van ruimtelijk aggregeren dan het stroomgebied te modelleren als één of twee hellingen. Het VIC model, met zijn statistische benadering kon zowel afvoer als verdamping redelijk nauwkeurig simuleren en is blijkbaar in staat de processen die gekoppeld zijn aan bodemvochtvariabiliteit in het Rietholzbach-stroomgebied in voldoende mate te kunnen representeren, ook al is het niet fysisch-gebaseerd en wordt grondwaterdynamiek niet meegenomen in de berekeningen.

Appendix: Extreme value distributions¹

The Generalized Extreme Value distribution

The Generalized Extreme Value distribution is a family of extreme value distributions that combines the Weibull, Fréchet and Gumbel distributions. Because it is a limit distribution of random variables, it is in practice often used to model (annual) maxima of hydrological timeseries. The probability density function (pdf) of the GEV-distribution is given by:

$$f(x|\mu, \sigma, \kappa) = \frac{1}{\sigma} \exp \left(- \left(1 + \kappa \frac{(x - \mu)}{\sigma} \right)^{-\frac{1}{\kappa}} \right) \left(1 + \kappa \frac{(x - \mu)}{\sigma} \right)^{-1 - \frac{1}{\kappa}}, \quad (8.1)$$

for $1 + \kappa \frac{(x - \mu)}{\sigma} > 0$, where μ is the location parameter, σ is the scale parameter and κ is the shape parameter ($\kappa \neq 0$). Three sub-distributions of the GEV-distribution exist, which mainly differ in their tail behavior. The Type II case ($\kappa > 0$), is related to the Fréchet distribution, the Type III case ($\kappa < 0$), to the Weibull distribution, and the limit case for $\kappa \rightarrow 0$, the Type I case, is related to the well-known Gumbel distribution and is given by:

$$f(x|\mu, \sigma, 0) = \frac{1}{\sigma} \exp \left(- \exp \left(- \frac{(x - \mu)}{\sigma} \right) - \frac{(x - \mu)}{\sigma} \right). \quad (8.2)$$

Each sub-distribution is the limit distribution of a specific type of underlying distribution: Type I corresponds to distributions with an exponentially decreasing tail (e.g., normal), Type II to distributions with a polynomial decreasing tail (e.g., Student's t), and Type III to distributions with a finite tail (e.g., beta).

The Generalized Pareto distribution

The Generalized Pareto (GP) distribution is typically used to model the distribution of extremes of data which represents exceedences over (or under) a threshold. The pdf of the GP distribution is

given by:

$$f(x|\kappa, \sigma, \theta) = \frac{1}{\sigma} \left(1 + \kappa \frac{(x - \theta)}{\sigma} \right)^{(-1 - \frac{1}{\kappa})}, \quad (8.3)$$

where σ again is the scale parameter, κ is the shape parameter ($\kappa \neq 0$) and θ is the threshold parameter. In the case that $\kappa \rightarrow 0$, the pdf is given by:

$$f(x|0, \sigma, \theta) = \frac{1}{\sigma} e^{-\frac{(x-\theta)}{\sigma}}. \quad (8.4)$$

If $\kappa = 0$ and $\theta = 0$, the generalized Pareto distribution is equivalent to the exponential distribution. If $\kappa > 0$ and $\theta = \sigma$, the generalized Pareto distribution is equivalent to the Pareto distribution. Like the GEV-distribution, each of three sub-distributions of the GP distribution corresponds to the limiting distribution of data (above or below a threshold) from a specific class of underlying distributions. The sub-distribution with $\kappa \rightarrow 0$ corresponds to an exponentially decreasing tail, $\kappa > 0$ to polynomial decreasing tails, and $\kappa < 0$ corresponds to finite tails.

The Log Pearson Type III distribution

The Pearson distributions consist of seven basic types that are together embedded in a single parametric framework. From any valid mean, standard deviation, skewness and kurtosis of a dataset, a unique distribution can be derived. The Pearson Type III distribution describes the probability of occurrence of a given event in a Poisson process. When the population of events are very positively skewed, the data are usually log-transformed and the distribution is called the Log Pearson Type III Distribution. In the United States, the Log Pearson Type III Distribution is widely used to calculate flood recurrences. It is, for example, the default distribution used by the U.S. Geological Survey for flood studies. The pdf of the Pearson Type III distribution can be described by:

$$f(y; \lambda, \beta, \epsilon) = \frac{\lambda^\beta (y - \epsilon)^{(\beta-1)}}{\Gamma(\beta)} \exp[-\lambda(y - \epsilon)]. \quad (8.5)$$

where y are the log-transformed data, and λ , β and ϵ are the distribution parameters, that can be related to the moments of the distribution by $\lambda = \sqrt{\beta}/\sigma_y$, $\beta = (2/C_y)^2$ and $\epsilon = \mu_y - \beta/\lambda$. Here, μ_y , σ_y and C_y are respectively the mean, standard deviation and skewness as calculated from the (log-transformed) data. Γ is the Gamma-function: $\Gamma(x) = \int_0^\infty t^{(x-1)} e^{-t} dt$.

¹Much of this appendix is based on the MATLAB documentation: Statistics ToolboxTM 7 User's guide, The Mathworks, Inc., revised October 2008.

Bibliography

- Abbott, M. B., J. C. Bathurst, J. A. Cunge, P. E. O'Connell, and J. Rasmussen (1986), An introduction to the European Hydrological System-Système Hydrologique Européen, "SHE": 2. structure of a physically-based, distributed modelling system, *J. Hydrol.*, *87*, 61–77.
- Aerts, J. C. J. H., M. Kriek, and M. Schepel (1999), STREAM (Spatial Tools for River Basins and Environment and Analysis of Management Options): "set up and requirements", *Phys. Chem. Earth*, *24*, 591–595.
- Aerts, J. C. J. H., H. Renssen, P. J. Ward, H. de Moel, E. Odada, L. M. Bouwer, and H. Goosse (2006), Sensitivity of global river discharges under holocene and future climate conditions, *Geophys. Res. Lett.*, *33*, L19401, doi:10.1029/2006GL027493.
- Andersen Jr., W. P., and R. E. Emanuel (2008), Effect of interannual and interdecadal climate oscillations on groundwater in North Carolina, *Geophys. Res. Lett.*, *35*, L23402, doi:10.1029/2008GL036054.
- Arpe, K., and E. Roeckner (1999), Simulation of the hydrological cycle over Europe: model validation and impacts of increasing greenhouse gases, *Adv. Water Res.*, *23*, 105–119, doi:10.1016/S0309-1708(99)00015-9.
- Aryal, S. K., E. M. O'Loughlin, and R. G. Mein (2002), A similarity approach to predict landscape saturation in catchments, *Water Resour. Res.*, *38*(10), 1208, doi:10.1029/2001WR000864.
- Avissar, R., and R. A. Pielke (1989), A parameterization of heterogeneous land surface for atmospheric numerical models and its impact on regional meteorology, *Mon. Weather. Rev.*, *117*, 2113–2136.
- Barnett, T. P., and D. W. Pierce (2008), When will Lake Mead go dry?, *Water Resour. Res.*, *44*, W03201, doi:10.1029/2007WR006704.
- Barnett, T. P., J. C. Adam, and D. P. Lettenmaier (2005), Potential impacts of a warming climate on water availability in snow-dominated regions, *Nature*, *438*, 303–309, doi:10.1038/nature04141.
- Beersma, J. J. (2002), Rainfall generator for the Rhine basin: Description of 1000-year simulations, *Tech. Rep. 186-V*, KNMI.
- Beersma, J. J., T. A. Buishand, and R. Wojcik (2001), Rainfall generator for the Rhine basin: Multi-site simulation of daily weather variables by nearest-neighbour resampling., in *Generation of hydrometeorological reference conditions for the assessment of flood hazard in large river basins*, edited by P. Krahe and D. Herpertz, pp. 69–77, Lelystad, the Netherlands.

- Bergström, S., and A. Forsman (1973), Development of a conceptual deterministic rainfall-runoff model, *Nord. Hydrol.*, 4, 147–170.
- Berne, A., R. Uijlenhoet, and P. A. Troch (2005), Similarity analysis of subsurface flow response of hillslopes with complex geometry, *Water Resour. Res.*, 41, W09410, doi:10.1029/2004WR003629.
- Beven, K. J. (2001), *Rainfall-runoff modelling: the primer*, John Wiley & Sons, Ltd., Chichester, West Sussex, England, U.K.
- Beven, K. J., and M. J. Kirkby (1979), A physically based variable contributing area model of basin hydrology, *Hydrol. Sci. Bull.*, 24(1), 43–69.
- Bierkens, M. F. P., and B. J. J. M. van den Hurk (2007), Groundwater convergence as a possible mechanism for multi-year persistence in rainfall, *Geophys. Res. Lett.*, 34, doi:10.1029/2006GL028396.
- Bogaart, P. W., and M. Guardiola (2007), *The hsB toolkit in MATLAB*, Wageningen University.
- Bogaart, P. W., and P. A. Troch (2006), Curvature distribution within hillslopes and catchments and its effect on the hydrological response, *Hydrol. Earth Syst. Sci.*, 10, 925–936.
- Bondeau, A., et al. (2007), Modelling the role of agriculture for the 20th century global terrestrial carbon balance, *Global Change Biology*, 13, 679–706, doi:doi: 10.1111/j.1365-2486.2006.01305.x.
- Bosch, J. M., and J. D. Hewlett (1982), A review of catchment experiments to determine the effect of vegetation changes on water yield and evapotranspiration, *J. Hydrol.*, 55, 3–23.
- Bouwer, L. M., J. C. J. H. Aerts, P. Droogers, and A. J. Dolman (2006), Detecting the long-term impacts from climate variability and increasing water consumption on runoff in the Krishna river basin (India), *Hydrol. Earth Syst. Sci.*, 10, 703–713.
- Bouwer, L. M., J. E. Vermaat, and J. C. H. Aerts (2008), Regional sensitivities of mean and peak river discharge to climate variability in Europe, *J. Geophys. Res.*, 113, D19103, doi:10.1029/2008JD030301.
- Bradshaw, C. J. A., N. S. Sodhi, K. S.-H. Peh, and B. W. Brook (2007), Global evidence that deforestation amplifies flood risk and severity in the developing world, *Global Change Biol.*, 13, 1–17, doi:10.1111/j.1365-2486.2007.01446.x.
- Breuer, L., K. Eckhardt, and H.-G. Frede (2003), Plant parameter values for models in temperate climates, *Ecol. Model.*, 169, 237–293, doi:10.1016/S0304-3800(03)00274-6.
- Bronstert, A., D. Niehoff, and G. Bürger (2002), Effects of climate and land-use change on storm runoff generation: present knowledge and modelling capabilities, *Hydrol. Proc.*, 16, 509–529, doi:10.1002/hyp.326.
- Bronstert, A., et al. (2007), Multi-scale modelling of land-use change and river training effects on floods in the Rhine basin, *River. Res. Applic.*, 23, 1102–1125, doi:10.1002/rra.1036.
- Brooks, R. H., and A. T. Corey (1964), *Hydraulic properties of porous media*, Colorado State University, Fort Collins, USA.
- Brutsaert, W. (2005), *Hydrology: an introduction*, Cambridge University press, Cambridge, U.K.

- Buishand, T. A., and G. Lenderink (2004), Estimation of future discharges of the river Rhine in the SWURVE project, *Tech. Rep. TR-273*, KNMI.
- Cañon, J., J. González, and J. Valdés (2007), Precipitation in the Colorado River Basin and its low frequency associations with PDO and ENSO signals, *J. Hydrol.*, 333, 252–264, doi:10.1016/j.jhydrol.2006.08.015.
- Campbell, G. S. (1974), A simple method for determining unsaturated conductivity from moisture retention data, *Soil Sci.*, 117, 311–314.
- Cayan, D. R., K. T. Redmond, and L. G. Riddle (1999), ENSO and hydrologic extremes in the Western United States, *J. Climate*, 12, 2881–2893.
- Chahine, M. T. (1992), The hydrological cycle and its influence on climate, *Nature*, 359, 373–380.
- Christensen, J. H., F. Boberg, O. B. Christensen, and P. Lucas-Picher (2008), On the need for bias correction of regional climate change projections of temperature and precipitation, *Geophys. Res. Lett.*, 35, L20709, doi:10.1029/2008GL035694.
- Christensen, N. S., A. W. Wood, N. Voisin, D. P. Lettenmaier, and R. N. Palmer (2004), The effects of climate change on the hydrology and water resources of the Colorado river basin, *Clim. Change*, 62, 337–363.
- Claessens, L., C. Hopkinson, E. Rastetter, and J. Vallino (2006), Effect of historical changes in land use and climate on the water budget of an urbanizing watershed, *Water Resour. Res.*, 42, W03426, doi:10.1029/2005WR004131.
- Clapp, R. B., and G. M. Hornberger (1978), Empirical equations for some soil hydraulic properties, *Water Resour. Res.*, 14(4), 601–604.
- Clark, C. (1987), Deforestation and floods, *Environ. Conserv.*, 14(1), 67–69.
- Cole, J. E., J. T. Overpeck, and E. R. Cook (2002), Multiyear La Niña events and persistent drought in the contiguous United States, *Geophys. Res. Lett.*, 29(13), 1647, doi:10.1029/2001GL013561.
- Cook, E., C. Woodhouse, C. M. Eakin, D. Meko, and D. Stahle (2004), Long-term aridity changes in the Western United States, *Science*, 306, 1015–1018, doi:10.1126/science.1102586.
- Covey, C., K. M. AchutaRao, U. Cubasch, P. Jones, S. J. Lambert, M. E. Mann, T. J. Philips, and K. E. Taylor (2003), An overview of results from the Coupled Model Intercomparison Project, *Global Planet. Change*, 37, 103–133, doi:10.1016/S092108181(02)00193-5.
- Cressie, N. A. C. (1991), *Statistics for spatial data*, John Wiley & Sons, Inc.
- Cuo, L., D. P. Lettenmaier, B. V. Mattheussen, P. Storck, and M. Wiley (2008), Hydrologic prediction for urban watersheds with the Distributed Hydrology-Soil-Vegetation Model, *Hydrol. Proc.*, 22, 4205–4213, doi:10.1002/hyp.7023.
- Daamen, K., et al. (1997), Impact of climate change on hydrological regimes and water resources management in the Rhine basin, *Tech. Rep. I-16*, CHR.
- Dai, Y., et al. (2003), The Common Land Model, *B. Am. Meteorol. Soc.*, 84, 1013–1023.

- de Wit, M. J. M., and T. A. Buishand (2007), Generator of rainfall and discharge extremes (GRADE) for the Rhine and Meuse basins., *Tech. rep.*, Rijkswaterstaat RIZA report 2007.027/KNMI publication 218, Lelystad, The Netherlands.
- de Wit, M. J. M., B. van den Hurk, P. M. M. Warmerdam, P. J. J. F. Torfs, E. Roulin, and W. P. A. van Deursen (2007), Impact of climate change on low-flows in the river Meuse, *Clim. Change*, doi:10.1007/S10584-006-9195-2.
- Deardorff, J. W. (1978), Efficient prediction of ground surface temperature and moisture, with inclusion of a layer of vegetation, *J. Geophys. Res.*, 83(C4), 1889–1903.
- Déqué, M., et al. (2007), An intercomparison of regional climate simulations for Europe: assessing uncertainties in model projections, *Clim. Change*, 81, 53–70, doi:10.1007/S10584-006-9228-x.
- DeWalle, D. R., B. R. Swistock, T. E. Johnson, and K. J. McGuire (2000), Potential effects of climate change and urbanization on mean annual streamflow in the United States, *Water Resour. Res.*, 36(9), 2655–2664, doi: 10.1029/2000WR900134.
- Dibike, Y. B., and P. Coulibaly (2005), Hydrologic impact of climate change in the Saguenay watershed: comparison of downscaling methods and hydrologic models, *J. Hydrol.*, 307, 1445–1463, doi: 10.1016/j.hydrol.2004.10.012.
- Dickinson, R. E., A. Henderson-Sellers, P. J. Kennedy, and M. Wilson (1986), Biosphere-atmosphere transfer scheme (BATS) for the NCAR community climate model, *Tech. Rep. TN-275-293*, NCAR, Boulder, Colorado.
- Dow, C. L., and D. R. DeWalle (2000), Trends in evaporation and Bowen ratio on urbanizing watersheds in eastern United States, *Water Resour. Res.*, 36(7), 1835–1843.
- Eagleson, P. S. (1978), Climate, soil and vegetation, 3, A simplified model of soil moisture movement in the liquid phase, *Water Resour. Res.*, 14(5), 722–730.
- Eberle, M., H. Buiteveld, J. Beersma, P. Krahe, and K. Wilke (2002), Estimation of extreme floods in the river rhine basin by combining precipitation-runoff modelling and a rainfall generator, in *Proceedings International Conference on Flood Estimation*, edited by M. S. et al., CHR-Report No. II-17, pp. 459–467, International Commission for the Hydrology of the Rhine Basin (CHR), Lelystad, Netherlands, Berne, Switzerland.
- Eickhout, B., M. G. J. den Elzen, and G. J. J. Kreileman (2004), The atmosphere-ocean system of IMAGE 2.2, *Tech. Rep. 481508017*, RIVM, P.O. Box 1, 3720 BA Bilthoven, The Netherlands.
- Eickhout, B., H. van Meijl, A. Tabeau, and T. van Rheenen (2007), Economic and ecological consequences of four European land use scenarios, *Land Use Policy*, 24, 562–575, doi:10.1016/j.landusepol.2006.01.004.
- Ekström, M., P. D. Jones, H. j. Fowler, G. Lenderink, T. A. Buishand, and D. Conway (2007), Regional climate model data used within the SWURVE project 1: projected changes in seasonal patterns and estimation of PET, *Hydrol. Earth Syst. Sci.*, 11, 1069–1083.
- Eltahir, E. A. B., and R. L. Bras (1993), A description of rainfall interception over large areas, *J. Climate*, 6, 1002–1008.
- Entekhabi, D., and P. S. Eagleson (1989), Land surface hydrology parameterization for atmospheric general circulation models including subgrid scale spatial variability, *J. Climate*, 2, 816–831.

- Famiglietti, J. S., and E. F. Wood (1994), Multi-scale modeling of spatially-variable water and energy balance processes, *Water Resour. Res.*, 30, 3061–3078.
- Fan, Y., G. Miguez-Macho, C. P. Weaver, R. Walko, and A. Robock (2007), Incorporating water table dynamics in climate modeling: 1. Water table observations and the equilibrium water table, *J. Geophys. Res.*, 112, D10125, doi:10.1029/2006JD008111.
- Fleig, A. K., L. M. Tallaksen, H. Hisdal, and S. Demuth (2006), A global evaluation of streamflow drought characteristics, *Hydrol. Earth Syst. Sci.*, 10, 535–552.
- Franchini, M., J. Wendling, C. Obled, and E. Todini (1996), Physical interpretation and sensitivity analysis of the TOPMODEL, *J. Hydrol.*, 175, 293–338.
- Gershunov, A., and T. P. Barnett (1998), Interdecadal modulation of ENSO teleconnections, *Bull. Amer. Meteor. Soc.*, 79(12), 2715–2725.
- Gerten, D., S. Schaphoff, U. Haberlandt, W. Lucht, and S. Sitch (2004), Terrestrial vegetation and water balance - hydrological evaluation of a dynamic global vegetation model, *J. Hydrol.*, 286, 249–270, doi:10.1016/j.jhydrol.2003.09.029.
- Gilabert, M. A., F. J. García-Haro, and J. Meliá (2000), A mixture modeling approach to estimate vegetation parameters for heterogeneous canopies in remote sensing, *Remote Sens. Environ.*, 72, 328–345.
- Gochis, D. J., L. Brito-Castillo, and W. J. Shuttleworth (2007), Correlations between sea-surface temperatures and warm season streamflow in northwest Mexico, *Int. J. Climatol.*, 27, 883–901, doi:10.1002/joc.1436.
- Gurtz, J., M. Zappa, K. Jasper, H. Lang, M. Verbunt, A. Badoux, and T. Vitvar (2003), A comparative study in modelling runoff and its components in two mountainous catchments, *Hydrol. Proc.*, 17, 297–311, doi:10.1002/hyp.1125.
- Haan, C. T. (1977), *Statistical methods in hydrology*, Iowa State University Press, Ames, Iowa, U.S.A.
- Hamlet, A. F., and D. P. Lettenmaier (2005), Production of temporally consistent gridded precipitation and temperature fields for the continental United States, *J. Hydrometeorol.*, 6, 330–336.
- Hamlet, A. F., P. W. Mote, M. P. Clark, and D. P. Lettenmaier (2007), Twentieth-century trends in runoff, evapotranspiration and soil moisture in the Western United States, *J. Climate*, 20, 1468–1486.
- Han, S.-C., C. K. Shum, C. Jekeli, and D. Alsdorf (2005), Improved estimation of terrestrial water storage changes from GRACE, *Geophys. Res. Lett.*, 32, L07302, doi:10.1029/2005GL022382.
- Hansen, J., G. Russell, D. Rind, P. Stone, A. Lacis, S. Lebedeff, R. Ruedy, and L. Travis (1983), Efficient three-dimensional global models for climate studies: Models I and II, *Mon. Weather. Rev.*, 111, 609–662.
- Hasan, S., P. A. Troch, R. Uijlenhoet, R. Hurkmans, and M. Durcik (in prep.), The potential of distributed GRACE measurements to estimate spatially variable terrestrial water storage changes in the Colorado River Basin.
- Hay, L. E., M. P. Clark, R. L. Wilby, W. J. G. Jr., G. H. Leavesly, Z. Pan, R. W. Arritt, and E. S. Takle (2002), Use of regional climate model output for hydrologic simulations, *J. Hydrometeorol.*, 3, 571–590.

- Hidalgo, H. G., and J. A. Dracup (2003), ENSO and PDO effects on hydroclimatic variations of the Upper Colorado River Basin, *J. Hydrometeorol.*, 4, 5–23.
- Hirschi, M., S. I. Seneviratne, and C. Schär (2006), Seasonal variations in terrestrial water storage for major midlatitude river basins, *J. Hydrometeorol.*, 7, 39–60.
- Hisdal, H., L. M. Tallaksen, B. Clausen, E. Peters, and A. Gustard (2004), *Hydrological drought: processes and estimation methods for streamflow and groundwater*, chap. 5, pp. 139–198, first ed., Elsevier, Amsterdam, The Netherlands.
- Hu, Q., and S. Feng (2001), Variations of teleconnection of ENSO and interannual variation in summer rainfall in the central United States, *J. Climate*, 14, 2469–2480.
- Hundecha, Y., and A. Bárdossy (2004), Modeling of the effect of land use changes on the runoff generation of a river basin through parameter regionalization of a watershed model, *J. Hydrol.*, 292, 281–295, doi: 10.1016/j.jhydrol.2004.01.002.
- Hurkmans, R., C. Paniconi, and P. A. Troch (2006), Numerical assessment of a dynamical relaxation data assimilation scheme for a catchment hydrological model, *Hydrol. Proc.*, 20(3), 549–563, doi:10.1002/hyp5921.
- Hurkmans, R. T. W. L., H. de Moel, J. C. J. H. Aerts, and P. A. Troch (2008), Water balance versus land surface model in the simulation of Rhine river discharges, *Water Resour. Res.*, 44, W01418, doi: 10.1029/2007WR006168.
- Hurkmans, R. T. W. L., W. Terink, R. Uijlenhoet, E. J. Moors, P. A. Troch, and P. H. Verburg (2009a), Effects of land use changes on streamflow generation in the Rhine basin, *Water Resour. Res.*, in press.
- Hurkmans, R. T. W. L., W. Terink, R. Uijlenhoet, P. J. J. F. Torfs, D. Jacob, and P. A. Troch (2009b), Changes in streamflow dynamics in the Rhine basin during the 21st century under climate scenarios, *J. Climate*, submitted.
- IPCC (2000), Special report on emissions scenarios - a special report of working group III of the Intergovernmental Panel on Climate Change.
- IPCC (2007), Fourth assessment report: Climate change 2007: Climate change impacts, adaptation and vulnerability. Summary for policy makers.
- Jackson, T. J., R. Hurkmans, A. Hsu, and M. Cosh (2004), Soil moisture algorithm validation using data from the Advanced Microwave Scanning Radiometer (AMSR-E) in Mongolia, *Italian journal of Remote Sensing*, 30, 23–32.
- Jacob, D. (2001), A note to the simulation of the annual and inter-annual variability of the water budget over the Baltic Sea drainage basin, *Meteorol. Atmos. Phys.*, 77, 61–73.
- Jacob, D., H. Göttel, S. Kotlarski, P. Lorenz, and K. Sieck (2008), Klimaauswirkungen und anpassung in Deutschland – Phase 1: erstellung regionaler Klimaszenarien für Deutschland, *Forschungsbericht 204 41 138 UBA-FB 000969*, Bundes Umwelt Amt.
- Jacob, D., et al. (2007), An intercomparison of regional climate models for Europe: model performance in present-day climate, *Clim. Change*, 81, 31–52, doi:10.1007/S10584-006-9213-4.

- Johansson, A. (2007), Prediction skill of the NAO and PNA from daily to seasonal time scales, *J. Climate*, 20, 1957–1975, doi:10.1175/JCLI4072.1.
- Kleinn, J., C. Frei, J. Gurtz, D. Lüthi, P. L. Vidale, and C. Schär (2005), Hydrologic simulations in the Rhine basin driven by a regional climate model, *J. Geophys. Res.*, 110, D04102, doi:10.1029/2004JD005143.
- Koster, R., and P. C. D. Milly (1997), The interplay between transpiration and runoff formulations in land surface schemes used with atmospheric models, *J. Climate*, 10, 1578–1591.
- Koster, R., and M. Suarez (1996), Technical report series on global modelling and data assimilation: energy and water balance calculations in the Mosaic LSM, *Tech. Rep. Volume 9*, NASA Goddard Space Flight Center, Greenbelt, MD, USA.
- Koster, R. D., M. J. Suarez, A. Ducharme, M. Stieglitz, and P. Kumar (2000), A catchment-based approach to modeling land surface processes in a general circulation model. I. Model structure, *J. Geophys. Res.*, 105(D20), 24,809–24,822, doi:10.1029/2000JD900327.
- Kustas, W. P., A. Rango, and R. Uijlenhoet (1994), A simple energy budget algorithm for the snowmelt runoff model, *Water Resour. Res.*, 30(5), 1515–1527.
- Kwadijk, J. (1993), The impact of climate change on the discharge of the river Rhine, Ph.D. thesis, University of Utrecht.
- Kwadijk, J., and H. Middelkoop (1994), Estimation of impact of climate change on the peak discharge probability of the river Rhine, *Clim. Change*, 27, 199–224.
- Kwadijk, J., and J. Rotmans (1995), The impact of climate change on the river Rhine: a scenario study, *Clim. Change*, 30, 397–425.
- Lambert, S. J., and G. J. Boer (2001), CMIP1 evaluation and intercomparison of coupled climate models, *Clim. Dyn.*, 17, 83–106.
- Lammersen, R. (2004), Grensoverschrijdende effecten van extreem hoogwater op de Niederrhein, *Tech. Rep. ISBN: 9036956390*, Duits-Nederlandse Werkgroep Hoogwater.
- Laurance, W. F. (2007), Forests and floods, *Nature*, 449, 409–410.
- Leander, R., and T. A. Buishand (2007), Resampling of regional climate model output for the simulation of extreme river flows, *J. Hydrol.*, 332, 487–496, doi:10.1016/j.jhydrol.2006.08.006.
- Lenderink, G., T. A. Buishand, and W. P. van Deursen (2007), Estimates of future discharges of the river Rhine using two scenario methodologies: direct versus delta approach, *Hydrol. Earth Syst. Sci.*, 11(3), 1145–1159.
- Liang, X., and Z. Xie (2001), A new surface runoff parameterization with subgrid-scale soil heterogeneity for land surface models, *Adv. Water Resour.*, 24, S0309-1708(01)00021-X.
- Liang, X., D. P. Lettenmaier, E. F. Wood, and S. J. Burges (1994), A simple hydrologically based model of land surface water and energy fluxes for general circulation models, *J. Geophys. Res.*, 99(D7), 14,415–14,458.
- Liang, X., D. P. Lettenmaier, and E. F. Wood (1996), One-dimensional statistical dynamic representation of sub-grid spatial variability of precipitation in the two-layer Variable Infiltration Capacity model, *J. Geophys. Res.*, 101(D16), 21,403–21,422.

- Liang, X., Z. Xie, and M. Huang (2003), A new parameterization for surface and groundwater interactions and its impact on water budgets with the Variable Infiltration Capacity (VIC) land surface model, *J. Geophys. Res.*, *108(D16)*, doi:10.1029/2002JD003090.
- Liang, X., et al. (1998), The Project for Intercomparison of Land-surface Parameterization Schemes (PILPS) phase 2(c) Red-Arkansas river basin experiment: 2. Spatial and temporal analysis of energy fluxes, *Global Planet. Change*, *19*, 137–159, doi:10.1016/S0921-8181(98)00045-9.
- Lindström, G., B. Johansson, M. Gardelin, and S. Bergström (1997), Development and test of the distributed HBV-96 hydrological model, *J. Hydrol.*, *201*, 272–288, doi:10.1016/S0022-1694(97)00041-3.
- Lohmann, D., R. Nolte-Holube, and E. Raschke (1996), A large-scale horizontal routing model to be coupled to land surface parameterization schemes, *Tellus*, *48A*, 708–721.
- Lohmann, D., E. Raschke, B. Nijssen, and D. P. Lettenmaier (1998a), Regional scale hydrology: I. Application of the VIC-2L model coupled to a routing model, *Hydrol. Sci. J.*, *43(1)*, 131–141.
- Lohmann, D., E. Raschke, B. Nijssen, and D. P. Lettenmaier (1998b), Regional scale hydrology: II. Application of the VIC-2L model to the Weser river, Germany, *Hydrol. Sci. J.*, *43(1)*, 143–158.
- Lohmann, D., et al. (1998c), The Project for Intercomparison of Land-surface Parameterization Schemes (PILPS) phase 2(c) Red-Arkansas river basin experiment: 3. Spatial and temporal analysis of water fluxes, *Global Planet. Change*, *19*, 161–179.
- Lohmann, D., et al. (2004), Streamflow and water balance intercomparisons of four land surface models in the North American Land Data Assimilation System project, *J. Geophys. Res.*, *109*, D07S91, doi:10.1029/2003JD003517.
- Lorenz, P., and D. Jacob (2005), Influence of regional scale information on the global circulation: a two-way nesting climate simulation, *Geophys. Res. Lett.*, *32*, L18706, doi:10.1029/2005GL023351.
- Lyon, S. W., and P. A. Troch (2007), Hillslope subsurface flow similarity: Real world tests of the hillslope Péclet number, *Water Resour. Res.*, *43*, W07450, doi:10.1029/2006WR005323.
- MacDonald, G. M., and R. A. Case (2005), Variations in the Pacific Decadal Oscillation over the past millenium, *Geophys. Res. Lett.*, *32*, L08703, doi:10.1029/2005GL022478.
- Maity, R., and D. N. Kumar (2008), Basin-scale stream-flow forecasting using the information of large-scale atmospheric circulation phenomena, *Hydrol. Earth Syst. Sci.*, *22*, 643–650.
- Manabe, S. (1969), Climate and circulation, I. The atmospheric circulation and the hydrology of the earth's surface, *Mon. Weather. Rev.*, *97*, 739–774.
- Mantua, N. J., and S. R. Hare (2002), The Pacific Decadal Oscillation, *J. Oceanogr.*, *58*, 35–44.
- Mantua, N. J., S. R. Hare, Y. Zhang, J. M. Wallace, and R. C. Francis (1997), A Pacific interdecadal climate oscillation with impact on salmon production, *Bull. Amer. Meteor. Soc.*, *78(6)*, 1069–1079.
- Martinez, J., and A. Rango (1986), Parameter values for snowmelt runoff modelling, *J. Hydrol.*, *84*, 197–219.

- Mason, S. J., and L. Goddard (2001), Probabilistic precipitation anomalies associated with ENSO, *Bull. Amer. Meteor. Soc.*, 82(4), 619–638.
- Matheussen, B., R. L. Kirschbaum, I. A. Goodman, G. M. O'Donnell, and D. P. Lettenmaier (2000), Effects of land cover change on streamflow in the interior Columbia river basin (U.S.A. and Canada), *Hydrol. Proc.*, 14, 867–885.
- Maxwell, R. M., and S. J. Kollet (2008), Interdependence of groundwater dynamics and land-energy feedbacks under climate change, *Nature Geosciences*, 1, 665–669, doi:10.1038/ngeo315.
- Maxwell, R. M., and N. L. Miller (2005), Development of a coupled land surface and groundwater model, *J. Hydrometeorol.*, 6(3), 233–247, doi:10.1175/JHM422.1.
- McCabe, G. J., M. A. Palecki, and J. L. Betancourt (2004), Pacific and Atlantic Ocean influences on multidecadal drought frequency in the United States, *PNAS*, 101(12), 4136–4141, doi:10.1073/pnas.0306738101.
- McDonnell, J. J., et al. (2007), Moving beyond heterogeneity and process complexity: A new vision for watershed hydrology, *Water Resour. Res.*, 43, W07301, doi:10.1029/2006WR005467.
- Middelkoop, H., et al. (2001), Impact of climate change on hydrological regimes and water resources management in the Rhine basin, *Clim. Change*, 49, 105–128.
- Miguez-Macho, G., Y. Fan, C. P. Weaver, R. Walko, and A. Robock (2007), Incorporating water table dynamics in climate modelling, part II: Formulation, validation and soil moisture simulation, *J. Geophys. Res.*, 112, D13108, doi:10.1029/2006JD008112.
- Milly, P. C. D. (1986), An event-based simulation model of moisture and energy fluxes at a bare soil surface, *Water Resour. Res.*, 22(12), 1680–1692.
- Milly, P. C. D., K. A. Dunne, and A. Vecchia (2005), Global pattern of trends in streamflow and water availability in a changing climate, *Nature*, 438, 347–350.
- Misirli, F., H. V. Gupta, S. Sorooshian, and M. Thiermann (2003), Bayesian recursive estimation of parameter and output uncertainty for watershed models., in *Calibration of watershed models*, vol. 6, edited by Q. D. et al., pp. 113–124, American Geophysical Union, Washington DC.
- Monteith, J. L. (1965), Evaporation and environment, in *Proceedings of the 19th symposium of the Society for Experimental Biology*, pp. 205–233, Cambridge University Press, New York, NY, USA.
- Moore, R. J., and R. T. Clarke (1981), A distribution function approach to rainfall-runoff modelling, *Water Resour. Res.*, 17, 1367–1382.
- Mücher, S., K. Steinnocher, J.-L. Champeaux, S. Griguolo, K. Wester, C. Heunks, and V. van Katwijk (2000), Establishment of a 1-km Pan-European Land Cover database for environmental monitoring, in *Proceedings of the Geoinformation for All XIXth Congress of the International Society for Photogrammetry and Remote Sensing (ISPRS)*, *Int. Arch. Photogramm. Remote Sens.*, vol. 33, edited by K. J. Beek and M. Molenaar, pp. 702–709, GISC, Amsterdam.
- Nash, J. E., and I. V. Sutcliffe (1970), River flow forecasting through conceptual models. Part I - a discussion of principles, *J. Hydrol.*, 10, 282–290.

- Nelder, J. A., and R. Mead (1965), A simplex method for function minimalization, *Computer Journal*, 7, 308–313.
- Newman, M. (2007), Interannual to decadal predictability of tropical and north pacific sea surface temperatures, *J. Climate*, 20, 2333–2355, doi:10.1175/JCLI4165.1.
- Niehoff, D., U. Fritsch, and A. Bronstert (2002), Land-use impacts on storm-runoff generation: scenarios of land-use change and simulation of hydrological response in a meso-scale catchment in SW-Germany, *J. Hydrol.*, 267, 80–93, doi:10.1016/S0022-1694(02)00142-7.
- Nijssen, B., D. P. Lettenmaier, X. Liang, S. W. Wetzel, and E. F. Wood (1997), Streamflow simulation for continental-scale river basins, *Water Resour. Res.*, 33(4), 711–724.
- Nijssen, B., G. M. O'Donnell, D. P. Lettenmaier, D. Lohmann, and E. F. Wood (2001), Predicting the discharge of global rivers, *J. Climate*, 14, 3307–3323.
- Niu, G.-Y., and Z.-L. Yang (2006), Assessing a land surface model's improvements with GRACE estimates, *Geophys. Res. Lett.*, 33, L07401, doi:10.1029/2005GL025555.
- O'Connell, P. E. (1991), *Recent advances in the modeling of hydrologic systems*, chap. A historical perspective, pp. 3–30, Kluwer, Dordrecht.
- Oki, T., and S. Kanae (2006), Global hydrological cycles and world water resources, *Science*, 313, 1068–1072.
- Okin, G. S., and M. C. Reheis (2002), An ENSO predictor of dust emission in the southwestern United States, *Geophys. Res. Lett.*, 29(9), 1332, doi:10.1029/2001GL014494.
- Paniconi, C., and E. F. Wood (1993), A detailed model for simulation of catchment scale subsurface hydrologic processes, *Water Resour. Res.*, 29(6), 1601–1620.
- Paniconi, C., P. A. Troch, E. E. van Loon, and A. G. J. Hilberts (2003), Hillslope-storage Boussinesq model for subsurface flow and variable source areas along complex hillslopes: 2. Intercomparison with a three-dimensional Richards equation model, *Water Resour. Res.*, 39(11), doi:10.1029/2002WR001730.
- Penman, H. L. (1948), Natural evaporation from open water, bare soil and grass, in *Proceedings of the Royal Society*, vol. A193, pp. 120–146, London.
- Perkins, S. E., A. J. Pitman, N. J. Holbrook, and J. McAneney (2007), Evaluation of the AR4 climate models simulated daily maximum temperature, minimum temperature, and precipitation over Australia using probability density functions, *J. Climate*, 20, 4356–4376.
- Pfister, L., J. Kwadijk, A. Musy, A. Bronstert, and L. Hoffmann (2004), Climate change, land use change and runoff prediction in the Rhine-Meuse basins, *River Res. Applic.*, 20, 229–241, doi:10.1002/rra/775.
- Pitman, A. J., et al. (1999), Key results and implications from Phase 1(c) of the project for intercomparison of land-surface parameterization schemes., *Clim. Dyn.*, 15, 673–684.
- Power, S., M. Haylock, R. Colman, and X. Wang (2006), The predictability of interdecadal changes in ENSO activity and ENSO teleconnections, *J. Climate*, 19, 4755–4771.
- Quilbe, R., J.-S. M. A. N. Rousseau, S. Savary, and M. S. Garbouj (2008), Hydrological responses of a watershed to historical land use evolution and future land use scenarios under climate change conditions, *Hydrol. Earth Syst. Sci.*, 12, 101–110.

- Rasmussen, J. B. T., V. J. Polyak, and Y. Asmerom (2006), Evidence for Pacific-modulated precipitation variability during the late Holocene from the southwestern USA, *Geophys. Res. Lett.*, *33*, L08701, doi:10.1029/2006GL025714.
- Redmond, K. T., and R. W. Koch (1991), Surface climate and streamflow variability in the western United States and their relationship to large-scale circulation indices, *Water Resour. Res.*, *27*(9), 2381–2399.
- Reichler, T., and J. Kim (2008), How well do coupled models simulate today's climate?, *Bull. Amer. Meteor. Soc.*, *89*(3), 303–311, doi:10.1175/BAMS-89-3-303.
- Reynolds, C. A., T. J. Jackson, and W. J. Rawls (2000), Estimating water-holding capacities by linking the Food and Agriculture Organization soil map of the world with global pedon databases and continuous pedotransfer functions, *Water Resour. Res.*, *36*(12), 3653–3662.
- Rounsevell, M. D. A., et al. (2006), A coherent set of future land use change scenarios for Europe, *Agr. Ecosyst. Environ.*, *114*, 57–68, doi:10.1016/j.agee.2005.11.027.
- Saurral, R. I., V. R. Barros, and D. P. Lettenmaier (2008), Land use impact on the Uruguay River discharge, *Geophys. Res. Lett.*, *35*, L12401, doi:10.1029/2008GL033707.
- Seager, R., et al. (2007), Model projections of an imminent transition to a more arid climate in southwestern North America, *Science*, *316*, 1181–1184, doi:10.1126/science.1139601.
- Sellers, P. J., Y. Mintz, Y. C. Sud, and A. Dalcher (1986), A simple biosphere model (SiB) for use within general circulation models, *J. Atmos. Sci.*, *43*, 505–531.
- Seneviratne, S. I., P. Viterbo, D. Luth, and C. Schär (2004), Inferring changes in terrestrial water storage using ERA-40 reanalysis data: the Mississippi River basin, *J. Climate*, *17*, 2039–2057.
- Seneviratne, S. I., D. Lüthi, M. Litschi, and C. Schär (2006), Land-atmosphere coupling and climate change in Europe, *Nature*, *443*(14), 205–209.
- Shabalova, M. V., W. P. A. van Deursen, and T. A. Buishand (2003), Assessing future discharge of the river Rhine using regional climate model integrations and a hydrological model, *Climate Res.*, *23*, 233–246.
- Sheffield, J., and E. F. Wood (2007), Characteristics of global and regional drought, 1950–2000: analysis of soil moisture data from off-line simulation of the terrestrial hydrologic cycle, *J. Geophys. Res.*, *112*, D17115, doi:10.1029/20065JD008288.
- Sivalapan, M. (2003), Process complexity at hillslope scale, process simplicity at the watershed scale: is there a connection?, *Hydrol. Proc.*, *17*, 1037–1041, doi:10.1002/hyp.5109.
- Smakthin, V. (2001), Low flow hydrology: a review, *J. Hydrol.*, *240*, 147–186, doi:10.1016/S0022-1694(00)00340-1.
- Sprokkereef, E. (2001a), Extension of the flood forecasting model FloRIJN, *Tech. Rep. NCR Publication 12-2001*, NCR.
- Sprokkereef, E. (2001b), Eine hydrologische Datenbank für das Rheingebiet, International Commission for the Hydrology of the Rhine basin (CHR).
- Sun, Y., S. Solomon, A. Dai, and R. W. Portman (2006), How often does it rain?, *J. Climate*, *19*, 916–934.

- Swenson, S. C., and P. C. D. Milly (2006), Climate model biases in seasonality of continental water storage revealed by satellite gravimetry, *Water Resour. Res.*, 42, W03201, doi:10.1029/2005WR004628.
- Tallaksen, L. M., and H. A. J. van Lanen (Eds.) (2004), *Hydrological drought: processes and estimation methods for streamflow and groundwater*, no. 48 in *Developments in Water Science*, first ed., Elsevier, Amsterdam, The Netherlands.
- Tallaksen, L. M., H. Madsen, and H. Hisdal (2004), *Hydrological drought: processes and estimation methods for streamflow and groundwater*, chap. 6, pp. 199–271, first ed., Elsevier, Amsterdam, The Netherlands.
- Tapley, B. D., S. Bettadpur, M. Watkins, and C. Reigber (2004), The gravity recovery and climate experiment: mission overview and early results, *Geophys. Res. Lett.*, 31, L09607, doi:10.1029/2004GL019920.
- Tarboton, D. G. (1997), A new method for the determination of flow directions and upslope areas in grid digital elevation models, *Water Resour. Res.*, 33(2), 309–319.
- te Linde, A. H., J. C. J. H. Aerts, R. T. W. L. Hurkmans, and M. Eberle (2008), Comparing model performance of two rainfall-runoff models in the Rhine basin using different atmospheric forcing data sets, *Hydrol. Earth Syst. Sci.*, 12, 943–957.
- Terink, W., R. T. W. L. Hurkmans, R. Uijlenhoet, P. M. M. Warmerdam, and P. J. J. F. Torfs (2008), Bias correction of temperature and precipitation data for regional climate model application to the Rhine basin, *Tech. rep.*, Hydrology and Quantitative Water Management group, Wageningen University, Wageningen, The Netherlands.
- Tetzlaff, D., J. J. McDonnell, S. Uhlenbrook, K. J. McGuire, P. W. Bogaart, F. Naef, A. J. Baerd, S. M. Dunn, and C. Soulsby (2008), Conceptualizing catchment processes: simply too complex?, *Hydrol. Proc.*, 22, 1727–1730, doi:10.1002/hyp.7069.
- Teuling, A. J., and P. A. Troch (2005), Improved understanding of soil moisture variability dynamics, *Geophys. Res. Lett.*, 32, L05404, doi:10.1029/2004GL021935.
- Teuling, A. J., F. Hupet, R. Uijlenhoet, and P. A. Troch (2007), Climate variability effects on spatial moisture dynamics, *Geophys. Res. Lett.*, 34, L06406, doi:10.1029/2006GL029080.
- Thornthwaite, C. W., and J. R. Mather (1957), Instructions and tables for computing potential evapotranspiration and the water balance, *Publications in Climatology*, 10, 183–247.
- Todini, E. (1996), The ARNO rainfall-runoff model, *J. Hydrol.*, 175, 339–382.
- Trenberth, K. (1997a), Using atmospheric budgets as a constraint on surface fluxes, *J. Climate*, 10, 2796–2809.
- Trenberth, K. E. (1997b), The definition of El Niño, *Bull. Amer. Meteor. Soc.*, 78, 2771–2777.
- Trenberth, K. E., A. Dai, R. M. Rasmussen, and D. B. Parsons (2003), The changing character of precipitation, *Bull. Amer. Meteor. Soc.*, 84(9), 1205–1217, doi:10.1175/BAMS-84-9-1205.
- Troch, P. A., J. A. Smith, E. F. Wood, and F. P. de Troch (1994), Hydrologic controls of large floods in a small basin: Central Appalachian case study, *J. Hydrol.*, 156, 285–309.

- Troch, P. A., E. E. van Loon, and A. G. J. Hilberts (2002), Analytical solutions to a hillslope-storage kinematic wave equation for subsurface flow, *Adv. Water Resour.*, 25, 637–649, doi:10.1016/S0309-1708(02)00017-9.
- Troch, P. A., C. Paniconi, and E. E. V. Loon (2003), Hillslope-storage Boussinesq model for subsurface flow and variable source areas along complex hillslopes: 1. Formulation and characteristic response, *Water Resour. Res.*, 39(11), doi:10.1029/2002WR001728.
- Troch, P. A., M. Durcik, S. I. Seneviratne, M. Hirschi, A. J. Teuling, R. Hurkmans, and S. Hasan (2007), New data sets to estimate terrestrial water storage change, *EOS*, 88(45), 469–470.
- Uijlenhoet, R. (1992), A simple surface radiation budget model for a point in snow covered mountainous terrain, Rapport 20, Wageningen University, Vakgroep Waterhuishouding, Nieuwe kanaal 11, 6709 PA, Wageningen, The Netherlands.
- van den Hurk, B., et al. (2005), Soil control on runoff response to climate change in regional climate model simulations, *J. Climate*, 18, 3536–3551.
- van Meijl, H., T. van Rheenen, A. Tabeau, and B. Eickhout (2006), The impact of different policy environments on agricultural land use in Europe, *Agr. Ecosyst. Environ.*, 114, 21–38, doi:10.1016/k.agee/2005.11.006.
- van Ulden, A. P., and G. J. van Oldenborgh (2006), Large-scale atmospheric circulation biases and changes in global climate model simulations and their importance for climate change in Central Europe, *Atmos. Chem. Phys.*, 6, 863–881.
- Verburg, P. H., C. J. E. Schulp, N. Witte, and A. Veldkamp (2006a), Downscaling of land use change scenarios to assess the dynamics of European landscapes, *Agr. Ecosyst. Environ.*, 114, 39–56, doi:10.1016/j.agee.2005.11.024.
- Verburg, P. H., A. Veldkamp, and M. D. A. Rounsevell (2006b), Scenario-based studies of future land use in Europe, *Agr. Ecosyst. Environ.*, 114, 1–6, doi:10.1016/j.agee.2005.11.023.
- Verburg, P. H., B. Eickhout, and H. van Meijl (2008), A multi-scale, multi-model approach for analyzing the future dynamics of European land use, *Ann. Regional Sci.*, 42, 57–77.
- Verstraeten, W. W., B. Muys, J. Feyen, F. Veroustraete, M. Minnaert, L. Meiresonne, and A. D. Schrijver (2005), Comparative analysis of the actual evapotranspiration of Flemish forest and cropland, using the soil water balance model WAVE, *Hydrol. Earth Syst. Sci.*, 9, 225–2241.
- Wagner, T., M. Sivalapan, P. Troch, and R. Woods (2007), Catchment classification and hydrologic similarity, *Geography Compass*, 1, 1–31, doi:10.1111/j.1749-8198.2007.00039.x.
- Walko, R. L., et al. (2000), Coupled atmosphere-biophysics-hydrology models for environmental modeling, *J. of Appl. Meteorol.*, 39, 931–944.
- Ward, P. J., J. C. J. H. Aerts, H. de Moel, and H. Renssen (2007), Verification of a coupled climate-hydrological model against holocene palaeohydrological records, *Global Planet. Change*, 57(3-4), 283–300, doi:10.1016/j.gloplacha.2006.12.002.
- Warrach, K., M. Stieglitz, H.-T. Mengelkamp, and E. Raschke (2002), Advantages of topographically controlled runoff simulation in a soil-vegetation-atmosphere transfer model, *J. Hydrometeorol.*, 3, 131–148.

- Westhoek, H. J., M. van de Berg, and J. A. Bakkes (2006), Scenario development to explore the future of Europe's rural areas, *Agr. Ecosyst. Environ.*, *114*, 7–20, doi:10.1016/j.agee.2005.11.005.
- Wolter, K., and M. S. Timlin (1998), Measuring the strength of ENSO events: how does 1997/98 rank?, *Weather*, *53*(9), 315–323.
- Wood, A. W., A. Kumar, and D. P. Lettenmaier (2005), A retrospective assessment of National Centers for Environmental Prediction climate model-based ensemble hydrologic forecasting in the western United States, *J. Geophys. Res.*, *110*, D04105, doi:10.1029/2004JD004508.
- Wood, E. F. (1995), *Space and time scale variability and interdependencies in hydrological processes*, chap. Heterogeneity and scaling land-atmospheric water and energy fluxes in climate system, pp. 3–19, International hydrology series, Cambridge University Press.
- Wood, E. F., D. P. Lettenmaier, and V. G. Zartarian (1992), A land-surface hydrology parameterization with subgrid variability for General Circulation Models, *J. Geophys. Res.*, *97*(D3), 2717–2728.
- Wood, E. F., et al. (1998), The project for intercomparison of land-surface parameterization schemes (PILPS) Phase-2(c) Red-Arkansas River basin experiment: 1. Experiment description and summary intercomparisons., *Glob. Planet. Change*, *19*, 115–135.
- Xu, C.-Y., and D. Chen (2005), Comparison of seven models for estimation of evapotranspiration and groundwater recharge using lysimeter measurement data in Germany, *Hydrol. Proc.*, *19*, 3717–3734, doi:10.1002/hyp.5853.
- Zeng, X., M. Shaikh, Y. Dai, R. E. Dickinson, and R. Myneni (2002), Coupling of the Common Land Model to the NCAR Community Climate Model, *J. Climate*, *15*(14), 1832–1854.
- Zierl, B., and H. Bugmann (2005), Global change impacts on hydrol. process. in alpine catchments, *Water Resour. Res.*, *41*, W02028, doi:10.1029/2004WR003447.

Curriculum Vitae

Ruud Theodorus Wilhelmus Leonardus Hurkmans, 3 feburari 1980, Someren

- 1992–1998** VWO, Varendonck College, Asten.
- 1998–2004** Studie Bodem, Water & Atmosfeer met specialisatie Hydrologie, Wageningen Universiteit.
- 2001–2004** MSc Geo-information science and Remote Sensing, Wageningen Universiteit.
- 2002** Afstudeeronderzoek Stroomgebiedshydrologie, Wageningen Universiteit, resulterend in *Hurkmans et al.* (2006).
- 2003** Stage Geolink Consulting, Moskou, Rusland.
- 2003** Afstudeeronderzoek Remote Sensing, Hydrology and Remote Sensing Laboratory, Beltsville, MD, Verenigde Staten, resulterend in *Jackson et al.* (2004).
- 2004** Stage Alterra, Wageningen University and Research Centre.
- 2004–2009** Promotie-onderzoek bij de leerstoelgroep Hydrologie en Kwantitatief Waterbeheer, Wageningen Universiteit, resulterend in dit proefschrift.
- 2009–heden** Post-doc bij de leerstoelgroep Hydrologie en Kwantitatief Waterbeheer, Wageningen Universiteit.
- Juni 2009** Diploma Netherlands Research School for the Socio-Economic and Natural Sciences of the Environment (SENSE), met als belangrijke activiteiten:
- Deelname aan de cursus: Climate and the Hydrological cycle (Utrecht, 2005)*
 - Organsiatie van het SENSE Summer Symposium "Kyoto and Beyond" (Ede, 2005)*
 - Verblijf aan de University of Arizona (Tucson, Verenigde Staten, 2006)*
 - Participatie in het National Airborne Field Experiment (NAFE; Australië, 2006)*
 - Deelname aan de cursus: Understanding global environmental change (Hulshorst, 2007)*

List of publications

First-author peer-reviewed articles:

Hurkmans, R., C. Paniconi and P. A. Troch (2006), “Numerical assessment of a dynamical relaxation data assimilation scheme for a catchment hydrological model”, *Hydrol. Proc.*, 20, 549-563, doi:10.1002/hyp5921.

Hurkmans, R. T. W. L., H. de Moel, J. C. J. H. Aerts and P. A. Troch (2008), “Water balance versus land surface model in the simulation of Rhine river discharges”, *Water Resour. Res.*, 44, W01418, doi:10.1029/WR006168.

Hurkmans, R. T. W. L., W. Terink, R. Uijlenhoet, E. J. Moors, P. A. Troch and P. H. Verburg (2009), “Effects of land use changes on streamflow generation in the Rhine basin”, *Water Resour. Res.*, in press.

Hurkmans, R. T. W. L., P. A. Troch, R. Uijlenhoet, P. J. J. F. Torfs, and M. Durcik (2009), “Effects of climate variability on water storage in the Colorado River Basin”, *J. Hydrometeorol.*, submitted.

Hurkmans, R. T. W. L., W. Terink, R. Uijlenhoet, P. J. J. F. Torfs, D. Jacob, and P. A. Troch (2009), “Changes in streamflow dynamics in the Rhine basin in the 21st century under climate scenarios”, *J. Climate*, submitted.

Co-author peer-reviewed articles:

Jackson, T. J., R. Hurkmans, A. Hsu and M. Cosh (2004), “Soil moisture algorithm validation using data from the Advanced Microwave Scanning Radiometer (AMSR-E) in Mongolia”, *Italian journal of Remote Sensing*, 30, 23–32.

te Linde, A. H., J. C. J. H. Aerts, R. T. W. L. Hurkmans and M. Eberle (2008), “Comparing model performance of two rainfall-runoff models in the Rhine basin using different atmospheric forcing data sets”, *Hydrol. Earth Syst. Sci.*, 12, 943-957, <http://www.hydrol-earth-syst-sci.net/12/943/2008/hess-12-943-2008.html>.

Teuling, A. J., R. Uijlenhoet, R. Hurkmans, O. Merlin, R. Panciera, J. Walker and P. A. Troch (2007), “Dry-end surface soil moisture variability during NAFE’06”, *Geophys. Res. Lett.*, L17402, doi:10.1029/2007GL031001.

Troch, P. A., M. Durcik, S. I. Seneviratne, M. Hirschi, A. J. Teuling, R. Hurkmans and S. Hasan (2007), “New datasets to estimate terrestrial water storage change”, *EOS*, 88, 469–470.

Other publications:

Hurkmans, R., Z. Su and T. J. Jackson (2004), *"Evaluation of satellite soil moisture retrieval algorithms using AMSR - E data"*, In: Proceedings of the 2nd international CAHMDA workshop on : the terrestrial water cycle : modelling and data assimilation across catchment scales, October 25-27, 2004, Princeton. / edited by A.J. Teuling, H. Leijnse, P.A. Troch, J. Sheffield and E.F. Wood. pp. 45-49.

Hurkmans, R. T. W. L., P. A. Troch, R. Uijlenhoet and E. Moors (2007), *"Simulating Rhine river discharges using a land surface model"*, CAIWA conference, 12-15 November 2007, Basel, Switzerland.

Hurkmans, R. T. W. L., W. Terink, R. Uijlenhoet, E. J. Moors, P. A. Troch and P. H. Verburg (2009), *"Effecten van landgebruiksveranderingen op gemiddelde en extreme afvoer in het Rijnstroomgebied"*, Stromingen, 15(1), 61-74.

Terink W., R. T. W. L. Hurkmans, R. Uijlenhoet, P. M. M. Warmerdam, P. J. J. F. Torfs, *"Bias correction of temperature and precipitation data for regional climate model application to the Rhine basin"*, Report Hydrology & Quantitative Water Management group, Wageningen University.

